ULTRAFAST TIME-RESOLVED PHOTOLUMINESCENCE STUDIES OF GaAs

Thesis by

Matthew Bruce Johnson

In Partial Fulfillment of the Requirements
for the Degree of
Doctor of Philosophy

California Institute of Technology
Pasadena, California

1989

(Submitted August 15, 1988)

Acknowledgements

It is a pleasure to acknowledge Professor T.C. McGill, my advisor. I benefited greatly from being a part of his research group, and from his advice, both as a scientist and as a person.

I profited a great deal from interactions with Dr. Andy Hunter of Hughes, Malibu. Much of the success of the PECS technique used in this thesis is from his careful scientific skills in the lab and with a pencil and paper. I benefited from conversations with Mr. O.J. Marsh, also of Hughes, who kept me abreast of a variety of developments in the literature.

I profited from Dr. J.O. McCaldin, whose broad practical knowledge of semiconductor processing was appreciated.

I benefited from the hospitality extended to me by Los Alamos National Labs. This interaction involved Nick Paulter, Dr. Bob Hammond and Al Gibbs, as well as ongoing contact with Dr. Darryl Smith.

In the research group at Caltech my interaction with fellow group members was very important and rewarding both personally and scientifically. Of the distant graduates, I acknowledge: Drs. Reuben Collins, Christian Mailhiot, Arati Prabhakar, and Amikam Zur, and somewhat more recently, Ed Schlesinger, and Steve Hetzler. I enjoyed sharing an office and interacting with Dr. Bob Hauenstein, and I also appreciated my interactions with my classmates Drs. Alice Bonnefoi and George Wu. I interacted a great deal with Richard Miles both at work and outside work, and enjoyed this very much. I have profited in my association in the lab with Mike Jackson. I enjoyed designing the cleanroom and buying the MBE with Dave Chow. I have benefited from Dr. Ted Woodward especially knowledge of etching techniques. Others whom I acknowledge include Dr. Wesley Boudville, Yasantha Rajakunanyake, Dr. Dave Ting, and finally, Ed Croke, Ed Yu, and Pete Zampardi. I also enjoyed my work with Joel Seeley on computer graphics, and

with Brian Cole on the cleanroom and the MBE specifications.

In my construction of various pieces of equipment I interacted with various services provided by Caltech. Foremost was CES, where Norm Keidel, Lou Johnson, and others were always helpful in design and construction problems.

The day-to-day functioning of the group is more efficient and very much more pleasant through the work and conversation of Marcia Hudson and Carol McCollum. I also wish to acknowledge the efficient and friendly help of Vere Snell, who is still missed by those who worked with her.

I acknowledge the financial support of Caltech, the National Engineering and Research Council (NSERC) of Canada, International Business Machines (IBM) Corporation, along with the Army Research Office and the Office of Naval Research.

Finally, I would like to acknowledge those people outside my research who enriched time at Caltech. These include my family in Canada; Wyman and Wade with whom I learned to SCUBA dive; Malcolm and the Canadian Club with whom I played road hockey; those friends who shared skiing, hiking, and rock climbing; Matt who accompanied me on various bicycling adventures; those friends, especially Dave Hodge, who shared their music with me; and finally special thanks to Andrea who made life at Caltech much more enjoyable.

Abstract

This thesis concerns the study of ultrafast phenomena in semiconductor physics. At the heart of this research is the construction of a colliding-pulse mode-locked (CPM) ring-dye laser. This laser outputs ultrashort optical pulses at a high repetition rate. With a CPM laser, ultrafast semiconductor phenomena may be optically probed. In addition, using this laser to drive photoconductive circuit elements (PCEs), ultrafast electrical pulses can be generated and sampled, allowing novel high-speed devices to be electronically probed. For the measurement of ultrafast time-resolved photoluminescence (PL) a new pump/probe technique called photoluminescence excitation correlation spectroscopy (PECS) was used. The technique itself was investigated both theoretically and experimentally; it was applied to a variety of GaAs samples of interest in the development of high-speed devices.

Chapter 2 discusses the construction and alignment of the CPM laser, and the autocorrelator used to measure the ultrashort pulses. Although the laser can be run with pulse widths of < 100 fs full-width at half maximum (FWHM), in the work of this thesis, the laser was operated with pulse widths in the range 200 to 400 fs, with a repetition rate of about 120 MHz, and average output power of 10 to 30 mW.

In Chapter 3, the PECS method is investigated both experimentally and theoretically. PECS is a pulse-probe technique that measures the cross-correlation of photo-excited populations. PECS is theoretically investigated using a rate equation model for a simple three-level system consisting of an electron and hole band and a single trap level. The model is examined in the limits of radiative band-to-band dominated recombination, and capture-dominated recombination. In the former limit, no PECS signal is observed. However, in the latter limit, the PECS signal from the band-to-band PL measures the cross-correlation of the excited electron-hole population, and, thus, the electron and hole lifetimes. PECS is experimentally

investigated using a case study of PL in semi-insulating (SI) GaAs and In-GaAs. At 77 K, the PECS signal behaves as in the simple model, and an electron-hole lifetime in the range 200 ps is measured. This is much less than the expected radiative lifetime, and therefore the recombination in SI GaAs is capture-dominated. At 5 K, the behavior is more complicated, because of an acceptor, which is un-ionized at 5 K. PECS for the PL band-to-band decay, shows two decay modes: the fast decay (about 100 ps) is due to the saturable decay associated with the acceptor; and the slow decay (about 1 ns) is due to bulk capture. The acceptor-related PL also shows complicated behavior: A fast decay is associated with the band-to-acceptor transition, and the donor-acceptor PL saturates, producing a PECS signal that is negative and decays slowly.

In Chapter 4, PECS is used to investigate the large band-to-band PL contrast observed near dislocations in In-alloyed GaAs. It is found that the PL intensity contrast between a bright and dark area correlates with the ratio of the lifetimes measured using PECS in these areas. Thus, the PL intensity contrast is due to the difference in the carrier lifetimes in the different regions. The differences in the behavior of the lifetimes in the bright and dark regions with temperature suggest that the lifetime-governing defects in the two regions are different. Moreover, the defects are deep, and from the shortness of the lifetimes, neither defect is EL2. These results agree with earlier research, which indicated that defects are gettered and generated at these dislocations. The effects of surface recombination on the PL intensity and lifetimes in In-alloyed GaAs are important to the investigations of this chapter. These are investigated in Appendix E, where it is shown that both PL intensity and PECS-measured carrier lifetimes are greatly affected by surface properties and by laser dose and surface preparation. This is thought to be due to the creation of defects, which affects the surface recombination directly, and bends the electronic bands at the surface to affect the surface recombination indirectly.

These effects are reduced by minimizing the exposure to the laser and by using a recently developed Na_2S surface passivation layer.

In Chapter 5, the carrier lifetime of damaged GaAs is correlated to the cross-correlation of the PCEs fabricated on the same material. Implantation of 200 keV H^+ ions at doses in the range of 10^{11} - 10^{14} cm^{-2} is used to damage the GaAs. The carrier lifetimes are inversely proportional to the dose for doses $> 10^{12}$ cm^{-2}, and do not indicate a saturation of the damage within the range investigated. For the highest dose of 10^{14} cm^{-2}, a lifetime of 0.6 ± 0.2 ps was measured at 77 K. The PCE cross-correlation decreases less quickly than the lifetime, indicating that some effect other than the lifetime is governing the cross-correlation response speed.

Finally, two of the appendices present independent research that is worthy of note. Appendix C presents an attempt to grow HgTe on CdTe using a novel low-temperature Hg-rich melt liquid-phase epitaxial (LPE) growth technique, which involves an *in situ* cleave. Appendix D presents a program that models the behavior of ultrafast voltage pulses on a dispersive waveguide, which includes a lumped device.

List of Publications

Parts of this thesis have been or will be published under the following titles:

Chapter 3:

Picosecond time-resolved photoluminescence using picosecond excitation correlation spectroscopy,

M.B. Johnson, T.C. McGill, and A.T. Hunter, J. Appl. Phys. **63**, 2077 (1988).

Chapter 4:

Space and time resolved photoluminescence of defects at dislocations in In -alloyed GaAs substrate material,

M.B. Johnson, A.T. Hunter, and T.C. McGill, in *Mat. Res. Symp. Proc.*, Vol. 104, (Material Research Society, 1988), p.415.

Space- and time-resolved photoluminescence of defects at dislocations in In-alloyed GaAs substrate material,

M.B. Johnson, A.T. Hunter, and T.C. McGill, J. Appl. Phys. (in preparation).

Chapter 5:

Carrier Lifetimes in Ion-Damaged GaAs,

M.B. Johnson, N.G. Paulter, and T.C. McGill,Appl. Phys. Lett. (in preparation).

Appendix C:

Summary Abstract: Band offsets at HgTe CdTe interfaces,

M.B. Johnson, A. Zur, J.O. McCaldin, and T.C. McGill, J. Vac. Sci. Technol. **B 3**, 1260 (1985).

Appendix E:

The Effect of Surfaces on the Photoluminescence of In-alloyed GaAs,

M.B. Johnson, and T.C. McGill, Appl. Phys. Lett. (in preparation).

Contents

Acknowledgements ii

Abstract iv

List of Publications vii

1 Introduction 1

1.1 Introduction to Thesis 1

1.2 Ultrafast Measurement of Electronic Materials and Devices 2

1.2.1 Background 2

1.2.2 Ultrafast Measurements 6

1.2.3 Summary 24

1.3 Outline of Thesis 25

References 29

2 Colliding-Pulse Mode-Locked Laser **33**

2.1 Introduction 33

2.1.1 Result of this Work 33

2.2 CPM Laser 34

2.2.1 Background 34

2.2.2 Apparatus and Construction 41

2.2.3 Alignment Procedures 47

2.2.4 Characterization 51

2.3 Summary 55

References 56

3 Photoluminescence Excitation Correlation Spectroscopy 58

3.1 Introduction 58

3.1.1 Background 58

3.1.2 Results of Work 60

3.1.3 Outline of Chapter 61

3.2 Theory 62

3.3 Experiment 71

3.3.1 Apparatus 71

3.3.2 Samples 74

3.4 Results 75

3.4.1 Introduction 75

3.4.2 Conventional Photoluminescence 76

3.4.3 Time-resolved PL at 77 K 78

3.4.4 Time-resolved PL at 5 K 82

3.5 Discussion 87

3.5.1 Introduction 87

3.5.2 Time-resolved PL at 77 K 87

3.5.3 Time-resolved PL at 5 K 92

3.6 Summary of Results 98

References 101

4 Space- and Time-Resolved Photoluminescence 103

4.1 Introduction 103

4.1.1 Background 103

4.1.2 Results of Work 108

4.1.3 Outline of Chapter 109

4.2 Experimental 110

4.2.1 Apparatus 110

4.2.2 Samples and Processing 110

4.2.3 Procedure 111

4.3 Results 111

4.4 Discussion 119

4.5 Summary of Results 126

References 128

5 Carrier Lifetimes in Ion-Damaged GaAs **130**

5.1 Introduction 130

5.1.1 Background 130

5.1.2 Results of Work 132

5.1.3 Outline of Chapter 133

5.2 Experimental 133

5.2.1 Samples and Processing 133

5.2.2 Apparatus and Procedure 135

5.3 Results 136

5.4 Discussion 139

5.5 Summary of Results 148

References 150

A Lock-in Signal Calculations **151**

A.1 Introduction 151

A.2 Simple Case 151

A.3 Lock-in Detection in PECS 157

References 160

B Simulations of Pulses on a Waveguide with a Device 161

B.1 Introduction 161

B.2 Model -Theory 162

B.2.1 General Discussion 163

B.2.2 Detailed Discussion 165

B.3 Model -Implementation 169

B.3.1 General Discussion 169

B.3.2 Detailed Discussion 172

B.4 Results and Discussion 173

B.5 Summary and Conclusions 180

References 182

C A Novel Growth Technique for HgTe-CdTe Heterojunctions 184

C.1 Introduction 184

C.2 Apparatus and Procedure 185

C.3 Results 187

C.4 Summary and Conclusions 189

References 190

D Equipment 191

D.1 Introduction 191

D.2 CPM Laser 191

D.3 Diagnostic Tools 192

D.4 PECS Apparatus 193

E Variations of Photoluminescence and Lifetime with Laser Dose 200

E.1 Introduction 200

E.2 Experimental 201

E.3 Results 202

E.4 Discussion 207

E.5 Summary 209

References 211

List of Figures

1.1 Time Ranges of Technologies and Processes 6
1.2 Waveguide Structures 11
1.3 Photoconductive Circuit Element Pulser 12
1.4 Photoconductive Circuit Element Sampler 15
1.5 Electro-Optic Sampling Techniques 17
1.6 Michelson Interferometer 19
1.7 Pump/Probe and Pump/Sample Techniques 21
1.8 Optically Based Sampling Oscilloscope 23

2.1 CPM Laser, *circa* 1981 35
2.2 Compensated CPM Laser 38
2.3 Autocorrelators 39
2.4 Compensated CPM Laser, detail 42
2.5 Dye/Absorber Pump System 44
2.6 Collinear Autocorrelator, in detail 46
2.7 CPM Diagnosis Tools 48
2.8 Photo-Diode Signal 52
2.9 Autocorrelator Scans 53
2.10 Spectral Content of Pulses 54

3.1 Schematic of Pulse Trains on Sample 63

3.2 Simple Three Level System 64

3.3 Schematic of the PECS Apparatus 72

3.4 Schematic Band Diagram of In-alloyed GaAs 74

3.5 Photoluminescence Spectra of In-alloyed GaAs 77

3.6 Photoluminescence Spectra at 77 K 79

3.7 Delay-time Scans of GaAs Photoluminescence 80

3.8 Coherence Peak 81

3.9 Spectra from In-alloyed GaAs Sample 83

3.10 Delay-time Scans 85

3.11 Sequences of PECS Spectra 86

3.12 Table of PL Processes in GaAs at 77 K 88

3.13 Semilogarithmic Plot of Delay-time Scans 90

3.14 Table of PL Processes in In-alloyed GaAs at 5 K 94

4.1 Cathodoluminescence Image and Microphotogragh of
In-alloyed GaAs 107

4.2 Cathodoluminescence and Photoluminescence Maps of
In-alloyed GaAs 113

4.3 Photoluminescence Intensity Maps at 77 K 114

4.4 Photoluminescence Line Scans 115

4.5 Photoluminescence Spectra of Bright and Dark Areas 117

4.6 Delay-time Scans of Bright and Dark Areas 118

4.7 Intensity-Contrast Ratios and Lifetime Ratios versus Temperature . 122

4.8 Carrier Lifetimes of Bright and Dark Areas versus Temperature . . 124

5.1 Schematic of Co-planar Waveguide 134

5.2 PL Spectra for Ion-Damaged GaAs 137

5.3 PECS Delay-time Scans for Ion-Damaged GaAs 138

5.4 PCE Autocorrelation Scans 140

5.5 Simulation of Ion Damage in GaAs 141

5.6 Lifetime versus Ion Dose 144

5.7 PL Amplitude versus Ion Dose 146

5.8 PCE Autocorrelation half-width versus Ion Dose 147

B.1 Schematic of Signals on Waveguide with Device 165

B.2 Pulse Dispersion on Microstrip I 174

B.3 Pulse Dispersion on Microstrip II 176

B.4 Pulse on Microstrip with a Device I 177

B.5 Pulse on Microstrip with a Device II 179

B.6 S-Parameters Calculated from PCE Signals 181

C.1 *In Situ* Cleaving Apparatus 186

D.1 Compensated CPM Laser, in detail 192

D.2 Dye/Absorber Pump System 193

D.3 Diagnosis Tools 194

D.4 Collinear Autocorrelator, in detail 194

D.5 Schematic of the PECS Apparatus 198

E.1 PL Intensity versus Exposure Time 203

E.2 Lifetime versus Exposure Time 205

E.3 Lifetimes at 80 and 300 K 206

List of Tables

4.1 Carrier Lifetimes of Bright and Dark of Regions 119

4.2 Photoluminescence Intensity Contrast Ratio 120

A.1 Fundamental and Harmonics of ω_1, ω_2, $\omega_2 - \omega_1$, and $\omega_2 + \omega_1$ 157

D.1 Details of Compensated CPM Laser 195

D.2 Details of Dye/Absorber Pump Systems 196

D.3 Details of CPM Diagnostic Tools 196

D.4 Details of Autocorrelator 197

D.5 Details of PECS Apparatus 199

Chapter 1

Introduction

1.1 Introduction to Thesis

This thesis concerns the use of ultrafast optical pulses in investigating high-speed electronic-device technology with the intent of increasing the speed of these devices and exploring new device concepts. This is done by studying the ultrafast processes that affect the temporal behavior of electronic devices and by allowing direct measurement of the electronic characteristics of the device itself. Clearly, terms like ultrafast, ultrashort, and high-speed are relative terms that have changed with time and may refer to different time ranges for different technologies. In this thesis, ultrafast and ultrashort refer to a time range of a few picoseconds down to femtoseconds, and high-speed is used to describe electronic device speeds in a time range of nanoseconds down to picoseconds.

At the heart of the thesis work was the construction of a laser producing a train of subpicosecond pulses with a high-pulse repetition rate. This is described in detail in Chapter 2. This laser was used to make time-resolved photoluminescence (PL) studies on semiconductors, using a new pulse/probe technique. The technique itself was the subject of investigations, both theoretical and experimental,

to determine its capabilities and limitations. This is described in Chapter 3. Then the technique was applied to two problems of technological interest associated with high-speed semiconductors. The first involved the uniformity of carrier lifetimes over In-alloyed GaAs substrates, a problem of much technological interest for the fabrication of high-speed digital integrated circuits. This is described in Chapter 4. The second concerned the carrier lifetime of ion-damaged GaAs, which is used as an ultrafast photo-switch. This is described in Chapter 5.

The purpose of this introductory chapter is to provide the background relevant to this thesis research. We have not limited its scope just to the aspects of my research, but have tried to keep the view very broad to show how my research fits into this bigger picture. To achieve this, most of Chapter 1 introduces the tools and techniques used to explore ultrafast phenomena in semiconductors and to measure the electrical responses of ultrafast semiconductor electronic devices. The last section, Section 1.3, outlines the work to be reported in the remaining chapters of this thesis, along with the work reported in the appendices.

1.2 Ultrafast Measurement of Electronic Materials and Devices

1.2.1 Background

The prime focus of this thesis is the use of ultrafast optical pulses to investigate high-speed electronic technology. Ultrafast optical pulses themselves are not of interest in this study; they are used only as a tool to measure the performance of high-speed electronics and the speed of ultrafast processes. To show why special tools are necessary to make these measurements, it is useful to give an introduction to the past, and the current state, as well as future directions of

high-speed electronics, followed by the current limits of conventional measurement capabilities.

Electronic Devices

Since the first transistors were developed, semiconductor devices have been continually getting faster and smaller at a remarkable rate. On the average, device speed has increased by a factor of 10 every decade.[1] Much of this increase in speed has been due to a reduction in the size of the active areas of devices, and some has been due to improvements in device design.* The pressure to build faster devices remains today. It is being spurred by analog applications such as microwave, millimeterwave, and communications systems; and digital applications such as digital communications and high-speed switches for computers and processors.[2] (For analog applications, increased bandwidth or higher frequency operation is wanted, while for digital applications, faster switching times are required.) At present, there is still improvement to be gained by further scaling down the device size. However, there has been much improvement using new materials and structures, grown by new epitaxial growth techniques such as molecular beam epitaxy (MBE), and metal-organic chemical vapor deposition (MOCVD).[3] Materials and structures can be chosen to increase the speed of the carrier transport in the active areas of these devices, as in the case of the modulation-doped FET or MODFET.[3] In the future, scaling devices will not be as straightforward as it has been in the past. This is because of quantum-size effects and statistical fluctuations of bulk properties in the active region, which will become important at smaller dimensions. At that time, if semiconductor device speeds are to continue to increase, completely new device ideas may be required. Current examples of such exploratory devices are tunneling transistors,[4] which use tunneling transport, and ballistic electron

*The active area is the gate in field-effect transistors (FETs) and the base in bipolar transistors.

transistors,[5] which use ballistic transport.[6]

Conventional Measurements

In the design phase of a high-speed device, it is advantageous to be able to directly measure the device behavior operating at and above its intended speed. However, with conventional all-electrical measuring instruments, this is not possible. Consider a specific example of a typical state-of-the-art electrical device, the pseudomorphic InGaAs/AlGaAs modulation-doped FET based on 0.25μm lithography, as grown by Henderson *et al.*[7] This has characteristics that can be extrapolated to give a maximum frequency of oscillation, $f_{\mathbf{max}} = 200$ GHz. Note that it was necessary to extrapolate from lower frequency measurements to get $f_{\mathbf{max}}$. Direct measurement of this is very difficult using commercially available systems. (Spectrum and network analyzers typically operate up to 26.5 GHz,[8] but they can be extended with great difficulty up to 300 GHz for spectrum analyzers and to 100 GHz for network analyzers.[2]) This pseudomorphic MODFET used as a switch would have a switching delay (the time taken for the transistor to turn on) of about 2.5 picosecond (ps). This is much faster than currently available sampling oscilloscopes can observe. (Conventional sampling oscilloscopes can measure time responses of 25 ps,[9] while recently developed Josephson junction superconducting sampling oscilloscopes can measure time responses of 8 ps.[10]) Another way to measure the device's switching speed is to use it in a ring oscillator circuit. This involves making an oscillator ring, consisting of n identical devices, where n is of the order of 25, and determining the oscillation period of the ring.[1] The switching delay can be inferred to be the oscillation period divided by n. Such measurements are routinely made; however, the measurement yields only a switching time and does not give any details of the time response of the device. Thus, the high-frequency behavior of this device can be measured directly only, using

difficult electrical measurements, while the high-speed behavior cannot be directly measured at all, using conventional electrical means. This failure is not surprising. If there were electronic test equipment fast enough to make measurements of the high-speed properties of these devices, the devices themselves could not be fast enough to be of interest!

The situation for investigating ultrafast processes in semiconductors using conventional electrical techniques is similar to that for the measurement of devices. The ultrafast processes of interest are either those processes involved in limiting device speeds of current high-speed devices or those processes that the next generation of devices may use. If these processes are not faster than the fastest conventional electrical techniques, they are too slow to be of interest. Thus, conventional electronic techniques are not useful for measuring the temporal characteristics of the ultrafast processes of interest.

Summary

Conventional electronic instrumentation is too slow to allow direct time-resolved measurement of either the fast devices that are now being developed or allow direct measurement of the temporal behavior of the semiconductor processes needed to be understood for the next generation of devices. To make these measurements, novel instrumentation is required. This must be based on a technology capable of producing pulses much shorter than those produced electronically, and hence, having a bandwidth much higher than that available from electrical sources. Moreover, these pulses must be easy to use and easily converted to electrical pulses, which are shorter than those available from purely electrical means. The next subsection demonstrates that optical technology can satisfy these requirements.

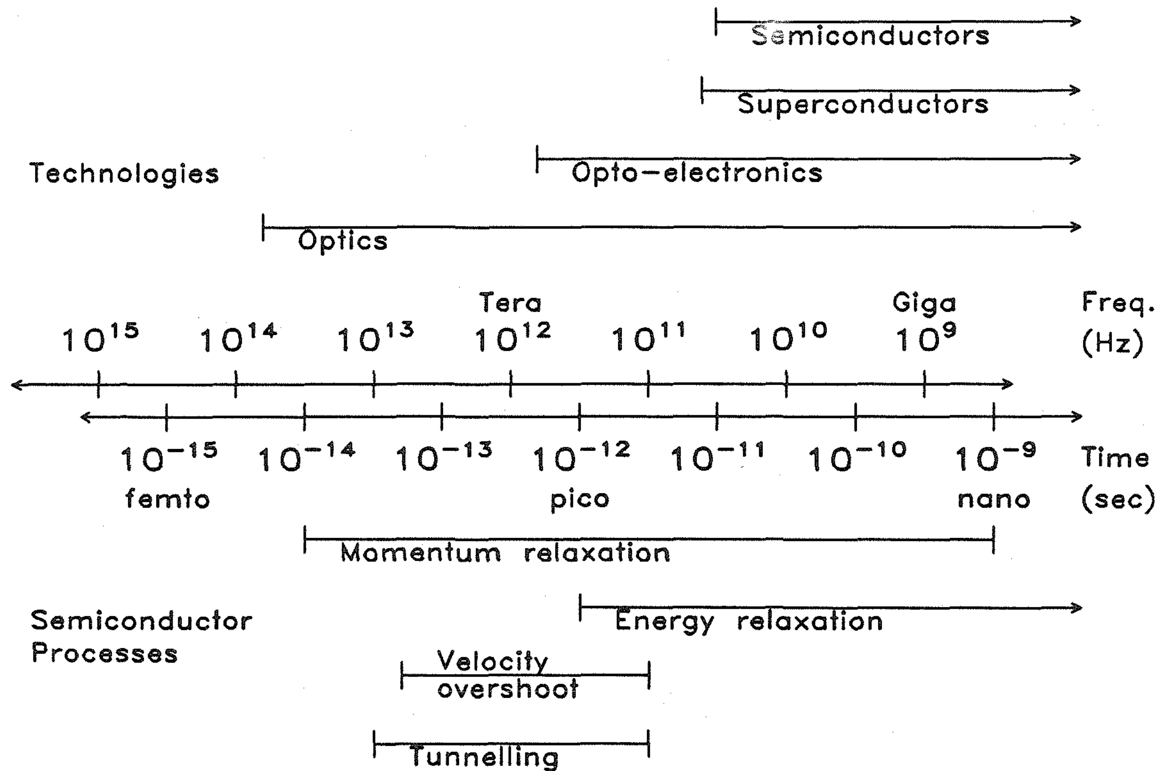

Figure 1.1: Time ranges of technologies and processes. The axes are bandwidth (frequency) and time. Above the axes the present time ranges of various technologies are shown. Below the axes, estimated ranges of important semiconductor processes are shown. (From Ref. 1.)

1.2.2 Ultrafast Measurements

Background

Consider the present state of the art of high-speed technologies. The top part of Fig. 1.1 shows the switching speeds or pulse widths that can be achieved using various technologies.[1] The left-hand end of the lines represents the fastest speed achieved. The bottom part of Fig. 1.1 shows the estimated ranges of time over

which various physical processes are important. The axes in the center show time from femtoseconds (fs) to nanoseconds (ns) and bandwidth from one thousand terahertz (THz) to gigahertz (GHz). Consider the speeds of the technologies. From Fig. 1.1 it is clear that optics is much faster than both superconducting and semiconductor electronics. Opto-electronics, which combines optical and electrical properties of materials, is at an intermediate speed. Thus, optics is the natural technology to explore the ultrafast behavior of semiconductors, or any of the other technologies. Furthermore, optics along with opto-electronics can be used to probe semiconductor devices and materials electrically.

The rest of this subsection on ultrafast measurements is broken up into measurement tools, measurement techniques, and a summary. The section headed Measurement Tools discusses the state of the art of ultrafast lasers and opto-electronic devices. The section headed Measurement Techniques discusses both how these optical tools are used to explore ultrafast processes in semiconductor materials and structures, and how the optical and opto-electronic tools are used to characterize semiconductor devices.

Measurement Tools

Optics

The requirements for an ultrafast laser used to make electrical pulses using opto-electronic devices are slightly different from that needed to directly probe materials with all-optical measurements. Both tasks require ultrafast pulses. However, driving opto-electronic devices used in making electrical measurements does not require wavelength tunability, whereas this is very useful in studying materials properties. We discuss the tunability of sources along with their pulse width because of its usefulness to optical studies.

In the last few years, a great deal of change has taken place in the availability

and reliability of ultrafast laser sources.[11,12] Moreover, optical stages that follow the sources, which compress[13] or amplify[14] these pulses, have been developed. This section briefly describes the ultrafast laser sources available, along with a brief discussion of compressors, amplifier stages, and measurements of pulse widths.

There are two main types of ultrafast lasers. These are synchronously-pumped (synch-pumped)[11,15] dye laser systems, and continuous wave (CW)-pumped colliding-pulse mode-locked (CPM) ring dye lasers.[12,16] (It is the CPM laser which is used in the work of this thesis. It is described in detail in Chapter 2.) The synch-pumped dye lasers are dye lasers that usually include a saturable absorber. They are pumped using an actively mode-locked pulsed high-powered laser such as an Ar^+ ion or a solid state YAG laser. Using various dye/saturable absorber pairs, they can produce pulse widths in the range of 100 fs over the wavelength range of 560 to 975 nm.[11] The optical power from such a laser is typically in the range of 10 mW average power or 100 pJ of energy per pulse. CPM ring dye lasers are dye lasers that include a saturable absorber jet in a passively mode-locked ring cavity. The first success of these lasers was achieved using the dye/saturable absorber pair Rhodamine 6G and DODCI with no wavelength-tuning capabilities.[17] With this pair, pulse widths as short as 30 to 40 fs with 100 MHz repetition rates at 630 nm are routinely achieved. Recently, other dye-absorber pairs have also been found to work in a CPM cavity, which includes a wavelength tuning element. Thus, the CPM laser now gives piecemeal coverage over the spectral range of 490 to 780 nm with pulse widths in the range of 100 fs.[12] The optical power from such a laser is typically in the same range as that of synch-pumped lasers.

There has been much effort to produce still shorter pulses.[18,19] This has been successfully done using compressor, and amplifier stages following the pulse laser.[13] Typically, a compressor stage consists of an optical fiber and a grating pair. The pulses from the laser are input into an optical fiber and the output pulses go

through a grating pair. The fiber broadens and chirps the pulses in the frequency domain due to nonlinearities. This means that the frequency content of the pulse is broadened such that the higher frequencies are behind the lower frequencies in both space and time.[13] (The pulse is temporally longer after the fiber.) However, by running the pulse through a grating pair, the different frequencies contained in the pulse travel different distances so that the higher frequencies can be made to catch up to the slower frequencies. This leaves a shorter or compressed pulse after the grating pair. Compression ratios of 10:1 are possible.[13] Currently, the shortest pulse produced is one generated by pulse-compressing the output of a CPM laser. The pulse produced is maximum 6 fs full-width at half-maximum (FWHM).[19] The spatial extent in air of such a pulse is 1.8 μm and it consists of about 3 periods of 630 nm light. Compression stages are now used in combination with many types of pulse-generating lasers to produce subpicosecond pulses.

The output from a pulsed laser can be amplified using a variety of optical amplifiers.[14] A typical single stage of one such amplifier consists of a dye jet, which is optically pumped using a high-power laser. This optically pumped medium amplifies the ultrafast pulse which travels through it. Amplifiers can achieve very large power gains of anywhere from 10^2 to 10^7. However, associated with this power gain is a reduction in the pulse repetition rate at the output.[14] Generally, the pulse repetition rate is inversely proportional to the gain of the amplifier. Such amplified pulses can be used to generate continuum pulses by focusing the pulses on to a plain ethylene glycol jet.[20] These continuum pulses are spectrally very broad, but remain temporally short. From them, pulses involving a small wavelength region can be selected easily and continuously over a large spectral range. However, this convenient and continuous broad-range wavelength tunability is achieved only at the expense of a reduced repetition rate. Such a reduction in repetition rate is a severe limitation since it reduces the experimental signal-to-noise ratio for a

measurement.

Measurement of ultrafast optical pulse widths must be done via completely optical means, because the optical pulses are much faster than the response times available in any other technology. Measurements of optical pulse widths are routinely made using second harmonic generation (SHG) in a nonlinear crystal such as KDP using an autocorrelation type technique.[21] (This technique is described in detail in Chapter 2.)

In summary, there are now many ways to routinely generate ultrafast optical pulses, especially with pulse compression techniques easily available. The choice of which method to pursue depends very much on the experiments to be accomplished. For the work described in this thesis, tunability was not considered important, so that a CPM laser was chosen.

Opto-Electronics

In this work, the interest in opto-electronics is to make use of ultrafast optical laser pulses in the area of electronic measurements. For such measurements, the opto-electronic devices of interest are either those converting ultrafast optical pulses to ultrafast electrical pulses, or those sampling ultrafast electrical signals using ultrafast optical pulses.[2,22] The first device is called a pulser, and the second device is called a sampler. Both pulsers and samplers are discussed below.

For the generation and propagation of ultrafast electrical pulses, high-frequency waveguide structures must be used. These are necessary, even over very short distances, to allow pulse propagation without large dispersion and absorption of the pulses.[1,3] The most commonly used waveguide structures are microstrip, coplanar waveguide, and coplanar stripline.[25] Figures 1.2(a)-(c) show the geometries and typical dimensions of these waveguides. The conductors in these waveguides are in good ohmic contact with the insulating substrate.

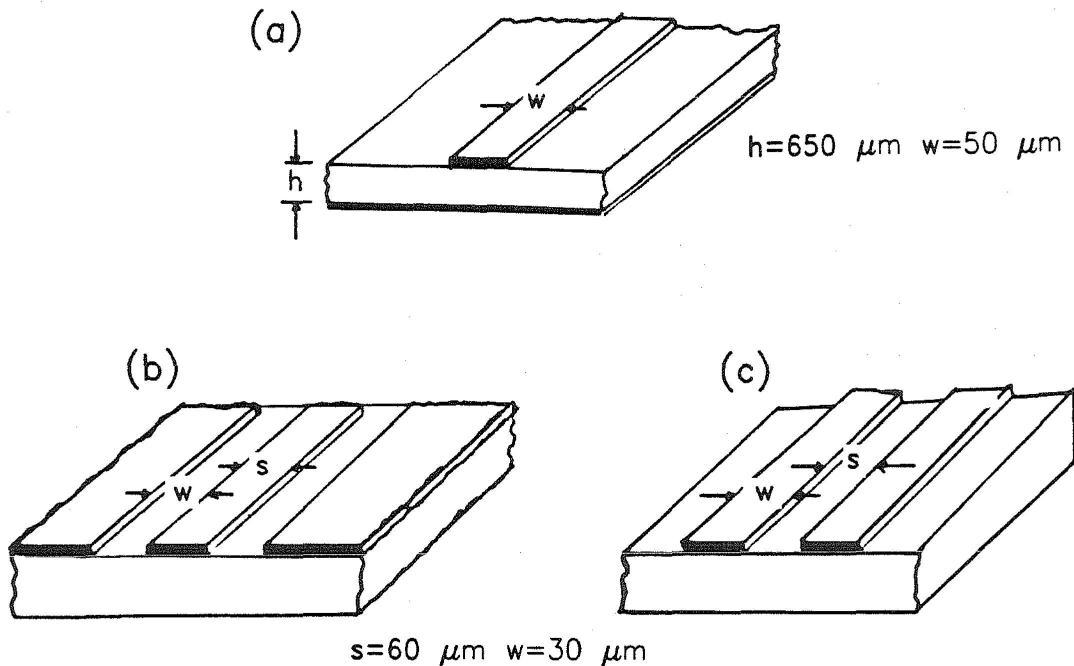

Figure 1.2: Waveguide structures: (a) Microstrip, (b) Coplanar waveguide, (c) Coplanar strips. (From Ref. 25.) See also Chapter 5.

Optical pulses can be used to generate electrical pulses in a waveguide structure by driving photoconductive circuit elements (PCEs), also known as Auston switches.[22,26] This involves illuminating a photoconducting substrate material in a narrow gap between conductors. Figure 1.3(a) shows a typical PCE on microstrip. In this case, a stripline electrode at voltage V_B is perpendicular to the center strip with a small gap separating them. This gap in the conductors, with the photoconductor in between, is the PCE. Figures 1.3(a)-(d) show the behavior of the PCE under the illumination of an ultrafast pulse. Figure 1.3(a) shows the PCE before the arrival of the optical pulse. There is no signal on the line because the PCE is insulating, so that the electrode strip and center strip are uncoupled. Illumination of the PCE produces carriers in the gap, making it conducting, so that current flows across the gap, producing a voltage signal on the center line at the PCE as

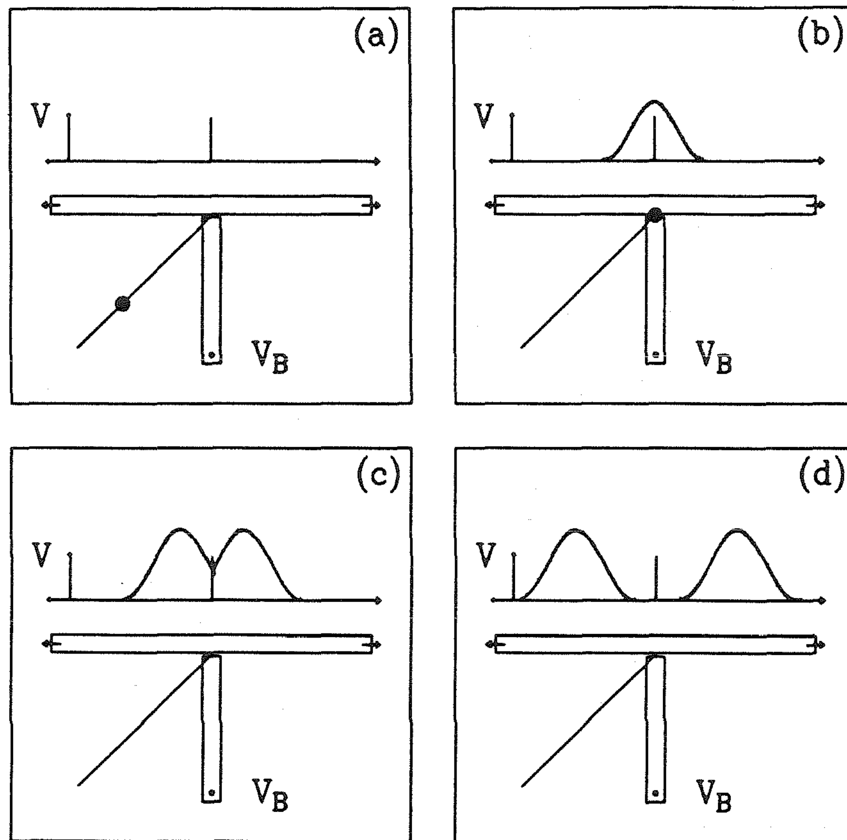

Figure 1.3: Photoconductive circuit elements (PCEs) on microstrip, in pulser configuration. V_B is the bias voltage on the PCE and V is the voltage signal on the waveguide. The operation of a typical PCE is shown in (a)-(d). (a) Before optical pulse - PCE is off. (b) About 0.5 ps after optical pulse - carriers have been generated in the gap and the PCE is turning on. (c) About 1.5 ps after optical pulse - carriers are starting to recombine and the PCE is turning off. (d) About 10.0 ps after optical pulse - carriers have recombined and the PCE is off.

shown in Fig. 1.3(b). The PCE remains conducting, even after illumination by the optical pulse, because the lifetimes of the carriers in the PCE are longer than the optical pulse itself. While the PCE remains conductive, current continues to flow across the gap as the voltage signal propagates away from the PCE in both directions, as shown in Figs. 1.3(c)-(d). The turn-on of the device is very sharp, since the carriers are generated over the short duration of the optical pulse. The geometry of the PCE governs the details of the actual leading edge of the pulse produced. The turn-off of the device is slower because of the longer lifetime of the carriers. Details of these processes have been investigated by Auston.[22]

For many, although not all applications, PCEs are required that not only turn on quickly but also turn off quickly.[22,27] To make PCEs turn off quickly, a substrate material with high mobility, yet low carrier lifetime, is necessary.[22] High carrier mobility will result in large electrical-pulse amplitudes, while short carrier lifetime gives a faster turn-off. Generally, short carrier lifetimes require high levels of trapping defects, which reduce the carrier mobility. Thus, there is a compromise between the pulse width and pulse amplitude. Typically, PCEs are made in two different ways. In one method, the required defects are grown into the substrate, such as with polysilicon,[28] or amorphous silicon.[29] The other method involves introducing defects by damaging a relatively defect-free substrate, such as GaAs, using ion-implantation. There are many different procedures for damaging both Si and GaAs to produce PCEs.[30,31] (Chapter 4 involves investigating the effectiveness of one of these procedures.) The fastest electrical pulses are produced using a variation of a PCE called a sliding contact switch.[32] This consists of photoconductively shorting a charged coplanar stripline, and the resulting pulses are 0.6 ps long.[32] However, typical PCEs have full-width at half-maximum (FWHM) in the range of 1 to 5 ps.[28,29,30,33,34] There has been much work to develop PCEs that can be made with techniques found on integrated circuit (IC) fabrication lines.[28,31]

These are used as sources of ultrafast electrical pulses on ICs themselves to study the device properties on the IC.

The other opto-electronic device required to make electrical measurements is the sampler. Samplers allow the measurement of ultrafast electrical pulses on a waveguide structure. Two important samplers, the PCE sampler,[22,32,31] and the electro-optic (E-O) sampler,[2] are discussed below. Two other samplers are the picosecond photo-electron scanning electron microscope[35] and the photo-emission sampler.[36] These samplers are particularly useful for measuring circuit response at different locations; however, they are not discussed further.

PCE samplers are similar in structure to the PCE generators.[22] Figure 1.4 shows the PCE structure used on microstrip in a sampling configuration. As with the pulser PCE, the sampler PCE turns on when illuminated by the optical pulse, which shorts the PCE gap. The sampler electrode is not biased, so that part of the charge on the center line associated with a passing voltage signal is shunted to the sampling strip, while the PCE remains on. This shunted charge can be detected using an ammeter. Thus, the PCE samples the voltage signal on the center line as it passes the PCE. The resolution of the sampler is given by the time the PCE is on, which is typically 1 to 5 ps.[28,33,32] Actual measurements require this sampling process to be repeated at high-repetition rates to produce currents large enough to be detected.

The second important type of sampler is the electro-optic (E-O) sampler.[2] There are various electro-optic (E-O) sampling schemes that can be used, all of which make use of the E-O effect to measure the electric field (E-field) in an E-O active material placed in proximity to the waveguide, so as to determine the voltage signal on the waveguide. The electro-optic effect used is the interaction in certain E-O active materials of an E-field with an optical pulse.[2] It causes a detectable change in the polarization of the optical beam by an amount proportional to the

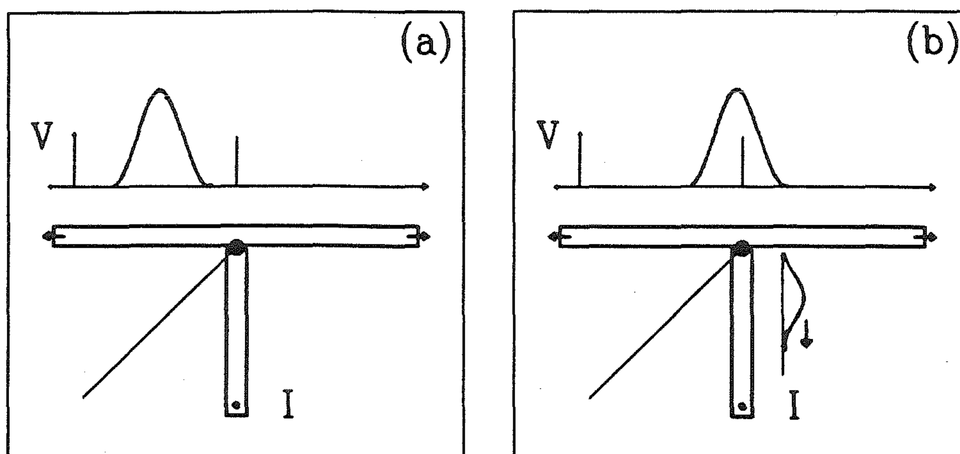

Figure 1.4: Photoconductive circuit elements (PCE) on microstrip in sampling configuration. *I* represents an ammeter that measures the current through the PCE and V is the voltage signal on the waveguide. (a) shows a laser pulse incident before the voltage signal reaches the PCE -no current is shunted. (b) shows a laser pulse incident as the voltage signal reaches the PCE -current is shunted.

E-field strength perpendicular to the optical path. The average *E*-field in the E-O material is measured by detecting the change in polarization of the probing beam. With suitable choice of geometry of optical beam and waveguide, this detected polarization change is proportional to the convolution of the voltage on the waveguide with a response function. This response function takes into account both the response of the E-O material and the effect of fringing fields.

The most common E-O sampling schemes are shown in Figs. 1.5(a)-(c) and briefly described below. In Fig. 1.5(a) the GaAs substrate itself is used as the E-O material.[2] An advantage of this scheme is that no external E-O material is required. A disadvantage, however, is that GaAs is not transparent to visible light, so that infrared pulses must be used in order to penetrate the GaAs and make use of its E-O properties. In Fig. 1.5(b), the optical pulse measures the *E*-field in a thin film

of an E-O active material, such as lithium niobate deposited on the waveguide.[37] Using lithium niobate visible pulses can be used. However, the presence of the E-O layer itself may affect the electrical pulses. Fig. 1.5(c) shows an elegant sampling scheme called an E-O needle probe that has recently been developed.[38] The E-O material is on the tip of a silica rod, about $40\mu m \times 40\mu m$ in size, and is positioned within the E-field of the waveguide. The optical pulse is confined to the silica rod and guides the light to the E-O tip and back again. This technique reduces the effect of the E-O material on the waveguide. Moreover, such probes can be easily moved, making them very versatile for circuit applications. Sampling speeds in the range of about 500 fs have been attained for the lithium niobate E-O sampler and E-O needle probe,[37,38] and in the range of about 1 ps for the internal GaAs E-O sampler.[2]

The choice of opto-electronic pulsers and samplers depends very much on the type of measurements to be made. Noninvasive sampling is best in the case of the probing of devices on a chip. Using the electro-optic properties of GaAs works well for GaAs circuits.[2] PCE pulsers and samplers can be used in the case of testing of single devices. PCE pulsing and sampling is used in this work.

Summary

Summarizing the measurement tools, firstly, we see that the fastest optical pulses are orders of magnitude faster than the fastest electronic device speeds, so that they can be readily used to explore semiconductor processes, which may limit device performance. Secondly, opto-electronics transducers are faster than the fastest electronic device speeds, so that they can be used to electrically measure the response of electronic devices. The techniques used to make such optical and electrical measurements are outlined below in the Measurement Techniques subsection.

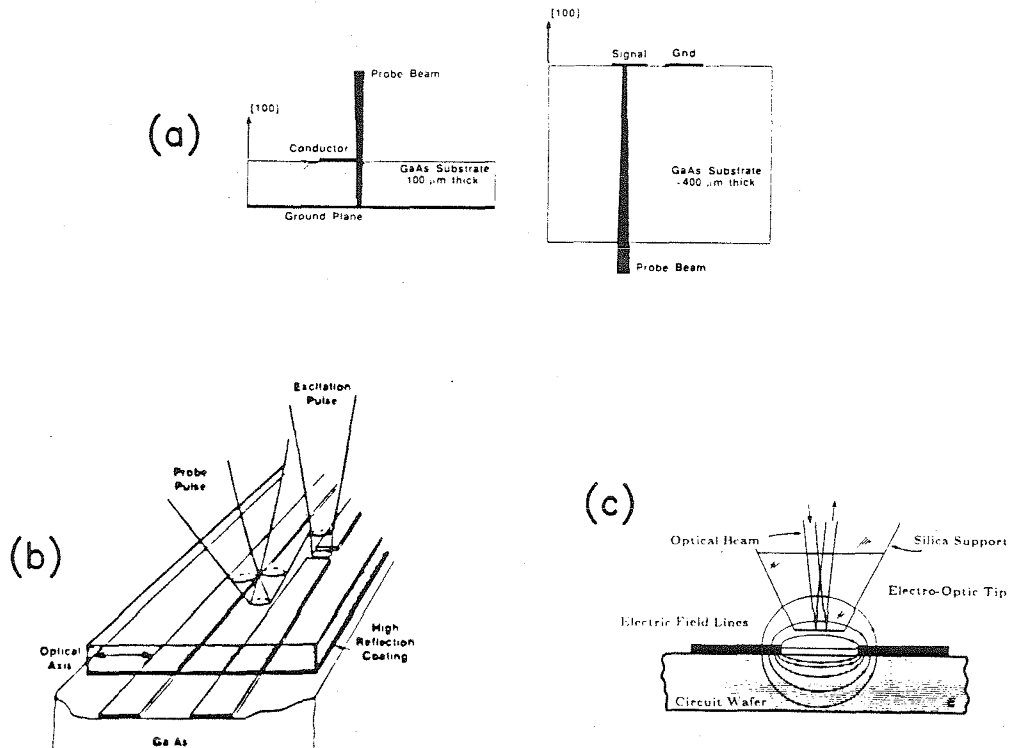

Figure 1.5: Electro-Optic Sampling Techniques. (a) Uses electro-optic (E-O) effect in GaAs substrate, itself. (From Ref. 2.) (b) Uses E-O material such as lithium niobate.(From Ref. 37.) (c) Uses E-O needle probe.(From Ref. 38.)

Measurement Techniques and Examples

The general method to measure ultrafast processes is to use pulse/sample type experiments.[39] This involves two pulses. The first pulse is used to excite the process of interest and the second pulse, which arrives a precisely controlled time after the first pulse, samples the effect of the first pulse. The temporal behavior of the process can be determined by varying the time between the pulsing and sampling. Such experiments involve repetitive excitations of the process, rather than single shots, and require the ability to continually vary the time between the pulser and sampler. The resolution of such a method is directly related to the width of the pulsing and sampling pulses, as well as jitter between the pulses. (Jitter is the uncontrolled variation in the time delay between the pulsing and sampling pulses.[2])

These pulse/sample types of experiments are routinely used in the electronic domain to investigate electronic phenomena, such as the turn-on of fast devices. Conventionally, this is done using a sampling oscilloscope. These were briefly mentioned earlier. In a conventional sampling oscilloscope, the electrical pulses are called the trigger and sampler. Specifically, an electrical trigger is input to a device and another pulse delayed in time is used to sample the device's output signal. By repeating over many shots, while changing the delay time, the output waveform is obtained. The fastest commercially available conventional sampling oscilloscopes have 25 ps resolution.[9] A new sampling oscilloscope based on Josephson junction superconducting technology was recently introduced. This has a time resolution of 8 ps.[10] In both of these types of sampling oscilloscopes, jitter is an important limitation on the performance.

The same sampling techniques can be used with optical pulse trains. Two pulse trains are required, one to excite and the other to sample. The time between nearest pulses in the exciting train and those in the sampling train must be continuously

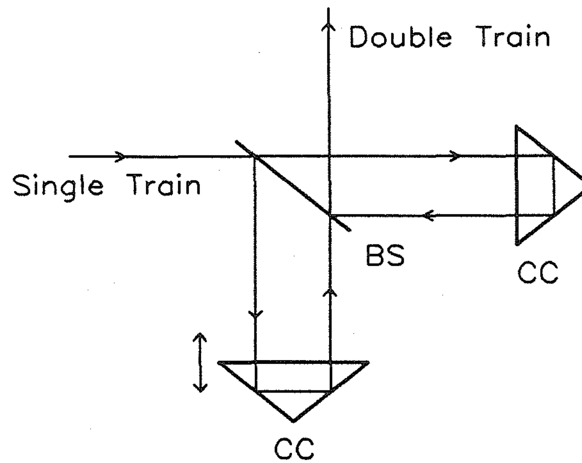

Figure 1.6: Michelson interferometer. A single pulse train is incident on the beam splitter, BS; the two beams generated are retroreflected using corner cubes, CC; and the two beams are recombined by the beam splitter. This produces two pulse trains superimposed on one another, or a double pulse train. The separation of pulses in the double pulse train is controlled by moving one of the corner cubes.

variable. This is achieved by using a Michelson interferometer, shown in Fig. 1.6. A single pulse train from an ultrafast laser is split into two trains using a beam splitter. The two trains are recombined after traveling down different arms of the interferometer. By varying the length of one of the interferometer arms, the times between the exciting and sampling pulses can be varied. The relationship between δd, the change in the arm length, and the change in time between the pulses, δt, is given by $\delta t = 2\delta d/c$. Using available translation stages, δd is easily controllable to 0.5 μm, giving a δt of 3 fs. Thus, the interferometer gives essentially jitter-free control of the delay between the pump and probe pulses. The interferometer is an important part in any pulse/sample apparatus. The temporal resolution of the interferometer is related only to the widths of the exciting and probing pulses since the jitter is negligible. Another benefit of using optical pulses is that high-pulse

repetition rates are involved, typically in the range of 100 MHz. This dramatically improves the signal-to-noise ratio for a measurement.

In the case of exploring physical phenomena directly with optical pulses, several different pulse/sample techniques may be used.[39] Figures 1.7(a),(b) schematically show such techniques. Figure 1.7(a) shows a pump/probe type experiment. In this type of technique, both the pump and probe pulses interact directly with the sample. In one version of this technique, two pulse trains of equal power are collinearly focused on a thinned sample, and the transmitted signal is monitored. This is called equal-pulse transmission correlation and has been used to investigate the interaction of hot carriers in GaAs.[40] Another version of the pump/probe technique uses two pulses of equal power to excite electrons and holes in the semiconductor sample. By looking at the photoluminescence (PL), carrier lifetimes can be determined. This method has been called population mixing[41] or photoluminescence excitation correlation spectroscopy (PECS).[42,43] The PECS experimental technique was investigated and used in this work. The time resolution of these pump/probe techniques is directly related to the width of the optical pulses.[43] Figure 1.7(b) shows a pulse/sample technique, which uses one pulse to excite the sample directly and another pulse to gate the optical output from the excited sample.[44,45] This requires an ultrafast optical gate, a nonlinear optical device in which the presence of the gating pulse allows the transmission of the PL signal. Versions of this technique are used to obtain ultrafast time-resolved PL. The time resolution of this technique is determined by the width of the optical pulses and the response of the optical gate.[44,45]

For the case of electronic measurements, the combination of a Michelson interferometer along with an opto-electronic pulser and sampler allows the construction of an optically based sampling oscilloscope.[1,2,6] The optical pulses generate the electrical trigger pulse using a PCE, and the sampling of the electrical output sig-

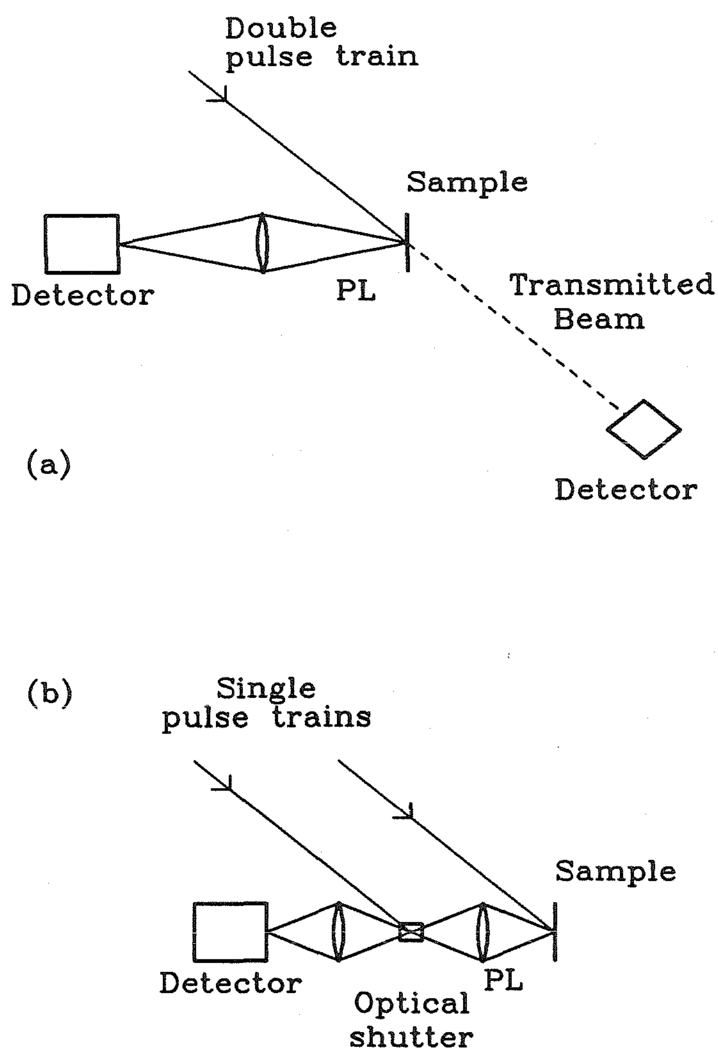

Figure 1.7: Schematic representations of Pump/Probe and Pump/Sample techniques. (a) Pump/Probe experiment. The delay time between pulses is varied, while the output beam is monitored. This gives a cross-correlation of the response to one pulse with the response to the other. (b) Pump/Sample experiment. The pulses incident on the optical shutter gate that the PL generated by the pulses incident on the sample. This gives the time-resolved PL response.

nal is done using an optical pulse with a sampler. The Michelson interferometer allows the time between the trigger pulse and sampling to be scanned. Figure 1.8 shows an optically based sampling oscilloscope used to probe a device. The time resolution of the optically based sampling oscilloscope is given by the width of the pulser and sampler response. (The jitter is negligible.) Currently, this is in the order of 1 to 5 ps.[2,33,37] There are numerous advantages to this type of measurement over conventional all-electronic measurements. They are: 1) The optically based oscilloscope has a much faster time response than the conventional sampling oscilloscope. 2) The optically based sampling oscilloscope is jitter-free, while jitter is a serious problem for conventional sampling oscilloscopes. 3) Conventional electrical-domain measurements rely on taking a high-frequency signal off the device under test, while the optically based sampling oscilloscope leaves the high-frequency signals on or near the device, since it requires only low-frequency connections to the pulser and sampler. Taking high-frequency signals off the device requires high-frequency connectors. These connectors add extraneous reflections to signals measured and they usually attenuate high frequencies, thus reducing the temporal resolution of the measurement.[2] 4) Using the optically based sampling oscilloscope devices can be probed in two different amplitude regimes. The first is the small signal regime, which gives the s-parameters of the device, which are important for analog applications.[12] The second is the large signal regime, which gives the turn-on characteristics of the device, which are important for digital applications. This covers the region of a conventional sampling oscilloscope and network analyzer.[2] 5) The optical measurements have a higher measurement repetition rate than conventional measurements, so that the signal-to-noise ratio (S/N) is better in the optical case. The major disadvantage of the optically based sampling oscilloscope is that it requires an ultrafast pulsed laser and special pulser and sampler devices. However, from the long list of advantages, it is clear

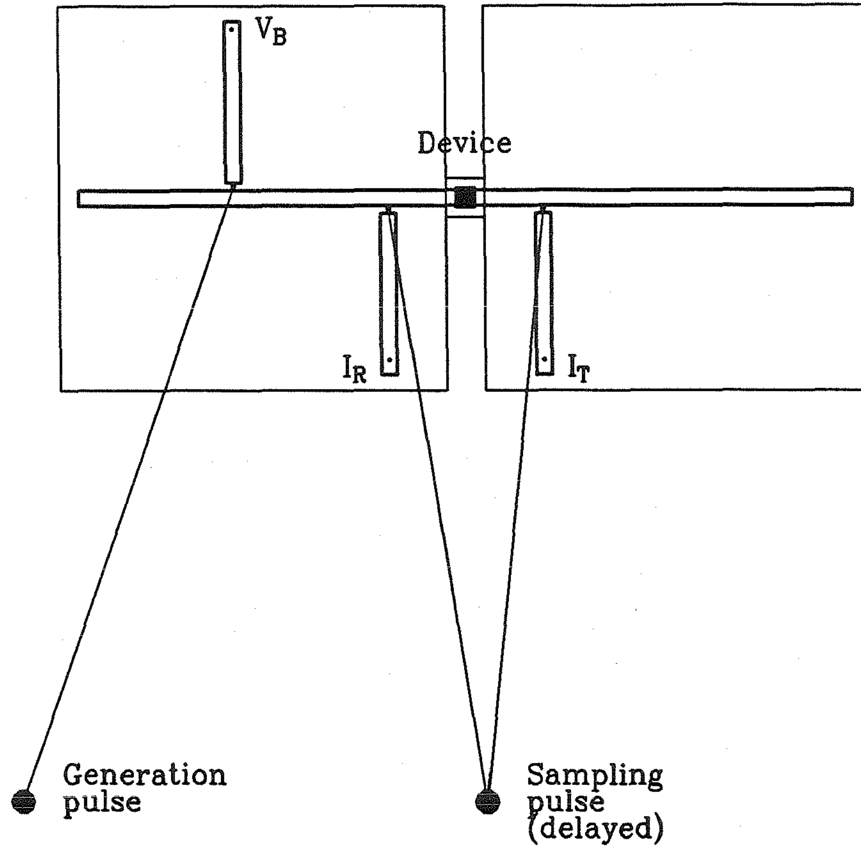

Figure 1.8: Optically based sampling oscilloscope measuring pulse response of a device. V_B is the bias voltage for pulse generation; I_R and I_T give the reflection and transmission response. A generation pulse generates a voltage pulse on the microstrip, which is incident on the device. The sampling pulse samples either the device's reflected or transmitted response.

that the optical sampling oscilloscope is a very promising technique to investigate high-speed devices.

Summary

Ultrafast optical pulses can be used directly to make optical measurements of the time behavior of processes in semiconductors, with temporal resolution governed by the optical pulse widths (typically 50 fs). As well, ultrafast optical pulses in conjunction with opto-electronic switches may be used to make an optically based sampling oscilloscope, which has a temporal resolution governed by the speed of the opto-electronic switches (typically in the range of 1 to 5 ps).

1.2.3 Summary

In Section 1.2 it has been shown that ultrafast optical techniques and ultrafast opto-electronic devices can be used to make two types of measurements, which are of great importance for the increase of the speed of high-speed electronics. The first type of measurement is the temporal resolution of the electrical behavior of high-speed devices of current interest. It was shown that these measurements cannot be made using conventional electronic techniques. However, using an ultrafast pulsing laser to drive opto-electronic switches, an optically based sampling oscilloscope can be constructed, which can make these time-resolved measurements. The second type of measurement is to resolve, temporally, the behavior of ultrafast semiconductor phenomena, that either affects the speed of high-speed electrical devices or can be used as the basis for a new generation of high-speed devices. These measurements can be made by using ultrafast optical pulses to perform optical pulse/sample or pulse/probe-type experiments directly on the semiconductors.

1.3 Outline of Thesis

This thesis describes the construction of a colliding-pulse mode-locked (CPM) ring dye laser capable of generating subpicosecond pulses. This laser was used to make ultrafast time-resolved photoluminescence (PL) measurements using a novel technique. This technique is called photoluminescence excitation correlation spectroscopy (PECS). Before using this technique, further understanding of the PECS technique was required. This was obtained by using a simple theoretical model and doing an experimental case study. PECS was then applied to two problems of technological importance involving semiconductors. The first involved time and space variations of carrier lifetime in In-alloyed GaAs. The second involved comparing carrier lifetimes in ion-damaged GaAs with the speeds of PCEs fabricated on these samples, for different ion-implantation doses. The following sections are a brief summary of the chapters of this thesis. This is followed by a brief summary of the appendices.

Chapter 2: CPM Ring Dye Laser

This chapter goes into the details of the colliding-pulse mode-locked (CPM) ring dye laser constructed. It starts with a brief background of CPM lasers, and then the construction and alignment of the CPM laser are discussed. This contains not only the techniques that are commonly used but also the specific procedures we have found useful. Finally, the characterization of the laser is discussed. This includes a brief background on second-harmonic generation (SHG) autocorrelators, which are used to determine pulse widths, and ends with the characterization of the pulses used in the experiments discussed in the following chapters. These pulses were measured and found to be 250 fs wide (FWHM), centered at a wavelength of 620 nm with a 120 MHz repetition rate and an average power of about 10 to 30 mW.

Chapter 3: Photoluminescence Excitation Correlation Spectroscopy

This chapter deals with photoluminescence excitation correlation spectroscopy (PECS), the novel technique used to do ultrafast time-resolved photoluminescence (PL) spectroscopy. This method is briefly compared to other time-resolved PL techniques, and then the PECS technique and apparatus are discussed. The technique is modeled using the rate equations for a simple two-band system with a trapping level. Finally, the experimental technique is applied to samples of semi-insulating (SI) GaAs and In-alloyed GaAs in a case study.

The results of the theoretical modeling indicate that a PECS signal for near band-to-band luminescence is observed only if some of the electrons and holes recombine by some parallel process, in this case through a deep level trap, rather than recombine only by band-to-band radiative recombination. In the case where a trap dominates the carrier recombination, the PECS signal gives the carrier lifetime.

At 77 K, the PECS signal behaves as in the simple model, and an electron-hole lifetime in the range 200 ps is measured. This is much less than the expected radiative lifetime, and therefore the recombination in SI GaAs is capture-dominated. At 5 K, the behavior is more complicated because of the acceptor, which is un-ionized at 5 K. PECS for the PL band-to-band decay shows two decay modes: the fast decay (about 100 ps) is due to a saturable decay associated with the acceptor, and the slow decay (about 1 ns) is due to bulk capture. The acceptor-related PL also shows complicated behavior: A fast decay is associated with the band-to-acceptor transition, and the donor-acceptor PL saturates, producing a PECS signal that is negative and decays slowly.

The most important result is that PECS can measure the carrier lifetime in a semiconductor whose lifetime is dominated by capture onto a trap.

Chapter 4: Carrier Lifetimes in In-Alloyed GaAs

Using PECS, a study of the variation of carrier lifetimes over the surface of semi-insulating In-alloyed GaAs substrate material was made. The purpose of this was to try to understand the contrast observed in photoluminescence (PL) intensity in the neighborhood of dislocations. This is of much technological interest because understanding the spatial variation of electrical properties of GaAs substrates is important for digital integrated circuits (ICs).

It is found that the PL intensity contrast is due to lifetime differences in the bulk material.* By studying the lifetimes at different temperatures, it is found that the dominant lifetime-governing defect in the bright regions is different from that in the dark regions. Furthermore, both the defects have electronically deep levels, and neither defect is EL2, an important defect in these materials. This supports the view that defects are generated and gettered at dislocations, giving rise to PL contrast in the neighborhood of the dislocation.

Chapter 5: Carrier Lifetimes versus Dose of Ion-Implanted GaAs

In this chapter, the effectiveness of a procedure for making photoconductive circuit elements (PCEs) on GaAs is investigated. The procedure uses 200 keV H^+ ions at doses in the range of 10^{11} to 10^{14} cm^{-2}. The approach of this study was to compare the carrier lifetimes measured, using PECS, with the speed of the PCE as measured using a PCE autocorrelation measurement.

Other work on the PCEs found that the fastest PCE was obtained for a dose of 6×10^{13} cm^{-2}, with no improvement at higher dose levels. It was thought that this may be due to a saturation in the amount of damage that can be introduced into GaAs, using this type of implant. However, experimentally, no such saturation was seen up to an implant of 1×10^{14} cm^{-2}. This dose gave rise to a carrier lifetime of

*In this context, bulk means the top 0.25 μm.

0.6 ± 0.2 ps. Thus, the limit of the PCE speed is not a saturation of damage.

Appendices

There are 5 appendices. They are outlined briefly below.

Appendix A: This appendix is a detailed analysis of the signal processing used in a double chopping difference lock-in scheme. The PECS analysis of the simple three-level semiconductor model is treated.

Appendix B: This appendix explains the details of a computer model used to generate movies simulating the generation and propagation of pulses on a waveguide, and to show how these pulses interact with a lumped element device. A brief example is included.

Appendix C: This appendix describes briefly some work on the growth of HgTe on CdTe using a novel liquid phase epitaxial (LPE) growth technique involving an *in situ* cleave.

Appendix D: This appendix lists details of the equipment used in the apparatus constructed for the work described in this thesis, and includes the CPM laser, the autocorrelator, and the PECS set up.

Appendix E: This appendix summarizes investigations into the effect of surfaces on the carrier lifetime measured, using PL decay, and the change in PL intensity with laser dose. These investigations were carried out on In-alloyed GaAs.

References

1. C.V. Shank and D.H. Auston, Science **215**, 797 (1982).

2. K.J. Weingarten, M.J.W. Rodwell, and D.M. Bloom, IEEE J. of Quantum Electron. **QE-24**, 198 (1988).

3. See, for example, *Synthetic Modulated Structures*, edited by L.L. Chang and B.C. Geissen (Academic Press, New York, 1985).

4. A.R. Bonnefoi, D.H. Chow, and T.C. McGill, Appl. Phys. Lett. **47**, 888 (1985).

5. M. Heilblum, I.M. Anderson, and C.M. Knoeller, Appl. Phys. Lett. **49**, 207 (1986).

6. N. Chand and H. Morkoc, in *Picosecond Electronics and Opto-electronics*, edited by G.A. Mourou, D.M. Bloom, C.H. Lee (Springer series in Electrophysics 21, New York, 1985), pp. 9-17.

7. T. Henderson, M. I. Aksun, C.K. Peng, H. Morkoc, P.C. Chao, P.M. Smith, K.-H.G. Duh, and L.F. Lester, IEEE Electron Dev. Lett **EDL-7**, 649 (1986).

8. Hewlett-Packard network analyzer HP 8510 works in the range 45 MHz to 26.5 GHz. The newly released HP 8510B works up to 100 GHz.

9. Tektronics sampling oscilloscope, with 7S11 sampler and S4 sampling head, has 25 ps risetime.

10. HYPRES sampling oscilloscope, using Josephson junctions has 8 ps risetime.

11. M.D. Dawson, T.F. Boggess, and A.L. Smirl, Opt. Lett. **12**, 254 (1987).

12. P.M.W. French, and J.R. Taylor in *Ultrafast Phenomena*, Vol. V, (Springer Series in Chemical Physics 46, New York, 1986). pp. 11-13.

13. B. Nikolaus and D. Grischkowski, Appl. Phys. Lett. **43**, 228 (1983).

14. W.H. Knox, IEEE J. of Quantum Electron. **24**, 388 (1988).

15. M.C. Nuss, R. Leonhardt, and W. Zinth,, Opt. Lett. **10**, 16 (1985).

16. J.A. Valdmanis, and R.L. Fork, IEEE J. of Quantum Electron. **QE-22**, 112 (1986).

17. R.L. Fork, B.I. Greene, and C.V. Shank , Appl. Phys. Lett. **38**, 671 (1981).

18. W.H. Knox, R.L. Fork, M.C. Downer, R.H. Stolen, C.V. Shank, and J.A. Valdmanis, Appl. Phys. Lett. **46**, 1120 (1985).

19. W.H. Knox, R.L. Fork, M.C. Downer, R.H. Stolen, C.V. Shank, J.A. Valdmanis, Appl. Phys. Lett. **46**, 1120 (1985).

20. R.L. Fork, C.V. Shank, C. Hirlimann, R. Yen, and W.J. Tomlinson, Opt. Lett. **8**, 1 (1983).

21. E.P. Ippen, and C.V. Shank, in *Ultrafast Light Pulses*, edited by S.L. Shapiro (Springer-Verlag, New York, 1977), Chap. 3.

22. D.H. Auston, IEEE J. of Quantum Electron. **QE-19**, 639 (1983).

23. D.H. Auston, in *Picosecond Opto-electronic Devices*, edited by C.-H. Lee (Acedemic Press, London, 1984) pp. 73-116.

24. D.E. Cooper, Appl. Phys. Lett. **47**, 33 (1985).

25. K.C. Gupta, R. Garg, I.J. Bahl, *Microstrip Lines and Slot Lines* (Artech House, New York, 1979).

26. B.Y. Hwang, F.A. Lindholm, and R.B. Hammond, IEEE J. of Quantum Electron. **QE-19**, 648 (1983).

27. K. Meyer, D.R. Dykaar, G.A. Mourou, in *Picosecond Electronics and Optoelectronics*, edited by G.A. Mourou, D.M. Bloom, C.H. Lee (Springer series in Electrophysics 21, New York, 1985), pp. 54-57.

28. W.R. Eisenstadt, R.B. Hammond, and R.W. Dutton, IEEE Electron. Device Lett. **EDL-5**, 296 (1984).

29. A.M. Johnson *Semiconductors Probed by Ultrafast Laser Spectroscopy*, Vol. II, edited by R.R. Alfano (Academic Press, New York, 1984), Chap. 14.

30. F.E. Doany, D Grischkowski, and C.-C. Chi, Appl. Phys. Lett. **50**, 460 (1987)

31. D.H. Auston, and P.R. Smith, Appl. Phys. Lett. **41**, 599 (1982).

32. M.B. Ketchen, D. Grischkowski, T.C. Chen, C-.C. Chi, I.N. Duling III, N.J. Halas, J.M. Halbout, J.A. Kash, and G.P. Li, Appl. Phys. Lett. **48**, 751 (1986).

33. N.G. Paulter, and R.B. Hammond have made PCEs by damaging GaAs, which have an autocorrelation FWHM of about 3 ps. Private communication.

34. P.M. Downey, and B. Schwartz, Appl. Phys. Lett. **44**, 207 (1984).

35. P.J. May, J.-M. Halbout, G. L.-T. Chiu, IEEE J. of Quantum Electron. **QE-24**, 234 (1988).

36. A.M. Weiner, P.S.D. Lin, R.B. Marcus, Appl. Phys. Lett. **51**, 358 (1987).

37. G.A. Mourou, and K.E. Meyer, Appl. Phys. Lett. **45**, 492 (1984)

38. J.A. Valdmanis and S.S. Pei, in *Picosecond Electronics and Optoelectronics.* (Springer-Verlag, New York, 1987).

39. D.L. Rosen, A.G. Doukas, A. Katz, Y. Budansky, and R.R. Alfano, in *Semiconductors Probed by Ultrafast Laser Spectroscopy*, Vol. II, edited by R.R. Alfano (Academic Press, New York, 1984), Chap. 24.

40. M.K. Rosker, F.W. Wise, and C.L. Tang, Appl. Phys. Lett. **49**, 1726 (1986).

41. D. Rosen, A.G. Doukas, Y. Budansky, A. Katz, and R.R. Alfano , Appl. Phys. Lett. **39**, 935 (1981).

42. M. Jorgensen, and J.H. Hvam, Appl. Phys. Lett. **43**, 460 (1983).

43. M.B. Johnson, T.C. McGill, A.T. Hunter, J. of Appl. Phys. **63**, 2077 (1988)

44. P.P. Ho, in *Semiconductors Probed by Ultrafast Laser Spectroscopy*, Vol. II, edited by R.R. Alfano (Academic Press, New York, 1984), Chap. 25.

45. J. Shah, IEEE J. of Quantum Electron. **QE-24**, 276 (1988).

46. G. Mourou, K. Meyer, J. Whitaker, M. Pessot, R. Grondin, and C. Caruso, in *Picosecond Electronics and Opto-electronics* II, (Springer Series in Electrophysics 24, New York, 1988).

47. D.E. Cooper, and S.C. Moss, in *Picosecond Electronics and Opto-electronics*, edited by G.A. Mourou, D.M. Bloom, C.H. Lee (Springer series in Electrophysics 21, New York, 1985), pp. 62-65.

Chapter 2

Colliding-Pulse Mode-Locked Laser

2.1 Introduction

Colliding-pulse mode-locked (CPM) ring dye lasers are the most commonly used lasers capable of producing ultrashort long optical pulses. As discussed in Chapter 1, these lasers allow the study of the temporal behavior of ultrafast phenomena on a subpicosecond time scale. This chapter discusses the following: the construction and alignment of a colliding-pulse mode-locked (CPM) ring dye laser; the tools used to aid in the alignment and measurement of the CPM laser output; and finally, the characteristics of the output pulses used in subsequent chapters of this thesis. The last section is a conclusion section, which summarizes the output characteristics of the CPM laser constructed and the pulses it produces.

2.1.1 Result of this Work

A dispersion-compensated CPM ring dye laser was constructed, aligned, and characterized. The compensated laser demonstrated ultrashort (< 100 fs) pulses.

However, the laser was not used in its highest performance mode for this thesis work; instead, the laser was operated in a noncompensated mode. The pulses in this mode are demonstrated to be about 250 fs full-width at half-maximum (FWHM), at a wavelength of 6115 Å and a spectral width of 20 Å, with a repetition rate of 115 MHz, and an average power of 10 to 30 mW. The noise of the laser output was estimated to be about 5%, and the laser output was found to be stable for periods of hours.

2.2 CPM Laser

2.2.1 Background

CPM Laser

Since the development of the first dye lasers in the 1960's, it was clear that they could lase over a large enough bandwidth to produce extremely short pulses. To obtain such ultrashort pulses, some method of locking the different longitudinal modes in phase, or mode-locking the laser, was necessary. Passive mode-locking of a continuous wave (CW)-pumped dye laser was first achieved in 1972,[1] and this became the primary technique used to generate subpicosecond pulses.[2] The CPM ring dye laser, a type of CW-pumped passively mode-locked dye laser, was developed in 1981.[8] These lasers generate ultrashort pulses down to a width of 50 fs. Figure 2.1(a) shows a CPM laser *circa* 1981. Figure 2.1(b) shows a schematic representation of this laser.[4] Briefly, the CPM laser works as follows. There are two pairs of focusing mirrors in the ring cavity. Within the first set of focusing mirrors there is a gain jet, consisting of a jet of ethylene glycol in which the dye, rhodamine 6G tetrafluoroborate (R6G), is dissolved. The dye jet fluoresces when it is CW-pumped by a pumping laser and thus provides the optical gain in the cavity. Within

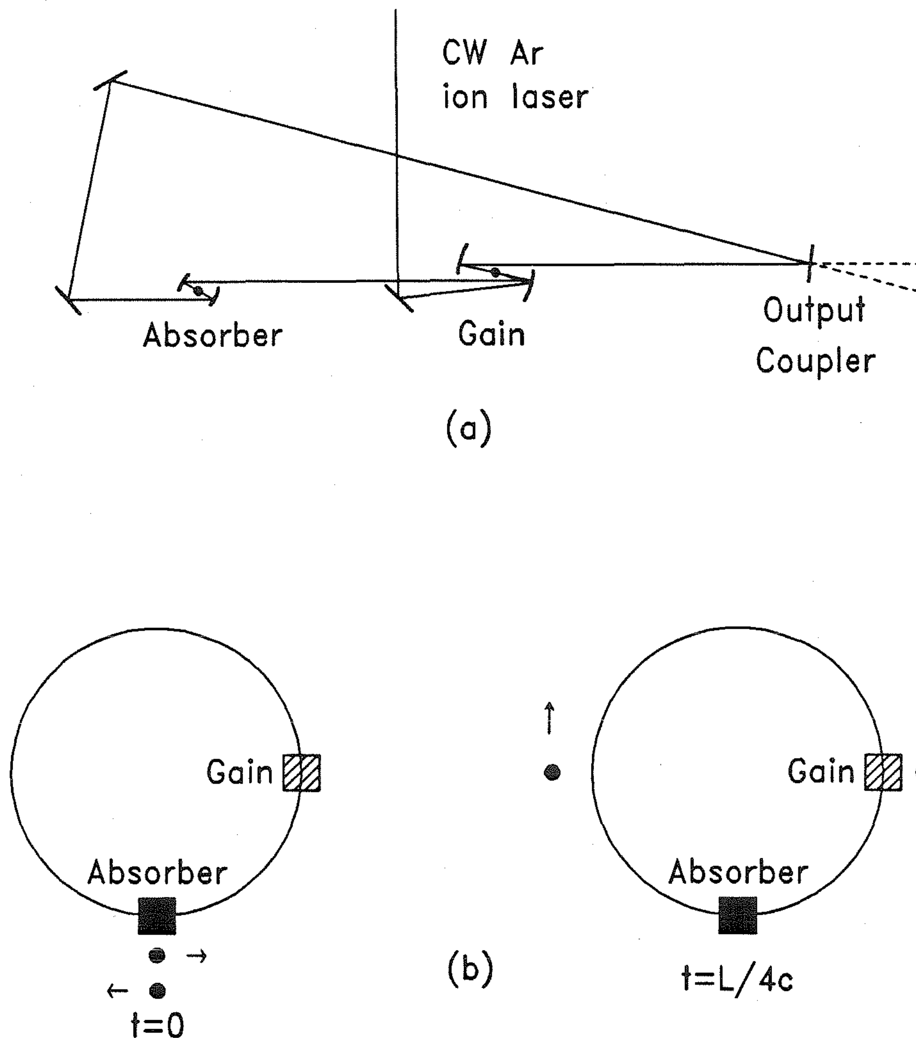

Figure 2.1: (a) Colliding-pulse mode-locked (CPM) ring dye laser, *circa* 1981, showing the the resonator cavity configuration. (From Ref. 8.) (b) Schematic representation of the pulse timing in the CPM laser. (From Ref. 4.) In (b) the filled circles represent the two optical pulses in the resonator cavity. The left drawing shows the pulses colliding in the saturable absorber; and the right drawing shows the pulses a quarter of the pulse round-trip time later, when one pulse is being amplified by the gain.

the second set of focusing mirrors, there is a saturable absorber jet, consisting of the saturable absorber, 3,3'-diethyloxadicarbocyanine iodide (DODCI), in a jet of ethylene glycol. The other mirrors provide the path to form a ring cavity, and the output coupler outputs a small fraction of the internal light. The schematic view of the cavity, Fig. 2.1(b), shows the saturable absorber medium at the six o'clock position and the gain medium at the three o'clock position. The desired stable mode of the cavity is for there to be two counter-rotating pulses that overlap both in space and time, *i.e.*, collide in the saturable absorber. The existence of this mode is due to the saturable properties of the absorber. That is, if the pulses collide in the absorber, they saturate it and they suffer less loss than if they do not collide and go through the absorber one at a time. In the collision mode, the cavity has enough gain to lase, while in the noncollision mode the cavity does not lase, hence, the name colliding-pulse mode-locked (CPM). The output of the laser consists of two trains of ultrafast pulses, one from each pulse in the cavity. The repetition rate of the pulses in the pulse train is given by the pulse round-trip time in the cavity. Typically, this is about 115 MHz, corresponding to a 2.5 m long cavity. The width of the output pulse depends on the thickness of the absorber jet in these lasers. As well, it is important that the gain jet is situated approximately a quarter of the ring length away from the saturable jet, so that both pulses pass separately through the gain after it has had equal time to recover. The cavities that produce the shortest pulses have no tuning element, so that the wavelength range over which it lases has to do with the spectral region in which the R6G provides sufficient gain, the DODCI acts as a saturable absorber, and the wavelength tuned coatings of the mirrors are optimized. Typically, these lasers run at about 620 nm and have bandwidths of about 50 nm, and repetition rates in the range of 120 MHz.[8] Introducing a tuning element allows tuning over the range 590-640 nm while maintaining 100 fs long pulses.[5] However, no tuning element is

used for most CPM applications.

There were many problems with the early lasers. The short pulses of < 100 fs were not consistently achieved.[11] Pulse widths for what were thought to be identical setups were found to be very different. In fact, simply interchanging mirrors with identical specifications was found to vary the pulse width.[4] Moreover, these CPM lasers were very difficult to align, and the output was noisy and susceptible to drift. It was found that intercavity dispersion plays an important role in governing the width of the laser pulses. This intercavity dispersion arises from the ethylene glycol jets and the mirrors in the cavity, and acts on the pulses to spread them out in time or space.[4] The solution to this problem is provided by prism pairs that provide negative dispersion.[7] Two prisms can be oriented so that the shorter wavelength light travels a shorter distance, while the longer wavelength light travel a longer distance. This is negative dispersion, since shorter wavelengths usually travel more slowly and fall behind the longer wavelengths. By including two negative dispersive prism pairs within the cavity, the positive dispersion of the ring cavity can be compensated, so that the net dispersion of the cavity is close to zero. Figure 2.2 shows such a compensated CPM cavity. This represents the present state-of-the-art CPM laser. This type of cavity routinely produces ultrashort pulses in the range of 30 to 50 fs, and the noise and long-term stability of these lasers are improved over the original CPM cavity. From theoretical analysis of these cavities, including the effects of dispersion, the shape of the envelope of the output pulses corresponds to $\mathrm{sech}^2(1.76t/\Delta t)$, where Δt is the full-width at half-maximum (FWHM) of the pulse.[8,9,10] Although the initial success of the CPM laser was achieved using the saturable absorber/dye pair DODCI/R6G, there has been some success in using other pairs in CPM lasers. Pairs have been found that allow operation over the range of 480 to 750 nm.[5] However, this was not used in this work.

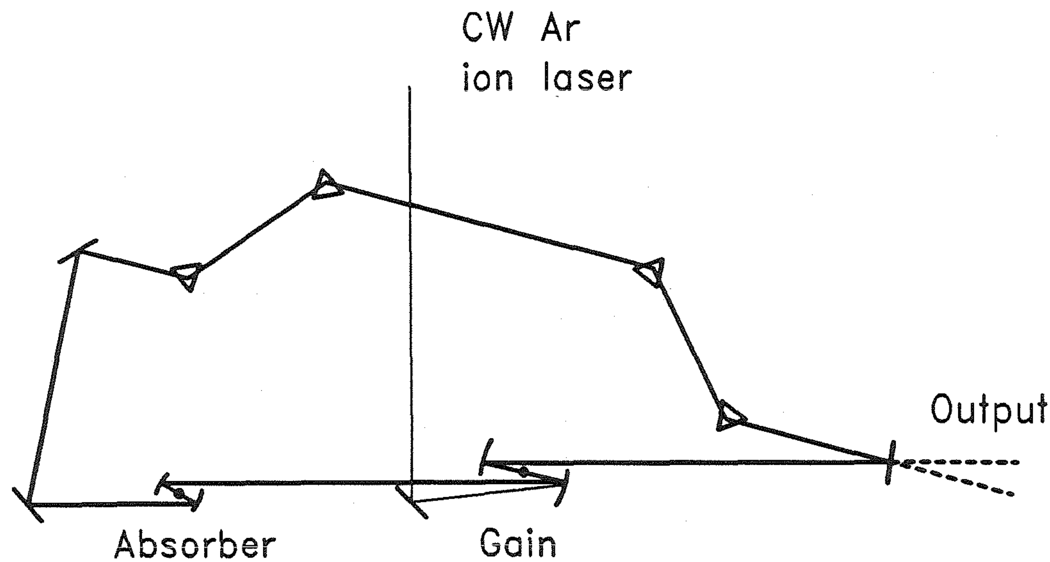

Figure 2.2: CPM laser resonator with two negative dispersion prism pairs for dispersion compensation.

Autocorrelator

As the lengths of optical pulses were shortened, the techniques used to measure the pulse widths were required to improved. Direct measurements of ultrafast pulses must be made using all optical techniques. The most common technique uses second-harmonic generation (SHG) in a crystal of a material such as potassium diphosphate (KDP).[10] SHG involves the nonlinear mixing of two pulses, which overlap in time and space to produce a third beam at the second harmonic. By detecting this third beam, the overlap of the two pulses can be determined. Figures 2.3(a),(b) show two types of SHG autocorrelators. Figure 2.3(a) shows a collinear autocorrelator, while Fig. 2.3(b) shows a noncollinear autocorrelator. Both autocorrelators use a Michelson interferometer to split a train of pulses from the laser into two pulse trains and to vary the time delay, γ, between the arrival at the KDP crystal of the pulses from the two trains. By scanning γ, the intensity of

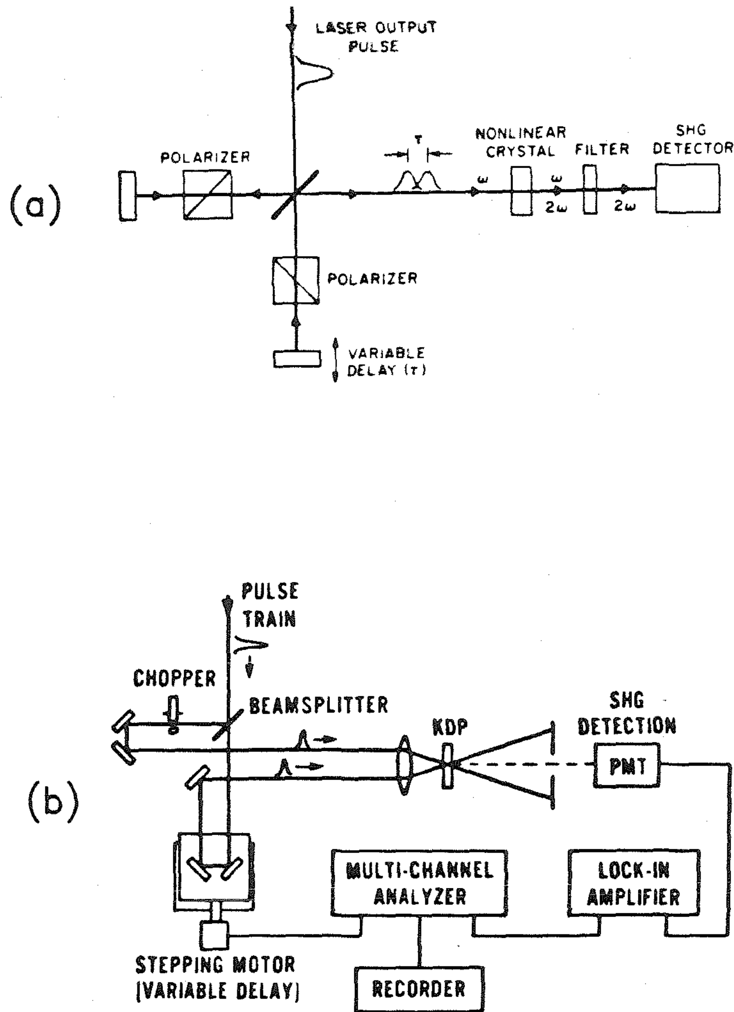

Figure 2.3: Autocorrelators. (a) Collinear autocorrelator -where the pulse trains enter the KDP collinearly. (b) Noncollinear autocorrelator -where the the pulse trains intersect one another in the KDP.(From Ref. 10)

the second harmonic beam gives the second-order autocorrelation of the pulses. If the intensity of one of the pulse trains as a function of time is $I(t)$, the second-order autocorrelation of the pulses is given by

$$G^2(\gamma) = \frac{\langle I(t)I(t+\gamma)\rangle}{\langle I^2(t)\rangle},$$

where the brackets, $\langle\cdots\rangle$, represent an average over a sufficiently long period of time. Although this is not sufficient to give the shape of the pulse itself, from other measurements and theoretical analysis it is known to be given by $\mathrm{sech}^2(1.76t/\Delta t)$. So that given $\Delta\gamma$, the FWHM of the autocorrelation, Δt, the FWHM of the pulse is given by $\Delta t = \Delta\gamma/1.55$.[10]

The details of the two types of autocorrelator techniques are different. The collinear autocorrelator measures the signal $f(\gamma) = 1 + 2G^2(\gamma)$.* This signal includes a background, which is due to the self-doubling of either pulse. This self-doubling comes from a single pulse interacting with itself to produce a doubled output. For any pulse shape, $G^2(0) = 1$, so the peak-to-background ratio of the collinear signal is 3:1. In detail, the autocorrelation peak should be a symmetric continuous smooth curve. Abrupt changes in the autocorrelation peak indicate a noise burst rather than a coherent pulse.[10] The self-doubling background makes the behavior of the wings of the pulse difficult to determine. A simple way to get rid of the background experimentally consists of chopping the two arms of the Michelson interferometer at two different frequencies and looking at the SHG signal at the sum or difference frequency. The autocorrelation signal, being due to a multiplication of the two pulse trains, will have sum and difference frequency components, while the self-doubling signals will vary only at the fundamental chopping frequencies. Thus, looking at the difference frequency, only the autocorrelation is

*There is also a rapidly varying component with zero average, which is due to the optical interference of the pulses. However, this is not usually seen here because the interferometer averages γ over a few optical periods.

measured.

The usual way to make a background-free autocorrelation measurement is to use the noncollinear technique, shown in Fig. 2.3(b). This SHG signal is generated in the direction bisecting the two intersecting noncollinear pulse trains. This second harmonic beam is present only if both pulses are present in the KDP at the same time, so that the technique directly measures $f(\gamma) = G^2(\gamma)$. The noncollinear autocorrelator is more difficult to align than the collinear autocorrelator, because there is no self-doubling.

2.2.2 Apparatus and Construction

CPM Laser

Figure 2.4 shows the CPM laser constructed. This shows a seven-mirror, cavity dispersion-compensated, CPM ring dye. The ring cavity is on a 2×4 foot optical breadboard, which is mounted on a 4×8 foot optical table. The breadboard is used because it is convenient to have holes in the breadboard for the drains that catch the dye and absorber jets. The pump laser is mounted partially above this breadboard and the optical table. The paragraphs below describe the elements of the laser in more detail, emphasizing the important details.* The laser description starts on the the pump laser and pump optics, then describes the dye and absorber pump systems, and finishes with the elements of the cavity itself.

The pump laser is a large-frame Ar^+ ion laser, Coherent model I-20UV. This is run CW on the 514.5 nm green line in the TEM_{00} spatial mode at power in the range of 3 to 5 W. Both the power stability and the angular stability of the pump laser are important for the stability of the CPM laser, since these affect the amount of power coupled into the CPM ring cavity through the dye. These were found to be an important source of long-term drift in the output of the CPM

*For details concerning cavity mirrors or pump system elements, see Appendix D.

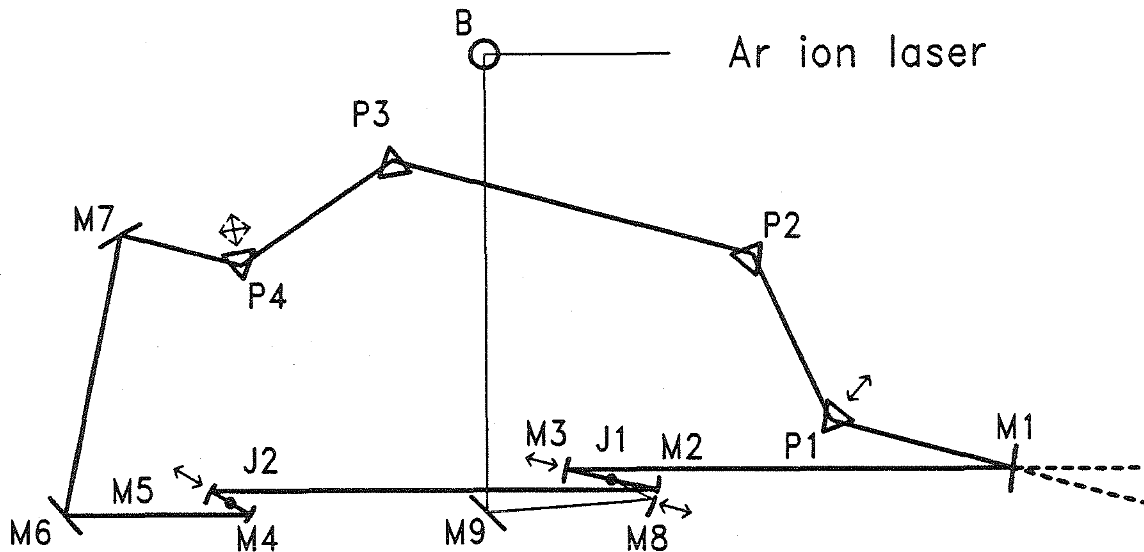

Figure 2.4: Compensated CPM laser, in detail. The elements of the cavity are: M6,M7 - high-reflective (HR) flat mirrors; M2,M3 - HR 10 cm radius of curvature mirrors; M4,M5 - HR 5 cm radius of curvature mirrors; M1 - output coupler; J1 - R6G dye jet; J2 - DODCI absorber jet; P1-P4 - quartz Brewster prisms. The elements of the pump beam are: B - beamsteerer; M9 - HR flat mirror; M8 - HR 10 cm radius of curvature focusing mirror. The arrows indicate translation.

laser. The pump power stability is best when running the laser open aperture and controlling the output power using the laser current. The effect of angular variations of the pump beam are minimized by keeping the pump laser as close as possible to the dye jet, which it pumps. The CW pump beam is focused onto the dye jet using a beamsteerer (B), a flat mirror (M9), and a 10 cm radius of curvature, concave focusing mirror (M8). The beamsteerer is important because not only does it change the direction of the laser beam, but it also changes the polarization of the beam from vertical to horizontal. A horizontal polarization is necessary for the vertical jets used in the laser. The 10 cm mirror, M8, focuses the pump onto the dye jet. To adjust the focus of the pump beam on the dye jet, the

dye jet is left stationary and the mirror, M8, is adjusted.

The mechanical and thermal stability of the dye and saturable absorber jets are crucial to the stable operation of the CPM laser. Both the dye, R6G, and the saturable absorber, DODCI, are dissolved in ethylene glycol. The concentration of R6G in the dye solution is approximately 3×10^{-3} Molar, and of DODCI in the absorber solutions is approximately 6×10^{-4} Molar. (See the alignment section for details.) Both of the jets are formed using closed-loop pump systems that pump the ethylene glycol solution through special nozzles. In the case of the dye jet, a stock Coherent nozzle of thickness 300 μm operates at a pressure of 40 psi, resulting in a thickness of about 80 μm at the center of the jet. The absorber jet uses a standard Coherent nozzle that has been squeezed down to a 120 μm opening.* This is operated at 20 psi, resulting in a jet thickness of about 50 μm at the center of the jet.

Both the dye- and absorber-jet pump systems are identical homemade systems. They are homemade because commercially available dye pumps at the time were not stable enough. The design was based on that used by Fork.[11] Figure 2.5 shows schematically the pump systems constructed. This system minimizes the pressure and temperature fluctuations of the ethylene glycol and produces a streamlined jet with few air bubbles in the stream. This is very important for the stability of the CPM laser. In fact, some researchers have found the presence of air bubbles in the jets to be the largest contributor to CPM laser noise.[11] The dye(absorber) solution is collected by directing the jet at a glancing angle on to the inside wall of the collecting tube. This minimizes the introduction of air into the solution. The collected solution flows into a reservoir above a variable-speed pump. The output of this pump is filtered using a 0.8μm pore filter, and pressure fluctuations that are due to the pump are dampened using a pulsation dampener. Next, the

---

*See Fork *et al.* (Ref. 4) for details on the method used to squeeze the nozzles.

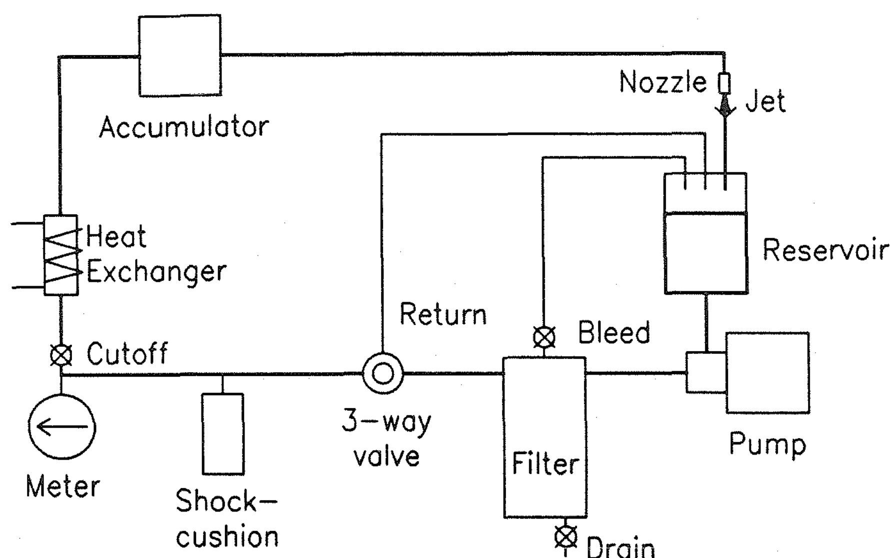

Figure 2.5: Dye/absorber pump system. Schematic diagram of the absorber/dye pump systems. (From Ref. 11.) See Appendix D for details.

dye(absorber) solution goes through a three-way valve, which controls the output pressure of the pump system by returning part of the solution to the reservoir. The other output goes: first, through a heat exchanger, which cools the solution to 20 °C; and then into a Spectra Physics accumulator, which filters out any turbulence; and finally, to the jet itself. The output pressure is measured using a pressure gauge on the output side of the bypass valve. The jet nozzles themselves are mounted on precision XYZ translation mounts to allow fine control of their positions. These pump systems have been found to give sufficiently stable jets for the operation of a CPM laser.

The mirrors used in the cavity were all single-stack dielectric mirrors rather than the more dispersive multistack dielectric mirrors. They are high-reflecting (HR) mirrors optimized for the Helium-Neon (He-Ne) laser wavelength of 632.8 nm for the angle at which they are used. For example, the absorber- and dye-focusing mirrors are half-inch diameter, 5 cm and 10 cm radii of curvature, respectively, single-

stack mirrors optimized for high reflectivity near 632.8 nm, for p-polarization, and 0° incidence. The mirrors M6 and M7 are flat one-inch diameter mirrors, optimized for high reflectivity near 632.8 nm for p-polarization, and 45° incidence. The output coupler M1 is one inch in diameter and 2% transmitting at 632.8 nm. It is crucial that the mirrors are mounted on rugged, precision mirror mounts and that the mirrors that are translatable are mounted on precision translation stages.

The prisms are silica Brewster angle prisms. They are used in an arrangement that allows the cavity to lase with or without the prisms, simply by moving prisms P1 and P4 in and out of the beam between M1 and M7. These prisms are used at an angle of incidence of Brewster's angle, so that the losses that are due to reflections are minimized as is necessary for intercavity optics. The separation of the prisms, which introduces the negative dispersion, P1 to P2, and P3 to P4 needs to be about 30 cm to add enough negative dispersion to compensate for the positive dispersion of the cavity, including the silica of the prisms themselves. All four prisms are mounted on precision prism mounts. Prisms P1 and P4 are on precision translation stages so that they can be removed from the cavity and adjusted to fine-tune the cavity dispersion itself.

Autocorrelator

Figure 2.6 shows the collinear autocorrelator used to measure the width of the laser pulses.* The pulse train is split using a beam splitter cube, and corner cube retro-reflectors at the ends of the Michelson interferometer arms return the trains, offset in position, to the beam splitter cube, where they are recombined and outputted collinearly to the focusing lens, L1. One of the retro-reflectors is mounted on a shaker, which modulates the interferometer arm length. The focusing lens, L1, focuses the pulse trains onto the KDP crystal, which is mounted so that

*For details concerning autocorrelator elements, see Appendix D.

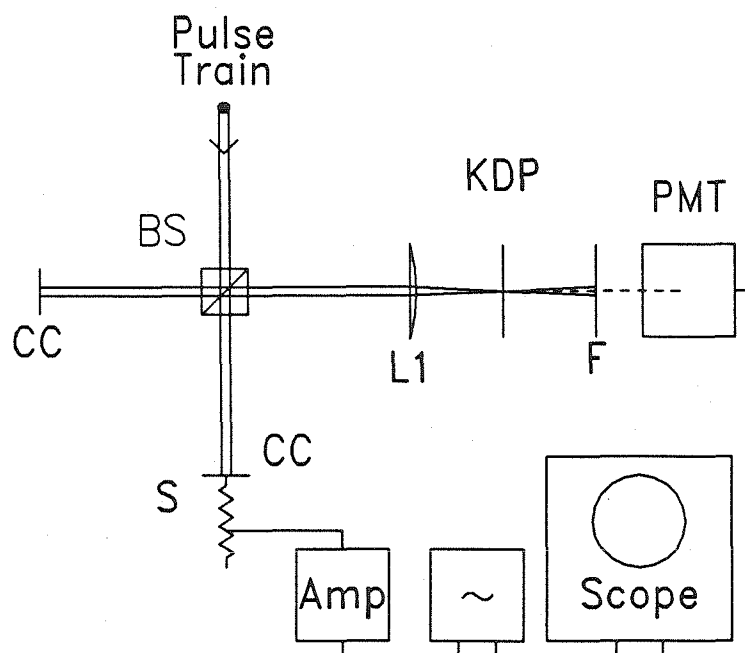

Figure 2.6: Schematic diagram of the collinear autocorrelator used to make real-time autocorrelation measurements. BS is a beamsplitter cube, CC are corner cubes, S is a shaker, L1 is a lens, F is a filter, which transmits only the doubled output from the KDP, and PMT is a UV sensitive photomultiplier tube. A signal generator drives the shaker through an amplifier (Amp). See Appendix D for details.

its azimuthal and polar angle to the beam can be adjusted to allow optimization of the phase-matching condition necessary for SHG output. A lens (not shown) after the KDP crystal, designed for ultraviolet (UV) light, focuses the second harmonic light ($\lambda \approx 310\mu$m) onto the UV-sensitive photomultiplier tube (PMT). A filter, F, which transmits UV but not the visible light, is used to transmit the doubled light while blocking the undoubled light to the PMT. The shaker is driven using an amplified low-frequency oscillator signal. Typically, a signal of 2.5 Hz was used. By using the oscillator signal output to drive the horizontal, and the PMT to drive

the vertical inputs of an oscilloscope, a real-time measurement is obtained. It is necessary to have such a real-time measurement of the autocorrelation while the laser itself is being aligned and optimized.[12]

The apparatus used in making the background-free collinear autocorrelation measurements is very similar to this except that, rather than using a shaker to control the interferometer arm length, a stepper motor is used. This measurement does not provide a real-time autocorrelation trace.

2.2.3 Alignment Procedures

CPM Laser

This section outlines the procedures used to align the CPM laser. The cavity includes many elements, each with at least two adjustments, so there are many degrees of freedom in the cavity. The general technique used to align the complete CPM laser is to start with a much simpler CW laser, align and optimize it, and then sequentially add more elements realigning the laser after each addition, finally ending up with an aligned CPM cavity. The laser alignment requires various real-time diagnostic tools to monitor the laser's performance. Fig. 2.7 schematically shows these diagnostic tools. For the alignment, the output mode shape is monitored by projecting a magnified image of the output beam onto the ceiling using a concave mirror, and the output power is monitored using a power meter. For the CPM laser, a high-speed diode and the real-time autocorrelator are also used to monitor the output pulses. The scope of the alignment discussion is to describe briefly the steps in setting up the CPM cavity, stressing important considerations, rather than to describe in detail how to align the laser completely from the initial setup.

The starting cavity is a simple ring dye laser with only the dye jet, J1, and mirrors M1-M4 and M7. This cavity requires removing M5 and turning off the

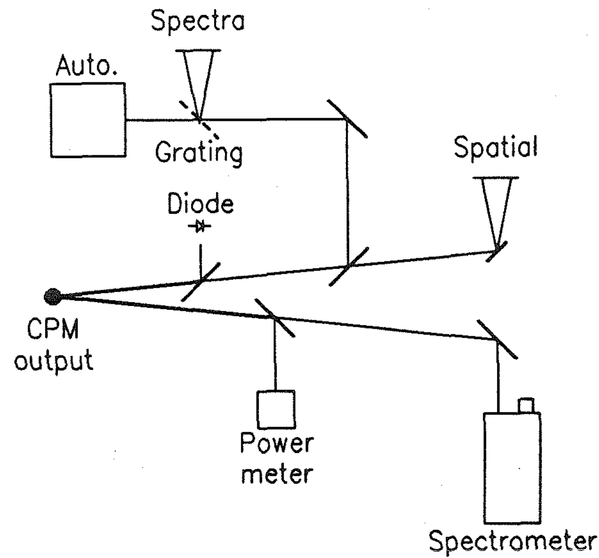

Figure 2.7: Block diagram showing the tools used to diagnose the CPM laser. The diode is a fast photo-diode, and the spatial image is generated using a concave mirror. See Appendix D for details.

absorber jet, J2, and allows optimization of the dye jet and focusing mirrors M2 and M3, and the pump-focusing mirror M8. Figure 2.4 shows the general positions of the elements. Care should be taken to keep the intercavity beam in one plane parallel to the surface of the breadboard. The dye jet should be oriented at Brewster's angle (about 57° for ethylene glycol) to the cavity laser-beam direction. This is done by adjusting the jet angle until the intensity of the Brewster angle reflection, the reflection of the intercavity laser beam from the jet, is at a minimum. There are actually two Brewster angle reflections from the dye jet, one from the front surface of the jet, and the other from the backside surface of the jet. By adjusting the dye-jet position within the focusing pair of mirrors, the two Brewster reflections should be made to overlap, producing a nearly round pattern with a dark spot in the interior. The jet should be positioned beyond the focus of

the pump laser, so that only a trace of thermal blooming* is observed in the transmitted pump laser beam, thus increasing the lasing threshold; however, it improves the stability of both this ring laser and the CPM laser. The dye concentration is chosen so that 5% of the pump beam is transmitted through the properly oriented dye jet. Typically, this corresponds to a 3×10^{-3} Molar solution. The "Z" fold that the cavity beam follows in the focusing mirror pair should be symmetric and the angle acute, to reduce the astigmatism of the beam. Adjusting the separation of the focusing mirrors sweeps the intercavity mode through several stable regions separated by unstable regions. The shortest cavity length giving rise to a stable mode produces the most stable CPM output. The aligned laser should be a deep orange TEM_{00} mode, with CW power of about 150 mW with both output beams for a 3 W pump.

Next, the absorber-jet focusing mirror pair is added by replacing M5 as shown in Fig. 2.4. These added elements are adjusted while the previously aligned elements, especially the dye-jet focusing mirror pair, are for the most part left untouched. To aid in the alignment of this cavity, it is useful to use iris diaphragms, between M1 and M3, and M2 and M6, to mark the positions of the beams before the new elements were added. As with the dye-focusing pair, the "Z" fold should be symmetric and acute to avoid beam astigmatism, and the length of the absorber mirror-pair separation should be the the shortest possible that gives rise to a stable mode. The aligned laser should remain a deep orange TEM_{00} mode, and the output about 150 mW per output beam.

Next, the absorber jet is added without any DODCI in solution, requiring some fine adjustments of the absorber-focusing mirrors. The jet should be positioned close to the focus of the cavity, so that one of horizontal axes of the XYZ translation

*Thermal blooming is the distortion (blooming) of the transmitted pump beam from a TEM_{00} shape, caused by the heating of the ethylene glycol in the jet. A trace of thermal blooming corresponds to an umbrella-shaped transmitted image.

mount is aligned to the beam direction, to allow the jet to be moved from the focus while the laser still lases. The beam is centered on the jet and the jet is at Brewster's angle. The Brewster's reflection of the aligned laser from the absorber jet should be very similar to that seen for the dye jet. The output mode, shape, color, and power at this step should be about the same as for the original cavity.

Next, the negative dispersion prisms are inserted as shown in Fig. 2.4. These are added sequentially, P1 through P4. First, P1 is added at Brewster's angle so that only part of the cavity beam is blocked and the laser still lases, while prism P1 deviates part of the beam along the path to prism P2. Then prism P2 is added at Brewster's angle, and then similarly for P3. The situation for P4 is slightly more complicated; it must be positioned correctly for both the beam from P3 and that from M7. The separation P1 to P2, and P3 to P4 must be close to 30 cm while the separation P2 to P3 is any convenient distance. The output characteristics with the prisms should be about the same as without them.

The final step is the addition of DODCI to the absorber-jet solution. This is done from a stock solution of DODCI dissolved in ethylene glycol, which should be added until the laser, which is initially CW, starts to run in a stable CPM mode. When this happens, the laser-beam color changes from orange to red and pulses may be detected, although not resolved, with a high-speed photo-diode. Typically the laser starts to operate in the CPM mode when the DODCI concentration is about 6×10^{-4} Molar. Now the laser is ready to be finely tuned to produce ultrafast pulses. This is done using the real-time autocorrelator to monitor the output pulse width and the diode to measure the repetition rate of the laser, to make sure there is only one pulse pair in the cavity at any one time.* The important adjustments to fine-tune the pulse width are: the distance of the absorber jet from the focus between the absorber mirrors, M4 and M5; and the amount of negative dispersion

*Two pulse pairs in the cavity double the repetition rate from that for only one pair.

in the cavity that is controlled by translating P1.[13]

Autocorrelator

Fig. 2.6 shows the autocorrelator used in this work. The alignment of the real-time autocorrelator much is easier than the alignment of the laser. The important alignments are focusing the collinear pulse trains to a single spot on the KDP crystal, and orienting the KDP crystal to optimize the SHG signal. The collinear cavity is particularly easy to align because of the background that is due to the self-doubling.

2.2.4 Characterization

The techniques and instruments used to diagnose the output from the CPM are shown in Fig. 2.7. As discussed above, the magnified reflection of the output beam is used to determine the mode shape, the fast photo-diode gives the repetition rate of the laser so that it can be used to monitor the number of pulse pairs in the cavity, and the real-time autocorrelator gives the real-time measure of the CPM pulse width. The remaining three tools have not been discussed directly. The background-free autocorrelation is used to provide a more precise and less noisy measurement of the pulse width. The grating is used to display the spectral contents of the CPM pulses, to give a real-time measure of the bandwidth of the pulses. Finally, the spectrometer is used to determine the precise spectral content of the pulses. The noise of the output is measured either using the power meter, which gives the noise in the average laser power, or using the high-speed diode, which gives the fluctuations in the optical-pulse peak intensity.

The capability of producing pulses < 100 fs has been demonstrated with this laser. However, for the experiments using this laser, reported in this thesis, these pulses are much shorter than those required to time-resolve the features being

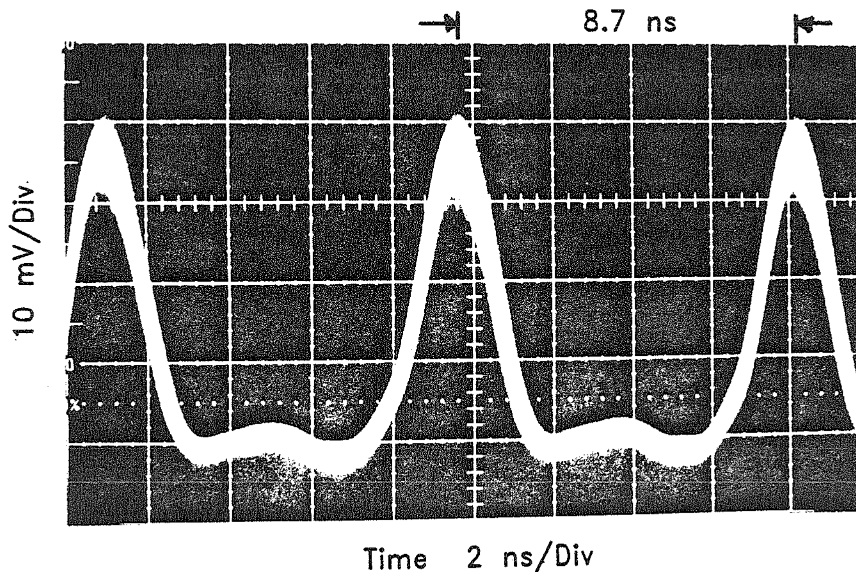

Figure 2.8: Photo-diode signal. This shows a typical oscilloscope trace of a photo-diode detecting the CPM pulse train. The repetition rate is 115 MHz.

studied. Because of this, rather than use the highest performance version of this laser, a cavity was used, which did not produce the shortest pulses. This cavity required less time to align and it was thought to be more stable for long-term measurements. The pulses generated by this cavity are characterized in the paragraph below.

Figure 2.8 shows a typical high-speed photo-diode signal. This shows a period of 8.7 ns corresponding to the round-trip time for a cavity of length about 2.5 m, which implies that there is only one pair of pulses in the laser cavity. The repetition rate is 115 MHz. The actual shape pulse of this signal is due to the bandwidth limit of the detector circuitry and the oscilloscope, and reflections in the detector circuit. Figures 2.9(a),(b) show the pulse autocorrelation. Figure 2.9(a) shows the real-time output from the collinear autocorrelator. This shows two similar

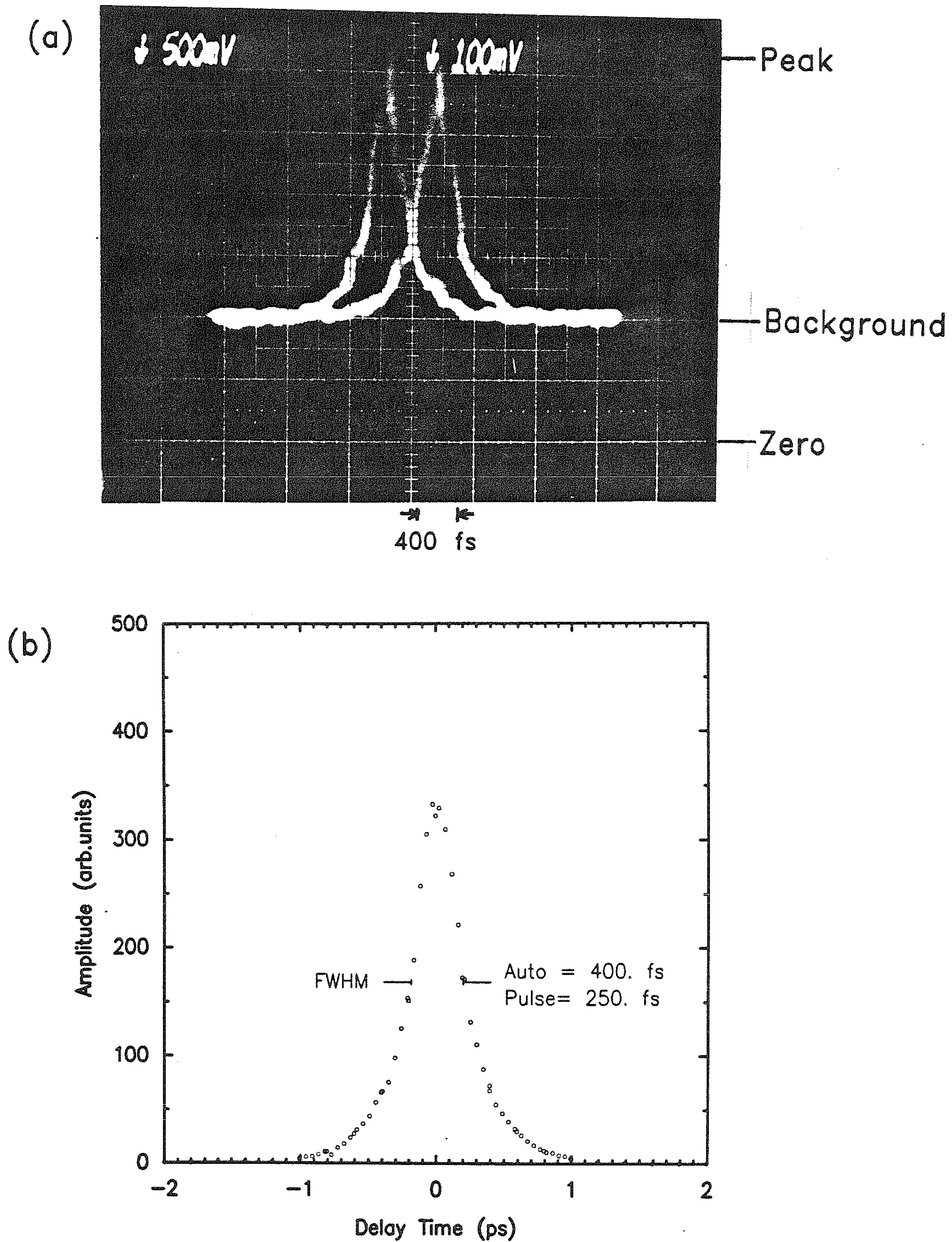

Figure 2.9: Autocorrelator scans. Scan (a) used real-time collinear autocorrelator. This shows a FWHM of about 400 fs. Scan (b) used background-free collinear autocorrelator. This shows a FWHM of 400 fs

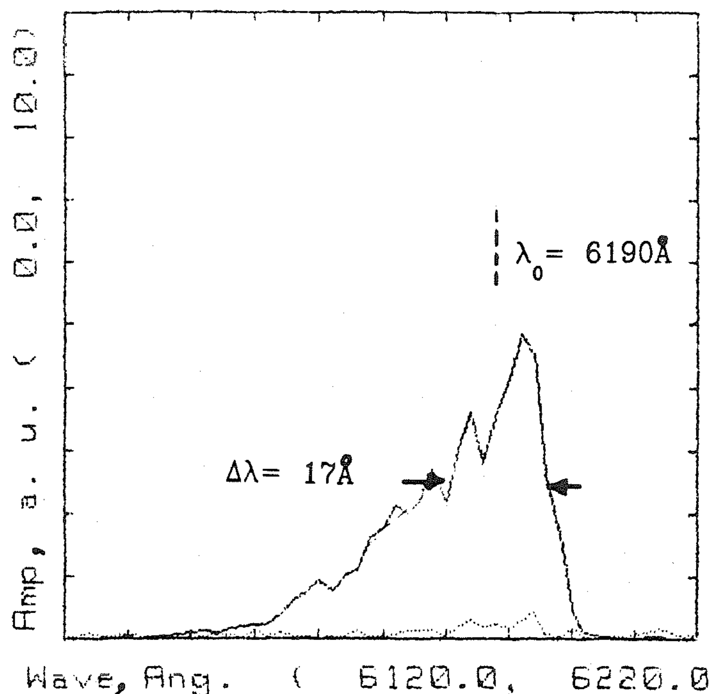

Figure 2.10: Spectral content of pulses. The mean wavelength is 6190 Å and the FWHM is 17 Å.

peaks because of the phase lag between the signal driving the oscillator and the mechanical position of the shaker. The peak-to-background ratio of the peaks is about 3:1, as expected for the collinear autocorrelator. Figure 2.9(b) shows the averaged output from a background-free collinear autocorrelator measurement. This shows a smooth peak with quickly decaying wings. Both autocorrelation scans have peaks that have a FWHM of about 400 fs. Assuming a sech^2-shaped pulse, these indicate a 250 fs FWHM pulse. Figure 2.10 shows the spectral content of the laser pulse. This shows a peak centered on a wavelength of 619 nm, with a FWHM of 1.7 nm. This shows a $\Delta t \Delta \nu$ product of 0.33, which is 5% longer than the Fourier transform limit of 0.315 for sech^2-shaped pulses.[10] The output power of the laser was typically adjustable from 10 to 30 mW average power for either output pulse

trains, corresponding to peak powers of 300 to 900 W, or pulse energies of 80 to 240 pJ. The noise of the laser output, with fresh dye and saturable absorber was estimated to be about 5%, with most of this noise being low frequency (< 20 Hz). With fresh dye and absorber, the laser could be run for periods up to 4 hours, without any realignments. Both the noise and the long-term drift increased as the life of the absorber and dye solutions increased. It was found that the absorber and the dye should be replaced every 2 weeks.

2.3 Summary

We have described in detail the construction, alignment and characterization of a self-compensated CPM ring dye laser. This laser was found to produce pulses < 100 fs wide. However, for the work of this thesis, pulses this short were not necessary, so that, rather than run the laser in the highest performance mode, it was run without intercavity dispersion compensation. In this mode 250 fs wide (FWHM), pulses are generated at a repetition rate of 115 MHz, with average output power between 10 and 30 mW. The amplitude noise of the laser pulses is approximately 5%, and the beam is stable up to a few hours at a time.

References

1. E.P. Ippen, C.V. Shank, and A. Dienes, Appl. Phys. Lett. **21**, 348 (1972).

2. C.V. Shank, R.L. Fork, F.A. Beisser, Laser Focus **19**, 59 (1983).

3. R.L. Fork, B.I. Greene, and C.V. Shank , Appl. Phys. Lett. **38**, 671 (1981).

4. R.L. Fork, C.V. Shank, R. Yen, and C.A. Hirlimann , IEEE J. of Quantum Electron. **IEEE QE-19**, 500 (1983).

5. P.M.W. French, and J.R. Taylor in *Ultrafast Phenomena*, Vol. V (Springer Series in Chemical Physics 46, New York, 1986) pp. 11-13.

6. M.J. Rosker, Ph.D. thesis, Cornell University, 1987.

7. R.L. Fork, O.E. Martinez, and J.P. Gordon, Opt. Lett. **9**, 150 (1984).

8. J.A. Valdmanis, R.L. Fork, and J.P. Gordon, Opt. Lett. **10**, 131 (1985).

9. O.E. Martinez, R.L. Fork, and J.P Gordon, Opt. Lett. **9**, 156 (1984).

10. E.P. Ippen, and C.V. Shank, in *Ultrafast Light Pulses*, edited by S.L. Shapiro (Springer-Verlag, New York, 1977), Chap. 3.

11. R.L. Fork, private communication.

12. R.L. Fork, and F.A. Beisser, Appl. Optics **17**, 3534 (1978).

13. J.A. Valdmanis, and R.L. Fork, IEEE J. of Quantum Electron. **QE-22**, 112 (1986).

Chapter 3

Photoluminescence Excitation Correlation Spectroscopy

3.1 Introduction

3.1.1 Background

Photoluminescence (PL) is produced by the recombination of semiconductor carriers, electron and holes that have been created by the photo-excitation of the semiconductor. This recombination may be direct, or through different levels present intentionally or unintentionally in the material. Examples of the former process are direct radiative band-to-band recombination (also called np product recombination), and exciton recombination. Examples of the latter recombination processes are recombination through acceptor or donor impurities, and through deep levels. Time-resolving the PL gives the lifetimes of carriers and determines the reaction rates of the dominant recombination processes. To make such time-resolved measurements, generally, one requires an optical pulse to generate the PL. The width of this pulse limits the time-resolution of the measurement. With the recent advances in laser technology, discussed in Chapters 1 and 2, it has become

possible to generate laser pulses with widths substantially less than one picosecond. Thus, it is possible to excite processes on this ultrafast time scale. To make true ultrafast time-resolved measurements of PL transients, both an ultrafast excitation and an ultrafast detector are required. The limitations on the time-resolution are usually due to the detector speed, not to the excitation speed. Time-correlated photon counting (TCPC) techniques using conventional photomultipier tubes (PMT) response times down to about 500 ps, while new microchannel plate photomultipliers tubes (MCP-PMT) have response times down to 30 ps.[1] Fast photo-diodes have response times less than 10 ps; however, they do not have very high sensitivity. Using streak cameras, resolutions in the range of 2 ps have been achieved; however, streak cameras are costly and difficult to operate. Another approach to the fast detection of PL is to use an optical pulse identical to that used to excite the sample, but delayed in time, to optically gate the PL signal. There are two such methods in use: One uses a Kerr cell to gate the PL, which requires a high-powered ultrafast laser to drive the Kerr cell; and the other uses parametric up-conversion to gate the PL, which requires a nonlinear crystal and a spectrometer operating in the ultraviolet. At present, these are the only two methods that directly measure the transient response of the PL signal down to the resolution of currently available lasers. Both of these techniques are experimentally sophisticated, both in the generation of the excitation pulses, and in the detection of the PL. Recently, another type of technique, was proposed.[2] This is a pulse-probe technique which gives temporal resolution of the PL decay. This technique has been called population mixing[3] or picosecond excitation correlation.[4] We refer to it as photoluminescence excitation correlation spectroscopy (PECS).[5] In this technique, pulses from a laser are divided into two separate pulse trains, which are delayed in time with respect to each other and chopped separately at two different frequencies. The photoluminescence signal at the sum or difference frequencies is

detected by a conventional slow detector. This signal gives the cross-correlation of the populations of the levels involved in the PL process, rather than the true transient decay of the PL signal. The resolution of this measurement is limited only by the laser pulse width, which can easily be as short as 50 fs. This experimental technique uses a much simpler detection scheme than the two techniques mentioned earlier, which directly measure the transient decay of the PL signal on a subpicosecond time scale. However, the interpretation of the results is not as simple and must be investigated.

In this chapter, we examine what is measured, using the PECS method. First, we make a detailed analysis of the PECS signals that would be obtained from PL for two limiting cases of recombination in semiconductors. These limiting cases are recombination by band-to-band radiative recombination only, and capture-dominated recombination. Second, we make an experimental case study of the technique. In this case study, semi-insulating (SI) In-alloyed, GaAs substrate material, and SI GaAs substrate material are studied. These substrates are important for GaAs digital integrated circuit (IC) technology, and these types of measurements are of much interest because they allow the characterization of the surface of a substrate.

3.1.2 Results of Work

From the theoretical analysis of PECS, it is found that the method will not give a signal for the band-to-band PL peak if there are only interband radiative recombination processes. However, parallel recombination processes, in which the recombination rate does not depend on the np product, will result in a signal. An example of such a parallel process is electron and hole capture by deep levels. For such non-np product recombination processes, the near band-to-band PL signal measured is then the cross-correlation of the time-dependent electron and hole

populations produced by the laser excitation. In this case, the signal gives the carrier lifetime. The PECS signal from other peaks also depends on the cross-correlation of the populations of the two levels involved in the processes producing the PL. Complications may arise if the levels are long lived in comparison to the pulse repetition time, t_{rep}, and if the processes are saturable. In the case of saturable processes, a negative PECS signal may arise.

In the case study, PECS is used on two different substrates, SI GaAs and SI In-alloyed GaAs. Both of these behave similarly. The nonalloyed material was used for the analysis at 77 K and the In-alloyed material was used for the 5 K study. The study at 77 K shows the behavior predicted by the simple theoretical model. The measured lifetime for both electrons and holes is 275 ± 20 ps. This lifetime indicates that the recombination of the material is capture-dominated. A coherence peak, that is due to the interference of the pump and probe optical pulses, is also seen at 77 K. The study at 5 K is more complicated because a near band-to-band peak as well as an acceptor related peak is observed. The near band-to-band peak indicates two decay regimes. The faster decay regime corresponds to the capture of carriers by the acceptors and has a time constant of about 100 ps. The slower decay regime corresponds to near band-to-band recombination and has a time constant of about 1 ns. The acceptor-related peak in In-alloyed GaAs at 5 K shows more complicated behavior. The part associated with band-to-acceptor recombination behaves as expected with a decay time of about 100 ps. The part attributed to the donor-to-acceptor recombination (A^0-D^0) gives rise to a negative signal, which indicates that this process saturates.

3.1.3 Outline of Chapter

In Section 3.2, we present a detailed analysis of the signals that would be obtained for two limiting cases of recombination: band-to-band radiative recombi-

nation only, and capture-dominated recombination. In Section 3.3, we give details of the experimental equipment and a description of the samples used in this study. Section 3.4 gives the results of our experiments. Finally, in Section 3.5, we discuss the meaning of our results, and Section 3.6 is a summary of this study.

3.2 Theory

In this section, we analyze the signal generated by PECS. Figure 3.1 schematically shows the pulse trains incident on the sample. The two trains of ultrafast pulses are focused onto the same area. One train of pulses is delayed in time by a delay time, γ, with respect to the other. The pulse trains are chopped independently at two different frequencies. These pulses generate photoluminescence (PL) from the sample, which is spectrally resolved and detected using a spectrometer and a slow detector. The detector signal is monitored with a lock-in amplifier either at one of the fundamental chopping frequencies, or at the sum or difference frequency. The frequencies are chosen such that the difference and its first few harmonics do not overlap with the fundamental chopping frequencies. The pulse trains involve three different time regimes,*

$$t_{\mathrm{pulse}} \approx 400 \ \ \mathrm{fs} << t_{\mathrm{rep}} \approx 8 \ \mu\mathrm{s} << t_{\mathrm{chop}} \approx 0.5 \ \mathrm{ms}.$$

In PL experiments, the generation function, which is the number of carriers produced by the exciting light per-unit, time-per unit volume, is important. The generation function produced in a sample by these trains is

$$G(t,\gamma,\omega_1,\omega_2) = g_1 S(t,\omega_1) \sum_{n=-\infty}^{+\infty} P(t - nt_{\mathrm{rep}}) + g_2 S(t,\omega_2) \sum_{n=-\infty}^{+\infty} P(t - \gamma - nt_{\mathrm{rep}}), \tag{3.1}$$

*Depending on the particular experiment, t_{pulse} was between 250 and 400 fs. For this analysis this is not important.

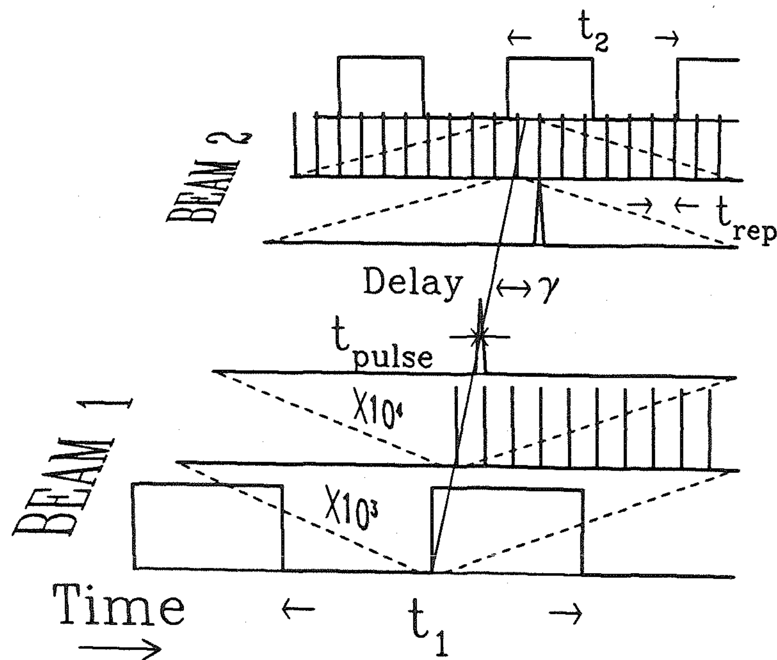

Figure 3.1: Schematic of two pulse trains incident on sample. Each pulse train is shown in three time regimes: (1) showing the chopping, (2) showing trains of individual pulses (10^3 magnification of 1), (3) showing a single pulse (10^4 magnification of 2). A delay time of γ between pulses is shown.

where: $S(t, \omega_i)$ is a square wave between 1 and 0 with frequency ω_i; g_1 and g_2 are proportional to the amplitudes of the laser pulses and take into account the depth over which a laser pulse is absorbed; and $P(t)$ describes the shape of a single laser pulse.

The response times of the processes we are interested in, are assumed to be much larger than t_{pulse} and much smaller than t_{rep}. Thus, the pulses can be treated as "delta" functions and adjacent pulses from the same train do not interact. This means that to determine the signal detected for the full generation function, we can consider the response of the sample and detector to one set of pulses $g_1\delta(t) + g_2\delta(t - \gamma)$ separately from the effect of repetition, chopping, and lock-in

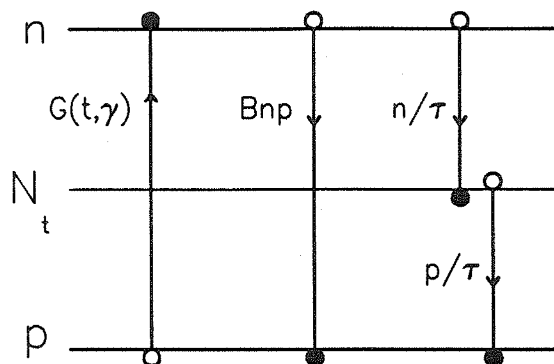

Figure 3.2: Simple Three Level System. The conduction, valence bands, and a deep level are shown, along with the generation process and recombination processes of interest. The band-to-band process is radiative, while both the band-to-deep-level processes may be radiative or nonradiative.

detection. The physics of the interaction of the carriers in the sample is contained in the first part, while the second part allows practical measurement of the correlation of the carrier populations produced by the two pulses. It is this correlation signal that is of interest, since it will be shown to vary with delay time, γ, and gives the time-resolution of the PL.

We are interested in the PL of a semiconductor pumped above bandgap by such pulse trains. For simplicity, consider an idealized system consisting of three levels: the valence band, the conduction band, and a deep level. Figure 3.2 shows such a system, along with the pertinent recombination mechanisms. Neglecting carrier diffusion and surface recombination, the rate equations for this system are[6]

$$\begin{aligned}
\frac{dn}{dt} &= G(t,\gamma) - Bnp - C_1 n\Big(N_t - n_t\Big), \\
\frac{dn_t}{dt} &= C_1 n\Big(N_t - n_t\Big) - C_2 p n_t, \\
\frac{dp}{dt} &= G(t,\gamma) - Bnp - C_2 p n_t,
\end{aligned} \tag{3.2}$$

where *nandp* are the densities of electrons in the conduction band and holes in the

valence band, respectively; n_t and N_t are the filled-trap and total-trap densities, respectively; B is the recombination rate; and C_1 and C_2 are the electron- and hole-capture rates of the trap, respectively.

In what follows, we calculate the signal that would be detected by a lock-in amplifier for the band-to-band recombination or the np product for this system. To determine this signal, we first look at the rate equations for adjacent pulses from the two trains separated by delay time, γ. Next, we calculate the detector output by integrating over the detector response time, which is long compared to semiconductor response time, yet much shorter than the chopping time. We call this detector output $I(t,\gamma)$. Finally, we determine the lock-in response at ω_1, ω_2, $\omega_2 - \omega_1$, and $\omega_2 + \omega_1$ by multiplying $I(t,\gamma)$ by the lock-in sampling square wave and taking the zero frequency component. We call this $I_{\mathrm{lock}}(\omega)$.

Returning to the rate equations, Eqns. 3.2, we consider solutions for this system in two limiting cases: the radiative band-to-band recombination-dominant mode, and the trapping recombination-dominant mode. If radiative band-to-band recombination is the dominant decay mode, the rate equations become

$$\begin{aligned} \frac{dn}{dt} &= G(t,\gamma) - Bnp, \\ \frac{dp}{dt} &= G(t,\gamma) - Bnp. \end{aligned} \tag{3.3}$$

For a single set of pulses, the generation function is

$$G(t,\gamma) = g_1\delta(t) + g_2\delta(t-\gamma). \tag{3.4}$$

Rearranging Eqn. 3.3 to solve for Bnp directly, then integrating over the detector response (for times long compared with the pulse width and γ, but short compared with the chopping time), and finally, putting in the effects of repetitive pulses and chopping, we obtain

$$I(t,\gamma) = \int Bnpdt = \int G(t,\gamma)dt - \int \frac{dn}{dt}dt. \tag{3.5}$$

Carrying out the integrals and applying the condition that n returns to zero so that the last integral on the right-hand side of Eqn. 3.5 is zero,*

$$I(t,\gamma) = \frac{g_1}{t_{\text{rep}}} S(t,\omega_1) + \frac{g_2}{t_{\text{rep}}} S(t,\omega_2). \tag{3.6}$$

Note that there is no mixed component of the two trains in the detected signal. The three lock-in signals are:

$$\begin{aligned} I_{\text{lock}}(\omega_1) &= \frac{g}{2t_{\text{rep}}}\,, \\ I_{\text{lock}}(\omega_2) &= \frac{g}{2t_{\text{rep}}}, \\ I_{\text{lock}}(\omega_2-\omega_1) &= I_{\text{lock}}(\omega_2+\omega_1) = 0. \end{aligned} \tag{3.7}$$

Thus, there is no signal detected at the mixed frequency. This result can be intuitively motivated. In a radiative band-to-band recombination-dominated regime, one photon *in* must always generate one photon *out* because there is no other decay process. Thus, the detector will always detect the same number of photons because of the two pulses, regardless of the delay time; and the number of photons detected will be the sum of the number detected for each pulse separately. Thus, there is no mixing.

If trapping is the dominant mode of recombination, then the np product term in Eqns. 3.2 can be neglected in solving for the carrier populations as a function of time. For large excitation densities, n and p are assumed to be much greater than N_t. Thus, during the decay of the carrier populations, n and p, a steady-state population of the empty traps, must be achieved, and the capture rate of the electrons and holes on the trap will be the same. Over this period of time, the population of empty traps remains constant. Thus, $\tau_n = [C_1(N_t - n_t)]^{-1}$ and $\tau_p = [C_2 n_t]^{-1}$ will be the same; call this time constant τ. Then the rate equations become

$$\frac{dn}{dt} = G(t,\gamma) - \frac{n}{\tau},$$

*The same result is found if n returns to some steady-state nonzero value.

$$\frac{dp}{dt} = G(t,\gamma) - \frac{p}{\tau}. \tag{3.8}$$

Solving these equations for a pair of adjacent pulses, we find*

$$\begin{aligned} n(t) &= g_1\Theta(t)e^{-\frac{t}{\tau}} + g_2\Theta(t-\gamma)e^{-\frac{t-\gamma}{\tau}}, \\ p(t) &= g_1\Theta(t)e^{-\frac{t}{\tau}} + g_2\Theta(t-\gamma)e^{-\frac{t-\gamma}{\tau}}, \end{aligned} \tag{3.9}$$

where $\Theta(t)$ is the unit-step function. The radiative band-to-band PL signal is found by: forming the Bnp product, integrating over the detector response, and including the effect of pulse repetition and chopping. Doing this we obtain

$$I(t,\gamma) = \frac{B}{t_{\mathrm{rep}}}\left[(g_1^2 S(t,\omega_1) + g_2^2 S(t,\omega_2))\frac{\tau}{2} + g_1 g_2 S(t,\omega_1)S(t,\omega_2)\tau e^{-\frac{|\gamma|}{\tau}}\right]. \tag{3.10}$$

Here, there is a mixed component of the two trains in the detected signal, which is to the product term $S(t,\omega_1)S(t,\omega_2)$. With equal intensity laser pulses ($g = g_1 = g_2$), the lock-in signals are*

$$\begin{aligned} I_{\mathrm{lock}}(\omega_2) = I_{\mathrm{lock}}(\omega_1) &= \frac{Bg^2\tau}{4t_{\mathrm{rep}}}(1 + e^{-\frac{|\gamma|}{\tau}}), \\ I_{\mathrm{lock}}(\omega_2 - \omega_1) = I_{\mathrm{lock}}(\omega_2 + \omega_1) &= \frac{\beta B g^2 \tau}{t_{\mathrm{rep}}} e^{-\frac{|\gamma|}{\tau}}, \end{aligned} \tag{3.11}$$

where

$$\beta = \frac{4}{\pi^3}\sum_{n=0}^{\infty}\frac{1}{(2n+1)^3} \approx 0.136.$$

For $\gamma = 0$,

$$\frac{I_{\mathrm{lock}}(\omega_2 - \omega_1)}{I_{\mathrm{lock}}(\omega_1)} = 0.27.$$

This is in contrast to the radiative recombination-dominated value of zero. Thus, there is a signal detected at the sum and difference frequencies, and the variation of these signals with delay time, γ, gives the carrier lifetime τ. Note that the signals at the fundamental chopping frequencies also give the carrier lifetime, but the exponential decay is superimposed on a constant background.

*See Appendix A for details of the solution of the rate equations and calculation of the lock-in signals.

Generally, recombination in a sample falls between the two limiting cases of purely radiative band-to-band, or trapping-dominated recombination, so that one expects to measure a difference frequency signal, or difference signal, smaller than that for the trap dominant case. The analysis of the method published by Rosen *et al.*[7] assumes, without stating, a capture-dominant regime, for which our analysis agrees with theirs.

It should be emphasized that the difference signal is not simply due to the non-linear nature of photoluminescence, since the radiative band-to-band recombination-dominated system is, itself, nonlinear, but gives no difference signal. To obtain a difference signal, there must be some alternate decay mechanism acting in parallel with the band-to-band radiative decay. Moreover, the decay rate of the alternate decay mechanism should not be proportional to the np product. The alternate mechanism, in the case reported in this section, is provided by trapping. In such a trapping-dominated regime, the PECS difference signal is due to population mixing. It represents the signal produced by the electron population generated by one pulse interacting, through band-to-band recombination, with the hole population generated by the other pulse and vice versa. In short, the signal is proportional to the cross-correlation of the two populations,

$$\int [n(t)p(t-\gamma) + n(t-\gamma)p(t)]\, dt \ . \tag{3.12}$$

PECS can also be used to monitor optical transitions other than band-to-band recombination. Thus, the time dependence of population of levels, such as shallow or deep acceptors or donors, can be observed. As an example, consider two levels, A and B. Let the populations produced by a single laser pulse be $a(t)$ and $b(t)$. Assuming the responses to two pulses to be independent, the populations generated by two pulses separated by delay time, γ, are

$$A(t) = a(t) + a(t-\gamma) \quad \text{and} \quad B(t) = b(t) + b(t-\gamma) \ .$$

If the instantaneous, radiative recombination between levels A and B is proportional to $A(t)B(t)$, then at the wavelength of the radiative recombination,

$$I_{\text{lock}}(\omega_2 - \omega_1) \propto \int [a(t)b(t-\gamma) + a(t-\gamma)b(t)]\, dt \ . \tag{3.13}$$

Thus, $I_{\text{lock}}(\omega_2 - \omega_1)$ is proportional to the cross-correlation of $a(t)$ and $b(t)$.

If the response to two adjacent pulses is not independent, then the situation is more complicated. A simple case occurs when the decay of the population is so slow that it can be neglected over times $t > t_{\text{rep}}$, but is much faster than the chopping time. Then, when either chopper allows light to pass through it, successive pulses quickly build up the population of levels A and B until they are saturated. This saturation implies that we obtain the same signal when one chopper or both choppers are on, and no signal when they are both off. Under these circumstances, instead of mixing the populations by straightforward multiplication (a logical AND), they are combined in a logical OR. That is, the same signal is obtained if either the pulse train chopped at ω_1 or the pulse train chopped at ω_2 is on the sample. This gives rise to a negative signal independent of delay time, γ, or a constant negative background.

The model developed above is for an idealized three-level system. The valence and conduction bands are treated as levels, not bands, and only radiative band-to-band recombination and recombination through a single trap are considered. The remaining paragraphs in this section discuss the application of this model to a real experiment in a real semiconductor.

What are the effects of valence and conduction bands rather than discrete levels? In a PL experiment, the photons used to excite carriers is above bandgap, so the carriers created will not necessarily be at the edge of the bands. The created carriers initially will be hot, but they will quickly establish a quasi-thermal equilibrium with a temperature above the initial lattice temperature within the bands. This equilibrium is established via intravalley scattering involving phonons

and should be attained in a few picoseconds.[11] This quasi-thermal equilibrium will cool to the lattice temperature over hundreds of picoseconds.[2] The carriers will be distributed in the bands, depending on the temperature of the quasi-thermal equilibrium. The higher states in the bands will be occupied only at higher temperatures. Thus, the luminescence from the band-to-band recombination will be spread in wavelength. The occupancy of the bottom of the bands should be fairly independent of temperature, and should give the largest contribution to the band-to-band recombination. Thus, the PECS signal from the peak of the luminescence spectrum should behave as in the simple three-level system. However, the occupancy of the higher levels in the bands changes with temperature because of intraband transitions, so they do not behave as in the simple three-level system. Instead, the intraband transitions themselves can be thought of as providing a decay mechanism parallel to the direct recombination. hence, a PECS signal should be seen from the part of the spectra associated with the recombination of these hot carriers. This idea was used by von der Linde *et al.* [2] to investigate the relaxation of hot carriers in GaAs. In the work reported in the experimental section, we are interested only in the PECS signal because of the peak of the PL spectra. As described above, this will behave as in the simple three-level system.

There are other parallel processes that can act between the bands that are not considered in the model. Examples of these are free or bound exciton recombination. These processes will be seen only at low temperatures. However, at low temperatures the effect of the hot carriers is most pronounced, so that for long times after a laser pulse, the populations of excitons are thermalized with carrier populations, n and p. In this case, the decay rates of these processes are proportional to the np product, so they do not contribute to a PECS signal.

What is the effect of different types of traps on the simple model? If the populations of the excited carriers are much greater than the densities of the different bulk

traps, then as discussed earlier, each trap can be characterized by a single lifetime for both electrons and holes. The effect of all the traps is to act in parallel, so the total trapping rate is just the sum of the rates for each trap. Then Eqns. 3.11 still hold, where now τ is due to all of the traps. Thus, the decay of the PECS signal observed should still be a single exponential. Usually, the recombination rate of one trap will dominate the others, so that one trap dominates the lifetime. In the case of higher trap densities, N_t, Eqns. 3.2 do not simplify to Eqns. 3.3. This is more difficult to solve for and is not attempted here. In this case the saturation of the process may be observed and the decay of the carriers and, hence, the PECS signal may be multimoded.

Diffusion and surface recombination were ignored in the rate equations used in the model. The two together give rise to surface capture. This is a parallel decay mechanism, which affects the decay of the PECS signal and hence, the lifetime measured. To see whether these effects are important, the size of the carrier diffusion length and the surface recombination velocity must be considered. It is important to do this in order to be able to associate unambiguously the lifetimes measured by PECS with bulk trapping rather than with surface capture.

3.3 Experiment

3.3.1 Apparatus

Figure 3.3 shows the experimental setup used for the PECS measurements.* The ultrafast pulses are produced using the colliding-pulse mode-locked (CPM)[8] ring dye laser described in Chapter 2. This output is a train of pulses with a pulse width of 250 to 400 fs full-width at half-maximum (FWHM), depending on the alignment of the laser, with a repetition rate of 120 MHz, wavelength of about

*For detailed information about the apparatus, see Appendix D.

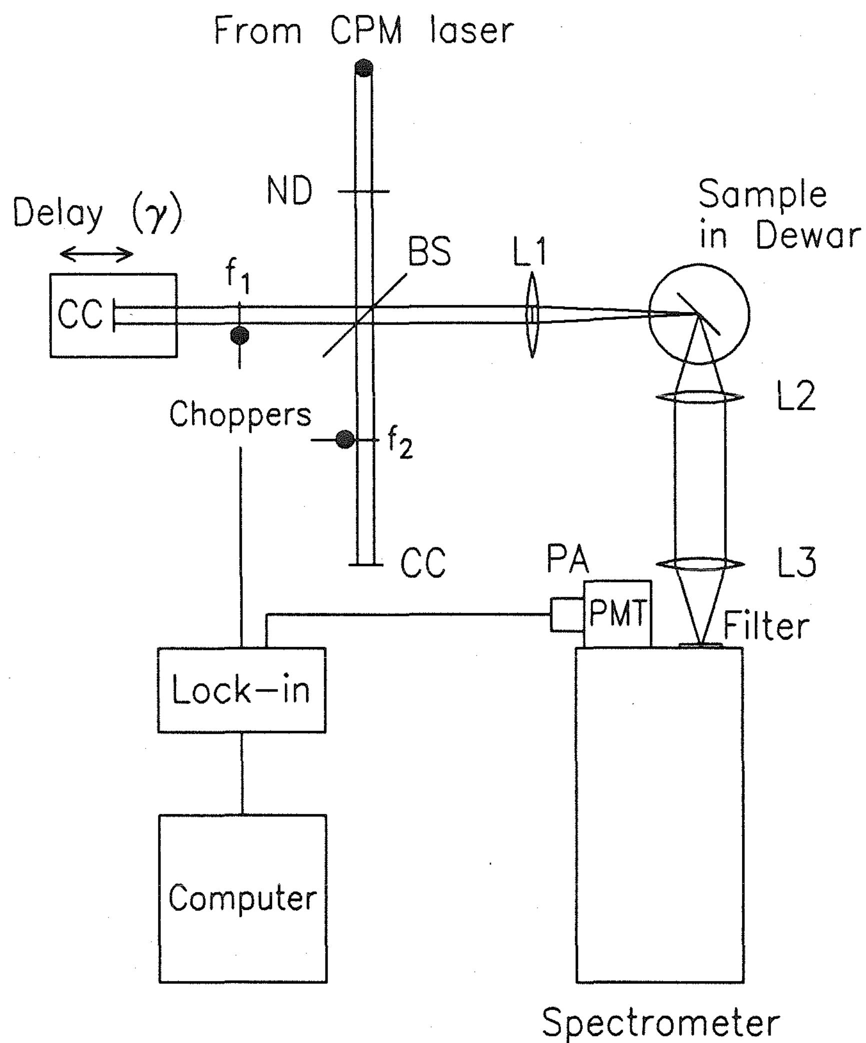

Figure 3.3: Schematic of the photoluminescence excitation correlation spectroscopy apparatus. Pulses are generated by a colliding-pulse mode-locked (CPM) laser. BS is a beamsplitter, L1 is a focusing lens, L2, L3 are PL collecting lenses, CC are corner cubes, ND is a neutral density filter, and PM is a current-sensitive preamplifier. The two choppers are operating at frequencies f_1 and f_2.

6200 Å, and a maximum average power in the range of 20 mW, or 17 pJ of energy per pulse. The power of this beam is adjusted using the variable attenuator, shown as ND This pulse train is input into a Michelson interferometer. The output of the interferometer is two equal intensity collinear pulse trains, one called the pump beam the other the probe beam. The delay time between pulses of the two trains, γ, is controlled by varying the path length of the interferometer arm, which gives rise to the probe beam. This length is controlled by a programmable stepper motor, which has a travel of 20 cm (1300 ps) and step size of 1 μm (7 fs). The pulse trains are individually chopped, one at 2005 Hz, the other at 1603 Hz. The output of the interferometer is focused using a 150 mm lens to a 25 μm (diameter) spot on the sample's surface. The average power of either unchopped beam at the sample is typically 1 to 2 mW (the energy per pulse is 8 to 16 pJ). The sample is held in a dewar to allow temperatures of 5 to 300 K to be maintained. The photoluminescence (PL) is collected using the two collecting lenses shown. Two different geometries of input beam, sample, and PL collection were used. Figure 3.3 shows one geometry. This has an input beam angle of incidence of 45° with the PL collection axis at an angle of 45°to the sample normal. In the other geometry used, the input beam angle of incidence was about 20° and the PL collection axis was along the sample normal. There was no apparent difference in the features of the signals measured in these two geometries, so no distinction is made between them. Two different dewar systems were used, one an immersion dewar and the other a cold finger dewar. Both were operated at temperatures of about 5, 77, and 300 K. Spectral resolution was provided by a Spex 1404 double pass spectrometer with a GaAs photomultiplier tube (PMT) monitoring the PL at the exit slit. The current signal output from the PMT was converted to a voltage signal using a current sensitive preamplifier, and this signal was input into a programmable lock-in amplifier. The lock-in amplifier could lock on to frequencies ω_1, ω_2, $\omega_2 -$

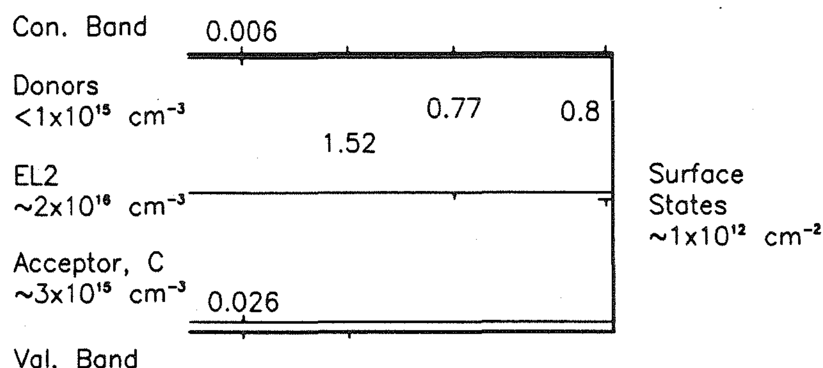

Figure 3.4: Schematic Band Diagram of In-alloyed GaAs. This shows the electronically active levels, including surface states. Energies are in eV. See Ref. 9.

ω_1, or $\omega_2 + \omega_1$. Frequencies ω_1 and ω_2 are called fundamental frequencies, while $\omega_2 + \omega_1$ and $\omega_2 - \omega_1$ are the sum and difference frequencies, respectively. The lock-in amplifier, spectrometer, and delay time stepper motor were controlled by a computer so that scans of signal versus wavelength or delay time could be made automatically. The overall temporal resolution of our PECS system was the laser pulse width.

3.3.2 Samples

Two samples are used in this case study. Both samples are semi-insulating (SI), liquid-encapsulated Czochralski (LEC)-grown substrate materials. One is GaAs, while the other is In-alloyed GaAs with a 0.3% mole fraction of InAs. The electronically active centers for the In-alloyed sample are known from earlier work[9] and are shown in Fig. 3.4. This shows carbon, a 26 meV deep acceptor, with a concentration of approximately 3×10^{15} cm^{-3}; shallow donors with a total concentration of no more than 1×10^{15} cm^{-3}; and EL2, which pins the Fermi level near midgap and has a concentration somewhat greater than 2×10^{16} cm^{-3}. The electronically active centers for the nonalloyed sample are similar to the alloyed sample in en-

ergy level and concentration. The major difference between the two samples is the dislocation density. For the In-alloyed material the density is 10^2 cm^{-2}, while for the nonalloyed material it is 10^4 to 10^5 cm^{-2}. This difference gives rise to large variations in the PL intensity across the In-alloyed materials surface, while the PL from the nonalloyed samples are more uniform.* In this study, the areas of the In-alloyed samples studied corresponded to bright areas or regions with large PL signals. Both of the wafers were polished with a chem-mechanical polish. For more details on the alloyed sample and its preparation, see Ref. 9. The samples were investigated at 5, 77 and 300 K, with most of the experiments done at 5 and 77 K. The optical penetration depth at 6200 Å is 0.25 μm[10], so that the average electron-hole density excited by a typical single pulse, with energy of 12 pJ in the excited volume of 25 μm, in diameter by a depth of 0.25 μm is in the range of 10^{17} cm^{-3}. Comments on the importance of carrier diffusion are made in the discussion section.

3.4 Results

3.4.1 Introduction

This section describes the results for various different PECS experiments on In-alloyed GaAs, and on GaAs samples at temperatures of 5 and 77 K. The behavior of the spectra and the delay time scans are very similar for the two samples. The work presented at 5 K is for the In-alloyed GaAs samples, and most of the work presented at 77 K is for the GaAs samples. This section starts with the description of the results from conventional PL measurements made at 5, 77, and 300 K. Then the results using PECS are described, first with the GaAs sample at 77 K, and second with the In-alloyed GaAs sample at 5 K.

*This difference is of much technological interest and is discussed in detail in Chapter 4.

3.4.2 Conventional Photoluminescence

Figures 3.5(a)-(c) show PL spectra for In-alloyed GaAs made using the PECS apparatus to monitor the signal from one of the fundamental frequencies rather than at the difference frequency. This corresponds to conventional non-time-resolved PL using a pulsed laser. The spectra in Figs. 3.5(a),(b), and (c) are for temperatures of 5, 77, and 300 K, respectively. The 5 K spectrum shows two distinct sharp peaks, while at 77 K a single wider peak is observed, and at 300 K a single peak, which is still wider than that at 77 K, is observed. These spectra are all for the same pump power and the amplitude scales are the same in the three plots. Thus, the 5 K signal is 3$\times$ larger than the 77 K signal, which is 30 times that at 300 K.

The assignment of the peaks in Fig. 3.5 was determined using the bandgap for the In-alloyed GaAs at 4.2 K, with a 5 meV free exciton, a 6 meV shallow donor, and a 26 meV carbon acceptor. The higher energy peak ($\lambda \approx 8240$Å) is seen to be a combination of direct band-to-band recombination ($e - h$), the free exciton (X), the donor-bound exciton ($D^0 - X$), and the donor-to-band ($D^0 - h$) recombination with a low-energy shoulder, including the acceptor bound exciton ($A^0 - X$). The lower-energy peak is a combination of band-to-acceptor ($A^0 - e$) and donor-acceptor ($A^0 - D^0$) recombination. In this study, the high-energy peak is referred to as the near band-to-band peak and the low-energy peak as the acceptor related peak.

The peak in the 77 K spectrum is the near band-to-band peak. Compared to the peak in the 5 K spectra, the 77 K peak is: wider because it is thermally broadened, and shifted in energy because of the decrease in the bandgap with temperature. At 77 K, the near band-to-band peak is mainly due to direct band-to-band recombination, since the excitons and donors are ionized at 77 K. The lower energy, acceptor-related peak is a small bump on the low-energy shoulder of

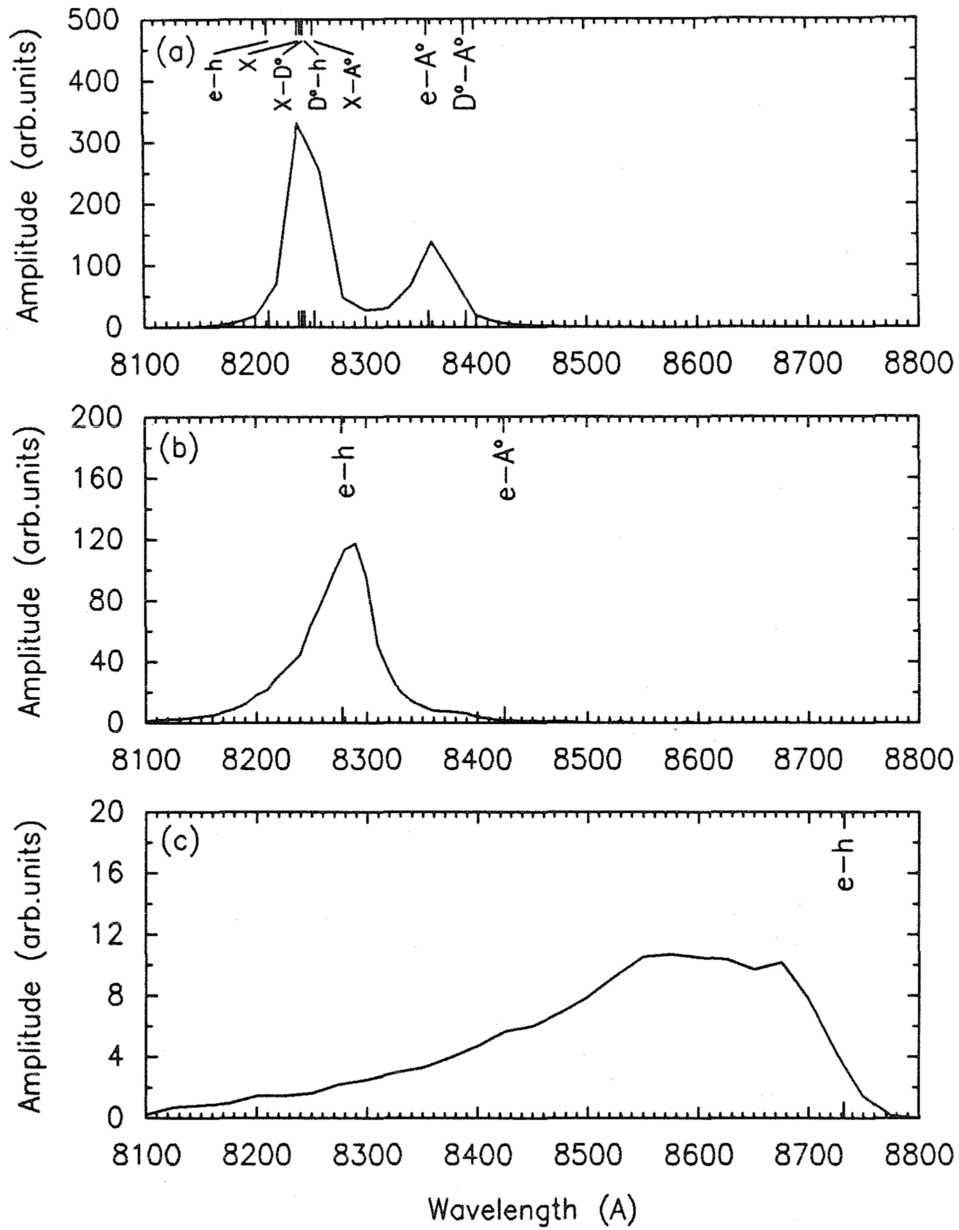

Figure 3.5: Photoluminescence spectra of In-alloyed GaAs taken using PECS at the fundamental frequency. Spectra (a), (b), and (c) were taken at T= 5, 77, and 300 K, respectively.

the band-to-band peak. The decrease in the size of the acceptor-related peak from the 5 K spectrum is because the acceptor is mainly ionized at 77 K.

The 300 K spectrum shows only a broad peak corresponding to a near band-to-band peak, which is thermally broadened and shifted in energy because of the change in the bandgap with temperature. This near band-to-band peak is due only to direct band-to-band recombination, because the acceptors and donors are completely ionized at 300 K.

The behavior of the conventional PL spectra is more complicated for 5 K than for 77 and 300 K because the acceptor is not ionized at 5 K. The same holds true for the PECS results, so the 5 K results are more complicated than the 77 and 300 K results. For this reason, we first describe the PECS study of the nonalloyed GaAs at 77 K, and then we look at the results for PECS of the alloyed GaAs at 5 K. The PECS behavior at 300 K is similar to that at 77 K and is not presented in this work.

3.4.3 Time-resolved PL at 77 K

Figure 3.6 shows for comparison the PECS spectra of GaAs at 77 K for both the fundamental and difference signals. The spectra are for delay time, γ, near zero. The peaks in both spectra are at 8240 Å, and the shapes are very similar. The ratio of the difference to fundamental peak heights is about 20%. This is lower than the value of 27% calculated for capture-dominated recombination. This discrepancy is probably due to small errors in the alignment of the PL collection optics.

Figure 3.7 shows delay time scans; these correspond to a scan of the PECS signal with delay time, γ. These are for GaAs at 77 K, and the wavelength is 8240 Å, the peak of the spectra shown in Fig. 3.6. Signals for both the difference and fundamental frequency are shown. These signals show the features predicted by Eqns. 3.11. That is, the fundamental signal shows an exponential decay on a

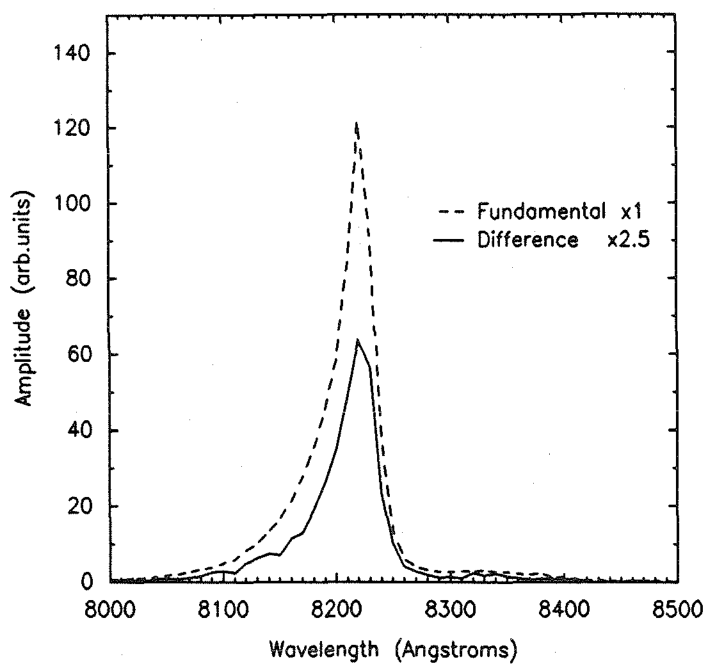

Figure 3.6: Photoluminescence spectra for GaAs sample at 77 K, with γ near zero. The dotted curve shows the PECS spectra at the fundamental frequency, while the solid curve shows the PECS spectra at the difference frequency ($\times 2.5$).

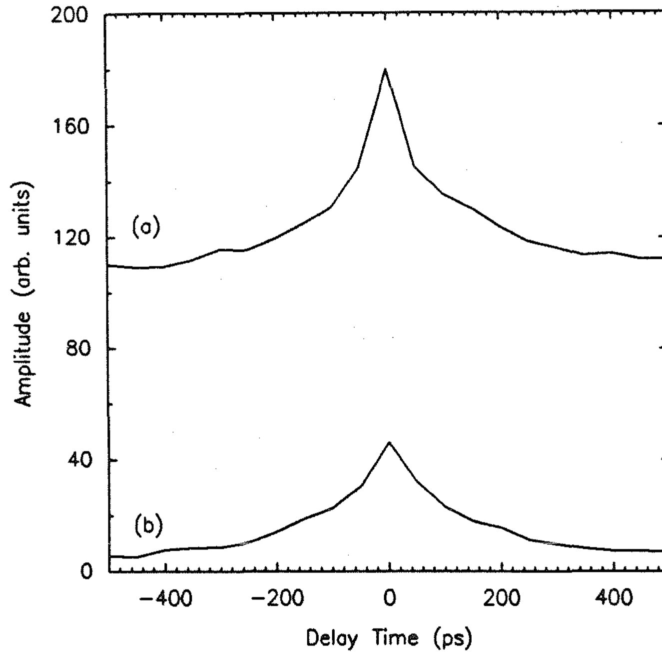

Figure 3.7: Delay-time scans at $\lambda = 8240$ Åof GaAs PL at 77 K using PECS. Scan (a) shows the fundamental signal, while Scan (b) shows the difference signal.

constant background, and the difference signal shows the same exponential decay without the background. The ratio of the difference to fundamental at $\gamma = 0$ is 25% which is close to the 27% value expected for capture-dominated recombination, strongly suggesting the samples are capture-dominated. The decay corresponds well to an exponential over the one decade of decay in which the data were taken. The decay constant corresponds to a lifetime of about 275 ps.

More detailed scans of the delay time near $\gamma = 0$ show that there is a very sharp peak at $\gamma = 0$. Figure 3.8 shows a series of delay-time scans of the difference signal. Figure 3.8(a) shows a scan from -500 to 500 ps with step 50 ps, along with a scan from -50 to 50 with step 5 ps. Neither of these scans resolves this peak. Figure 3.8(b) shows a scan from -2.5 to 2.5 step 0.5 ps, along with one from -0.5 to 0.5 ps with a 50 fs step. This last scan resolves the peak, showing a

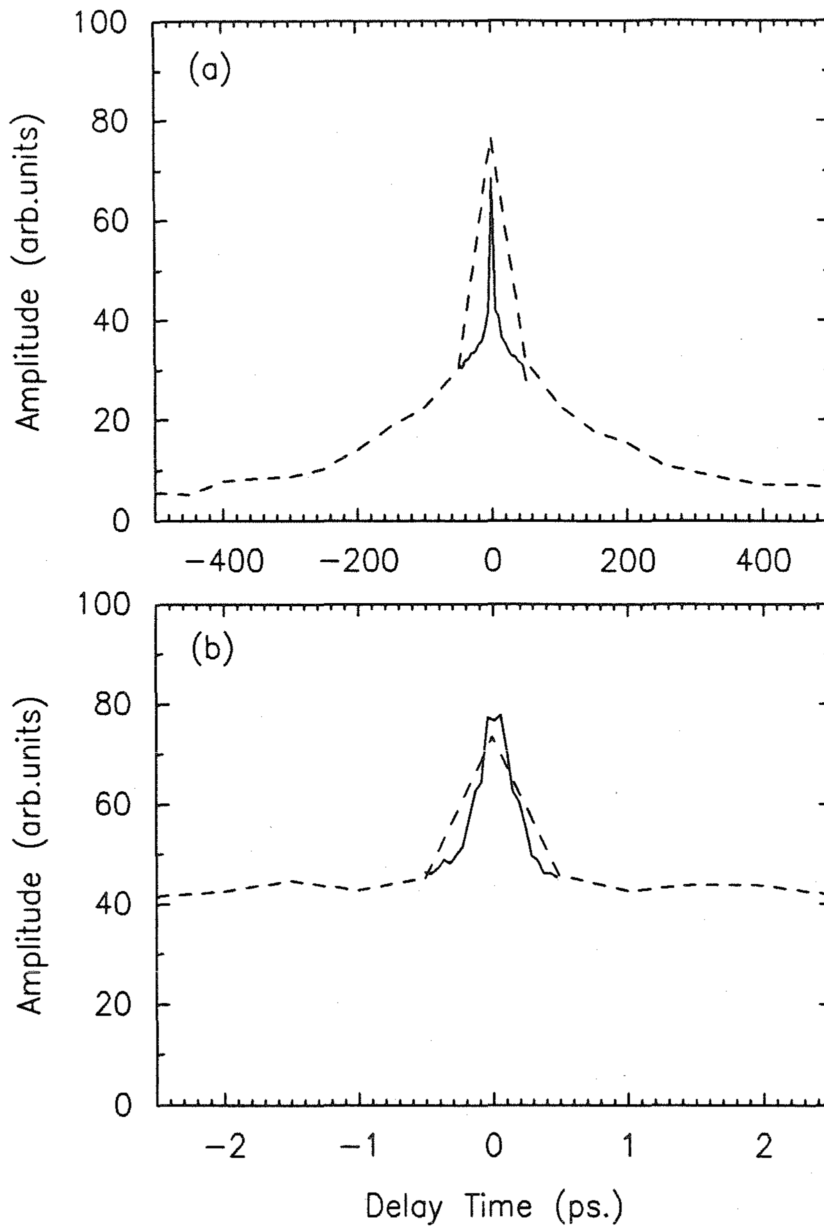

Figure 3.8: Coherence Peak. This shows a series of delay-time scans of the PECS difference signal for GaAs at 77 K. Plot (a) shows a scan from -500 to 500 ps with step 50 ps and a (dotted) scan from -50 to 50 ps step 5 ps (solid). Plot (b) shows a scan from -2.5 to 2.5 ps with step 0.5 ps (dotted) and a scan from -500 to 500 fs step 50 fs (solid).

400 fs FWHM peak with about a 2:1 peak to background ratio. The width of this peak corresponds closely to the autocorrelation width of the laser pulses used in this experiment, suggesting that the peak is due to the interference of the optical pulses. This is proved by the fact that the peak disappears when the pump and probe beams are polarized 90°apart to eliminate optical interference. This peak is called the coherence peak and is commonly seen in time-resolved PL; however, the reason it is seen in this set up is slightly different.

Summarizing, the measurements for the GaAs sample at 77 K, the results for the band-to-band peak, show exactly the behavior expected from the simple theory developed in Section 3.2 for recombination dominated by capture by traps. Thus, the recombination of the SI LEC GaAs substrate is capture-dominated. The lifetime measured for the SI LEC GaAs sample is about 275 ps. A similar result is found for the In-alloyed samples. However, the behavior of both these samples at 5 K is more complicated and is described for the In-alloyed GaAs sample below.

3.4.4 Time-resolved PL at 5 K

To understand the behavior of In-alloyed GaAs at 5 K, more than simple spectra and delay-time scans are necessary. The results described in this subsection include: difference and fundamental spectra for different laser-pulse powers, delay-time scans, and difference spectra for a series of different delay times using different pulse powers. The results described are for an area of the In-alloyed sample, which has a high PL intensity, corresponding to a bright region surrounding a dislocation.*

Figure 3.9(a) shows the pump-power dependence of the PL spectrum from one pulse train. The three spectra are for pulse energies incident on the sample of 12., 1.2, and 0.12 pJ, and are normalized by factors 1×, 10×, and 100×, respectively,

*See Chapter 4 for details

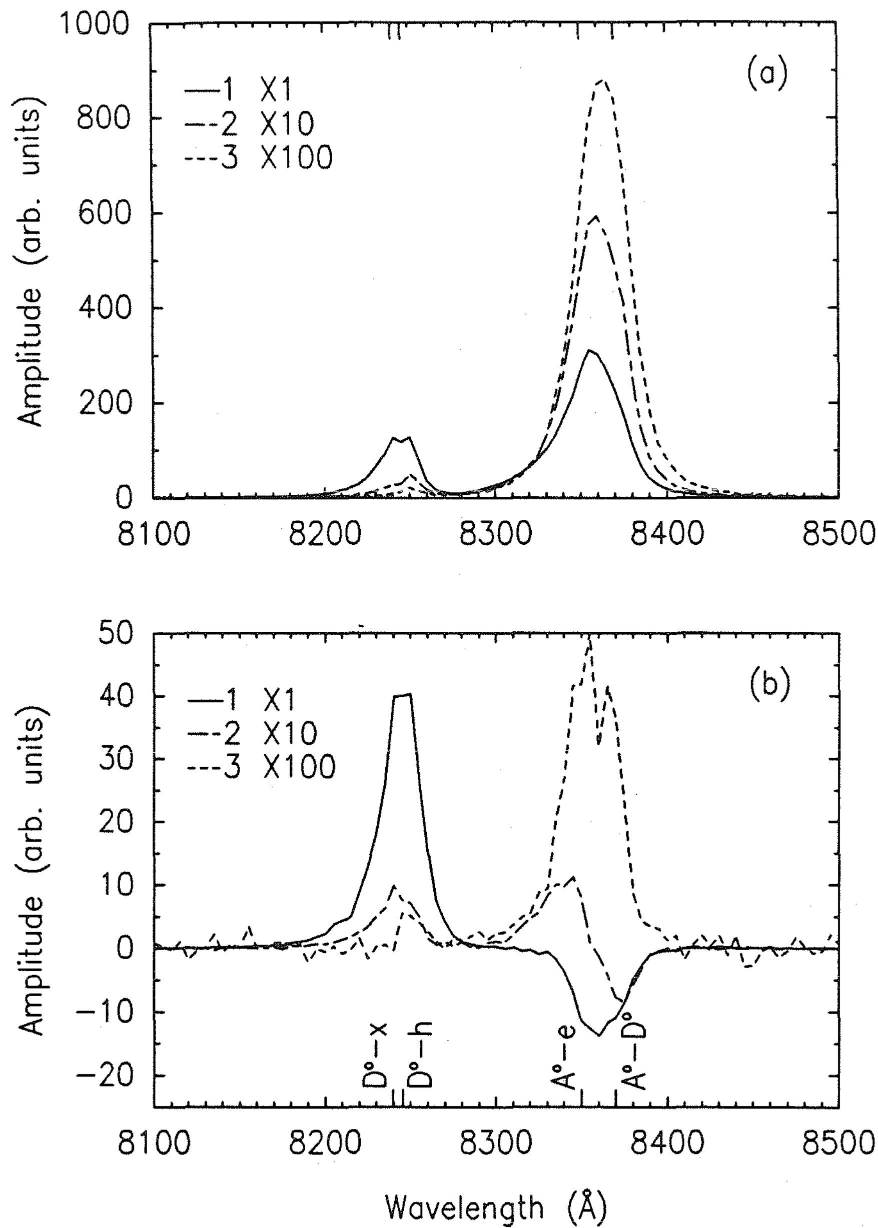

Figure 3.9: Spectra from In-alloyed GaAs sample at 5 K. Plot (a) shows spectra for a single pulse train pump, with lock-in at ω_1; while plot (b) shows spectra for a double pulse train pump, with lock-in at $\omega_2 - \omega_1$. Curves labeled (1), (2), (3) are for pulse energies of 12., 1.2, and 0.12 pJ, respectively. The curves are scaled as shown in the legend.

so that a peak with linear pump-power dependence would be the same height for the three spectra. This experiment is similar to the usual CW-pumped PL experiment except that the pulses have much higher peak power, so the excited electron-hole densities are much higher. The peak labels in Fig. 3.9 are the same as those in Fig. 3.5. The two peaks behave differently with pump power. The near band-to-band peak is superlinear with an α of 1.2, where $I_{\text{out}} \propto (P_{\text{in}})^{\alpha}$; and the acceptor-related peak ($\lambda \approx 8350$ Å) is sublinear with pump power with an α of 0.8 .

Figure 3.9(b) shows difference spectra for $\gamma = 0$ in the same format as that used for Fig. 3.9(a). The prominent features are at the same wavelengths as those for the single pulse PL in Fig. 3.9(a). The high-energy section of the spectra ($\lambda < 8300$ Å) shows a single peak whose shape and behavior with pump-power are quite simple. The ratio of this peak's amplitudes for the difference spectrum to the fundamental spectrum at the maximum pump intensity is about 20 %. The lower-energy section of the spectra ($\lambda > 8300$ Å) shows more complicated behavior. At the highest pump power the peak is negative, but at lower powers a positive peak on the high-energy side of this negative peak appears. At the lowest pump powers used, the positive peak completely dominates the negative peak.

Figure 3.10 shows scans of the amplitudes of the prominent peaks with delay time. The curve labeled 1 shows delay-time scans of the amplitude of the high energy near band-to-band peak ($\lambda = 8240$ Å) versus time between pulses. This shows two decay regimes. For $|\gamma| < 300$ ps, the amplitude decays exponentially with a decay constant of about 100 ps. For longer delay times, the decay is much slower, having a decay rate of about 1 ns. The extent of these tails was not investigated because the stepper motor could scan only from -500 to 500 ps. Note that no coherence peak is observed. The curve labeled 2 shows the amplitude of the acceptor-related peak ($\lambda = 8350$ Å) with delay time. This shows a positive

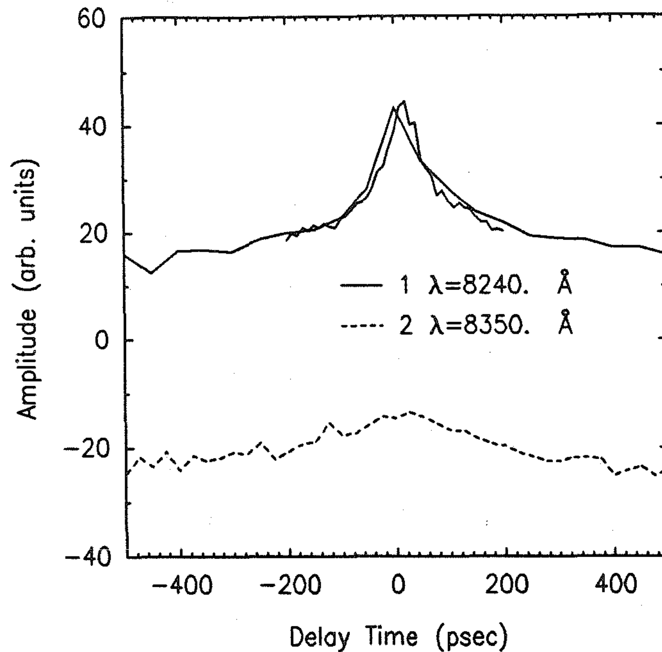

Figure 3.10: Delay-time scans. Curves labeled (1) show two scans of the high-energy band-to-band peak (λ = 8240 Å), and curve labeled (2) shows scans of the low-energy acceptor-related peak (λ = 8350 Å).

going peak superimposed on a negative background.

Figures 3.11(a),(b) show sequences of spectra for pulse energies of 12 and 1.2 pJ, respectively. These map out the PECS behavior for delay time, γ, and wavelength, λ. Earlier scans, Figs. 3.9 and 3.10, represent cuts of these sequences of spectra in either the γ or λ direction going through the distinctive features. The higher energy section of these scans ($\lambda < 8300$ Å) shows no more information than the earlier scans. However, the lower-energy section ($\lambda > 8300$ Å) shows more information. At lower pump powers, a second peak is clearly seen on the higher-energy shoulder. The behavior is most simply described by two different processes resulting in two overlapping peaks with different pump-power dependences. The lower-energy process gives rise to the negative peak, which slowly varies with de-

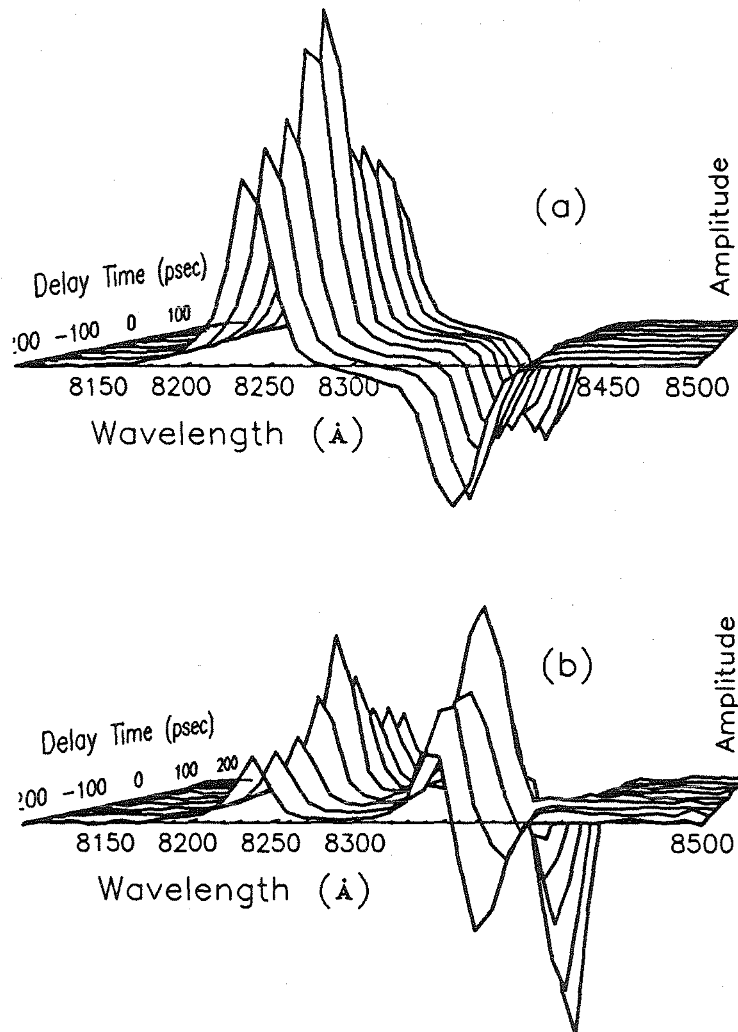

Figure 3.11: Sequences of photoluminescence excitation correlation spectra. Plot (a) 12 pJ pulse energy and plot (b) 1.2 pJ pulse energy.

lay time. This process is $A^0 - D^0$ recombination. The higher-energy process gives rise to the positive peak, which varies rapidly with delay time. This process is $A^0 - e$ recombination. The pump-power behavior of these processes is different. At high pump power $A^0 - D^0$ recombination dominates and $A^0 - e$ recombination gives rise to a small reduction in the negative background at $\gamma = 0$. At low pump power, the latter process dominates, giving rise to a positive peak at $\gamma = 0$. The delay-time behavior of the $A^0 - e$ recombination is about the same as that of the higher-energy peak ($\lambda \approx 8240$Å).

3.5 Discussion

3.5.1 Introduction

The results of using PECS to study SI GaAs at 77 K are those expected from the simple analysis of Section 3.2. However, the results of using PECS to study SI In-alloyed GaAs at 5 K show more complicated behavior. In this discussion section, first, the results at 77 K are discussed, including the appearance of the coherence peak; and second, the more complicated results at 5 K are discussed.

3.5.2 Time-resolved PL at 77 K

Figure 3.12 summarizes the important states and processes involved in producing PL in GaAs at 77 K using PECS. The states are the unexcited state and the excited state. The processes are near band-to-band recombination, and recombination by capture of electrons and holes. The following paragraph discusses the different states, while the next paragraphs discuss the processes.

As shown in Fig. 3.12, there are two states. The unexcited state is the relaxed state of the sample in thermal equilibrium at 77 K. There are no carriers in the bands because the material is semi-insulating. Furthermore, the donor states are

STATES

Unexcited state:
- carriers: $n = p = 0 \quad cm^{-3}$
- donors: $D^+ = D$
- acceptors: $A^- = A$

Excited state:
- carriers: $n = p \sim 10^{17} \quad cm^{-3}$
- donors: $D^+ \sim D$
- acceptors: $A^- \sim A$

DECAY PROCESSES

Near band-to-band:

$$e + h \rightarrow \quad \rightarrow h\nu_{e+h}$$

Capture:

$$T^o + h \rightarrow T^+ + \Delta E_1$$

$$T^+ + e \rightarrow T^o + \Delta E_2$$

Figure 3.12: States and processes involved in the photoluminescence of GaAs at 77 K. D^+, A^- are the charged states of the donor and acceptor, respectively. T^0, T^+ are the neutral and charged states of a typical trap. (The choice of T^+ rather than T^- is arbitrary.) ΔE_i represents the energies liberated in the interactions of the trap.

all empty and the acceptor states are full. The initial excited state is the state produced by a single laser pulse. This consists of equal numbers of electrons and holes with densities in the range of 10^{17} cm^{-3} for the pulses typically used. The energy of an incident photon is 2.0 eV compared to the bandgap of GaAs at 77 K of about 1.5 eV, so there is 0.5 eV excess energy given to each electron-hole pair. As discussed earlier, the generated carriers are initially high up in the bands. These hot carriers first equilibrate into quasi-static, electron-hole plasma with a temperature higher than the lattice temperature. This electron-hole plasma then cools to the lattice temperature. Other researchers have investigated the details

of these relaxations.[2,11] They find that the initial quasi-thermal equilibrium is achieved in a few picoseconds at a temperature of several hundred degrees K and that this plasma cools to the lattice temperature in a few hundred picoseconds. In the work reported in this chapter, these processes are important, but not of direct interest. The repetition time between sets of pump/probe pulses is about 8 ns. Figure 3.7 shows this to be enough time for the excited state to decay completely to the unexcited state.

Figure 3.12 shows the recombination processes of importance. The only direct recombination is near band-to-band. Other recombination processes such as exciton processes or donor-to-band processes are unlikely because the excitons and donors are ionized at the lattice temperature of 77 K. Similarly, acceptor processes are not important because the 26 meV carbon acceptor is sufficiently ionized at the temperatures involved. Thus, at 77 K the PL monitored is due only to band-to-band or np product recombination. This is the situation described by the simple model proposed in the theory section. The fact that a difference signal is observed indicates that there are capture processes acting in parallel with this np product recombination. The ratio between the difference and fundamental signal amplitudes of 20-25% indicates that these parallel capture processes dominate the np product recombination. Figure 3.13 shows a semilogarithmic plot of the delay-time scan shown in Fig. 3.10. This shows a decay of 275 ± 20 ps over nearly one decade. Thus, the lifetime that is due to these capture processes is 275 ± 20 ps. This lifetime is much shorter than those found by Nelson and Sobers[12] for purely radiative decay of minority carriers in material with much higher carrier densities (*i.e.*, 1 ns for carrier densities of about $1 \times 10^{19}\text{cm}^{-3}$). This is consistent with our conclusion that the capture process dominates direct recombination.

What type of capture processes are capable of giving rise to this 275 ± 20 ps carrier lifetime? As discussed, the effect of surface capture may be important.

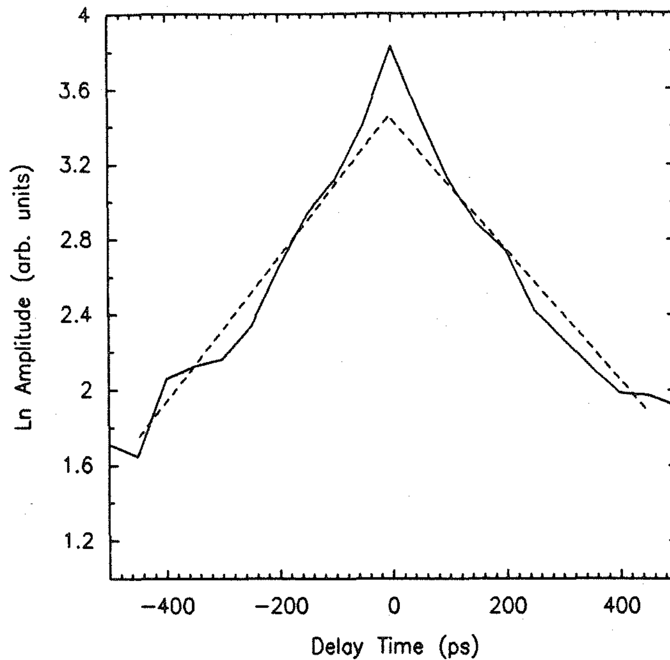

Figure 3.13: Semilogarithmic plot of the difference delay-time scan of GaAs PL at 77 K using PECS. (See Fig. 3.7 for the linear plot.) The dashed lines show the straight lines fitted to each side. The point at $\gamma = 0$ is not included in the fit because of the coherence peak. The lifetime from the left and right sides are 260 and 290 ps, respectively. Thus, the average lifetime is 275 ± 20 ps.

Surface capture requires the diffusion of carriers to the surface and recombination at the surface. So, for the surface to be important, the diffusion length of the carriers over their lifetime must be long enough for the carriers to be able to reach the surface, and the surface recombination velocity must be large enough to provide sufficient capture. The ambipolar diffusion rate for 77 K is estimated to be 125 cm^2/s.[10] Using this diffusion rate, the diffusion length for a lifetime of 275 ps is about 2 μm. This is larger than the probe depth of 0.25 μm, so that diffusion to the surface does not limit surface capture. However, other experiments* demonstrate

*These experiments involved passivating the surface of the sample; see Chapter 4 for details.

that the surface recombination velocity at 77 K is not large enough to provide sufficient capture to produce a 275 ps lifetime. Thus, the lifetime measured is due to capture by bulk levels that arise from defects, and is unrelated to the surface. Because the carrier diffusion length is much smaller than the 25 μm diameter of the illuminated spot, the defects must be distributed over the area of the spot. As described in the theory, section multiple types of traps would give rise to a single exponential decay; however, one trap usually dominates the others and governs the lifetime.

What can be said about the dominant trapping process responsible for the carrier capture? The decay shown in Fig. 3.13 is exponential, so it may be concluded that the electrons and holes decay at the same rate and that their densities are much higher than the trap densities, implying that the actual total speed of the capture process (capture of an electron and a hole) must be fast enough to allow multiple numbers of captures of electrons and holes to take place in the 275 ps lifetime. The actual determination of the defect producing the dominant trap is not easy and is discussed in Chapter 4.

What is the cause of the coherence peak? A coherence peak is observed in many pulse/probe experiments.[2,11] In this experiment, the pump and probe beams are collinear so that the optical interference does not cause fringes on the surface as it does in the case of von der Linde *et al.*[2] Instead, the entire optical wave fronts interfere when the pulses overlap. Thus, when the pulses overlap, the total incident intensity at the sample is given by $I_{\text{in}}(\gamma) = 2I + 2I cos(\omega\gamma)$, where I is the peak intensity of pulse. Thus, instead of remaining constant, $I_{\text{in}}(\gamma)$ varies with γ from 0 to $4I$ with an average of $2I$. Because of mechanical instabilities of the interferometer, γ varies by a few optical periods at frequencies in the range of about 10 Hz. This smears out I_{in} as being the average $2I$. However, the effect of the variation of I_{in} on the PL output signal, I_{out}, will be seen if the output signal is not

linear with the incident intensity. In the case of a superlinear process, $I_{out} \propto (I_{in})^{\alpha}$ with $\alpha > 1$, more signal would be seen for the varying incident intensity than for the average intensity. Thus, in the case of a superlinear process like band-to-band recombination at 77 K, where α is measured to be 1.8, more PL is generated when the pulses from the two pulse trains overlap. This is analogous to the behavior of the second harmonic generation (SHG), autocorrelator described in Chapter 2, where now the PL signal behaves like the doubled signal. For $\alpha = 2$, the peak-to-background ratio should be 3:1. The experimental peak-to-background value of about 2:1 is in reasonable agreement with $\alpha = 1.8$. This peak is useful because it demonstrates that the process being observed is superlinear, and it allows the interferometer to be precisely aligned.

In summary, the PECS measurements of GaAs at 77 K behave as predicted for a capture-dominated system, because the monitored PL represents the band-to-band PL and is dominated by a parallel capture process. The measured carrier lifetime is 275 ± 20 ps. This lifetime is due to the capture of carriers onto trapping levels distributed in the bulk over the optically excited spot. Surface capture is not important. The coherence peak observed is due to the optical interference of the laser pulses, together with the superlinear behavior of the band-to-band PL intensity with input power. These measurements indicate that PECS successfully measures the carrier lifetime in a sample, where trapping is the dominant recombination mode.

3.5.3 Time-resolved PL at 5 K

PECS results for SI In-GaAs at 5 K are more complicated than those for 77 K, as demonstrated in the results section. The measurements described in the results section do not completely determine the processes that are taking place. However, these results provide enough information to determine the contribution of the bulk

traps to the carrier decay.

Figure 3.14 summarizes the pertinent states and processes in the In-alloyed GaAs for PL at 5 K. The states are: the unexcited state, the excited state, and a quasi-static state. The processes are sorted into the same near band-to-band processes and acceptor processes that were used in the results. The near band-to-band processes are comprised of band-to-band, donor-to-band, and free and bound exciton recombination processes. The acceptor processes are comprised of band-to-acceptor and donor-to-acceptor recombination processes.

Figure 3.14 shows the three different sample states. The unexcited state is identical to that at 77 K; there are no carriers, the donors are empty, and the acceptors are filled. As well, the excited state at 5 K is similar to that at 77 K. The absorption of the exciting photons produces hot carriers. According to von der Linde *et al.*,[2] these hot carriers generate an electron-hole plasma whose initial temperature is several hundred degrees and the plasma cools to about 35 K in 100 ps. Rapid interactions between the electrons and phonons and the phonons amongst themselves are likely to produce a phonon distribution with approximately the same temperature behavior. After still longer times, the temperature of the plasma cools to the sample temperature of 5 K. This large change in the temperature of the carriers has a great effect on the PECS measurements made at 5 K. This is because this temperature relaxation changes the carrier temperature from a high-temperature regime, in which the acceptors and donors are ionized, to a low-temperature regime in which the donors and acceptors are partially un-ionized. At 5 K, there is a third quasi-static state that is important, corresponding to the decayed excited state after the repetition time of the laser or just before the next set of laser pulses. At 5 K, this state is different from the unexcited state because the decay of the neutral donors and acceptors at 5 K is very slow. In fact, this decay is so slow that even after the pulse repetition time of about 8 ns,

STATES

Unexcited state:

carriers	$n = p = 0 \quad cm^{-3}$
donors	$D^+=D$
acceptors	$A^-=A$

Excited state:

carriers	$n = p = 10^{17} \quad cm^{-3}$
donors	$D^+<D$
acceptors	$A^-<A$

Quasi-static state:

carriers	$n = p = 0 \quad cm^{-3}$
donors	$D^+<<D$
acceptors	$A^-<<A$

DECAY PROCESSES

Near band-to-band:

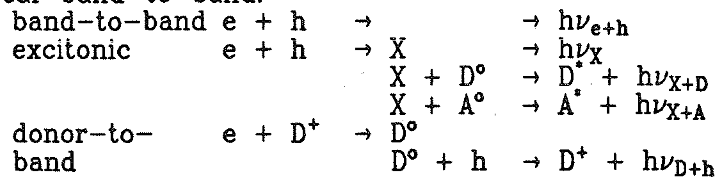

band-to-band	$e + h$	$\rightarrow$	$\rightarrow h\nu_{e+h}$
excitonic	$e + h$	$\rightarrow X$	$\rightarrow h\nu_X$
		$X + D^o$	$\rightarrow D^* + h\nu_{X+D}$
		$X + A^o$	$\rightarrow A^* + h\nu_{X+A}$
donor-to-	$e + D^+$	$\rightarrow D^o$	
band		$D^o + h$	$\rightarrow D^+ + h\nu_{D+h}$

Acceptor related:

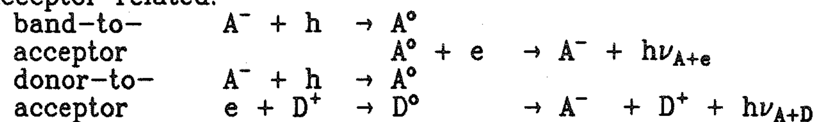

band-to-	$A^- + h$	$\rightarrow A^o$	
acceptor		$A^o + e$	$\rightarrow A^- + h\nu_{A+e}$
donor-to-	$A^- + h$	$\rightarrow A^o$	
acceptor	$e + D^+$	$\rightarrow D^o$	$\rightarrow A^- + D^+ + h\nu_{A+D}$

Capture:

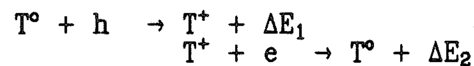

$T^o + h$	$\rightarrow T^+ + \Delta E_1$	
	$T^+ + e$	$\rightarrow T^o + \Delta E_2$

Figure 3.14: States and processes involved in the photoluminescence of In-alloyed GaAs at 5 K. T^0, T^+ are the neutral and charged state of a typical trap. (The choice of T^+ rather than T^- is arbitrary.) ΔE_i represents the energies liberated in the interactions of the trap.

there are still neutral donors and acceptors present, although all the carriers have recombined.

Figure 3.14 shows two groups of recombination processes. There are three near band-to-band recombination processes, direct band-to-band, exciton, and donor-to-band recombination. The binding energies of the donors and bound excitons involved with these processes are comparable to the thermal energy, over the time when the temperature of the electron-hole plasma temperature is elevated (estimated to be 100 ps). Thus, during this time, we expect these levels to approach thermal equilibrium with the carriers in the bands. So, over a time interval of about 100 ps after either optical pulse, the near band-to-band processes behave as if they are between two simple bands. At times long after both pulses, the electron-hole plasma tends to condense and become excitonic. At 5 K, recombination involving the acceptors is also important. Figure 3.14 shows these two recombination processes. The higher-energy process is a band-to-acceptor recombination, the recombination of an electron with a neutral acceptor. The lower-energy process is donor-to-acceptor recombination, which involves the transfer of an electron from a neutral donor to a neutral acceptor producing a donor and an acceptor that are ionized.

In discussing the results of PECS at 5 K, it is very important to remember that PECS is a measurement involving cross-correlations such as those shown in Eqns. 3.12 and 3.13. It is not a true, time-resolved technique, so the PECS measurement for a certain delay time between pulses involves the integration of the PL signal of the sample over times long compared to the repetition rate. Thus, populations over the whole repetition time contribute to the PECS signal. With this in mind, the near band-to-band difference signal is due to the interaction of a hot plasma with one that has cooled by an amount depending on the size of γ. Thus, the near band-to-band signal will mostly involve the interaction of the bands when each band can

be considered as a single equilibrated level, so the simple model for PECS should apply for the near band-to-band recombination at 5 K. However, at 5 K there is not only carrier capture through trapping levels; the acceptor level is involved in carrier capture as well. As described in the subsection 3.4.4, Fig. 3.10 shows two decay rates involved in the decay of the carrier population. One decay involves a fast process with a time constant of about 100 ps, and the other involves a slow process with a time constant of about 1 ns. The fast process does not take place for times much longer than about 100 ps. This is either because this fast process saturates, or because it takes place only while the electron-hole plasma is sufficiently hot, or a combination of both. If this were not the case, only this fast process would be observed. This process involves the un-ionized acceptors because this process is not observed at 77 K when the acceptors are ionized. Indeed, a fast component is observed in the band-to-acceptor peak. Thus, the fast process is related to recombination through the acceptor. The slow process is due to the capture of the carriers onto a deep trap. The fact that this is much slower than the same process seen at 77 K is probably due to the fact that for times long after a laser pulse, the carriers are possibly present as excitons, and the cross section of interaction of these with the deep traps may be smaller than the interactions with single carriers. The ratio of the difference to a fundamental signal at $\gamma = 0$ is 20%, in reasonable agreement with the value derived in the theory for recombination dominated PL. The fact that the process is superlinear, whereas α is only 1.2, indicates that the signal we observe is not completely due to band-to-band recombination, and that exciton recombination may also be taking place. The lack of the coherence peak at 5 K is explained by the fact that the near band-to-band process is nearly linear with the input laser.

As described in the results section, the two acceptor-related peaks show very different behavior. The band-to-acceptor recombination peak decay is fast, while

the donor-to-acceptor recombination process gives rise to a negative background. The decay rate of the band-to-acceptor peak is not easy to measure because it overlaps with the donor-to-acceptor peak. However, it appears to decay with a rate slightly slower than about 100 ps. This is the process that produces the fast decay in the near band-to-band peak. As described in the paragraph above, this process seems to act only over about 100 ps, either because the process saturates or because the process takes place only when the temperature of the carriers is sufficiently high. The PECS delay-time signal from the donor-to-acceptor process is a constant negative background. This donor-to-acceptor peak arises from the interaction of neutral donors and acceptors, which are not present when the electron-hole plasma is at elevated temperatures, so this signal arises from times after the arrival of either optical pulse, when neutral donors and acceptors are present. The interaction between these levels is small, giving rise to a slow decay in their populations, which generates a constant background.* This signal is negative because the populations involved in the process saturate. This means that the PL signal for one pulse train is similar in strength to that for two pulse trains. So, the donor-to-acceptor signal is the logical OR of the two pulse trains, rather than the usual logical AND. Thus, as discussed in the theory section, a negative background is obtained. The fact that the normal PL acceptor-related peak is sublinear is reasonable, since it results mainly from the donor-to-acceptor peak which is saturates.

What type of capture processes are capable of giving rise to the carrier lifetime of about 1 ns? As with surface capture at 77 K, even though the carrier diffusion length at 5 K allows the carriers to reach the surface, the surface recombination velocity is not sufficient to produce this lifetime.* Thus, the lifetime is governed by defects distributed in the bulk. The nature of these defects is investigated in

*Donor-to-acceptor recombination decay times in GaP are in the range of microseconds and longer; see Ref. 13.

*See Chapter 4 for details.

Chapter 4.

In summary, the PECS measurements of In-alloyed GaAs at 5 K are more complicated than those at 77 K, because the acceptor and donor levels are not sufficiently ionized at 5 K, whereas they are ionized at 77 K. However, even with this complication, the near band-to-band PECS delay-time scan behaves as expected by the model developed. Only in this case, there is more than one decay rate, one fast and the other slow. The fast decay is a result of band-to-acceptor interactions, and the long decay is due to deep levels. The fast decay involves the acceptor and saturates or acts only over a limited time. (This is why there are two decay rates observed in the delay-time scans of the near band-to-band PL.) The fast decay of the PECS signal from the band-to-acceptor PL substantiates the fact that this is the process responsible for the fast decay in the near band-to-band PECS signal. The PECS signal from the donor-to-acceptor process gives a negative background because the neutral donor and acceptor populations saturate and decay very slowly.

3.6 Summary of Results

The intent of the work of this chapter was to investigate the use of photoluminescence excitation correlation spectroscopy (PECS) to time-resolve ultrafast PL behavior. This was investigated by first determining what the technique measures, using a simple model for the generation of PL, and then experimentally applying the technique to various samples in a case study. This section gives the conclusions of this analysis, and of the case study.

The PECS technique is modeled by analyzing the signals for radiative band-to-band recombination luminescence that would be observed in a two-band system with a trap level. It is found that no difference frequency signal is observed in the

limit where radiative band-to-band recombination dominates, while a difference signal is observed in the limit of recombination by capture. In the latter case, the difference signal has an exponential decay with the delay time, γ, and the decay constant is the carrier lifetime associated with the trap levels involved in the capture.

The PECS technique is applied to SI GaAs at 77 K and SI In-alloyed GaAs at 5 K. At 77 K, the PECS of GaAs behaves as expected from the analysis. The delay-time scans show a single decay with a time constant representing a carrier lifetime of 275 ± 20 ps. This lifetime is much shorter than the lifetime for band-to-band radiative recombination. Moreover, this lifetime is due to the capture of carriers by bulk traps, not by surface traps. A coherence peak is observed at $\gamma = 0$; this is due to the interference of the input laser pulses.

At 5 K, the PECS study of the In-alloyed GaAs shows more complicated behavior than that expected from the simple three-level model. Two decay processes are seen in the delay-time scans. The faster process has a decay rate of about 100 ps and takes place only for times in the range of 100 ps after a laser pulse. This process involves the decay of carriers through the acceptors and takes place only over about 100 ps, either because it saturates, or because it takes place only when the electron-hole plasma is hot. The slower process has a decay time of about 1 ns. As with the result at 77 K, this lifetime is shorter than the expected band-to-band radiative lifetime, so that this sample is capture-dominated at 5 K. This process is due to the recombination of carriers through bulk traps, not surface capture. The behavior of the acceptor-related processes is also interesting. The delay-time scan of the band-to-acceptor recombination peak shows a fast decay similar to that for the near band-to-band process, corresponding to the decay of the carriers through the acceptor. The delay-time scan of the donor-to-acceptor recombination peak shows a negative background, because the neutral donors and

acceptors are long-lived, and their concentrations saturate.

Thus, PECS successfully determines the carrier lifetime at 5 and 77 K. So, the case study demonstrates that photoluminescence excitation correlation spectroscopy (PECS) can measure the carrier lifetime in capture-dominated materials.

Generalizing, PECS can be used to measure capture-dominated lifetimes in the range of the laser pulse width to the pulse repetition time. In the experimental setup used, this corresponds to 250 fs to 8 ns. (The lower limit can easily be extended to as low as 50 fs.) Moreover, this technique can be used in circumstances where processes other than capture by traps dominate the direct recombination of carriers, for example, in samples where surface recombination is important, or in more exotic samples such as double-barrier tunneling structures, where tunneling limits the lifetime of carriers in the well between the barriers.

References

1. H. Kume, K. Koyama, K. Nahataugawa, S. Suzuki, D. Fatlowitz , APP. Optics **27**, 1170 (1988).

2. D. von der Linde, J. Kuhl, and E. Rosengart, J. Lumin. **24/25**, 675 (1981).

3. D.L. Rosen, A.G. Doukas, A. Katz, Y. Budansky, and R.R. Alfano, in *Semiconductors Probed by Ultrafast Laser Spectroscopy*, edited by R.R. Alfano (Academic Press, Orlando Fl, 1984), pp. 393-407.

4. M. Jørgensen and J.M. Hvam, Appl. Phys. Lett. **43**, 460 (1983).

5. M.B. Johnson, T.C. McGill, and A.T. Hunter, J. of Appl. Phys. **63**, 2077 (1988).

6. See any text on semiconductor physics, such as,
S.M. Sze,*Physics of Semiconductor Devices*, 1st ed. (Wiley, New York, 1969), p.631.

7. D. Rosen, A.G. Doukas, Y. Budansky, A. Katz, and R.R. Alfano , Appl. Phys. Lett. **39**, 935 (1981).

8. R.L. Fork, C.V. Shank, R. Yen, C.A. Hirlimann , IEEE J. of Quantum Electron. **QE-19**, 500 (1983).

9. A.T. Hunter, Diffusion and Defect Data **48**, 1 (1986).

10. J.S. Blakemore, J. Appl. Phys. **53**, R123 (1982).

11. M.J. Rosker, Ph.D. thesis, Cornell University, 1987.

12. R.J. Nelson, and R.G. Sobers, Appl. Phys. Lett. **49**, 6103, (1978).

13. D. G. Thomas, J. J. Hopfield, and W. M. Augustyniak, Phys. Rev. **140**, A202, (1965).

Chapter 4

Space- and Time-Resolved Photoluminescence

4.1 Introduction

4.1.1 Background

Wafers of semi-insulating (SI) GaAs are widely used as substrates for the fabrication of GaAs high-speed digital integrated circuits (ICs) using field effect transistors (FETs). A critical part of the fabrication process is the formation of the active region under the gate of the FET. This region is formed by directly implanting dopant ions into the substrate and annealing. It is crucial that the properties of the activated region are uniform over the surface of the wafer; otherwise, large-scale integration is not possible. Commonly, arrays of field effect transistors (FETs) are fabricated on the surface of the substrate to check the uniformity of the device characteristics over the substrate.[1–5] Variations are seen because of processing and initial nonuniformities in the substrate material. In this work, the nonuniformities in the substrate material are studied. This topic has been the subject of much research. Variations of FET gate threshold voltages have been seen across the wafer.

These are found to vary as the average density of dislocations in the substrate by some researchers, and with dislocation proximity by others.[1–5] The nature of the variation is also found to vary depending on the processing steps used, specifically for the activation anneal.[3,4]

There has been much effort to reduce the number of dislocations in as-grown substrates. At present, the most common substrate material is semi-insulating (SI) liquid encapsulated Czochralski (LEC)-grown GaAs, which has an average dislocation density of 10^4 to 10^5 cm^{-2}, or an average separation of 50 to 15 μm.[6] The substrate studied in this work is SI LEC In-alloyed GaAs, which has a InAs mole fraction of about 0.3%, which reduces the dislocation density of most of the area of a typical wafer to less than 10^2 cm^{-2}, or an average dislocation separation of 0.5 mm.[6] There is much active research into other growth techniques.

There are many nondestructive techniques used to investigate the uniformity of substrates,[7] including: x-ray topography, which is sensitive to crystallographic defects such as dislocations; IR imaging, which is sensitive to point-defects, such as EL2, which absorb in the IR; scanning photoluminescence (PL), which is sensitive to variations in dopants and native defects; and cathodoluminescence, which is analogous to PL, except that an electron beam is used to excite the luminescence rather than an optical beam (it is sensitive to similar properties to which PL is sensitive). These techniques are often done in combination with the more destructive techniques, including fabrication of an array of FETs over the substrate;[1,2,4,5] fabrication of an array of devices for Hall measurements to measure sheet resistance over the substrate;[3] and making etch pit density (EPD) measurements, which measure the dislocation density by using an etch such as molten KOH to preferentially etch the dislocations.

Scanning PL is particularly well suited as a diagnostic tool because it is simple, relatively fast, and is sensitive only to about the top 1 μm of the substrate, as

are the electrical devices themselves. Moreover, spectral information can give information concerning the defects present, and carrier lifetimes can be directly measured, using time-resolved PL.

Much work has been done using scanning PL to map LEC GaAs substrates.[7–10] These show variations in the near band-to-band PL intensity over two length scales, one over about 200 μm, the other over the whole wafer. The variation over the finer scale corresponds to PL imaging of the cellular structure formed by the dislocations in LEC GaAs.[8,9] The intensity and carrier lifetimes vary by a factor of two over these features.[9] Over the whole wafer, intensity of near band-to-band PL correlates with EPD across the wafer. Typically, both PL intensity and EPD vary in a W shape across the wafer diameter.[3,8,7,9] The dislocation densities vary from 10^4 to 10^5 cm^{-2}, while the near band-to-band PL, typically, varies by a factor of three over the wafer. Measurements of carrier lifetime, made using time-resolved PL, show variations in carrier lifetimes across the wafer, which correlate with PL intensity variations and etch-pit density. The lifetimes measured are between 200 and 500 ps at 5 K.[9] The intensity of a 0.8 eV emission band associated with a trap is found to anticorrelate with the dislocation density, suggesting that this deep trap governs the lifetime. From this, it is thought that dislocations getter defects, which affect the lifetime of the material and hence the PL intensity.[8,9] Thus, there is PL contrast near a dislocation, and an increase in intensity with higher dislocation density, because of the dislocation "cleaning" up the material in its immediate vicinity.[8] This explains both the fine and the coarse variation of PL intensity. However, because of the small separation of dislocations, the effects of an individual dislocation are not directly seen.

Some work has also been done using scanning PL to map LEC In-alloyed GaAs substrates.[6,7,10,11,12] The dislocation separation in In-alloyed GaAs is much larger than that in GaAs, so that the effects of individual dislocations can be observed.

The top part of Fig. 4.1 shows a cathodoluminescence scan of a typical as-grown In-GaAs substrate. The lower part of Fig. 4.1 shows an optical microphotograph of the outlined region shown in the cathodoluminescence scan after KOH etching was used to show the dislocations. From the two images it can be seen that the single dislocation on the right gives rise to a dark circular region, while the dislocation cluster on the left gives rise to a dark circular region with a bright spot at the position of the dislocation cluster. Around these dark regions are bright annular regions. In the case shown, because of the proximity of the dislocations, these annuli run into one another, creating a large complicated bright pattern. Isolated single dislocations or clusters of dislocations are often seen, and are surrounded by a single bright annulus. The bright spot in the center of the dark region is seen only for clusters of dislocations. Typically, the dark region is in the range of 200 μm in diameter and the surrounding bright annulus has an outer diameter of about 400 μm. These features are larger than the dislocation separation in GaAs, so they are not seen in GaAs. Attempts to measure the carrier lifetime show that it is less than about 1.4 ns.[10] As seen in GaAs, the intensity of the 0.8 eV emission band associated with a trap anti-correlates with the dislocation density.[10] Thus, it is thought that this trap is involved in governing the lifetimes in the different regions.

It has been proposed that the pattern around a single dislocation is the result of one type of defect being gettered at the dislocation producing the bright annulus; at the same time, another type of defect is generated by the dislocation and diffuses away, giving rise to the dark region within the annulus.[10] It is not clear what causes the bright spot at the center of the features caused by dislocation clusters. The behavior of dislocations in GaAs is expected to be similar. However, this will not be directly observable because the separation of the dislocations is too small for the effect of an individual dislocation to be seen.

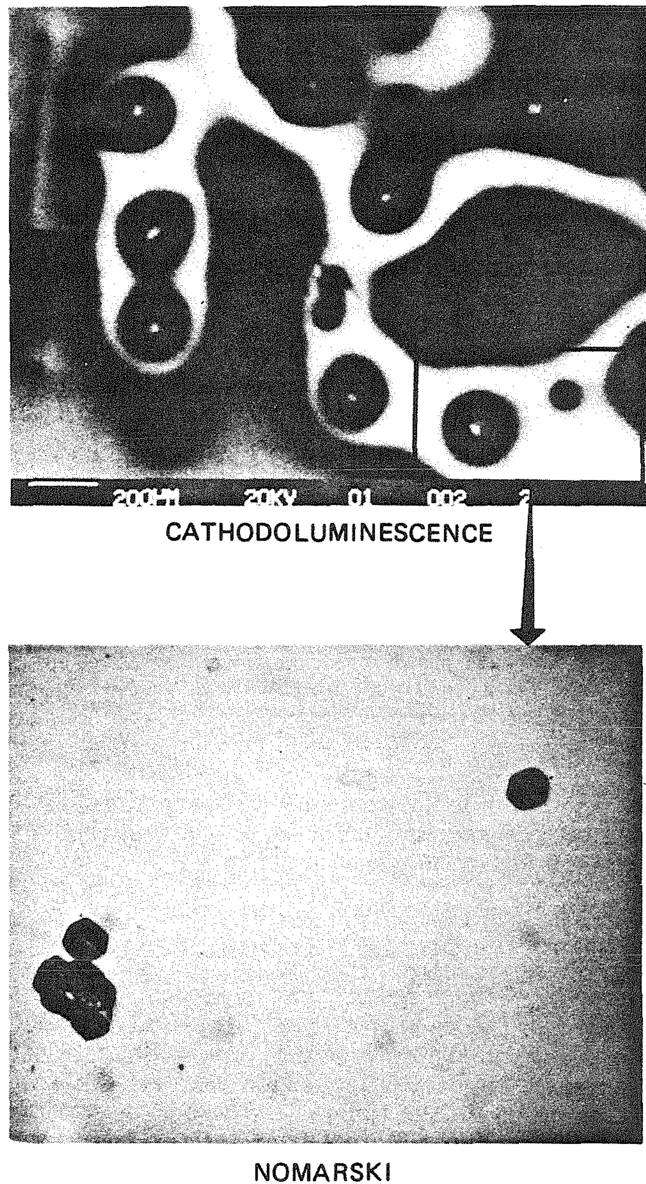

Figure 4.1: Cathodoluminescence image and microphotograph of In-alloyed GaAs substrate. On top is a cathodoluminescence image of a region near the center of a typical as-grown In-alloyed wafer. Below is a visible microphotograph, taken using Nomarski phase contrast, after KOH etching of the segment outlined in the box in top image. (From Ref. 6.)

The PL maps of both GaAs and In-alloyed GaAs substrates depend strongly on thermal history of the substrates.[8,12,13] After annealing in an arsenic rich atmosphere for 30 min. at about 800 °C, to prevent the loss of As from the substrate surface, the PL intensity contrast disappears and the PL becomes uniformly bright, suggesting that defects diffuse during the anneal and supports the view that diffusion of defects is responsible for the contrast.

In both of these substrates, surfaces are found to play an important role in PL measurements. Photoluminescence intensities are found to vary with surface processing and with the dose of the exciting laser.[8,14] Both of these effects are thought to be due to surface capture. The effect of surface processing is to change the surface recombination velocity. The variation with laser exposure time is thought to be due to the creation of surface defects by the laser beam itself.[14]

In this work, photoluminescence excitation correlation spectroscopy (PECS) is used to investigate the region around dislocations in In-alloyed GaAs. The PECS method is discussed and investigated in detail in Chapter 3, and is found to be well suited for these measurements. The effect of surface recombination is investigated to determine its importance in the PL intensity contrast observed. Time- and space-resolved PL measurements are made to see if the carrier lifetimes correlate with the PL intensity variations.

4.1.2 Results of Work

For In-alloyed GaAs, surface capture can affect the PL intensity and the carrier lifetime measured by PECS. Using a recently proposed passivating layer,[3] the effects of surface capture could be dramatically reduced. In this work, measurements for both passivated and unpassivated surfaces were made, so the importance of surface capture on the measurements could be directly deduced. When surface passivation affects the measurements, the results described are for the passivated

surface. Thus, surface capture is not involved in the effects described in this work.

Photoluminescence intensity maps of an as-grown In-alloyed GaAs wafer are made. Line scans of near band-to-band PL intensity are made across a bright annulus at 5, 77, and 300 K. Using PECS, lifetimes are measured at bright and dark positions at 5, 77, and 300 K. The lifetimes are found to vary as the PL intensity varies, with longer lifetime corresponding to larger PL intensity. For example, at 77 K, an intensity contrast ratio of 6.0 ± 0.5 is seen and the corresponding lifetime ratio is 3.6 ± 1.0, corresponding to lifetimes of 850 ± 20 ps in the bright region and 240 ± 10 ps in the dark region. Thus, the PL intensity is due to the difference in carrier lifetime. Further, the temperature dependence of the carrier lifetimes in the bright and dark regions is very different. So the dominating defects, which govern the lifetimes in the different regions, must be different. (They are not the same defects with different concentrations.) This result supports the model, that one type of defect is gettered by the dislocation, while at the same time another type of defect is generated by the dislocation. The defects in both regimes have an electronically deep level rather than a shallow one because the lifetime does not increase at 300 K as would be expected for a shallow level. Furthermore, neither type of defect is EL2, an important defect in these materials, because the lifetimes associated with EL2 at the concentrations in this sample are in the range of microseconds, not picoseconds.

4.1.3 Outline of Chapter

Section 4.2 contains: the details of the PECS experimental apparatus, details of the samples used and the surface passivation process, and the procedures used to make PL maps. Section 4.3 gives the results of PL maps, line scans, delay-time scans and spectra around a typical dislocation feature. Finally, Section 4.4 discusses these results, and Section 4.6 is a summary of this study.

4.2 Experimental

4.2.1 Apparatus

The PECS apparatus is discussed in detail in Section 3.3. The apparatus used in the work of this chapter is the same, but the sample can be scanned. This is achieved by using computer-controlled translation stages to move the cold-finger dewar holding the sample. This is a particularly simple approach since the optics remains stationary, and the sample is moved in the x-y directions of the plane of the sample (the y-direction is vertical). The resolution limit of scans is the 25 μm laser spot size. The laser pump power was typically 1 to 2 mW per unchopped beam at sample, or 8 to 16 pJ per pulse. The cold-finger dewar is run with liquid helium, liquid nitrogen and empty, to achieve temperatures estimated to be about 5, 77, and 300 K, respectively.

4.2.2 Samples and Processing

The samples are (100) In-alloyed GaAs with an InAs mole fraction of about 0.3%. Annealed material was used for the study of surface capture that is briefly discussed in this chapter. The mapping studies were done using as-grown material. For more details on the samples, see Section 3.3 or Ref. 6. As discussed in Chapter 2 the absorption depth is 0.25 μm, so that for the pump powers, used the excited carrier density is about 10^{17} cm^{-3}. A recently reported passivation scheme is used to reduce the effect of surface capture.[3] It consists of spinning on a 0.5 to 1.0 M aqueous solution of $Na_2S \cdot 9H_2O$, after a mild etch (1:8:500 $H_2SO_4 : H_2O_2 : H_2O$) is used to strip off any native oxide, resulting in a colorless crystalline film. The effect of this film is stable from hours to days. Because the film is water-soluble it can be easily stripped off, the sample re-etched, and a new passivation layer applied. In all the work done here, the passivation layer was less than a day old.

4.2.3 Procedure

The mapping experiments done in this work require the same part of the sample to be reanalyzed after the sample is taken out of the dewar and processed. Repositioning of the sample was achieved by scribing a mark on the sample and using it as the origin of the maps. The scribed mark could be aligned with an accuracy of about 50 μm. At 5 K the level of liquid He is found to change the vertical position of the sample slightly; this is accommodated by doing line scans in the vertical direction and aligning the feature of interest based on the last line scan made. The spectra and delay-time scans are all made the same way as in Chapter 3.

4.3 Results

The results of the experiments directly investigating the effect of surface capture are not shown in this chapter. Instead, see Appendix E for details. The important results are quoted in this chapter. The PL intensity and the carrier lifetime measured using PECS are affected by the surface preparation. Moreover, the PL intensity and the carrier lifetime measured using PECS are found to change irreversibly with laser exposure because of surface defects introduced by the laser. These variations are most prominent at 300 K. Both of these effects are due to the capture of carriers at surface defects. The effects of the surface defects are dramatically decreased by using the sodium sulfide etch described earlier. In this work, measurements for both passivated and unpassivated surfaces were made, so the importance of surface passivation on the measurements was directly investigated. Even so, much attention was paid to reducing the amount of time the laser was on the sample during a measurement.

Figure 4.2 shows a cathodoluminescence scan and a PL scan of the same region

near the center of the as-grown In-alloyed GaAs used in this work. For details of the cathodoluminescence scan, see Ref. 6. The PL map is a low-resolution map using 100 μm steps at 77 K while monitoring the near band-to-band PL at 8280Å. The sample was stationary for each pixel and the measurement for each pixel lasted about two seconds. The similarity between the two maps is evident. The images show the center of the wafer, around which a circular network of dislocations is seen. These give rise to the large circular irregular bright pattern, very similar to the pattern seen in Fig. 4.1.

Figure 4.3 shows the same low-resolution PL map shown in Fig. 4.2 along with a high-resolution map of the region outlined in the low resolution map. The high-resolution map uses a 25 μm step, and again about 2 s per pixel. The three white lines marked on the high-resolution map and labeled A, B, and C, show the lines used to make line scans at 5, 77, and 300 K, respectively. Three different adjacent lines were used to reduce any possible laser dose effects. From the map at 77 K, the peaks and minima along these three adjacent lines are within 10% of one another so that features in the different line scans can be directly compared. The features shown in the high-resolution plot are very similar to those seen in Fig. 4.1. There are dark circular regions with and without a bright spot inside, corresponding to dislocation clusters and single dislocations, respectively. Surrounding these dark regions are bright annuli which have joined together as in Fig. 4.1.

Figure 4.4 shows the line scans made at temperatures of 5, 77, and 300 K along the lines A, B, and C for the passivated and unpassivated surfaces. Comparing the passivated to unpassivated line scans at the three temperatures, at 5 K, very little difference is observed; the contrast ratio is about 20:1. At 77 K, again, very little difference is observed; the contrast ratio is about 8:1. However, at 300 K a noticeable difference is observed; in the passivated case the contrast ratio is 4:1, while in unpassivated case the contrast ratio is 2:1. On the y-position axes of

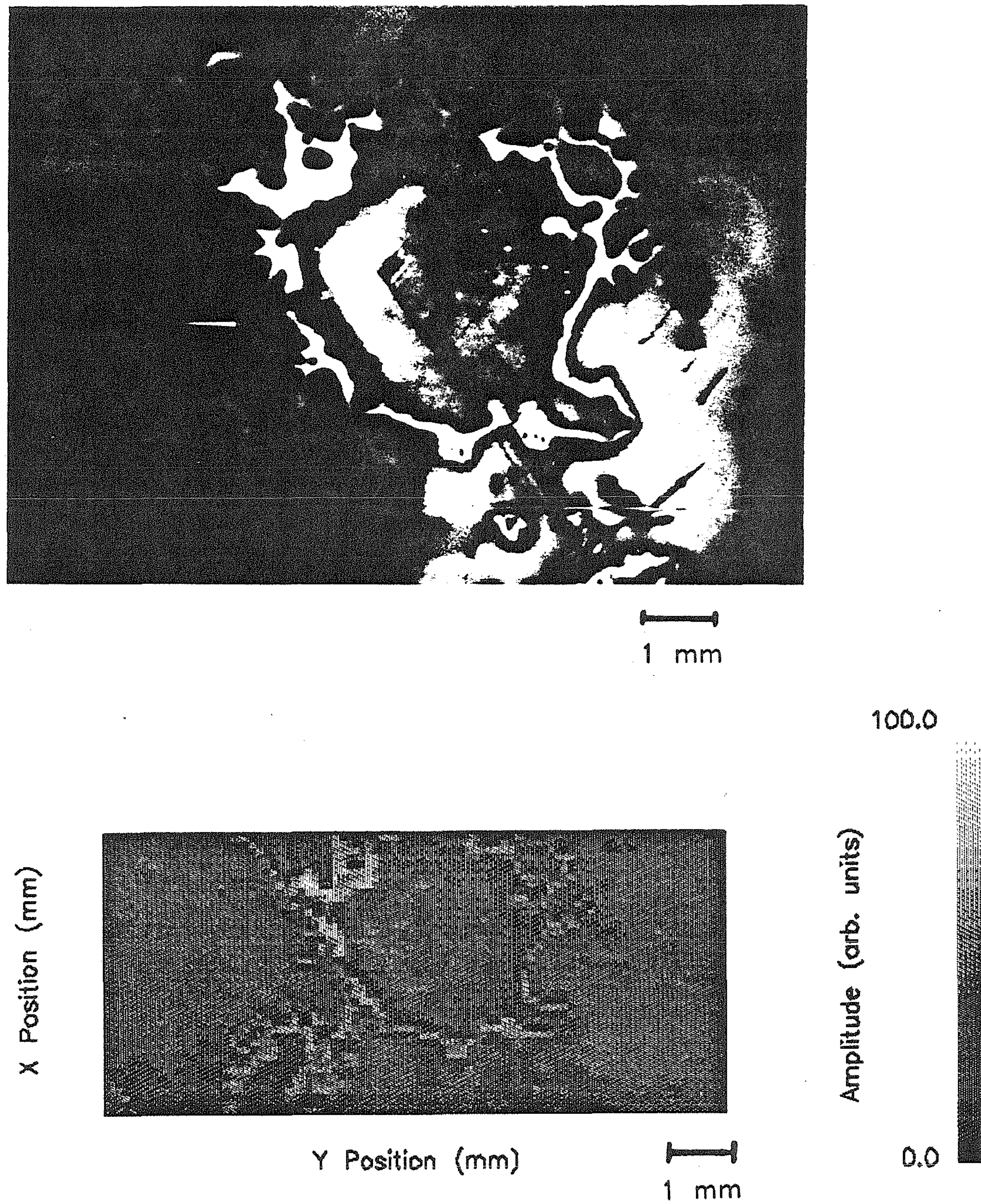

Figure 4.2: Cathodoluminescence and photoluminescence maps of In-alloyed GaAs substrate at 77 K. Top map is a cathodoluminescence image of the center region of the wafer analyzed in this work. Bottom map is a photoluminescence map of the same center region. Note the two images show the same circular bright pattern.

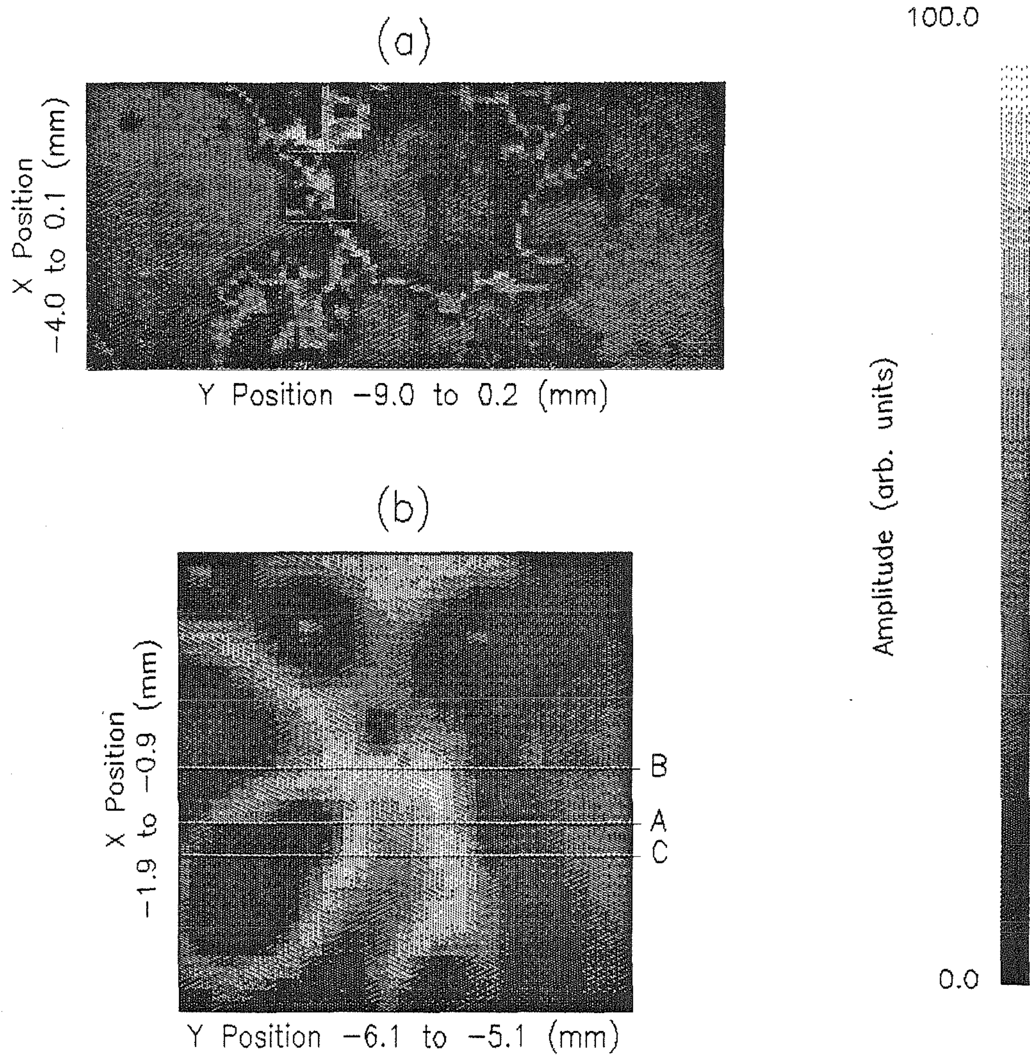

Figure 4.3: Photoluminescence intensity maps of the sample at 77 K. The top map is a low resolution (0.1 mm step size) map of a large region, while the bottom map is a high resolution (0.025 mm) map of the region outlined in the box in the upper map. PL intensity was monitored at 8280Å. Lines A, B, and C on the bottom map show the positions of line scans at sample temperatures of 5, 77, and 300 K.

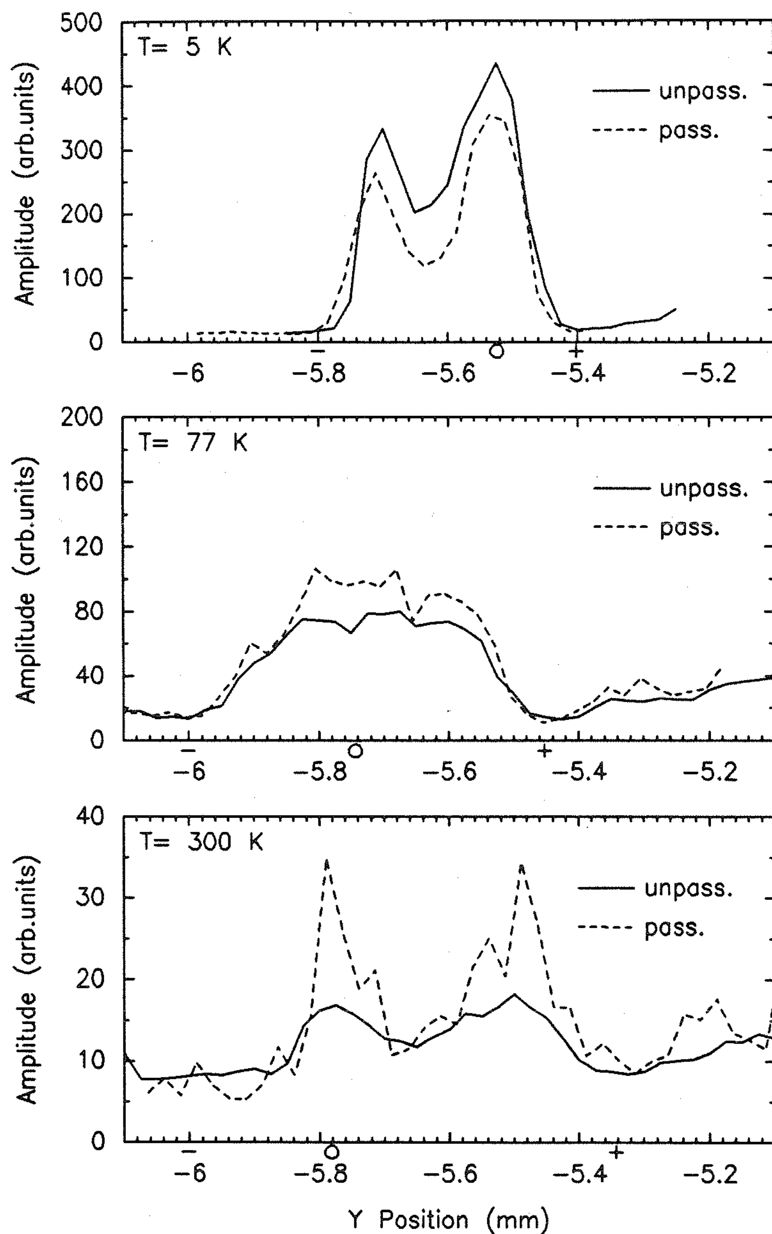

Figure 4.4: Photoluminescence line scans on sample. Line scans of photoluminescence intensity are plotted for the lines shown in Fig. 4.3. The graphs are for temperatures of 5, 77, and 300 K as marked. Solid curves are for unpassivated surfaces. Dotted curves are for passivated surfaces. The symbols $-$, o, and $+$ mark the positions of the left-hand dark, bright, and right-hand dark regions, respectively.

Fig. 4.4, the bright region, and left- and right-hand dark regions are marked with o, +, and − respectively. These mark the regions used to make spectra- and delay-time scans considered typical of these areas. From Fig. 4.3, it appears that the left and right regions in all scans correspond to a dark area that is in proximity to a dislocation rather than outside the effect of a dislocation.

Figure 4.5 shows the spectra made at the fundamental frequency of the bright and dark positions at 5, 77, and 300 K. The spectra at 300 and 77 K are for a passivated surface, and the spectra at 5 K are for an unpassivated surface. The spectra at 77 and 300 K show the near band-to-band peak. The shapes of the respective bright and dark spectra are the same, only the sizes are different. The spectra at 5 K show the near band-to-band peak and the acceptor related peak which are described more fully in Chapter 3. The near band-to-band peak does not change appreciably in shape, except that the size is different. However, there is a large difference in the size of the acceptor-related peak relative to the near band-to-band peak in the two positions. In the bright region, the acceptor-related peak is about 20% the size of the near band-to-band peak, while in both dark regions the ratio is less than 5%.

Figure 4.6 shows semilogarithmic plots of the delay-time scans made at the difference frequency at the bright and dark positions at 5, 77, and 300 K. These are for the passivated surface. Similar delay-time scans were seen for the unpassivated surface at 5 and 77 K. However, the delay-time scans of the unpassivated surface at 300 K were not symmetrical about zero delay time, indicating that laser dose effects, in this case degradation, were taking place. For this reason, only the delay-time scans from the passivated surface were used to determine carrier lifetimes. The scans at 77 and 300 K show the coherence peak at $\gamma = 0$ and the symmetric exponential decay on either side (linear on a semilogarithmic plot). The scans at 5 K show peaks at $\gamma = 0$ much wider than the coherence peak, with a FWHM of

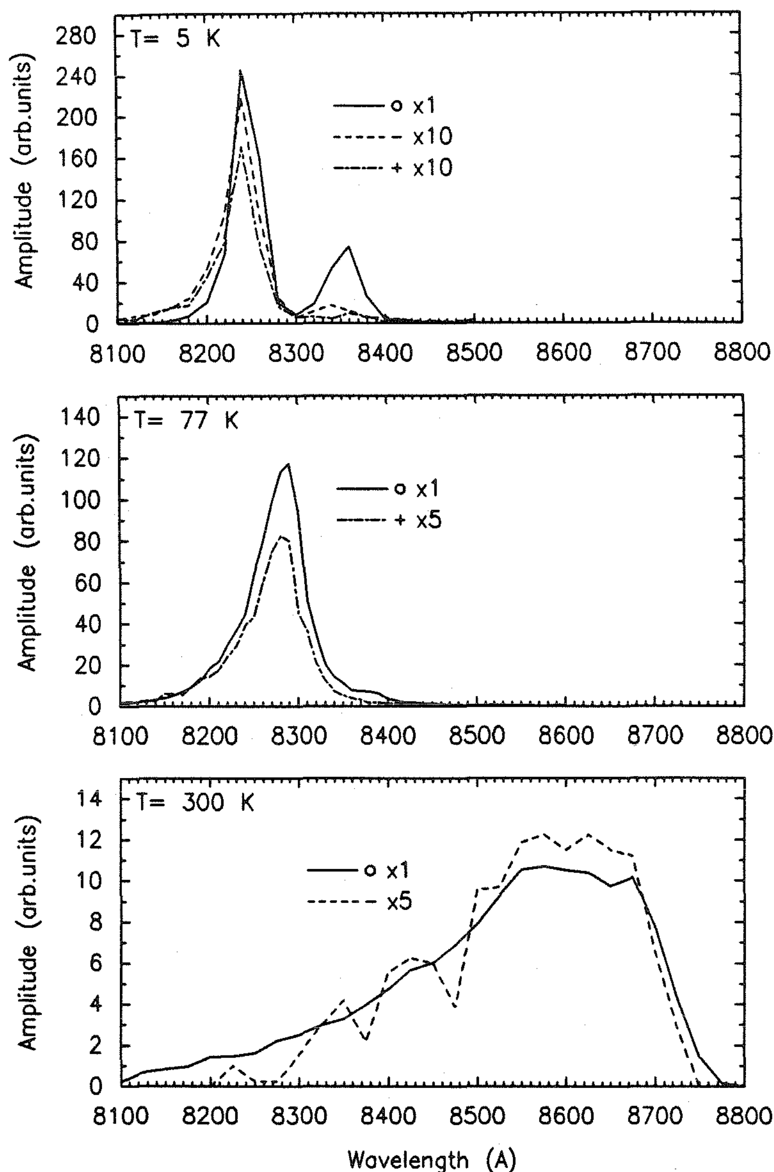

Figure 4.5: Photoluminescence spectra of bright and dark areas. Spectra are at the fundamental frequency, at 5, 77, and 300 K. Solid curves are for the bright region, dashed curves are for the left-hand dark region, and dashed-dotted curves are for the right-hand dark region, corresponding to the positions marked o, –, and +, respectively, on Fig. 4.4. The spectra from the dark regions were scaled as shown. The spectra at 5 K were for an unpassivated surface, while the 77 K and 300 K spectra were for passivated surfaces.

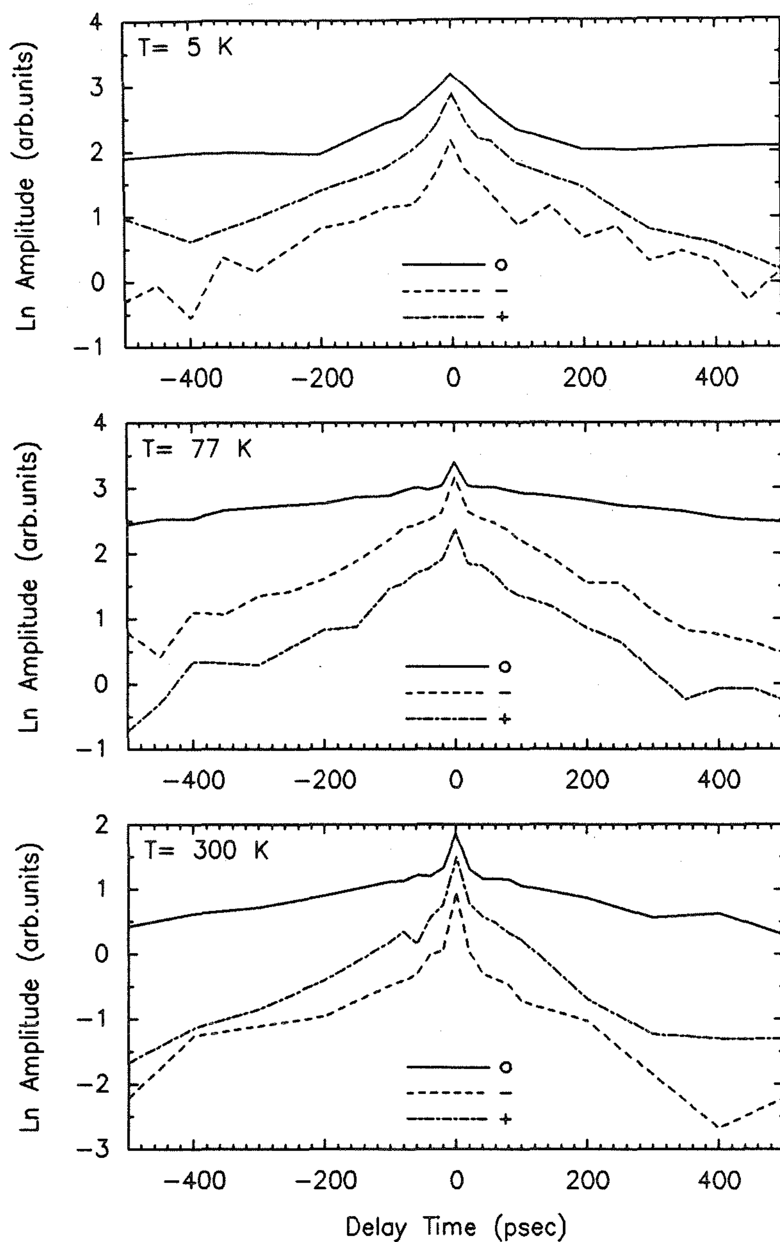

Figure 4.6: Delay-time scans of bright and dark areas. Scans are at the difference frequency, at 5, 77, and 300 K. Solid curves are for the bright region, dashed curves are for the left-hand dark region, and dashed-dotted curves are for the right-hand dark region, corresponding to the positions marked o, –, and +, respectively, on Fig. 4.4. The scans are scaled for convenient display. All scans are for passivated surfaces.

Table 4.1: Carrier Lifetimes of Bright and Dark of Regions.

Sample Temperature (K)	Lifetime (ps) Bright region (○)	Left-hand dark region (−)	Right-hand dark region (+)
5	2100^{+2000}_{-700}	340 ± 60	260 ± 20
77	850 ± 30	230 ± 15	230 ± 20
300	580 ± 30	220 ± 60	220 ± 20

about 100 ps. In Chapter 3, this was shown to be due to capture of carriers by the acceptors, and is not of interest in this work. The carrier decay associated with the bulk traps is the decay after the fast decay. The carrier lifetimes are determined by fitting the two sides of the semilogarithmic plot, excluding the coherence peak or the acceptor capture peak at $\gamma = 0$, to a straight line. Table 4.1 summarizes the data from these passivated scans. The PL intensity for the different regions is determined from the same fits of the delay-time scans as for the lifetime fits. So this measure of the PL intensity does not include the effect of the coherence peak or the acceptor-related capture peak. The PL intensity for the bright and dark regions and the ratio of these, called the contrast ratio, along with the ratio of lifetimes between these two regions are shown in Table 4.2.

4.4 Discussion

The effect of carrier diffusion on PL measurements was discussed in detail in Chapter 3. In the work of this chapter, the typical carrier lifetime is in the range

Table 4.2: Photoluminescence Intensity Contrast Ratio. The dark region with the best data was used. Values are from delay-time scans (difference) and from line scans (fundamental), along with the corresponding lifetime ratio. Results are for the passivated surface.

Sample Temperature (K)	Intensity Contrast Ratio		Lifetime Ratio
	Difference	Fundamental	
5	7.5 ± 2.0	17.5	$8.0^{+9.0}_{-3.0}$
77	6.0 ± 0.4	5.6	3.7 ± 0.5
300	4.3 ± 1.0	5.0	2.6 ± 0.3

of 500 ps, so that the associated diffusion length is in the range of 1 μm. Thus, the contrast seen does not involve the diffusion of carriers over distances larger than 1 μm. Comparing this to the 25 μm laser spot, it is clear that lateral diffusion is not important. Although this diffusion length is large enough to allow the carriers to reach the surface, the fact that the contrast is seen both with and without the surface passivation layer for all temperatures directly indicates that surface capture is not important in this work. Thus, the PL intensity contrast observed is due to the average bulk properties of the substrate, which vary over the features observed.

In earlier work, Hunter[11] observed a PL contrast ratio of 600:1 at 10 K. This contrast ratio is much larger than the 17.5:1 or 9:1 ratio shown in Table 4.2 for the contrast ratio observed at a comparable temperature in the fundamental or difference spectra, respectively. The discrepancy is probably due to the differences

in the two experiments. The earlier work used a 1 mW CW laser with energy just above the bandgap of the substrate, while in this work a 1 mW pulsed laser with energy 0.5 eV above the bandgap is used. The pulsed laser generates peak carrier concentrations much larger than the CW laser. Moreover, the pulsed laser generates a much higher-temperature electron-hole plasma than the CW laser. These differences are significant enough to account for the difference of a factor of 30 in the intensity contrast. The difference between the contrast ratio as determined by the fundamental and difference signals is observed at 5 K, but not at 77 or 300 K. From Eqn. 3.10 of Chapter 3, the difference and fundamental intensity ratio for zero delay time should be the same for capture-dominated PL. The discrepancy at 5 K probably occurs because in the bright region where the lifetime is larger than 1 ns, the electron-hole recombination is not completely capture-dominated. If this were the case, the difference ratio would be less than the fundamental ratio as is observed.

Figure 4.7 shows a plot of the lifetime ratio and difference-frequency intensity ratio of the bright to the right-hand dark region at 5, 77, and 300 K. From Eqn. 3.10, the difference signal is given by

$$I_{\mathrm{lock}}(\omega_2 - \omega_1) \propto \frac{g^2 \tau}{t_{\mathrm{rep}}} e^{-\frac{|\gamma|}{\tau}}, \tag{4.1}$$

where g is related to the pulse power, t_{rep} is the laser-pulse repetition rate, and γ is the delay time. So the difference signal is proportional to the lifetime for $\gamma = 0$. Figure 4.7 shows that this is indeed the case, although the agreement is not perfect. Thus, the intensity contrast is simply due to the lifetime contrast and is in agreement with earlier work for GaAs.[9]

At 5 K, the ratio of the carbon acceptor-related peak to the near band-to-band peak is found to vary strongly with the position in the neighborhood of the dislocation. In the dark area the ratio is less than 5%, while in the bright region the ratio is about 20%. This could be a consequence of the acceptor's

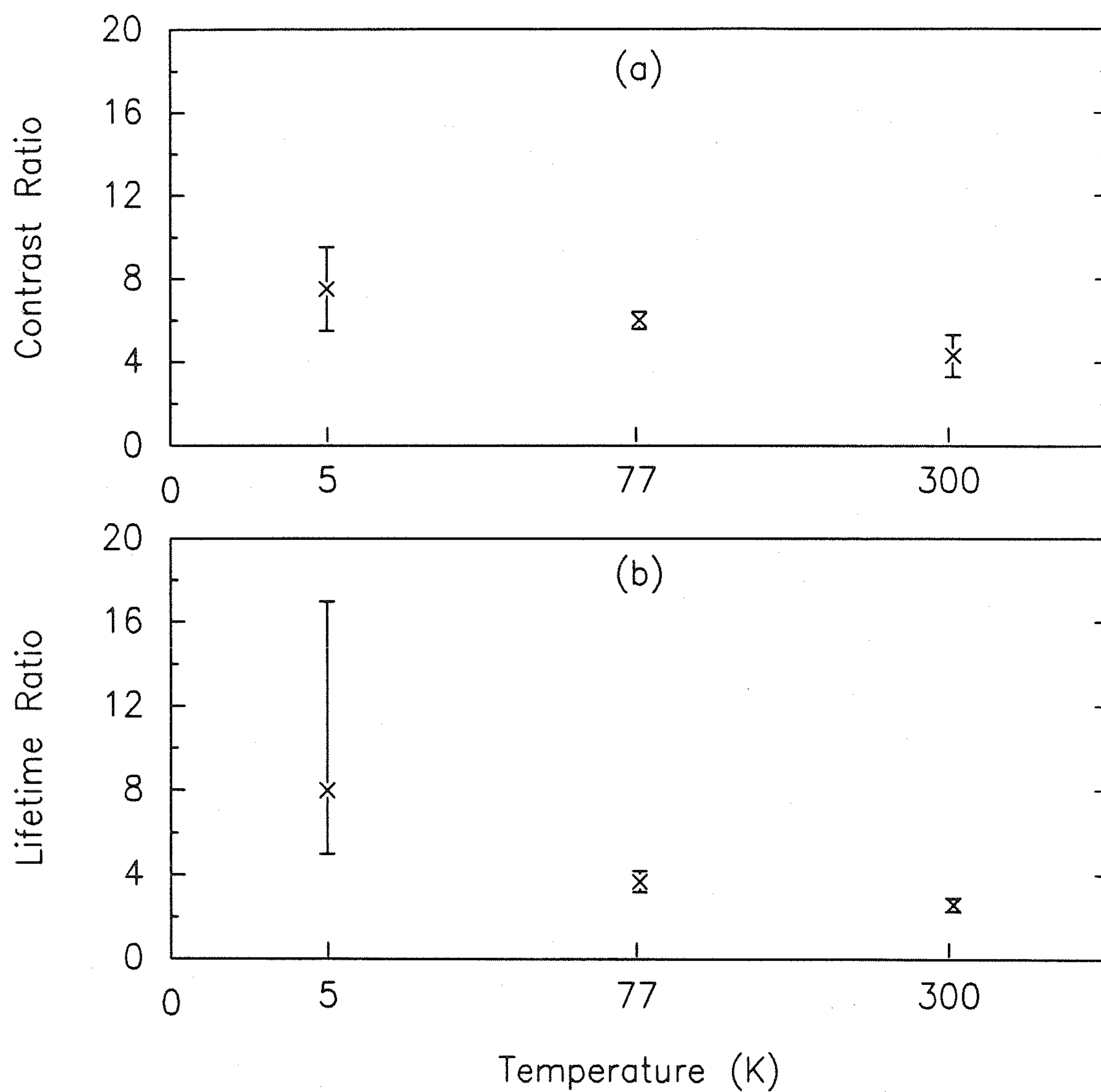

Figure 4.7: Intensity-contrast ratios and lifetime ratios versus temperature. Plot (a) shows intensity contrast ratios at 5, 77, and 300 K for the difference signal. Plot (b) shows lifetime ratios at 5, 77, and 300 K. The ratios are those tabulated in Table 4.2.

concentration changing near the dislocation; however, this is not likely since earlier CW PL measurements do not show this effect.[11] The difference is more likely a consequence of the large difference in lifetime in the bright and dark regions. This lifetime difference in combination with the carrier temperature effects discussed in Chapter 3 could give rise to such a difference in peak ratios. Thus, the variation in the carbon peak is probably a consequence of the large lifetime variation, not the other way around.

Figure 4.8 shows a plot of the lifetimes given in Table 4.1 with temperature. The temperature axis should be treated with caution because the actual temperature of the carriers producing the PL is substantially higher than the substrate temperature used in the plot, and varies in time, as discussed in Chapter 3. Thus, the temperatures plotted are only suggestive of the carrier temperatures involved. From Fig. 4.8 it is clear that both right-and left-hand dark areas have the same temperature dependence, and both of these are very different from that of the bright region.

Much information can be inferred from the lifetime behavior with temperature. The lifetime of either carrier that is due to one type of bulk trap is given by

$$\tau = (v_{\text{th}} N_t^* \sigma_t)^{-1}, \tag{4.2}$$

where v_{th} is the thermal velocity, σ_t is the trapping cross section, and N_t^* is the density of the trap level in the state to capture the carrier being considered. The thermal velocity is proportional to $\sqrt{kT}$, where T is the temperature of the carriers. As discussed in Chapter 3, the capture rate of the electron and holes must be equal during the decay of carriers so that $N_t^* \propto N_t$, where N_t is the total density of the trap. The trapping cross section and its variation with temperature, $\sigma_t(T)$, is a characteristic of the trap. Thus,

$$\tau \propto (\sqrt{T} N_t \sigma_t(T))^{-1}.$$

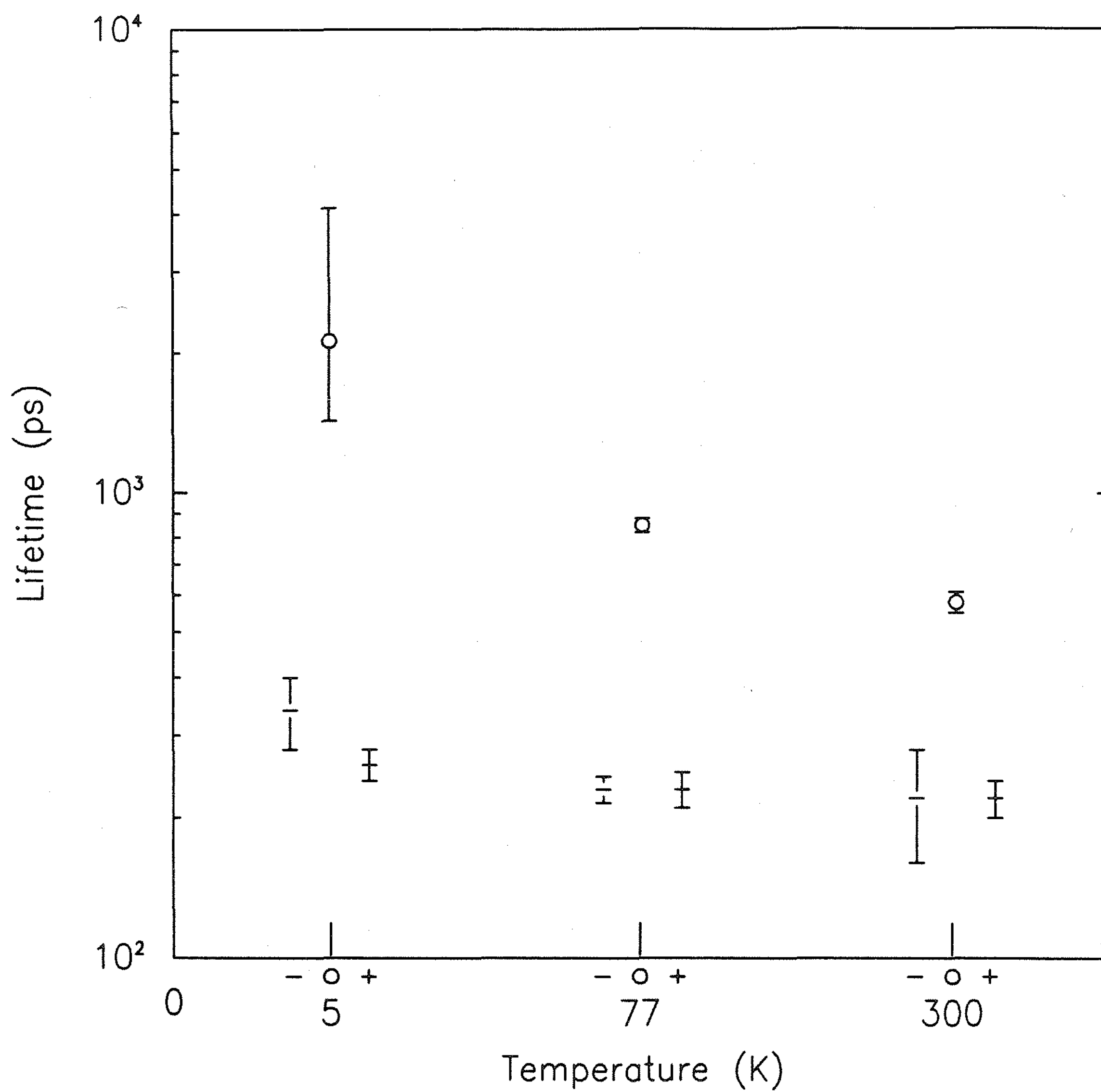

Figure 4.8: Carrier lifetimes from bright and dark areas versus temperature. Carrier lifetimes from bright areas, left and right dark areas are marked o, −, and +, respectively. The temperature axes serves only to display the points for sample temperatures of 5, 77, and 300 K.

The change in τ with position is due to the variation in N_t for the dominant trap with position. However, in the case of the bright and dark regions, the different temperature behavior cannot be explained simply by a variation in N_t. Instead, there must be different traps dominant in the bright and dark regions. Thus, the same type of defect is dominant in the two dark areas, while a different type of defect is dominant in the bright area. For both dark areas to be similar indicates that both the dark areas are due to the proximity of dislocations, as the high-resolution map in Fig. 4.3 suggests. The fact that the dark and bright areas are due to different defects supports the model proposed by Hunter,[10] that the lifetime killer responsible for the dark areas away from the dislocation is gettered in the neighborhood of the dislocation, while another type of defect is generated by the dislocation. This model gives rise to a bright region because of the reduction of the population of one type of defect and to the central dark region because of the increased population of the generated defects.

It is a difficult problem to determine the identity of the defects involved; however, they can be characterized to some extent. Firstly, neither defect is shallow. If either defect were shallow, then higher temperatures would ionize the defect and reduce its effectiveness as a trap, causing an increase in the carrier lifetime. However, this effect is not observed. Secondly, neither defect is EL2, the defect responsible for the pinning of the fermi level near midgap in this material. This is because the electron and hole lifetimes at 77 K for the known concentrations of EL2 in this material, using the accepted values for the cross sections, are 10 and 7 ps, respectively.[10] These lifetimes are four orders of magnitude larger than the measured lifetimes. Finally, from Eqn. 4.2 a measurement of lifetime of about 500 ps, and a thermal velocity of 10^7 cm/s (typical for 300 K), give a value of $N_t\sigma_t$ of about 200 cm^{-1}. If either of the dominant defects is electrically active, then N_t must be in the range of 10^{15} cm^{-3}; otherwise, they would dominate the electrical

properties, which is not observed to be the case.[10] This condition on the density of defects requires the defects to have a cross section greater than 2×10^{-13} cm^2, which is quite large. If the defect is not electrically active, then the trap density could be larger so that the cross section need not be as high. From these measurements, it is not possible to tell whether or not the defect is electronically active.

The practical interest of the work is the effect these defects have on devices. Clearly, the nonuniform nature of the PL intensity indicates that the as-grown material is not at equilibrium. This lack of equilibrium is confirmed by the result, that annealing the material causes the PL intensity to become more uniformly bright. Thus, it is not surprising that the effect of the dislocations on the final devices is very much dependent on the processing used.

4.5 Summary of Results

In this chapter the first space- and time-resolved PL measurements of the region associated with a single dislocation in a SI LEC In-alloyed GaAs substrate are described and discussed. The advantage of In-alloyed GaAs over GaAs substrates for such measurements is that the much larger dislocation separation in the alloyed material reduces the overlap of the effects of dislocations. In the alloyed material the effects seen can be associated with the effects of a single dislocation. The time resolution is obtained using PECS and allows the measurement of the carrier lifetimes. The PL maps show the PL intensity variation in the neighborhood of dislocations. These maps show the same bright annular feature surrounding a dark central region at the dislocation, seen elsewhere.[6,12] Measurements of the PL intensity over a line scan for different temperatures with and without a surface passivation layer show that the intensity contrast is not due to surface capture. Lifetime measurements at various positions along these line scans show that the

intensity variations are caused by carrier lifetime variations. Carrier lifetimes in the dark regions were in the range of 200 to 300 ps, while in the bright region, 500 to 3,000 ps. The temperature behavior of these measurements indicates that these variations in lifetime are due not simply, to the variations in the defect density of a single dominant trap. Instead, they are due to two different dominating traps, one in the bright annular region, and another in the dark regions near the dislocation, supporting the model proposed by Hunter, [10] that one type of defect is gettered by the dislocation while another type of defect is generated by the dislocation. From the lifetimes and their temperature behavior, neither type of defect is shallow, nor are they directly due to capture onto EL2. The effect that these defects have on FET devices was not investigated.

References

1. S. Miyazawa, Y. Ishii, S. Ishida, Y. Nanishi, Appl. Phys. Lett. **43**, 853 (1983).

2. H.V. Winston, A.T. Hunter, H.M. Olsen, R.P. Bryan, and R.E. Lee , Appl. Phys. Lett. **45**, 447 (1984).

3. F. Hyuga, K. Watanabe, J. Osaka, K. Hoshikawa, Appl. Phys. Lett. **48**, 1742 (1986).

4. T. Egawa, Y. Sano, H. Nakamura, and K. Kaminishi , Jpn. J. Appl. Phys. **25**, L973 (1986).

5. M. van Hove, W. de Raedt, M. de Potter, M. van Rossum, and J.L. Weyher in *Mat. Res. Soc. Symp. Proc.*, Vol. 104 (Materials Research Society, 1988).

6. A.T. Hunter, H. Kimura, H.M. Olsen, and H.V. Winston , J. Electron. Mat. **15**, 215 (1986).

7. D. Guidotti, H.J. Hovel, M. Albert, and J. Becker, in *Review of Progress in Quantitative Nondestructive Evaluation*, Vol. 6B, edited by D.O. Thompson, and D.E. Chimenti (Plenum Publishing Corp., 1987), p. 1369.

8. H.J. Hovel, D. Guidotti, IEEE Trans. Electron Devices **ED-32**, 2331 (1985).

9. K. Leo, W.W. Rühle, and N.M. Haegel, J. Appl. Phys. **62**, 3055 (1987).

10. A.T. Hunter, Defect and Diffusion Data **48**, 1 (1986).

11. A.T. Hunter, Appl. Phys. Lett. **47**, 715, (1985).

12. H.J. Hovel, M. Albert, E. Farrell, D. Guidotti, and J. Becker, in *Semi-Insulating III-V Materials* (Ohmsha, Ltd., 1986), p. 97.

13. N.M. Haegel, A. Winnaker, K. Leo, W.W. Rühle, and S. Gisdakis, J. Appl. Phys. **62**, 2946 (1987).

14. D. Guidotti, E. Hasan, H.J. Hovel, M. Albert, Appl. Phys. Lett. **50**, 912 (1987)

15. C.J. Sandroff, R.N. Nottenburg, J.-C. Bischoff, and R. Bhat, Appl. Phys. Lett. **51**, 33 (1987).

Chapter 5

Carrier Lifetimes in Ion-Damaged GaAs

5.1 Introduction

5.1.1 Background

There is much interest in the generation of ultrashort electrical pulses. As discussed in the introduction, these ultrashort electrical pulses are generated on high-frequency waveguide structures using photo-switches called photoconductive circuit elements (PCEs). The PCEs are also used to sample these ultrashort electrical pulses. Such pulses can be used to measure ultrafast electrical transients of high-speed devices or ultrafast electrical properties of materials.

As discussed in Chapter 1, a typical PCE consists of a gap between two metal conducting electrodes connected by a photo-sensitive insulating semiconductor substrate. The PCE is turned on when a laser pulse is incident on the semiconductor in the gap, which generates electrical carriers, causing the gap to conduct or turn on. The PCE turns off after the carriers recombine and the gap returns to the insulating state. The speed of a PCE is governed by the lifetime of the carriers

in the gap and the geometry of the PCE.[1] Short carrier lifetime material is produced by damaging a good crystalline semiconductor using ion implantation, or by growing intentionally poor electrical quality material. In the work reported in this chapter, we are interested in materials damaged using ion implantation. There are various procedures used to damage semiconductors to make PCEs. For GaAs substrates, ion implantation with 2 MeV H^+ or 200 to 300 keV H^+ has been successfully used.[2,3,4] For silicon-on-sapphire substrates, a particularly successful procedure uses implantation of O^+ at 200 keV and 100 keV.[5]

Measurements of the response speeds of PCEs are carried out by making a cross correlation measurement. This measurement uses two PCEs, each of which is separately activated by a subpicosecond optical pulse. One of the PCEs has a dc bias applied to it, while the other PCE is biased by the output from the first. In other words, this is a correlation measurement with the first PCE acting as a pulser and the second PCE acting as a sampler. For identical PCEs adjacent to one another, the measured charge $Q(\gamma)$ is proportional to the autocorrelation function $Q(\gamma) \propto \int_{-\infty}^{\infty} v(t)v(t+\gamma)dt$, where $v(t)$ is the response of a single biased PCE and γ is the delay time between the optical pulses.[6] In the work of this chapter, a cross correlation is measured because the pulser and sampler are separated by a small distance.

It is interesting to compare the response speed of a PCE to the carrier lifetime of the substrate in the gap. This has been done for PCEs on silicon-on-sapphire implanted with 200 and 100 keV O^+ ions.[7,8] The response speeds of the PCE are measured using an autocorrelation type measurement[5] and the carrier lifetime is measured using time-resolved reflectivity to measure the decay of the charge in the Si layer.[7] In that work the carrier lifetime decreases inversely with the implant dose up to a critical ion dose of 10^{14} cm^{-2}. Above this dose the lifetime reaches a lower limit of 600 fs. This limit is thought to be due to amorphization or a saturation of

the effective trap density in crystalline Si[7] and above this critical dose no further decrease in carrier lifetime is observed. This lifetime limit corresponds to the 0.6 ps electrical pulses produced by Ketchen *et al.*,[5] which suggests that it is the carrier lifetime that limits the PCEs speed and therefore, the 0.6 ps-wide electrical pulse is the shortest pulse that can be produced using PCEs on implanted silicon-on-sapphire.[7]

In the work reported here, PCEs on ion-implanted GaAs are investigated. The PCE is on a 300 GHz coplanar waveguide structure. The response of the PCE is measured using an autocorrelation measurement, and the lifetime of the ion-damaged material is measured using photoluminescence excitation correlation spectroscopy (PECS)[9] looking at the PL from near band-to-band recombination.

5.1.2 Results of Work

We have looked at samples of GaAs that are undamaged, and damaged with 200 keV H^+ ions at doses in the range of 1×10^{11} to 3×10^{14} cm^{-2}. The lifetimes measured using PECS at 77 and 300 K showed the same behavior with ion dose. For doses lower than about 6×10^{12} cm^{-2}, the lifetimes are relatively insensitive to dose because the capture associated with native defects dominates the defects introduced by the ion damage. For doses larger than about 6×10^{12} cm^{-2}, the lifetime versus ion dose has slope of -1 because the capture associated with ion-damage defects dominates the native defects. The lifetime of the undamaged material is in the range of 100 to 300 ps, and the smallest lifetime measured was 0.6 ± 0.2 ps corresponding to a dose of 1×10^{14} cm^{-2}. Experimentally, no lifetime saturation with ion dose is observed up to a dose of 1×10^{14} cm^{-2}, the maximum dose for which a lifetime measurement was made. The PCE autocorrelation measurements show a decrease in width of the autocorrelation peak with ion dose as expected. However, the width decays less quickly with ion dose than the carrier

lifetime does, suggesting that other effects in addition to the lifetime governs the PCE speed in this dose range. The autocorrelation measurements do not show a lower limit of this peak width; however, decreased sensitivity and increased background limit the fastest speed of a practical PCE. The optimum PCE uses an ion dose of 6×10^{13} cm^{-2}, which yields a pulse with a FWHM of 9 ps.

5.1.3 Outline of Chapter

Section 5.2 contains a description of the samples and sample processing including the PCE structure and its fabrications and the ion implantation; and a brief discussion of the experimental apparatus and procedures. Section 5.3 gives the results for both the PCE autocorrelation scans and the PECS measurements. Section 5.4 discusses the experimental results and compares them to calculations made using TRIM©, which models the implantion process, and compares them to the results seen by Doany *et al.* for silicon-on-sapphire.[7,8] Finally, Section 5.6 is a summary of this study.

5.2 Experimental

5.2.1 Samples and Processing

The samples used in the work reported here were fabricated on (100) semi-insulating (SI) liquid encapsulated Czochralski (LEC)-grown GaAs substrates. The PECS lifetime studies were made on the same samples that the PCEs were fabricated on in an adjacent area that was ion-implanted but not metalized.

The PCE structure is on a 300 GHz coplanar waveguide structure. Figure 5.1 shows this PCE and waveguide structure. The structure is defined using conventional lift-off photolithography. The metalization is 0.2 μm of Au:Ge:Ni in the ratio 88:12:10 by weight, which is annealed at 425 $^{\circ}$C for 3 minutes in H_2/He

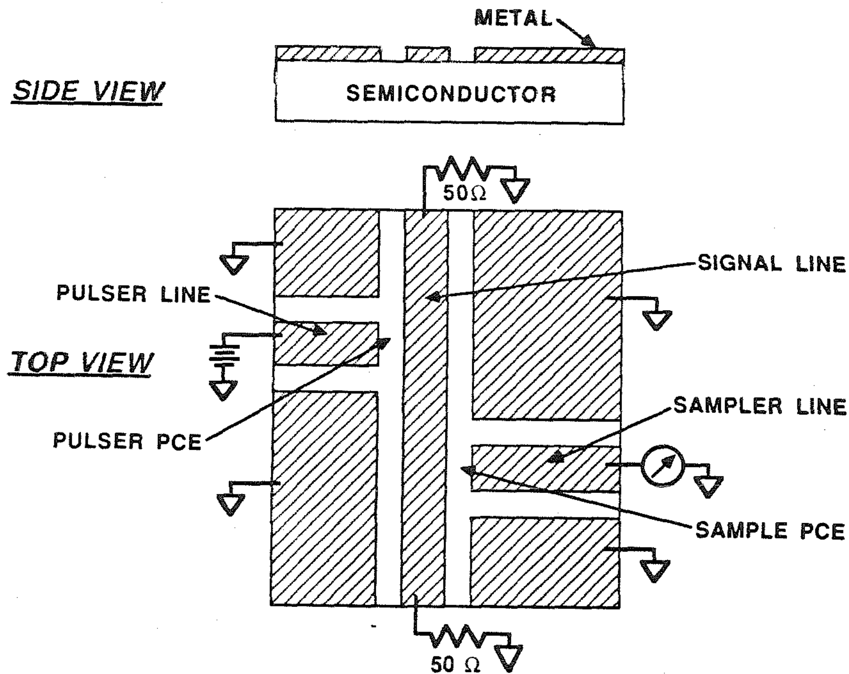

Figure 5.1: Schematic of PCE on a Co-planar waveguide. (From Ref. 4.)

forming gas to make an ohmic contact to the substrate. The center conductor is 60 μm wide, and the space between the center line and the ground plane on either side is 30 μm. The pulser and sampler strips are identical to the center strip. The gaps between the pulser and sampler are 10 μm, and the distance from the center of the pulser to the center of the sampler is 33 μm.

Following the anneal to form the ohmic contacts, the entire structure is ion damaged with 200 keV H^+ ions using a Varian ion implanter. Total doses in the range 1×10^{11} to 3×10^{14} cm^{-2} were implanted. Over small ranges of implantation dose, the implantation time was used to vary the dose; however, to implant over such a large dose, range the current density of the implantation was also changed. The maximum current density used was 3.7×10^{-8} A/cm^2 or 2.3×10^{11} ions/cm^2. During the implant the sample was cooled on a steel block to 8 $^{\circ}$C to reduce the

effects of heating caused by the ion beam.

Two sets of samples, labeled #1 and #2, were investigated in this work. Set #1 consisted of ion doses of 0 (undamaged): 1, 3, and 6×10^{11}; 1, 3, and 6×10^{12}; and 1, 3, and 6×10^{13}. Three different implantation current densities were used for this range of implants. Set #2 consisted of ion doses of 0 (undamaged): 1, 3, and 6×10^{12}; 1, 3, and 6×10^{13}; and 1 and 3×10^{14}. Two different implantation current densities were used for this range of implants. The current density was changed between the implant doses of 3×10^{12} and 6×10^{12} cm^{-2}.

5.2.2 Apparatus and Procedure

The apparatus and procedure used to make the PECS measurements are the same as that described in Chapters 3, so they are described only briefly here. A CPM laser is used to generate 200 fs-wide pulses at a wavelength of 6200 Å. The train of pulses from one beam incident on the sample has a typical energy of 17 pJ per pulse and a beam width ($1/e^2$) of about 25 μm. The absorption depth in GaAs is about 0.25 μm, so that each laser pulse excites a carrier density in the range of 10^{17} cm^{-3}. The PL spectra were taken at one of the chopping fundamental frequencies, and the delay-time scans were taken at the difference of the chopping frequencies.

The apparatus and procedures used to make the PCE autocorrelation measurements are described in detail in Ref. 4, so they are described only briefly here. The pulser is biased at 5, 10, or 20 V, and this was changed to increase the autocorrelation signal, as necessary. The center line is terminated to ground by 50 Ω at either end of the line to reduce unwanted reflections. The pulser beam is chopped at 808 Hz to allow lock-in detection techniques to be used; the sampler beam is not chopped. The sampler signal goes directly into a lock-in amplifier at an input impedance of about 8 Ω at 808 Hz.

5.3 Results

PECS lifetime and PCE autocorrelation measurements of both sets of samples were made. Sample uniformity was investigated for sample set #1 by looking for variations in PL intensity over the surface of the sample. Variations in the difference signal amplitude of about 30 to 40% were seen across a region of about 5 mm; these variations were not further investigated. The PL signal amplitude was not affected by the laser exposure dose, and therefore, the measurements of the PL spectra and carrier lifetime were made without importance placed on the position of the probing beam or on the amount of laser exposure. The PL spectra, delay-time scans, and PCE autocorrelation scans are described in the paragraphs below.

Figure 5.2 shows the PL spectra for ion-damaged GaAs at 5, 77, 300 K. At 5 K the dominant peak is that associated with the carbon acceptor. The peak shape does not change much with dose. At 77 and 300 K the dominant peak is the near band-to-band peak. These peaks shift to a slightly higher energy with increasing ion dose, while the width of the peaks does not change substantially with ion dose.

Delay-time scans of both sets of samples at 77 K and 300 K were made. These scans were made using the wavelength corresponding to the maximum of the near band-to-band PL peak. Delay-time scans at 5 K were not useful because the the acceptor-related peak dominates the recombination. Figure 5.3 shows delay-time scans at 77 K for various doses of selected samples from sample sets #1 and #2. The results for 300 K for both sample sets #1 and #2 are very similar. The scans in Fig. 5.3 show the coherence peak at zero delay and symmetric decay about this. Each scan shows linear decay over at least one decade. The tails for ion dose of 10^{11} cm^{-2} are in the background noise. On the semilogarithmic plot the decay is linear, so the decay is exponential in character, corresponding to a single carrier lifetime. The carrier lifetime is the reciprocal of the slope of

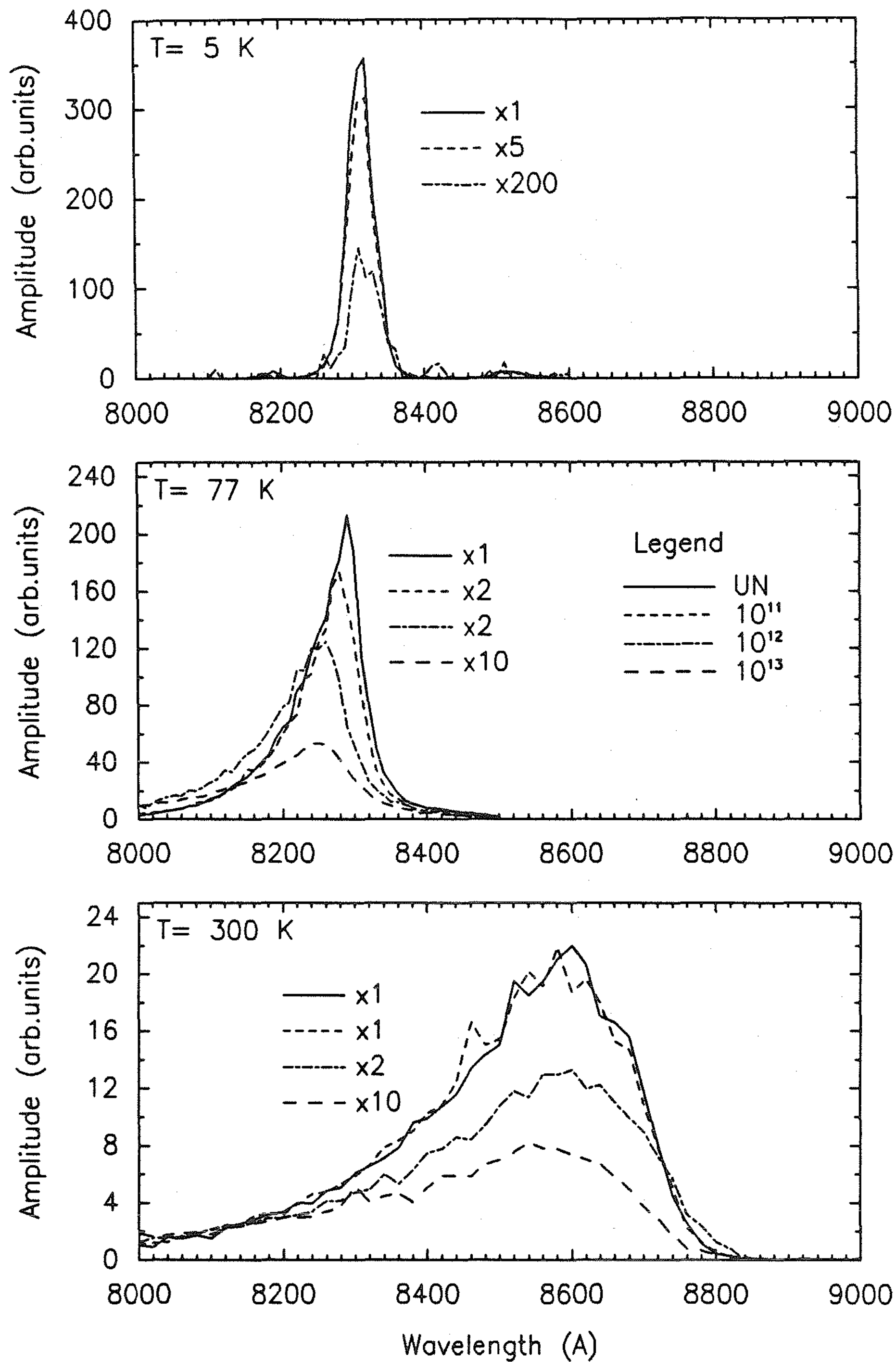

Figure 5.2: PL spectra for ion-damaged GaAs. The three plots show spectra taken at 5, 77, and 300 K, as labeled. The ion doses are 0 (undamaged), 10^{11}, 10^{12}, and 10^{13} cm^{-2}, as shown in the legend.

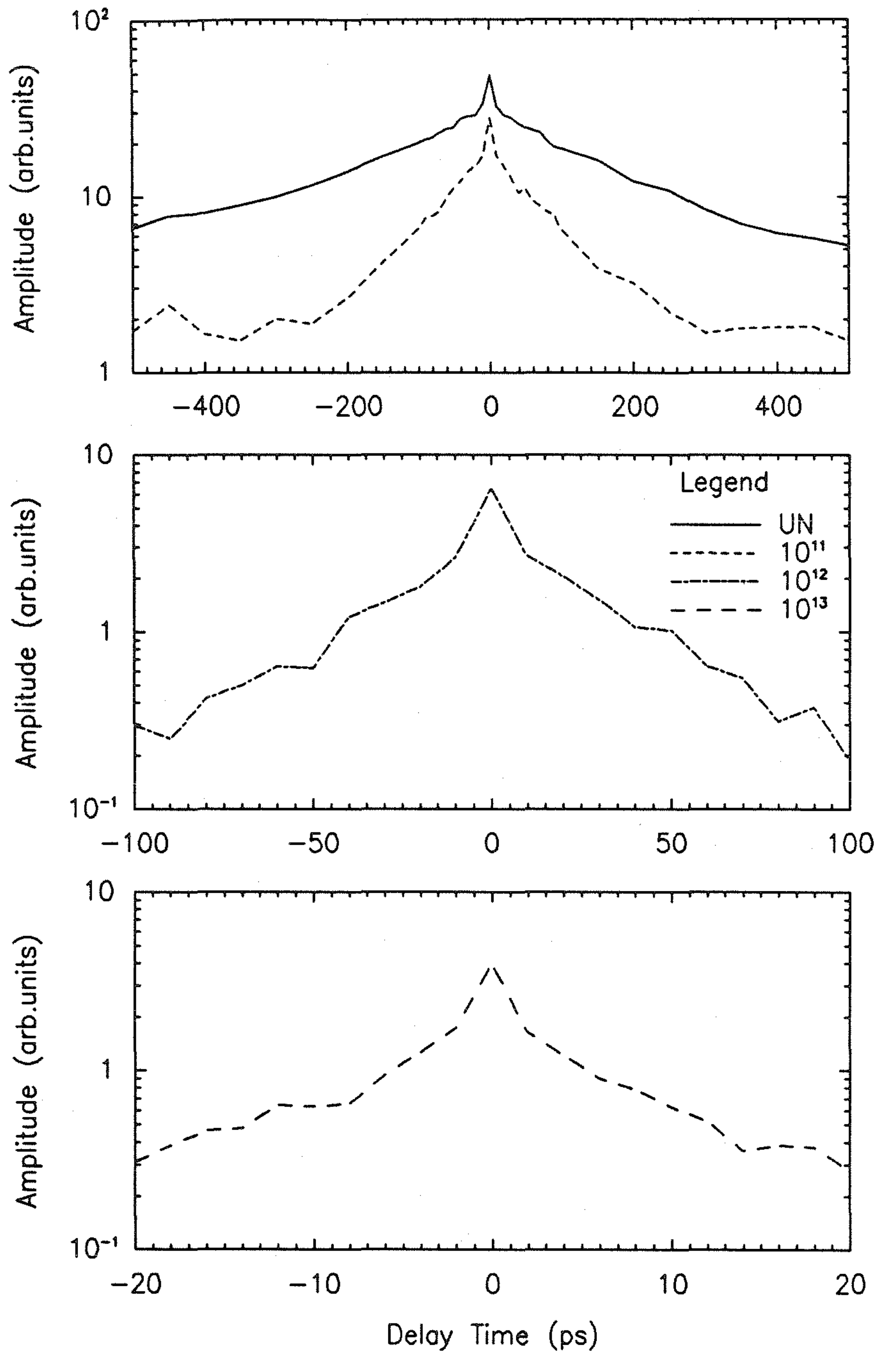

Figure 5.3: PECS delay-time scans for ion-damaged GaAs. Scans are for sample temperature of 77 K. The three different plots show scans for ion doses of 0 (undamaged), and 10^{11} cm^{-2}, from sample set #1; and 10^{12}, and 10^{13} cm^{-2}, from sample set #2, as shown in the legend.

this linear decay. For the delay-time scans shown in Fig. 5.3 the lifetimes are: 240 ± 80, 107 ± 10, 38 ± 2, 7 ± 2 ps for doses of 0, 10^{11}, 10^{12}, and 10^{13} cm^{-2}, respectively. These lifetimes are the average of several delay-time scans and their errors are the standard deviation of this average. The smallest lifetime measured was 0.6 ± 0.2 ps at a temperature of 77 K and dose 1×10^{14} cm^{-2}. For this dose the lifetime was measured only at 77 K because the PL signal at 77 K is stronger than that at 300 K, and there was not enough signal to make a measurement at 300 K. Lifetimes of more heavily ion-damaged samples could not be made because of too much noise in the delay-time data.

PCE autocorrelation scans for both sets of samples were made at 300 K. Figure 5.4 shows the PCE autocorrelation scans for samples from sample set #2 for ion doses of 10^{12}, 10^{13}, and 10^{14} cm^{-2}. The scans are plotted without showing the background; however, it is indicated by the offset of the y-axis. The zero of the x-axis does not represent coincidence of the optical pulses. Instead, the beams are coincident for a delay time of about 45 ps as indicated by the autocorrelation scan for dose 1×10^{14} cm^{-2}. The lower delay-time side of the autocorrelation peaks for all three scans are smooth and monotonic. However, on the high delay-time side of the peak there are small peaks that are due to pulse reflections. To compare the PCE responses for different doses the half-width at half-maximum (HWHM) is used because this value is not affected by these reflections. The HWHM of the autocorrelation peaks shown are 30, 13, and 4 ps for doses of 10^{12}, 10^{13}, and 10^{14} cm^{-2}; respectively.

5.4 Discussion

In this discussion, the experimental results described above are compared with the calculations of ion damage using TRIM© and contrasted with the results found

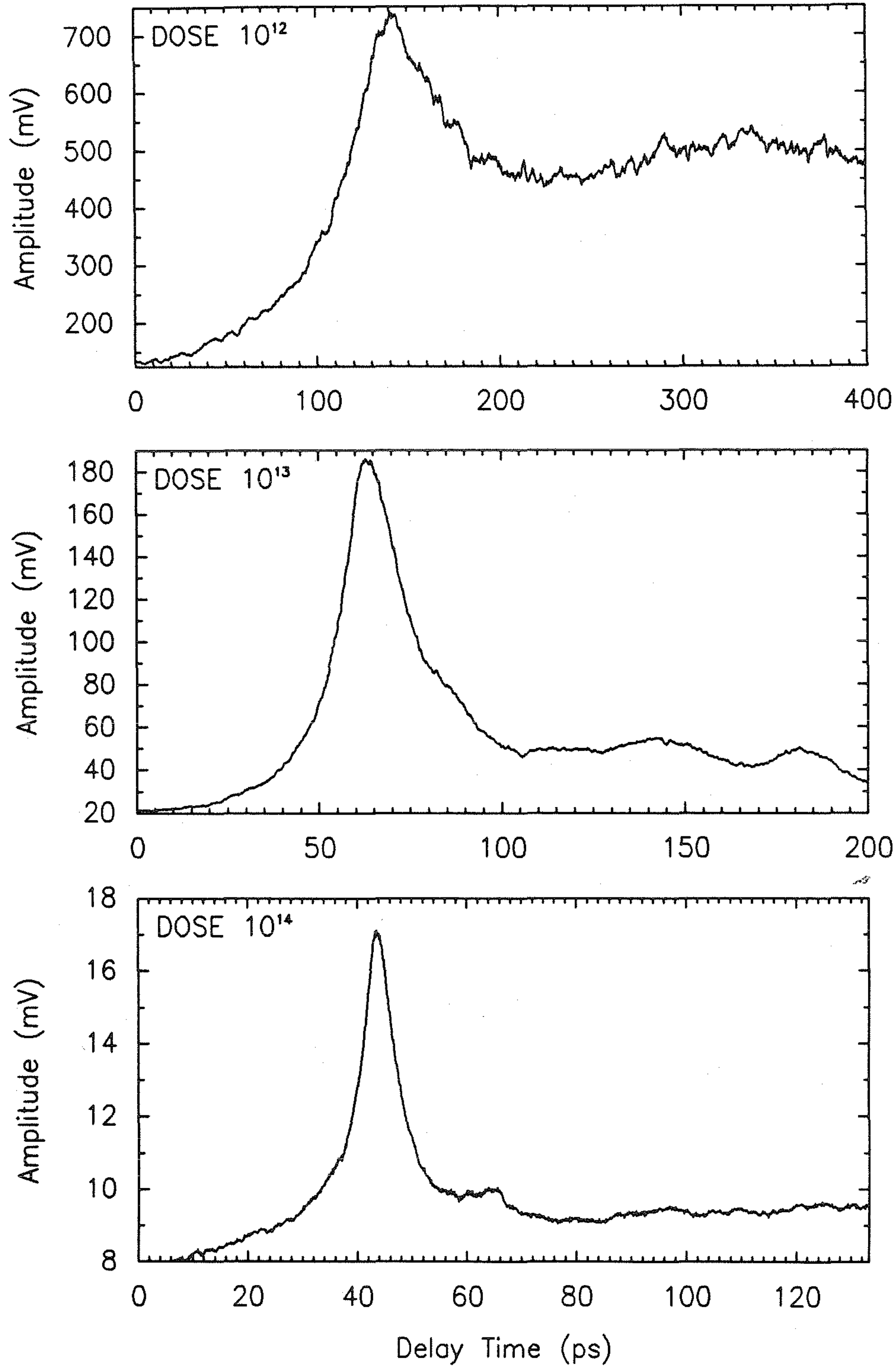

Figure 5.4: PCE autocorrelation scans for sample set #2. The three plots show scans for ion doses of 10^{12}, 10^{13}, and 10^{14} cm^{-2}, as labeled.

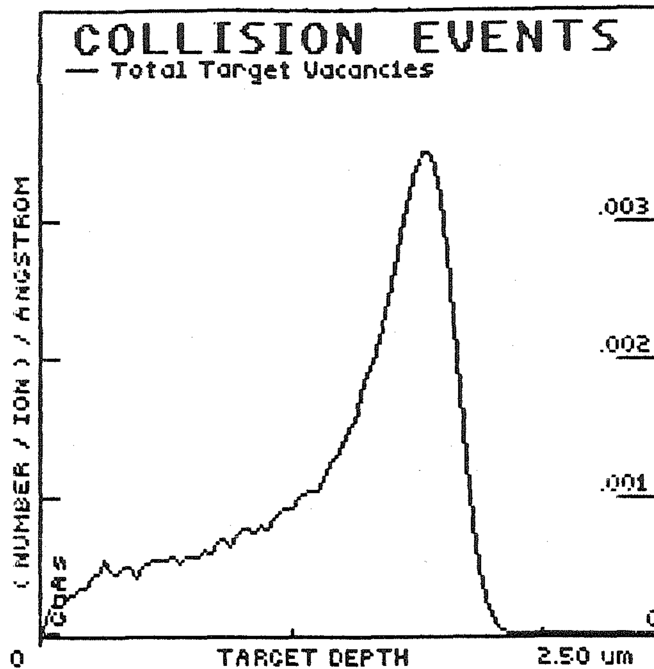

Figure 5.5: Simulation of ion damage in GaAs. Shows the vacancy distribution in GaAs that is due to ion implantation. Calculated using TRIM© with 200 keV H^+ ions implanted into GaAs.

for silicon-on-sapphire in Refs. 5 and 7.

The effect of ion bombardment of GaAs with 200 keV H^+ ions is modeled using TRIM©,[10] which is a Monte Carlo model that simulates the ions' collisions as they penetrate the surface of the substrate. The simulation keeps track of the number and position of the vacancies produced by the collisions in the cascade.[11] Figure 5.5 shows the calculated distribution of vacancies with depth. Along with these vacancies, the collision cascades will introduce other trapping defects into the crystal. It is reasonable that the distribution of trapping defects is similar to the vacancy distribution. The peak of the vacancy distribution is at 1.5 μm, which is much deeper than the 0.25 μm depth probed by the PL measurements.

In the top 0.25 μm, the vacancy distribution is nonuniform. For an ion dose of 1×10^{14}, cm^{-2} it goes from 0 to $5. \times 10^{18}$ cm^{-3} with an average of 2.5×10^{18} cm^{-3}. This vacancy density is an average density of 1 vacancy per ten thousand atomic sites, and is probably still below the damage threshold of GaAs. So for doses up to 1×10^{14} cm^{-2}, the average number of vacancies in the top 0.25 μm is proportional to the dose. Similarly, the average number of trapping defects is expected to be proportional to the dose in the range of implantation doses used. In the case of the implantation of 200 keV O^+ in silicon-on-sapphire used in Ref. 7, TRIM© indicates that there is a more average density of vacancies in the 0.5 μm Si layer. For a dose of 3×10^{14} cm^{-2}, the average vacancy density is 2.4×10^{21} cm^{-3} in the Si layer. This is a density of 1 vacancy in 10 atomic sites, so it is not surprising that this dose is found to be the threshold of amorphization or saturation of the effective trap density in crystalline silicon.[7] Summarizing, TRIM© indicates that the implantation of 200 keV H^+ into GaAs for the range of doses used in this experiment is below the amorphization limit of the top 1 μm, while the implantation of 200 keV O^+ into silicon-on-sapphire is near the amorphization limit of the top Si layer.

The TRIM© simulation shows that the vacancy distribution is nonuniform in the ion-damaged GaAs, so it is reasonable to expect the trap distribution to be similarly nonuniform. The effect of such a nonuniform distribution would be for the carriers not to decay with a single lifetime. This would be especially evident for samples with faster lifetimes, because for them carrier diffusion would not be fast enough to allow carriers to diffuse from regions of low-trap to regions of high-trap density. However, even for the fast lifetime material the carriers are found experimentally to decay with a single lifetime. Thus, the final distribution of defect traps in the top 0.25 μm is more uniform than the vacancy distribution calculated by TRIM©.

Figure 5.6 shows the lifetime versus ion dose for sample sets #1 and #2 at

77 and 300 K. Both sample sets show the same sort of carrier lifetime behavior with ion dose, and also, the lifetimes at 77 and 300 K for a given dose are the same to within experimental error. The lifetime of the undamaged material is in the range of 100 to 300 ps. For doses less than 10^{12} cm^{-2}, the lifetime is insensitive to the ion dose and for doses greater than 10^{12} cm^{-2} the lifetime is inversely proportional to the dose, as shown by the slope of -1 on Fig. 5.6. This is the expected behavior. At the lower ion doses, the carrier capture rate of the ion-damage defects is dominated by the capture rate of the native defects. So the lifetime is governed by the native defects and is insensitive to the dose. At the higher ion doses, the capture rate of the ion-damage defects dominate the capture rate of the native defects, and the lifetime is governed by the ion-damage defects. The lifetime is inversely proportional to the dose as Fig. 5.6 shows, because the density of the ion-damage defects is proportional to the dose. This relationship between the lifetime and dose continues up to and including a dose of 10^{14} cm^{-2}. This was the largest dose for which a measurable signal was obtained, and this dose gave rise to a 0.6 ± 0.2 ps lifetime. Thus, no saturation of the density of ion-damage defects was observed up to a dose of 10^{14} cm^{-2}.

Both sample sets have discontinuities in the plots of lifetime versus ion dose. These discontinuities occur where the implant current density was changed. For example, for sample set #2 the implantation current was changed between does of 3×10^{12} and 6×10^{12} cm^{-2}, causing the observed discontinuity. For discontinuities observed in both curves, the slope of the curve is -1 before and after the implant current change. For the higher implant current, the lifetime is longer, indicating that there are fewer of the lifetime governing defects. These discontinuities must be the result of increased surface heating because of the increase in the implant current. The higher surface temperature must allow some of the implantation damage to be annealed out, so that fewer defects remain in the sample at the

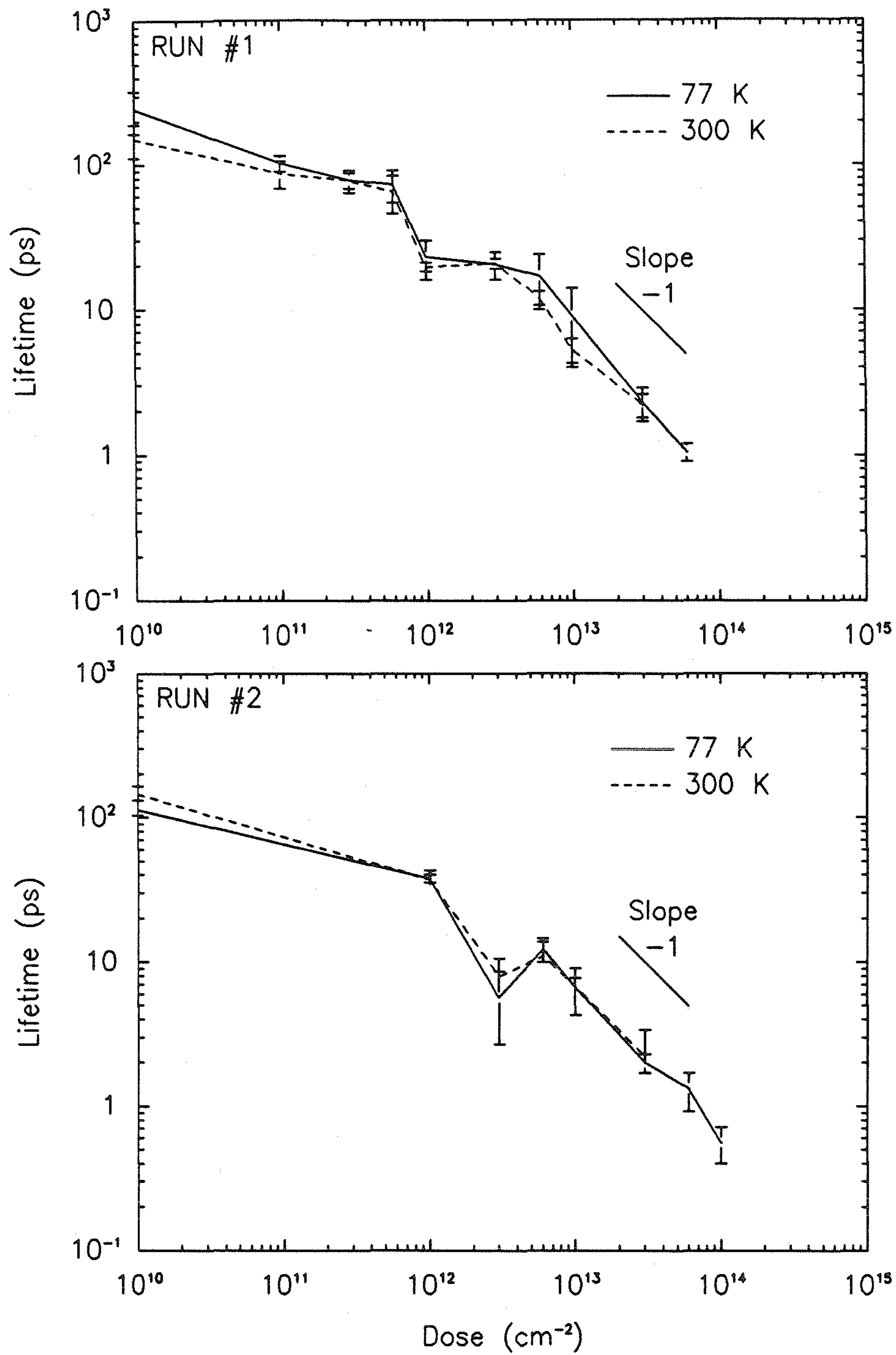

Figure 5.6: Lifetime versus ion dose. The top plot is for sample set number 1, while the bottom plot is for sample set number 2. The lifetimes at 77 and 300 K are shown as solid and as dashed lines, respectively.

higher implant currents and the lifetime is correspondingly longer. This heating occurs even though the substrate is mounted on a block cooled to 8 °C.

The minimum lifetime found in the work of this chapter is similar to that found in Ref. 7 for silicon-on-sapphire. There, the carrier lifetime versus ion dose reaches a limit of 600 fs. This limit is believed to be due to amorphization or a saturation of the effective trap density in crystalline silicon.[7] In the work reported here, a 600 ± 200 fs lifetime is measured for GaAs. However, the plot of lifetime versus ion dose shown in Fig. 5.6 shows that this is not a lower limit, and shorter lifetimes should result from ion doses larger than 10^{14} cm^{-2}. Thus, it appears that shorter carrier lifetimes can be obtained in SI LEC GaAs than in silicon-on-sapphire.

Figure 5.7 shows a plot of near band-to-band peak heights from the PL spectra at 77 and 300 K with ion dose. Both the 77 and 300 K curves show the same sort of behavior observed for the lifetime versus ion dose. For low doses the PL peak height does not change much with ion dose, while for the higher ion doses, the PL peak height does change quickly with ion dose. In fact, for the higher doses, the fall-off is faster than the -1 slope observed for the lifetimes, indicating that the decrease in the PL peak height is not just due to the decrease in the carrier lifetime.

The behavior of the PCE cross correlation with ion dose is more complicated than that of carrier lifetime with ion dose. Careful examination of Fig. 5.4 indicates that there are several features important to the PCE performance which vary with ion dose. These include the PCE speed, the peak amplitude and the background.

The response speed of the PCE is measured by using the half-width at half-maximum (HWHM) of the lower delay-time side of the autocorrelation peak, so that the effects of pulse reflections seen on the high delay-time side are not included. Note that this HWHM includes the effects of both the turn-on of the pulser PCE and the turn-off of the sampler PCE. Figure 5.8 shows a plot of this HWHM

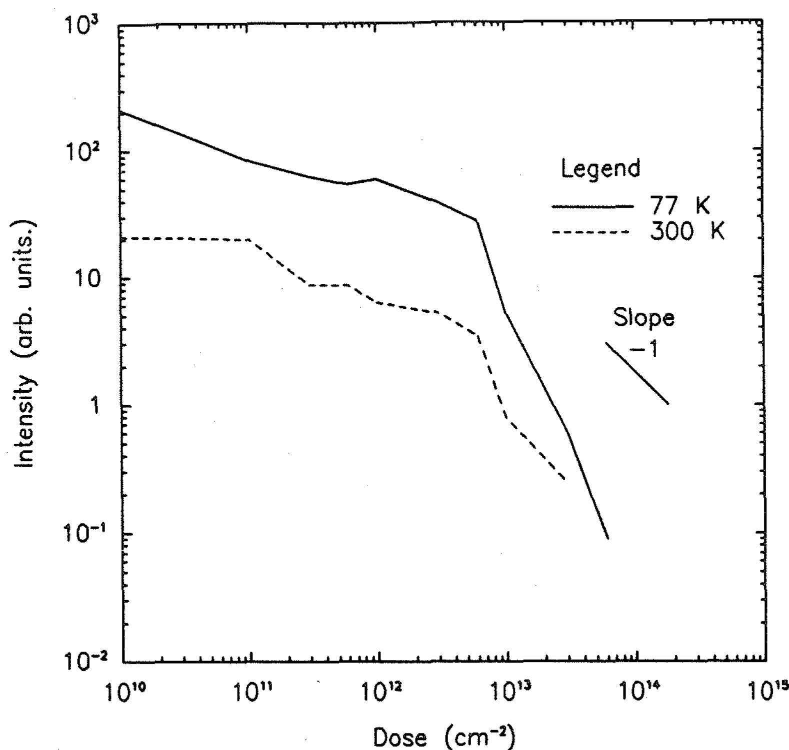

Figure 5.7: PL amplitude versus ion dose. The solid, dashed, and dash-dotted curves show the amplitude of the dominant peak for 5, 77, and 300 K, respectively, for sample set #2. The acceptor-related peak is dominant at 5 K, while the near band-to-band peak is dominant at 77, and 300 K.

of the autocorrelation peaks versus dose. The plot is similar to that of lifetime versus ion dose shown in Fig. 5.6. The dips correspond to the point at which the implant current density was changed. For both sample sets #1 and #2, the risetime decreases with ion dose; however, the slope of the decrease is less steep than -1, suggesting that it is not only the carrier lifetime that determines the PCE switching speed within this range of PCE speeds.

The amplitude of the autocorrelation peaks decrease with ion dose while the relative size of the background increases with ion dose. The decrease in amplitude is due to the reduction of the conductance of the gap because of the reduction of

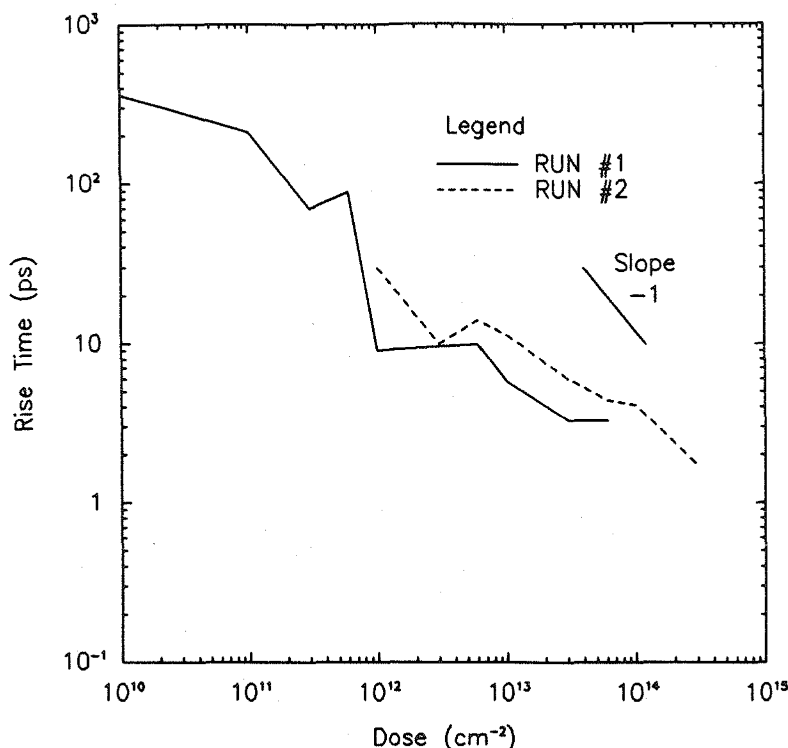

Figure 5.8: PCE autocorrelation half-width versus Ion Dose. The half-width is the HWHM value. The solid and dashed curves are for sample sets # 1 and # 2, as shown. The half-maximum is taken as halfway between the peak and background.

the carrier lifetime. This would also cause the relative size of the background to increase if the dark current that causes the background does not decrease by the same amount. It is this loss of sensitivity and the relative increase in background which practically limit the speed of the PCEs measured. The dose used to produce the optimum PCE is 6×10^{13} cm^{-2}, producing a pulse with a HWHM of 4 ps and FWHM of 9 ps, while still having good sensitivity and low background. Higher ion doses produce faster pulses, but their low sensitivity and high relative background make them less useful. Thus, in the work reported here, the speed of the PCE is not observed to saturate with ion dose as was found for silicon-on-sapphire.[7] Instead, other factors practically limit the speed of the PCE.

5.5 Summary of Results

In this chapter we have described observations of carrier lifetimes, and response speeds of PCE structures, on GaAs damaged with 200 keV H^+ ions. These results were compared with similar results observed for silicon-on-sapphire by Refs. 5 and 7 and calculations made using TRIM©.

Lifetime measurements made using PECS for the ion-damaged GaAs show that the carriers decay with a single lifetime, indicating that the trap distribution is more uniform in the top 0.25 μm excited region than is the distribution of vacancies calculated by TRIM©. The carrier lifetimes are found to be inversely proportional to the ion doses for doses larger than about 6×10^{12} cm^{-2}. The minimum lifetime measured was 0.6 ± 0.2 ps, corresponding to a dose of 1×10^{14} cm^{-2}. Experimentally, no damage saturation with ion dose is observed up to this dose, so that 0.6 ± 0.2 ps is not the minimum lifetime attainable for GaAs. This result is different from the results for silicon-on-sapphire damaged with 200 and 100 kev O^+ ions. For this, Doany *et al.*[7] find there is a minimum lifetime of 0.6 ps. TRIM© calculates the average vacancy level of the top 0.25 μm layer of GaAs at about one vacancy in ten-thousand atomic sites, while the average vacancy level in the silicon layer of the silicon-on-sapphire is about one vacancy in ten atomic sites. Based on this result it is not surprizing that the ion damage in the silicon-on-sapphire saturates while the ion damage in the GaAs does not. It is interesting to note that for the same lifetimes produced, it appears that very different amounts of damage are required.

Cross-correlation measurements of the response of the PCEs fabricated on the ion-damaged GaAs substrates show that the PCEs' speed increases with increasing ion dose. However, the width of the autocorrelation peak does not decrease as fast as the lifetime decreases, indicating that the geometry of the PCE structure may also be limiting the PCE speed. The PCE response speed is not found to saturate with ion dose. However, the decrease in sensitivity and decrease in relative

background of the PCE response with ion dose limit the maximum response of the PCE. The best PCE is obtained for a dose of 6×10^{13} cm^{-2}. For this ion dose the FWHM of the autocorrelation peak is 9 ps.

References

1. D.H. Auston, IEEE J. Quantum Electon. **QE-19**, 639 (1983).

2. R.B. Hammond, N.G. Paulter, R.S. Wagner, Appl. Phys. Lett. **45**, 289 (1984).

3. D.H. Auston and P.R. Smith, Appl. Phys. Lett. **41**, 599 (1982).

4. N.G. Paulter, IEEE Trans. Instrum. Meas.(to be published Sept. 1988).

5. M.B. Ketchen, D. Grischkowsky, T.C. Chen, C-C. Chi, I.N. Duling III, N.J. Halas, J-M. Halbout, J.A. Kash, and G.P. Li, Appl. Phys. Lett. **48**, 751 (1986).

6. D.H. Auston, A.M. Johnson, P.R. Smith and J.C. Bean , Appl. Phys. Lett. **41**, 599 (1982).

7. F.E. Doany, D. Grischkowsky, and C.-C. Chi, Appl. Phys. Lett. **50**, 460 (1987).

8. F.E. Doany and D. Grischkowsky, Appl. Phys. Lett. **52**, 36 (1988).

9. M.B. Johnson, A.T. Hunter, T.C. McGill, J. Appl. Phys. **63**, 2077 (1988).

10. J.F. Ziegler, J.P. Biersack and U. Littmark, in *The Stopping and Range of Ions in Solids* (Pergamon Press , New York, 1985).

11. *Ibid.*, pp. 115-116.

Appendix A

Lock-in Signal Calculations

A.1 Introduction

This appendix describes the signal detection used in the photoluminescence excitation correlation spectroscopy (PECS) technique described in Chapter 3. These measurement techniques involve lock-in amplifier detection of a signal produced by the nonlinear interaction of two pulse trains, which are chopped at two different frequencies. This appendix is divided into two sections: The first section determines the lock-in signal for a simple signal involving chopping envelopes; the second section uses this result to calculate, in detail, the signal detected using the PECS technique for the case of capture-dominated recombination.

A.2 Simple Case

In this section, we look at the lock-in signal detected for a simple signal similar in form but simpler than the signal from a real experiment. This signal is composed of the sum plus the product of the envelope functions of two choppers, one running

at ω_1 and the other at ω_2. The signal is given by

$$I(t) = A\,S(\omega_1;t) + B\,S(\omega_2;t) + C\,S(\omega_1;t)S(\omega_2;t), \tag{A.1}$$

where A, B, and C are constants, and $S(\omega_i;t)$ is square wave with a maximum and a minimum, of 1 and 0, and a frequency ω_i. Using the Fourier series for a square wave,

$$S(\omega_i;t) = \frac{1}{2} + \frac{2}{\pi}\sum_{n\,\mathrm{odd}} \frac{1}{n}\sin(n\omega_i t), \tag{A.2}$$

where the sums over n run over the odd numbers ($n = 1,3,5\ldots$). Detecting the signal using a lock-in amplifier set at a frequency ω involves multiplying the signal by a square wave with a maximum and a minimum, of -1 and 1, and with a frequency ω, and varying its phase to get the maximum dc output. The lock-in signal is this maximum dc output. Algebraically,

$$I_{\text{Lock-in}}(\omega) = \max_{\text{wrt }\delta}\Big\langle \mathrm{DC}\Big\{I(t)\Big[2S(\omega;t+\delta)-1\Big]\Big\}\Big\rangle,$$

where $\mathrm{DC}\{\cdots\}$ takes the dc component and $\max_{\text{wrt }\delta}\langle\cdots\rangle$ takes the maximum with respect to δ, which introduces an arbitrary phase. The signals $I_{\text{Lock-in}}(\omega_1)$, $I_{\text{Lock-in}}(\omega_2)$, and $I_{\text{Lock-in}}(\omega_2 \pm \omega_1)$ are of interest.

Consider $I_{\text{Lock-in}}(\omega_1)$:

$$\begin{aligned} I_{\text{Lock-in}}(\omega_1) &= \max_{\text{wrt }\delta}\Big\langle \mathrm{DC}\Big\{[A\,S(\omega_1;t) + B\,S(\omega_2;t) + C\,S(\omega_1;t)S(\omega_2;t)] \times \\ &\qquad [2S(\omega_1;t+\delta)-1]\Big\}\Big\rangle. \end{aligned} \tag{A.3}$$

This equation can be solved by looking at the dc component of the A, B, and C terms, along with the effect of δ on them, and then separately considering $\max_{\text{wrt }\delta}$ of the sum of the three terms.

Consider the A-term:

$$A\text{–term} = \mathrm{DC}\Big\{S(\omega_1;t)[2S(\omega_1;t+\delta)-1]\Big\}.$$

This term is clearly a maximum for $\delta = 0$. For $\delta = 0$, using $S(\omega_1;t)S(\omega_1;t) = S(\omega_1;t)$ along with Eqn. A.2,

$$A\text{−term} = \mathrm{DC}\Big\{S(\omega_1;t)\Big\} = \frac{1}{2}.$$

Consider the B-term:

$$B\text{−term} = \mathrm{DC}\Big\{S(\omega_2;t)[2S(\omega_1;t+\delta)-1]\Big\}.$$

Expanding the square waves using Eqn. A.2,

$$B\text{−term} = \mathrm{DC}\Big\{\frac{1}{2}\sin(\omega_2 t) + \frac{4}{\pi^2}\sum_{n\,\mathrm{odd}}\sum_{m\,\mathrm{odd}}\frac{1}{nm}\sin[n\omega_1(t+\delta)]\sin(m\omega_2 t)\Big\}.$$

The first term has zero dc component, and for ω_1 and ω_2 noncommensurate,* each term of the double sum has zero dc contribution. So, for any δ,

$$B\text{−term} = 0.$$

Consider the C-term:

$$C\text{−term} = \mathrm{DC}\Big\{S(\omega_1;t)S(\omega_2;t)[2S(\omega_1;t+\delta)-1]\Big\}.$$

The maximum is obtained for $\delta = 0$. For $\delta = 0$, using $S(\omega_1;t)S(\omega_1;t) = S(\omega_1;t)$, the fact that the frequencies are noncommensurate, and Eqn. A.2,

$$C\text{−term} = \mathrm{DC}\{S(\omega_1;t)S(\omega_2;t)\} = \frac{1}{4}.$$

Each of the three terms is maximum for $\delta = 0$. Thus for Eqn. A.3 the $\max_{\mathrm{wrt}\ \delta}$ is obtained for $\delta = 0$, and

$$I_{\mathrm{Lock-in}}(\omega_1) = \frac{A}{2} + \frac{C}{4}.$$

*Two frequencies ω_a and ω_b are commensurate if ω_a/ω_b is a rational fraction.

Similarly,

$$I_{\text{Lock-in}}(\omega_2) = \frac{B}{2} + \frac{C}{4}.$$

Consider $I_{\text{Lock-in}}(\omega_2 \pm \omega_1)$:

The same results are obtained for both $\omega_2 + \omega_1$ and $\omega_2 - \omega_1$, so in the derivation below, only the $\omega_2 - \omega_1$ case is treated.

$$\begin{aligned} I_{\text{Lock-in}}(\omega_2 - \omega_1) &= \max_{\text{wrt } \delta}\Big\langle \text{DC}\Big\{[A\,S(\omega_1;t) + B\,S(\omega_2;t) + C\,S(\omega_1;t)S(\omega_2;t)] \times \\ &\qquad [2S(\omega_2 - \omega_1; t+\delta) - 1]\Big\}\Big\rangle \end{aligned} \quad \text{(A.4)}$$

Again, this equation can be solved by looking at the dc component of the A, B, and C terms, along with the effect of δ on them, and then separately considering $\max_{\text{wrt } \delta}$ of the sum of the three terms.

Consider the A-term:

$$A\text{−term} = \text{DC}\Big\{S(\omega_1;t)[2S(\omega_2 - \omega_1; t+\delta) - 1]\Big\}.$$

Expanding the square waves using A.2,

$$\begin{aligned} A\text{−term} &= \text{DC}\Big\{\frac{1}{2}\sin[(\omega_2 - \omega_1)(t+\delta)] + \\ &\qquad \frac{4}{\pi^2}\sum_{n\,\text{odd}}\sum_{m\,\text{odd}} \frac{1}{nm}\sin(n\omega_1 t)\sin[m(\omega_2 - \omega_1)(t+\delta)]\Big\}. \end{aligned}$$

For ω_1 and $\omega_2 - \omega_1$ noncommensurate, each term of the double sum has zero dc contribution, independent of δ. So, for all δ,

$$A\text{−term} = 0.$$

Similarly, for all δ,

$$B\text{−term} = 0.$$

Consider the C-term:

$$C\text{−term} = \text{DC}\Big\{S(\omega_1;t)S(\omega_2;t)[2S(\omega_2 - \omega_1; t+\delta) - 1]\Big\}.$$

Expanding the square waves using Eqn. A.2,

$$\begin{aligned} C\text{-term} &= \mathrm{DC}\Bigg\{\left[\frac{1}{2}+\frac{2}{\pi}\sum_{n\,\mathrm{odd}}\frac{1}{n}\sin(n\omega_1 t)\right]\times\left[\frac{1}{2}+\frac{2}{\pi}\sum_{m\,\mathrm{odd}}\frac{1}{m}\sin(m\omega_2 t)\right]\times \\ &\qquad \left[\frac{4}{\pi}\sum_{p\,\mathrm{odd}}\frac{1}{p}\sin\{p(\omega_2-\omega_1)(t+\delta)\}\right]\Bigg\}. \end{aligned}$$

The dc contributions that are due to the constants in the square brackets are zero. Then

$$\begin{aligned} C\text{-term} &= \mathrm{DC}\Bigg\{\frac{16}{\pi^3}\times \\ &\qquad \sum_{n\,\mathrm{odd}}\sum_{m\,\mathrm{odd}}\sum_{p\,\mathrm{odd}}\frac{1}{nmp}\sin(n\omega_1 t)\sin(m\omega_2 t)\sin[p(\omega_2-\omega_1)(t+\delta)]\Bigg\}. \end{aligned}$$

The triple product of the sin functions can be rewritten using

$$\begin{aligned} &\sin(n\omega_1 t)\sin(m\omega_2 t)\sin[p(\omega_2-\omega_1)(t+\delta)] = \\ &\frac{1}{4}\Big(\sin\{[n\omega_1+m\omega_2-p(\omega_2-\omega_1)]t-p\delta'\}-\sin\{[n\omega_1-m\omega_2+p(\omega_2-\omega_1)]t+p\delta'\} \\ &-\sin\{[n\omega_1+m\omega_2+p(\omega_2-\omega_1)]t+p\delta'\}+\sin\{[n\omega_1-m\omega_2-p(\omega_2-\omega_1)]t-p\delta'\}\Big) \end{aligned}$$

where $\delta' = (\omega_2-\omega_1)\delta$. For any pair of ω_1, ω_2, and $\omega_2-\omega_1$ noncommensurate, there can be only a dc contribution from the second term with $n = m = p$. The maximum contribution is for $\delta' = n\frac{\pi}{2}$, for which

$$C\text{-term} = \mathrm{DC}\left\{\frac{16}{\pi^3}\sum_{n\,\mathrm{odd}}\frac{1}{4n^3}\right\}.$$

Using $\sum_{n\,\mathrm{odd}}\frac{1}{n^3} = 1.0518$ *

$$C\text{-term} = 0.1357\,C.$$

Because the C-term is the only nonzero term in Eqn. A.4, the $\max_{\mathrm{wrt}\ \delta}$ condition for this equation is the same as for the C-term. Thus,

$$I_{\mathrm{Lock\text{-}in}}(\omega_2-\omega_1) = 0.1357\,C.$$

*Using manipulations of series and Ref. 1

$$\sum_{n\,\mathrm{odd}}\frac{1}{n^3} = \frac{7}{8}\times\sum_{n=1,2,\cdots}\frac{1}{n^3} = \frac{7}{8}\times 1.202 = 1.0518\,.$$

Similarly,

$$I_{\text{Lock-in}}(\omega_2 + \omega_1) = 0.1357\,C.$$

In summary, for a signal given by

$$I(t) = A\,S(\omega_1; t) + B\,S(\omega_2; t) + C\,S(\omega_1; t)S(\omega_2; t).$$

The lock-in amplifier signals are:

$$\begin{aligned} I_{\text{Lock-in}}(\omega_1) &= \frac{A}{2} + \frac{C}{4}; \\ I_{\text{Lock-in}}(\omega_2) &= \frac{B}{2} + \frac{C}{4}; \\ I_{\text{Lock-in}}(\omega_2 - \omega_1) &= I_{\text{Lock-in}}(\omega_2 + \omega_1) = 0.1357\,C. \end{aligned}$$

where any pair of ω_1, ω_2, and $\omega_2 - \omega_1$ are noncommensurate. This result shows that the lock-in signals at the fundamental frequencies, ω_1 or ω_2, include two contributions, one from the sum term corresponding to that frequency, as well one from the product term. However, the lock-in signal at the difference or sum frequencies, $\omega_2 - \omega_1$ or $\omega_2 + \omega_1$, have contributions only from the product term.

What is the practical importance of the noncommensurate condition place on each pair of ω_1, ω_2, and $\omega_2 - \omega_1$? This condition is imposed so that the harmonics of the three frequencies do not overlap. Overlap means something quite different for real signals than for the ideal signals considered above. The frequency of real signals vary over a band, and the frequency of the lock-in detection also varies over a band, while the ideal signals are perfectly sharp. In practice, to see if the noncommensurate condition holds, the the overlap of harmonics of $\omega_2 - \omega_1$, ω_2, and ω_1 can be directly considered. Frequencies of $\omega_1 = 2005$ Hz and $\omega_2 = 1603$ Hz were used in the measurements made in Chapters 2 and 3. Table A.1 shows the fundamentals and first three harmonics of ω_1, ω_2, $\omega_2 - \omega_1$, and $\omega_2 + \omega_1$. The smallest separation of 5 Hz is between the fourth harmonic of $\omega_2 - \omega_1$ and ω_1,

Table A.1: Fundamental and Harmonics of ω_1, ω_2, $\omega_2 - \omega_1$, and $\omega_2 + \omega_1$.

	Fundamental and Harmonics in Hz.			
	fund.	1st	2nd	3rd
ω_1	2,005	4,010	6,015	8,020
ω_2	1,603	3,206	4,809	6,412
$\omega_2 - \omega_1$	402	804	1,206	1,608
$\omega_2 + \omega_1$	3,608	7,216	10,824	14,432

itself. In the PECS experiment, lock-in amplifier time constants longer than 1 s are typically used so that the 5 Hz separation can be discriminated and there is no overlap of these frequencies. Thus, frequencies $\omega_1 = 2005$ Hz and $\omega_2 = 1603$ Hz satisfy the noncommensurate condition necessary for the equations derived above.

A.3 Lock-in Detection in PECS

This section provides a more detailed solution for the PECS signal of a simple three-level capture-dominated system outlined in Chapter 3. This more detailed solution follows the solution outlined in Chapter 3.

As shown in Eqns. 3.8, the capture-dominated rate equations are

$$\begin{aligned} \frac{dn}{dt} &= G(t,\gamma) - \frac{n}{\tau}, \\ \frac{dp}{dt} &= G(t,\gamma) - \frac{p}{\tau}. \end{aligned}$$

We seek a solution to these equations for a pair of delta-function pulses, or

$$G(t,\gamma) = g_1\delta(t) + g_2\delta(t-\gamma).$$

This is easily found to be

$$n(t) = g_1\Theta(t)e^{-\frac{t}{\tau}} + g_2\Theta(t-\gamma)e^{-\frac{(t-\gamma)}{\tau}},$$
$$p(t) = g_1\Theta(t)e^{-\frac{t}{\tau}} + g_2\Theta(t-\gamma)e^{-\frac{(t-\gamma)}{\tau}},$$

where $\Theta(t)$ is the unit step function. Next, we seek the radiative PL signal by integrating Bnp over the detector response, and including the effect of pulse repetition and chopping. First, integrating over the detector response for the pair of pulses,

$$\begin{aligned} I_{\text{pair}}(\gamma) &= \int_{-\infty}^{\infty} dt\, Bn(t)p(t) \\ &= B\int_{-\infty}^{\infty} dt\left[g_1^2\Theta(t)e^{(-2\frac{t}{\tau}}\right. \\ &\quad \left. +g_2^2\Theta(t-\gamma)e^{-2\frac{(t-\gamma)}{\tau}} + g_1g_2\Theta(t)\Theta(t-\gamma)e^{-\frac{(2t-\gamma)}{\tau}}\right]. \end{aligned}$$

Using

$$\int_{-\infty}^{\infty} dt\, \Theta(t)e^{-2\frac{t}{\tau}} = \frac{\tau}{2}$$

and

$$\int_{-\infty}^{\infty} dt\, \Theta(t)\Theta(t-\gamma)e^{-\frac{(2t-\gamma)}{\tau}} = \frac{\tau}{2}e^{-\frac{|\gamma|}{\tau}}.$$

then

$$I_{\text{pair}}(\gamma) = B\left[(g_1^2+g_2^2)\frac{\tau}{2} + 2g_1g_2\tau e^{-\frac{|\gamma|}{\tau}}\right]. \quad (A.5)$$

The effect of repetition and chopping of the pulses is equivalent to multiplying I_{pair} in Eqn. A.5 by $1/t_{\text{rep}}$ and using $g_1 = g_1S(\omega_1;t)$ and $g_2 = g_2S(\omega_2;t)$. So, the detector signal for the actual pulse trains is

$$\begin{aligned} I(t,\gamma) &= \frac{B}{t_{\text{rep}}}\left\{[g_1^2S(t,\omega_1) + g_2^2S(t,\omega_2)]\frac{\tau}{2}\right. \quad (A.6) \\ &\quad \left. +g_1g_2S(t,\omega_1)S(t,\omega_2)\tau e^{-\frac{|\gamma|}{\tau}}\right\}. \quad (A.7) \end{aligned}$$

This signal is of the same form as the simple signal used in the earlier section in Eqn. A.1. Comparing Eqns. A.1 and A.7, the lock-in signals obtained from $I(t,\gamma)$ are

$$\begin{aligned} I_{\text{lock}}(\omega_2) = I_{\text{lock}}(\omega_1) &= \frac{Bg^2\tau}{4t_{\text{rep}}}(1+\mathrm{e}^{-\frac{|\gamma|}{\tau}}), \\ I_{\text{lock}}(\omega_2-\omega_1) = I_{\text{lock}}(\omega_2+\omega_1) &= \frac{\beta Bg^2\tau}{t_{\text{rep}}}\mathrm{e}^{-\frac{|\gamma|}{\tau}}, \end{aligned}$$

where

$$\beta = \frac{4}{\pi^3}\sum_{n\,\text{odd}}\frac{1}{n^3} \approx 0.136,$$

and $g_1 = g_2 = g$. This is the same result shown in Eqns. 3.11.

References

1. L.B.W. Jolly, in *Summation of Series* (Dover, New York, 1961), Series 1133, p.240.

Appendix B

Simulations of Pulses on a Waveguide with a Device

B.1 Introduction

The scattering parameters or s-parameters of high-speed devices are of much interest. It has been proposed that these can be measured to ultrahigh frequencies by integrating the device on a waveguide structure and using photoconductive circuit elements (PCEs) to generate and sample ultrashort electrical pulses.[1,2] Such measurements are described in Chapter 1. Briefly, a pulse is generated on the waveguide at one PCE, this pulse propagates with dispersion along the waveguide. Then, the pulse is incident on a device on the waveguide, creating a reflected pulse and a transmitted pulse according to the properties of the device. The reflected and transmitted pulses then propagate on the waveguide and can be sampled by the sampling PCE's. This PCE s-parameter measurement is a time-domain measurement, which is very different from the more usual frequency-domain measurements made using a network analyzer. The advantages and disadvantages of such a measurement are discussed in Chapter 1. For these measurements to be

meaningful, it is important to understand the measurement technique in detail. To this end, it is useful to model the technique on the computer. This modeling is useful in two ways: First, it allows the experimenter to obtain an intuitive feel for the technique; and secondly, it allows the determination of actual measurements to changes in device characteristics, as well as changes in the measurement system.

This appendix deals with the implementation of a program that models the measurement of s-parameters using PCEs on waveguides. There are three parts to such a measurement: i) the generation of pulses using a PCE; ii) the propagation of the generated pulse and the interaction of this pulse with the device; and iii) sampling the reflected and transmitted pulse with PCEs. The generation of the pulses using PCEs has been treated by Bowman,[3] and this work can be extended to treat the sampling of pulses. The work described in this appendix models the propagation of ultrashort pulses on dispersive waveguides, and the interaction of these pulses with a localized or lumped device on the waveguide.

The remaining part of this appendix is divided into four sections: The first, entitled Model -theory, discusses the theory of the model, first in general terms and then in specific terms; the second, entitled Model -implementation, discusses the implementation of this model; the third presents and discusses results for thinned and unthinned microstrips with and without a simple device; and the final section is a short summary and conclusion.

B.2 Model -Theory

This section discusses the model first in general terms and then in more detail.

B.2.1 General Discussion

Waveguides

The behavior of voltage pulses on waveguides is discussed in Refs. 4 and 5. In these references harmonic analysis is used to describe the propagation of a pulse on a waveguide. This consists of using Fourier analysis to decompose the pulse into a set of plane waves, whose behavior is known from the dispersion relation of the waveguide. It is possible to decompose the pulse as a set of temporal plane waves, *i.e.*, using the pairs (ω, t); or as a set of spatial plane waves, *i.e.*, using the pairs (k, z). Where ω and k are the plane-wave temporal and spatial frequencies, respectively, t is the time, and z is the position along the waveguide.

For the pair (ω, t):

$$V(z,t) = F_{t,\omega}^{-1}\Big[e^{-ik(\omega)z} \times F_{t,\omega}[V(0,t)]\Big],$$

where $F_{t,\omega}$ and $F_{t,\omega}^{-1}$ are the Fourier and inverse-Fourier transforms between ω-space and t-space, and $k(\omega)$ is a form of the dispersion relation. This equation calculates the temporal voltage signal at a position z based on the signal at $z = 0$. This decomposition has been used by researchers to determine the voltage signals at positions farther down the waveguide from where the signals were generated.[6,7,8] Using this decomposition, the effects of energy losses, such as from absorption losses in the waveguide, can easily be included. This is done by using the more general propagation factor $e^{-i\beta(\omega)z}$, in which the imaginary part of β represents the losses of the waveguide. However, this (ω, t) decomposition cannot describe the scattering of the pulse from a localized device.

For the pair (k, z):

$$V(z,t) = F_{z,k}^{-1}\Big[e^{i\omega(k)t} \times F_{z,k}[V(z,0)]\Big],$$

where $F_{z,k}$ and $F_{z,k}^{-1}$ are the Fourier and inverse-Fourier transforms between k-space and z-space. This equation calculates the spatial voltage signal at a time t based

on the signal at $t = 0$. This decomposition allows a localized device to act as a scattering center. However, it does not lend itself to the direct calculation of the temporal voltage signal at a specific position on the waveguide, nor does it easily allow the effects of losses to be easily included. The first shortcoming can be overcome by generating a movie showing the spatial signal at a set of times, so the voltage signal at a given position may be determined from the frames of the movie.

Because only the (z, k) decomposition allows scattering from a lump device, this is the decomposition used in the model. The determination of the voltage signal at a position as a function of time is determined by keeping track of the voltage at a given position, as time changes. Losses in the waveguide are not considered.

Dispersion

The dispersion relation $k(\omega)$ or $\omega(k)$ describe the dispersion of the waveguide. In this work

$$k(\omega) = \frac{\omega}{c\sqrt{\epsilon_{\mathrm{re}}(\omega)}}$$

is used. The functions $\epsilon_{\mathrm{re}}(\omega)$ for the waveguides used in this work are from Ref. 8, 9, and 10. These were determined by solving Maxwell's equations for the particular waveguide in a quasi-static TEM approximation. The actual equations giving the dispersion relations for microstrip are given in the next subsection.

Device

The devices modeled are in the small signal region where they can be satisfactorily described by s-parameters $S_{ij}(\omega)$. See Ref. 5 for a detailed description of s-parameters.

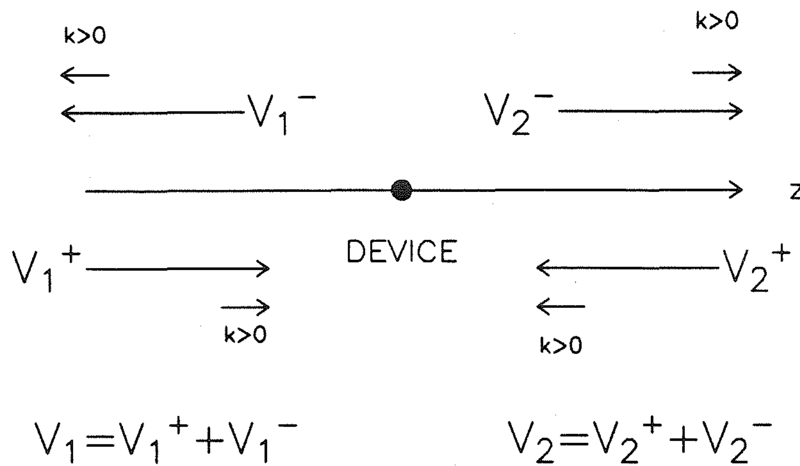

Figure B.1: Schematic of signals on a waveguide with a device. This shows the sign convention chosen for the k of the incident, reflected, and transmitted waves.

B.2.2 Detailed Discussion

In this detailed discussion, the modeling of the device on the waveguide is discussed, the dispersion relations used are shown, the s-parameters of simple devices are calculated, and finally, the treatment of generating a pulse on the waveguide and sampling a pulse on the waveguide are discussed.

Device on a Waveguide

As described earlier, to include scattering that is due to a lumped device, the harmonic decomposition must be with respect to (k, z).

Scattering for a single k

Figure B.1 shows the incident, reflected, and transmitted waves along with the sign conventions for k used for the different waves. The plane waves in z-space and k-space are $V_i^{\pm}(z,t)$ and $v_i^{\pm}(k)$, respectively, where $i = 1$ represents the region to the left of the device and $i = 2$ represents the region to the right of the device, and the $+$ represents waves incident on the device, and the $-$ represents waves coming from the device. Consider a single plane-wave incident from the left with spatial

frequency k and amplitude $v_1^+(k)$. The equations for the waves are:

$$\begin{aligned} V_1^+(z,t) &= \mathrm{Re}\Big[v_1^+(k)\mathrm{e}^{-ikz+i\omega t}\Big], \quad V_1^-(z,t) = \mathrm{Re}\Big[v_1^-(k)\mathrm{e}^{+ikz+i\omega t}\Big], \\ V_2^+(z,t) &= \mathrm{Re}\Big[v_2^+(k)\mathrm{e}^{+ikz+i\omega t}\Big], \quad \text{and} \quad V_2^-(z,t) = \mathrm{Re}\Big[v_2^-(k)\mathrm{e}^{-ikz+i\omega t}\Big]. \end{aligned}$$

The voltages in the two regions are:

$$\begin{aligned} V_1(z,t) &= V_1^+(z,t) + V_1^-(z,t), \\ V_2(z,t) &= V_2^+(z,t) + V_2^-(z,t). \end{aligned}$$

The scattering parameters relate the amplitudes of the plane waves $v_i^\pm(k)$ through

$$\begin{pmatrix} v_1^-(k) \\ v_2^-(k) \end{pmatrix} = \begin{pmatrix} S_{11}(k) S_{12}(k) \\ S_{21}(k) S_{22}(k) \end{pmatrix} \times \begin{pmatrix} v_1^+(k) \\ v_2^+(k) \end{pmatrix}.$$

Using the fact that there is only a wave incident from the left, $v_2^+(k) = 0$ and $V_2^+(z,t) = 0$. So,

$$\begin{aligned} v_1^-(k) &= S_{11}(k) v_1^+(k) \\ v_2^-(k) &= S_{21}(k) v_2^+(k), \end{aligned}$$

and

$$\begin{aligned} V_1^-(z,t) &= S_{11}(k) v_1^+(k) \mathrm{e}^{+ikz+i\omega t} \\ V_2^-(z,t) &= S_{21}(k) v_1^+(k) \mathrm{e}^{-ikz+i\omega t}. \end{aligned}$$

Thus, for a plane wave with spatial frequency k,

$$\begin{aligned} V_1(z,t) &= \mathrm{Re}\Big[v_1^+(k)\mathrm{e}^{-ikz+i\omega t} + S_{11}(k) v_1^+(k) \mathrm{e}^{+ikz+i\omega t}\Big] \\ V_2(z,t) &= \mathrm{Re}\Big[S_{21}(k) v_1^+(k) \mathrm{e}^{-ikz+i\omega t}\Big] \end{aligned} \qquad \text{(B.1)}$$

Scattering for a pulse

Using Fourier analysis, a pulse incident on the device from the left is a superposition of plane waves analyzed above, such that

$$V_1^+(z,t) = \mathrm{Re}\Big[\frac{1}{\sqrt{2\pi}} \int_{-\infty}^{\infty} dk\, v_1^+(k) \mathrm{e}^{-ikz+i\omega t}\Big],$$

where

$$v_1^+(k) = \frac{1}{\sqrt{2\pi}} \int_{-\infty}^{\infty} dz\, V_1^+(z,0) e^{+ikz}.$$

Then, using Eqn. B.1,

$$\begin{aligned} V_1(z,t) &= \mathrm{Re}\left[\frac{1}{\sqrt{2\pi}} \int_{-\infty}^{\infty} dk \left[v_1^+(k) + S_{11}(k) v_1^+(k)\right] e^{-ikz+i\omega(k)\,t}\right], \\ V_2(z,t) &= \mathrm{Re}\left[\frac{1}{\sqrt{2\pi}} \int_{-\infty}^{\infty} dk\, S_{11}(k) v_1^+(k) e^{-ikz+i\omega(k)\,t}\right]. \end{aligned} \tag{B.2}$$

These equations give the voltage signal spatially on the waveguide at a given time t. V_1 is the signal to the left of the device, while V_2 is the signal to the right of the device. Using this expression, a movie of the voltage signal on the waveguide can be made. Each frame consisting of a calculation of the above expression for a given t_i yielding $V_1(z,t_i)$ and $V_2(z,t_i)$, and t_i is stepped through to make the movie.

Dispersion relations

The dispersion relations and references for microstrips, coplanar waveguides, and coplanar strips are shown below. For effects of strip thicknesses and losses. see Ref. 10.

Microstrip

Figure 1.2 of the introduction shows the microstrip waveguide with a linewidth w, substrate thickness h, and permittivity ϵ_r. From Refs. 10 and 9, using the quasi-static TEM approximation

$$\begin{aligned} \sqrt{\epsilon_{re}(f)} &= \sqrt{\epsilon_{req}} + \frac{(\sqrt{\epsilon_r} - \sqrt{\epsilon_{req}})}{(1+4F^{-1.5})} \\ \text{and} \qquad Z_0(f) &= Z_0 \frac{\sqrt{\epsilon_{req}}}{\sqrt{\epsilon(f)}}, \end{aligned} \tag{B.3}$$

where

$$\begin{aligned} F &= \frac{f}{f_{te}}[0.5 + \{1 + 2\log_{10}(1+\frac{w}{h})\}^2], \quad f_{te} = \frac{c}{4h\sqrt{\epsilon_r - 1}}, \\ \epsilon_{req} &= 0.5[(\epsilon_r + 1) + (\epsilon_r - 1)(1 + 10\frac{h}{w})^{-\frac{1}{2}}], \end{aligned}$$

$$\text{and} \quad Z_0 = \frac{\eta}{2\pi\sqrt{\epsilon_{req}}} \ln(\frac{8h}{w} + 0.25\frac{w}{h}) \quad \text{for} \quad \frac{w}{h} \leq 1,$$

$$\text{or} \quad Z_0 = \frac{\eta}{\sqrt{\epsilon_{req}}}(\frac{w}{h} + 1.393 + 0.667\ln[\frac{w}{h} + 1.444])^{-1} \quad \text{for} \quad \frac{w}{h} \geq 1.$$

Above, f is the frequency and frequency f_{te} is the cutoff frequency of the lowest order TE mode.

Coplanar Waveguide and Coplanar Strip

See Ref. 10 for the formulae for ϵ_{req} and Z_0 calculated using the quasi-static TEM approximation, and see Ref. 8 for the extension of these formulae to high frequency to include dispersion.

Device S-Parameters

This paragraph shows the s-parameters that result from embedding impedance $Z(f)$ into a waveguide whose impedance is $Z_0(f)$. Such a device can act as a shunt between the center conductor and ground, or can act in series with the center conductor across a gap in the center conductor.

Using $z = Z(f)/Z_0(f)$:

for a shunting device,

$$S_{11} = S_{22} = \frac{-1}{2z+1}$$

$$\text{and} \quad S_{12} = S_{21} = \frac{2z}{2z+1};$$

and for a series device,

$$S_{11} = S_{22} = \frac{z}{2+z}$$

$$\text{and} \quad S_{12} = S_{21} = \frac{2}{2+z}.$$

Pulse Generation

The approach for pulse generation is to assume the shape of the temporal voltage signal on the waveguide at the generating PCE. This signal is used to set the

voltage on the waveguide at the PCE at the same time as the signal is propagated on the waveguide.

Pulse Sampling

The approach for sampling is to neglect the effect that the PCE itself has on the voltage signal on the waveguide. Then the sampling signal is generated by taking the voltage on the waveguide adjacent to the PCE, as the spatial pulse moves frame by frame. The effect of the temporal response of a real PCE is found by convolving the sampled signal described above with the response function of the PCE.

B.3 Model -Implementation

This section discusses the implementation of the model. The first section discusses the implementation of a discrete Fourier transform, and the second section discusses the implementation of the model itself.

B.3.1 General Discussion

The Fourier transform used in the theory section is for continuous functions. For implementation on a computer, $V_i^{\pm}$ and $v_i^{\pm}$ must be represented discretely and the Fourier transformation must be discrete. The discrete Fourier transform used is a fast-Fourier transform (FFT). See Ref. 11 for a good introduction to discrete Fourier transforms including the FFT. The paragraphs below outline the implementation of Fourier transformation for discrete functions and compare the results to the transformation of continuous functions.

For discrete functions.

$$V(x) = \int_{-\infty}^{\infty} v(k) e^{-i2\pi kx}\, dk \quad \text{becomes} \quad \mathrm{V(n)} = \frac{1}{\mathrm{N}} \sum_{\mathrm{k}=0}^{\mathrm{N}-1} \mathrm{v(k)} e^{-i2\pi \frac{\mathrm{nk}}{\mathrm{N}}},$$

$$\text{and} \quad v(k) = \int_{-\infty}^{\infty} V(x), \mathrm{e}^{+i2\pi kx}\, dx \quad \text{becomes} \quad \mathrm{v(k)} = \frac{1}{\mathrm{N}} \sum_{\mathrm{n}=0}^{\mathrm{N}-1} \mathrm{V(k)} \mathrm{e}^{-i2\pi \frac{\mathrm{nk}}{\mathrm{N}}}.$$

For the continuous functions $V(x)$ and $v(k)$:

$x-$ is the position coordinate and

$k-$ is now the wave number $k = \frac{1}{\lambda}$ (not $k = \frac{2\pi}{\lambda}$).

For the discrete functions V(n) and v(k):

V(n)$-$ is a set of discrete values of $V(x)$, where $\mathrm{V(n)} = V(x_{\mathrm{n}})$,

with $x_{\mathrm{n}} = \Delta x\,(\mathrm{n} - \frac{\mathrm{N}-1}{2})$, for $\mathrm{n} = 0$ to $\mathrm{N} - 1$, with Δx the sampling step size;

and v(k)$-$ is a set of discrete values of $v(k)$, where $\mathrm{v(k)} = v(k_{\mathrm{k}})$,

with $k_{\mathrm{k}} = \Delta k\,\mathrm{k}$, for $\mathrm{k} = 0$ to $\frac{\mathrm{N}}{2}$, and $k_{\mathrm{k}} = -\Delta k\,(\mathrm{k} - \frac{\mathrm{N}}{2})$ for $\mathrm{k} = \frac{\mathrm{N}}{2} + 1$ to $\mathrm{N} - 1$, with $\Delta k = \frac{1}{\mathrm{N}\Delta x}$.

There are two important considerations inherent in using discrete representations of functions and a discrete Fourier transform. First, the discrete representation samples the voltage signal $V(x)$ with a step size, Δx, which limits the extent of the spatial frequency of the discrete representation V(n) to $k_{\mathrm{max}} = 1/(2\,\Delta x)$. Thus, Δx must be smaller than the minimum feature of the signal to be represented. Second, the discrete representation is only over a length of $L = \mathrm{N}\,\Delta x$. Using a discrete Fourier transform, the signal represented by V(n), is periodic with period L. So the signal is repeated every length L, which is called aliasing. Thus, N must be chosen to be large enough so that aliasing does not produce harmful artifacts as the signal propagates in time.

The discrete version of Eqn. B.2, which describes the propagation of signals, is:

$$\begin{aligned} \mathrm{V_1(n)} &= \frac{1}{\mathrm{N}} \mathrm{Re}\Big[\sum_{\mathrm{k}=0}^{\mathrm{N}-1} \Big[\mathrm{v(k)} + \mathrm{S_{11}(k)}\, \mathrm{v(-k)}\Big] \mathrm{e}^{i2\pi f(\mathrm{k})\, t} \mathrm{e}^{-i2\pi \frac{\mathrm{nk}}{\mathrm{N}}}\Big], \\ \text{and} \quad \mathrm{V_2(n)} &= \frac{1}{\mathrm{N}} \mathrm{Re}\Big[\sum_{\mathrm{k}=0}^{\mathrm{N}-1} \mathrm{S_{12}(k)}\, \mathrm{v(k)}\, \mathrm{e}^{i2\pi f(\mathrm{k})\, t} \mathrm{e}^{-i2\pi \frac{\mathrm{nk}}{\mathrm{N}}}\Big], \end{aligned} \tag{B.4}$$

where $\mathrm{S_{11}(k)}$, and $\mathrm{S_{12}(k)}$ are discrete representations of $S_{11}(\mathrm{k})$ and $S_{12}(\mathrm{k})$ de-

fined analogously to v(k), and v(−k) is meant to be the discrete representation of $v(-k)$. These are the propagation equations of the voltage signals in the discrete representation.

B.3.2 Detailed Discussion

A flow chart summarizing the model is shown below.

Initialization

PCE Structure: Set length of the waveguide and sampling number, N. Choose generator position, n_{GEN}, and sampler positions n_{REF} and n_{TRAN}.

Movie: Choose time between frames, t_{FRAME}, and number of frames, N_{FRAME}.

Waveguide: Choose size and type of waveguide. Calculate f(k).

Device: Choose type of device. Calculate S(k).

PCE: Choose shape of pulse and response behavior of PCE, $V_{GEN}(t)$ and $V_{RES}(t)$, respectively.

Pulse Propagation

Propagate pulse for $t = 0$, to $N_{FRAME} \times t_{FRAME}$, with step size t_{FRAME}.

IF t is such that $V_{GEN}(t)$ has not returned to zero,

THEN, the time step t_{FRAME} is broken up into finer steps and between propagating with the finer steps using Eqns. B.4, v(k) is recalculated, such that $V(n_{GEN}) = V_{GEN}(t)$.

ELSE, propagate by t_{FRAME} using Eqns. B.4.

SET $V_{REF}(t) = V(n_{REF}, t)$ and $V_{TRAN}(t) = V(n_{TRAN}, t)$.

CONTINUE propagation.

Output

Output the movie of the pulse on the waveguide, $V(z,t)$; the *real* reflection and transmission signals, which are the convolution of V_{RES} with $V_{REF}(t)$ and $V_{TRAN}(t)$, respectively; and the s-parameters determined from the real reflection

and transmission signals.

B.4 Results and Discussion

The results of waveguide simulations are described and discussed in this section. Two simulations are shown in this section: The first is for a pulse on a microstrip waveguide; and the second is for a pulse on a microstrip waveguide with a simple passive device.

Plots (a) and (b) of Fig. B.2 show the propagation of ultrashort pulses on two microstrips, which are identical except that the microstrip for (b) is much thinner than that for (a). The plots show a sequence of snapshots of the voltage on the waveguide at the times shown. These snapshots are part of a larger set of snapshots that together make a movie of the voltage signal as it propagates on the waveguide. Both sets of plots show a pulse put on the waveguide at the position of the pulser PCE and show the pulse propagating with dispersion in either direction, as expected. Normal dispersion results in the higher frequencies propagating at a slower velocity, causing a broadening of the leading edge and a sharpening of the following edge with distance propagated, which is observed for both sets of plots. In fact, for both waveguides, the higher-frequency components shifting to the trailing edge produce a negative pulse on the trailing edge, which grows with the distance propagated. Comparison of the thinned and unthinned dispersion shows that the pulse on the unthinned microstrip is dispersed more than that on the thinned microstrip and is most clearly observed by comparing the two leading edges of the pulses. This result is expected because the thinned microstrip is less dispersive since f_{te}, the turn-on of the lowest TE mode, is larger for the thinned microstrip than the unthinned microstrip (see Eqns. B.3). Note

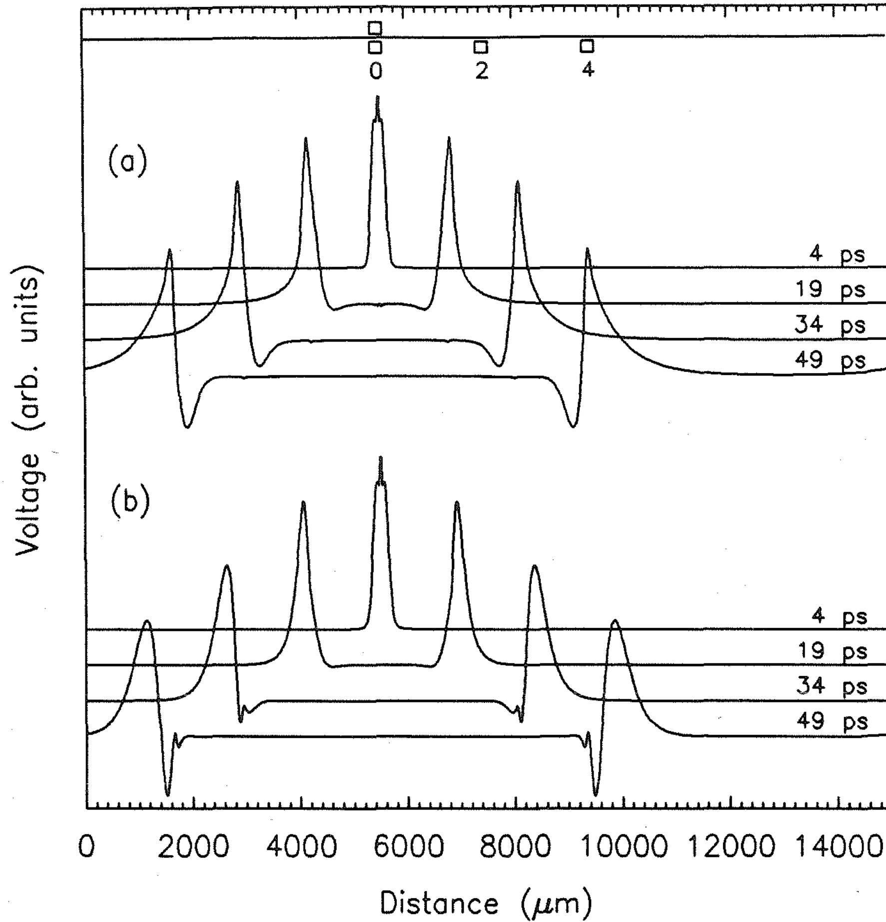

Figure B.2: Pulse dispersion on microstrip I. The two sets of plots labeled (a) and (b) show the spatial voltage on two different microstrips at the sequence of different times shown on the plots. The pulses are generated by a pulser at 5500 μm, which generates an asymmetric Gaussian pulse with rise time half-width at half-maximum (HWHM) of 0.75 ps and fall-time HWHM of 2.25 ps. The plots in set (a) are for an unthinned microstrip, with strip width, $w =$ 50 μm, thickness, $h =$ 624 μm, and dielectric constant, $\epsilon_r =$ 13; and the plots in set (b) are for a thinned microstrip, which is identical except for the thickness, $h =$ 94 μm. Above the plots the positions of PCEs on the microstrip are schematically shown. The labels 0, 2, and 4 mark the separation, in mm, of the samplers (boxes below the line) from the pulser (box above the line).

that for the thinned microstrip, several oscillations of the voltage are observed on the trailing edge of the pulse. These negative features on the trailing edge of the pulses after propagation down the waveguides are observed, using other models.[8].

Figure B.3 shows the signals that would be detected by PCEs positioned 0, 2, and 4 mm down the waveguide from the pulser PCE for the thinned microstrip. The solid curves represent the voltage signal on the waveguide at the PCE, while the dashed curves represent the signal that would be detected using a PCE with identical response to the pulser PCE. The voltage signals at the PCEs show the the features expected from Fig. B.2. The PCE signal is formed by convolving the voltage on the waveguide at the PCE with the response function of the PCE. Comparing the dashed and solid curves for the same positions shows that the detected signal is spread out in time, and some of the details, especially in the trailing edge, are lost. The PCE signal at 4 mm shows a slight negative excursion on the trailing edge as expected. This reversed polarity region in the trailing edge of the pulse has been observed experimentally.[12] These simulations demonstrate that the propagation of ultrashort pulses on waveguides is not simple.

The sets of plots labeled (a) and (b) of Fig. B.4 show the propagation of ultrashort pulses on two different microstrips with a device present. The microstrip in set (a) is dispersionless with an impedance of 50 Ω, and the other microstrip is the same unthinned microstrip used in Fig. B.2. The voltage pulse in Fig. B.4 is the same as that used for Fig. B.2.

The device is a 50 Ω resistor in parallel with a 0.10 pF capacitor acting as a shunt. Such a device is dominated by the resistance at low frequencies and by the capacitor at high frequencies. The cross-over frequency is $f_{\mathrm{RC}} = (RC)^{-1} =$ 200 GHz. For a 50 Ω resistor in a 50 Ω line, the reflection coefficient is $-1/3$ and the transmission coefficient is $+2/3$. The capacitor at very high frequency becomes a short, which has a reflection coefficient of -1 and transmission coefficient 0.

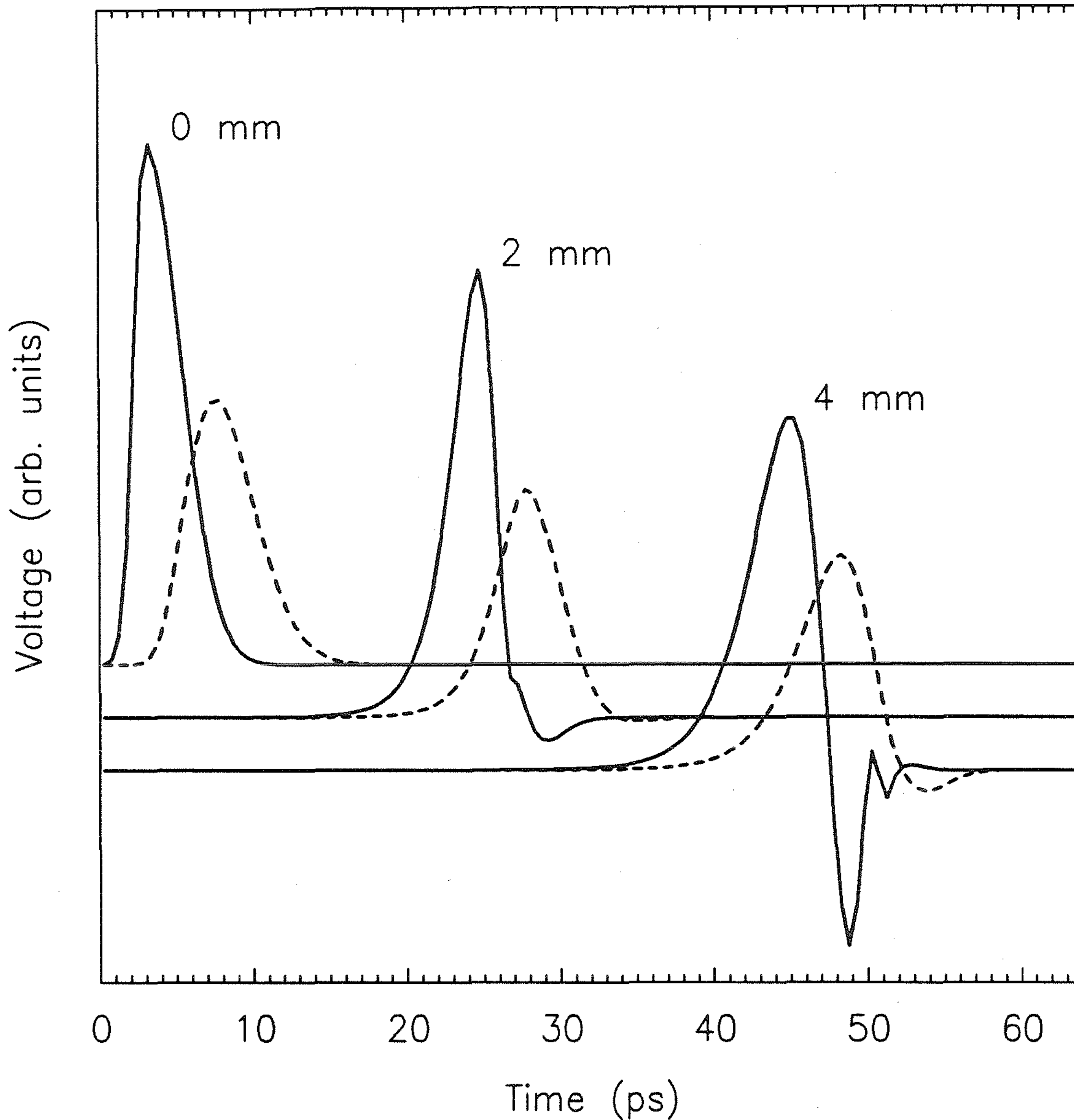

Figure B.3: Pulse dispersion on microstrip II. The three pairs of plots show the temporal voltage signals that would be detected by sampler PCEs shown in Fig. B.2 for the signals on the thinned microstrip shown in Fig. B.2. The plots are labeled by the separation of sampler and pulser 0, 2, and 4 mm. The solid curves show the actual voltage on the waveguide at the sampling PCE, while the dashed curves show the signal measured, using a PCE whose response function is the same shape as the pulse generated by the pulser PCE.

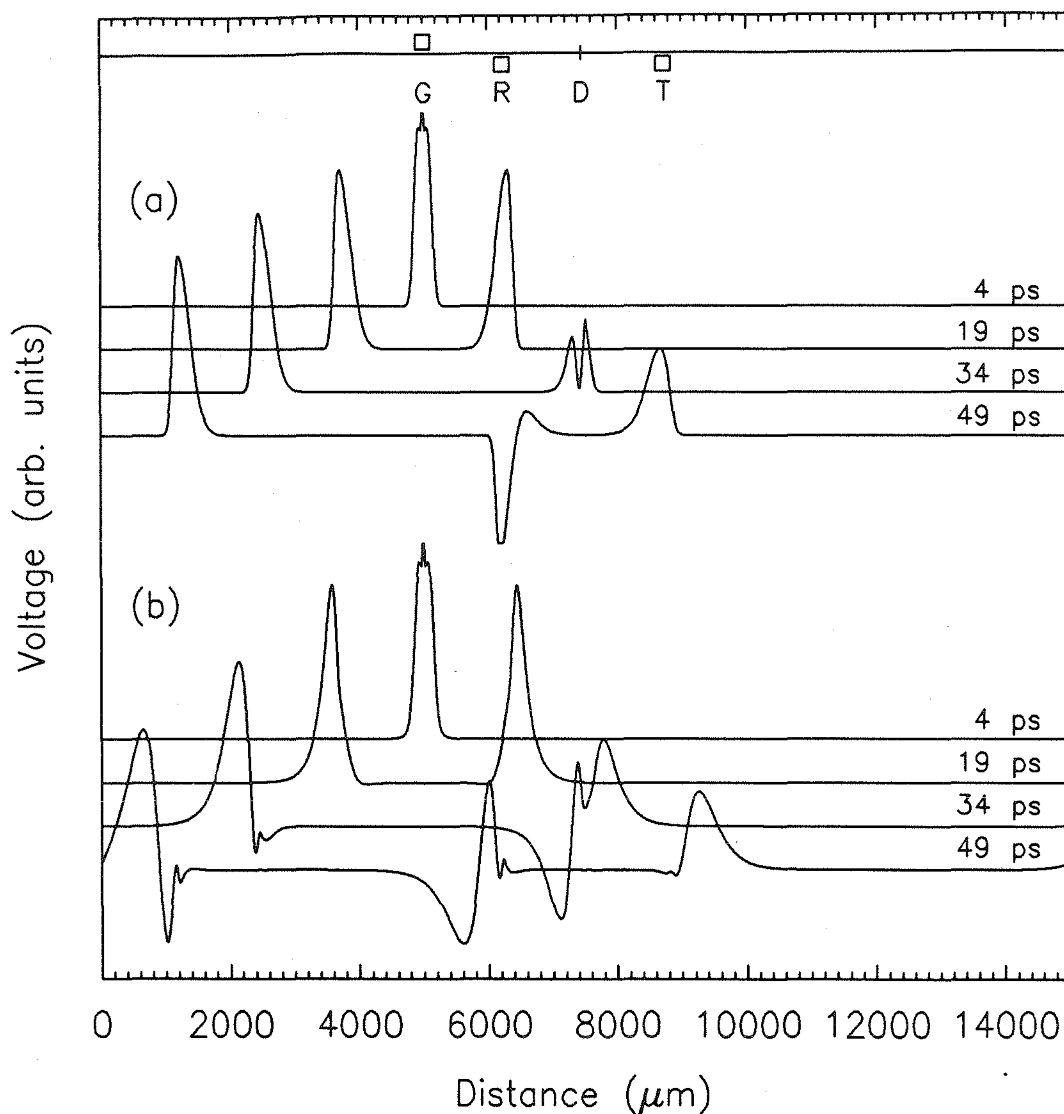

Figure B.4: Pulse on microstrip with a device I. The two sets of plots labeled (a) and (b) show the spatial voltage signal at the times shown, for two different microstrips with a device. The microstrip in plot (a) is nondispersive, while the microstrip in (b) is the thinned microstrip of Fig. B.2. The initial pulse is the same as in Fig. B.2. The device is a 50 Ω resistor in parallel with a 0.10 pF capacitor acting as a shunt to ground. The labels G, R, and T on the inset schematic above the plots show the positions of the generation pulser PCE, and the reflection and transmission sampler PCEs, respectively. Label D shows the position of the device.

In Fig. B.4, the plot set (a) shows the results expected from the discussion of the behavior of the device. The reflected pulse is inverted, while the transmitted pulse is not inverted. Because of the capacitor, the reflected pulse contains more of the high-frequency components of the incident pulse, resulting in an amplitude larger than the $-1/3$ expected for the resistor alone, and the positive polarity trailing edge. Similarly, because of the capacitor, the transmitted pulse is smaller than expected and it has also been noticeably broadened. Plot set (b) shows similar results as set (a) except that dispersion further complicates the results. Again, the reflected pulse is inverted and contains more high-frequency components than the transmitted pulse, which is not inverted.

Figure B.5 shows the temporal signals for the placement of the PCEs shown in Fig. B.4. Plot (a) shows the pulse generated by the PCE, which is also the response of the sampler. The pairs of plots (b) and (c) are the reflection and transmission signals, respectively. The solid curves are the actual voltages on the waveguide, while the dashed curves are the signals detected by the PCE. The dashed curves are what an experiment would measure. Pair (b) shows two separate peaks: The one at about 20 ps is from the pulse incident on the device, and the one at about 50 ps is the reflected pulse. Pair (a) shows the transmitted pulse.

In a real experimental situation, it is only the dashed curves of pairs (b) and (c) of Fig. B.5 that are measured, and plot (a) of the same figure is known from other measurements. From these it is possible to determine the vector s-parameters of the device which in an experimental situation are unknown. This is done by separating the reflection and incident peaks in plot (b) so that individual plots of the incident, reflected, and transmitted pulses are obtained. One can deconvolve the pulse response of the PCE out of this to obtain the solid curves of pairs (b) and (c). Note that in practice one does not completely obtain the solid curves because noise in the data requires a cutoff frequency for the deconvolution. From

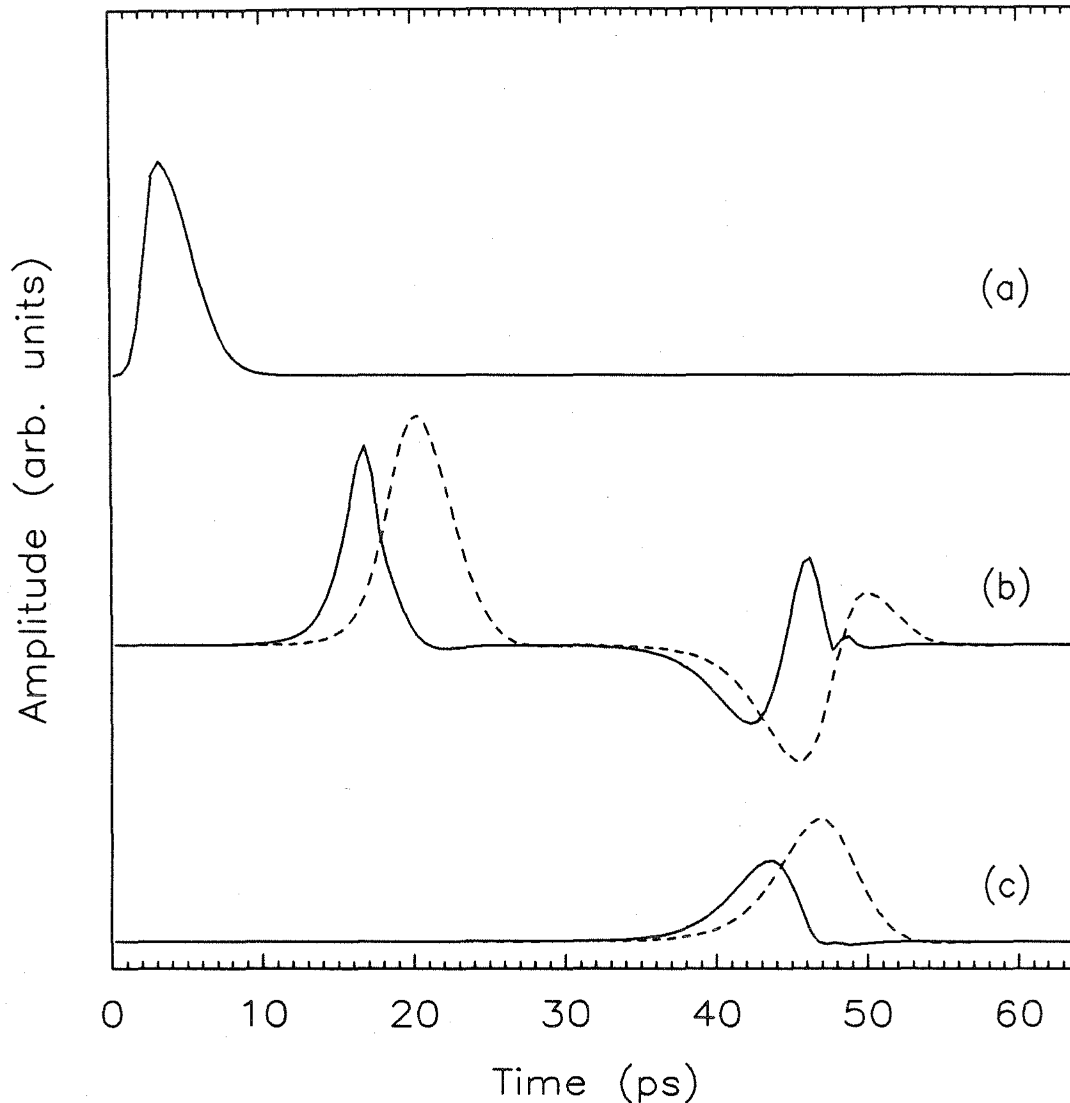

Figure B.5: Pulse on microstrip with a device II. The plot labeled (a) shows the pulse generated by the pulser PCE in Fig. B.4, and the two pairs of plots labeled (b) and (c) show the temporal voltage signals that would be detected by the reflection and transmission sampler PCEs, respectively, for the signals shown in Fig. B.4 for the thinned microstrip. The solid curves show the actual voltage on the waveguide at the sampling PCE, while the dashed curves show the signal measured, using a PCE whose response function is the same shape as the pulse generated by the pulser PCE.

the deconvoluted incident, reflected, and transmitted pulses the s-parameters are calculated by taking ratios of the Fourier components. By properly taking into account the distances between the PCEs and the device, the vector s-parameters are obtained. Figure B.6 shows the result of just such a calculation except that for ease of display only, the magnitudes of the s-parameters are displayed.

Plot (a) shows the frequency content of the incident pulse (the 3 dB point is about 100 GHz). The solid curves of pairs (b) and (c) show the s-parameters calculated using the signals and they are plotted with the dashed curves that are the s-parameters used in the simulation itself. The agreement up to about 400 GHz is good; above this, noise that is due to the sample spacing used in simulated movies and other sources becomes large and the deconvolution is not stable. This ssituation occurs where the spectral intensity of the incident pulse is about 3% of the peak intensity. In real experiments, noise in the data will probably produce problems in the deconvolution at a frequency of about 200 GHz.

B.5 Summary and Conclusions

In this appendix a computer model that simulates the behavior of ultrashort pulses on a waveguide with a device is described, and its implementation discussed. Examples of the simulations for simple cases are shown and discussed. From these examples for the simple passive device used, this model simulates the measurement of s-parameters using PCEs on waveguides successfully. The extension to active devices such as FET amplifiers should be straightforward.

This simulation program is useful because it can be used to determine the sensitivity of the measurements to different parameters in the experimental technique, such as the waveguide properties, the device packaging, and most importantly, the device characteristics. Thus, it aids in the development of the intuition required for

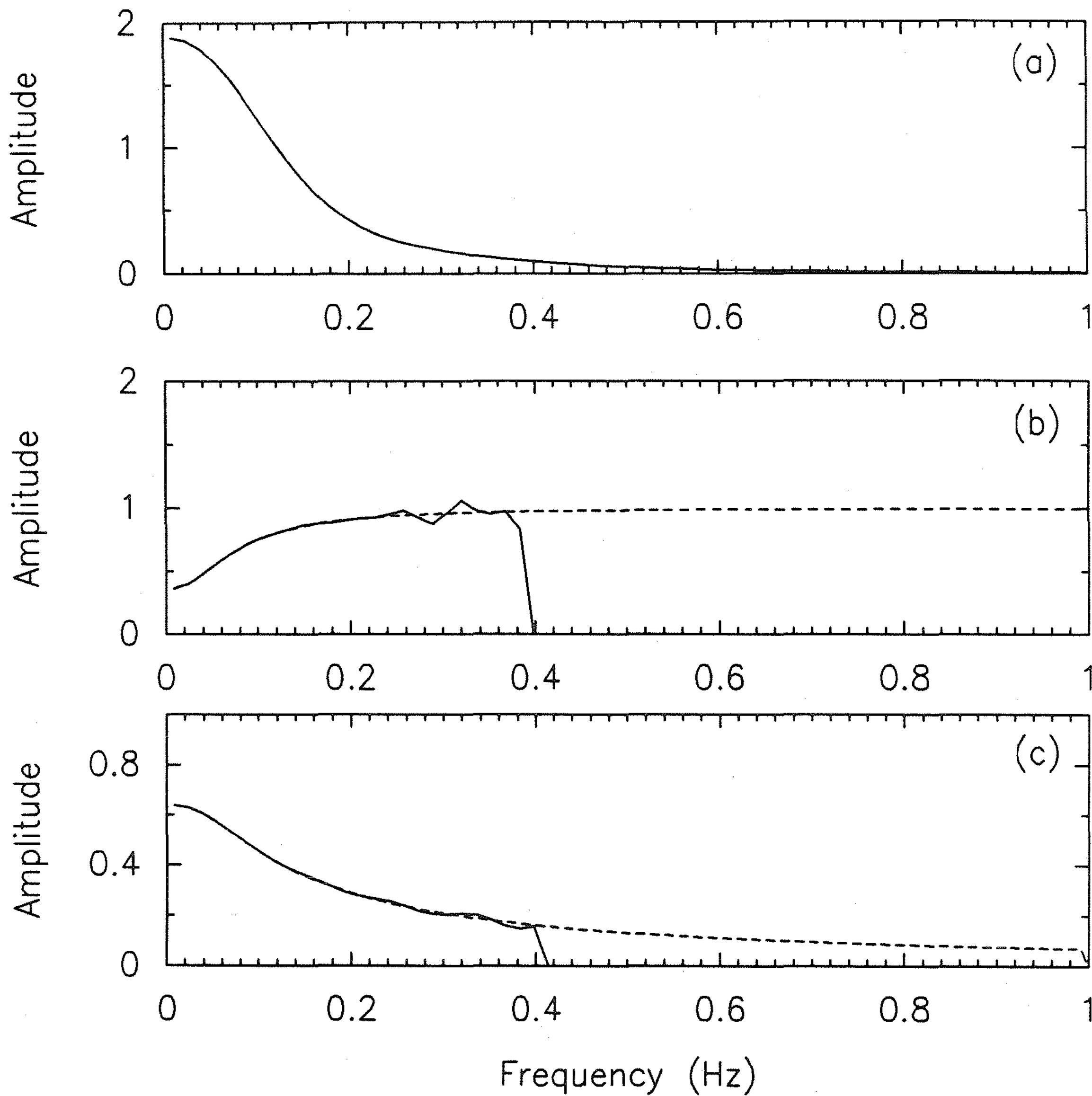

Figure B.6: S-parameters calculated from PCE signals. These plots show the results of the calculation of the S-parameters for the PCE signals shown in Fig. B.5. Plot (a) shows the frequency content of the pulse put on the stripline. The pairs of plots (b) and (c) show the calculation of the magnitude of the s-parameters S_{11} and S_{12}, respectively. The solid curves are the calculations from the PCE signals, while the dashed curves are the calculations from the characteristics of the device and the waveguide.

making s-parameter measurements of high-speed devices using this new technique.

References

1. D.E. Cooper, and S.C. Moss in *Picosecond Electronics and Opto-electronics*, edited by G.A. Mourou, D.M. Bloom, C.H. Lee (Springer series in Electrophysics 21, New York, 1985), pp. 62-65.

2. W.R. Eisenstadt, R.B. Hammond, D.R. Bowman, and R.W. Dutton, in *Picosecond Electronics and Opto-electronics*, edited by G.A. Mourou, D.M. Bloom, C.H. Lee (Springer series in Electrophysics 21, New York, 1985), pp. 66-69.

3. D.R. Bowman, in *High-Speed Polycrystaline Photoconductors for On-Chip Pulsing and Gating*, Ph. D. dissertation. Stanford University, Stanford, CA, June 1986.

4. J.D. Jackson, in *Classical Electrodynamics* (Wiley, New York, 1975).

5. S. Ramo, J.R. Whinnery, and T. Van Duzer, in *Fields and Waves in Communication Electronics* (Wiley, New York, 1984).

6. K.K. Li, G. Arjavalingam, A. Dienes, and J.R. Whinnery , IEEE Trans. Microwave Theory Tech. **MTT-30**, 1270 (1982).

7. K.W. Goosen, and R.B. Hammond, in *Picosecind Electronics and Optoelectronics*, edited by G.A. Mourou, D.M. Bloom, C.H. Lee (Springer series in Electrophysics 21, New York, 1985), pp. 70-73.

8. G. Hasnain, A. Dienes, and J.R. Whinnery, IEEE Trans. Microwave Theory Tech. **MTT-34**, 738 (1986).

9. E. Yamashita, K. Atsuki, and T. Ueda, IEEE Trans. Microwave Theory Tech. **MTT-34**, 738 (1986).

10. K.C. Gupta, R. Garg, and R. Chadha, in *Computer-Aided Design of Microwave Integrated Circuits* (Artech House, Dedham MA, 1981).

11. E.O. Brigham, in *The Fast Fourier Transform* (Prentice-Hall, Engelwood Cliffs, NJ, 1974).

12. D.E. Cooper, Appl. Phys. Lett. **47**, 33 (1985).

Appendix C

A Novel Growth Technique for HgTe-CdTe Heterojunctions

C.1 Introduction

This appendix describes a novel Hg-rich, liquid-phase epitaxy (LPE) technique used to grow HgTe on CdTe. The motivation for developing this technique was to grow HgTe-CdTe heterojunctions at a low temperature so that an estimate of the band offset in this heterojunction could be made. However, the growth technique was not entirely successful because the growth process was not easily controllable, and the layers grown were partially polycrystalline. Thus, definitive measurements of band offsets using these samples could not be made.

Band offsets are an important physical characteristic of any heterojunction. The HgTe-CdTe offset is particularly important because it affects the properties of the HgTe-CdTe superlattice, which has been proposed as an IR detector material.[1,2] Band offset measurements require an abrupt high-quality interface with limited interdiffusion between each material. These conditions necessitate a low-temperature technique to grow a HgTe epitaxial layer on CdTe. Conventional

Te-rich liquid-phase epitaxy (LPE) causes too much interdiffusion for a meaningful band offset measurement. The same may be true of metal-organic chemical vapor deposition (MOCVD), which can be done at 325 °C.[3] To date the lowest temperature growth technique has been molecular beam epitaxy (MBE) which grows in the range 120 to 200 °C with best epitaxy near 200 °C.[4] Below is a description of the novel Hg-rich LPE technique, which also utilizes growth temperatures in the range 125 to 200 °C.

C.2 Apparatus and Procedure

The Hg-rich LPE technique consists of cleaving a CdTe crystal in a Hg melt supersaturated with Te. Growth then takes place on the freshly cleaved (110) planes. The apparatus used for the *in situ* cleave is shown in Figure C.1 and consists of an outer container, a middle sleeve, and an inner cleaver guide and sample holder. All Hg-wetted parts are quartz except for the cleaver, which is a sapphire rod polished to a knife edge. The outer container contains the Hg melt (typically a 2" depth of Hg). The inner sleeve has holes that allow the Hg-melt inside, but are small enough to prevent the samples from falling out. This arrangement provides for the removal of the samples from the melt from after growth. The inner cleaver guide allows the CdTe to be clamped in position with the cleaver resting in a notch in the CdTe. The CdTe substrates are n-type and have a cross section of about 2×3 mm. They are notched along the top in a line parallel to the (110) cleavage plane to allow the cleaver to be properly aligned on the sample and to help initiate the cleave. The cleave is made by increasing the pressure on the cleaver from above with a press. Heating of the melt was achieved either by standing the quartz ware in an oil bath or by heating tape wrapped around the quartz ware. The temperature was measured with a thermocouple

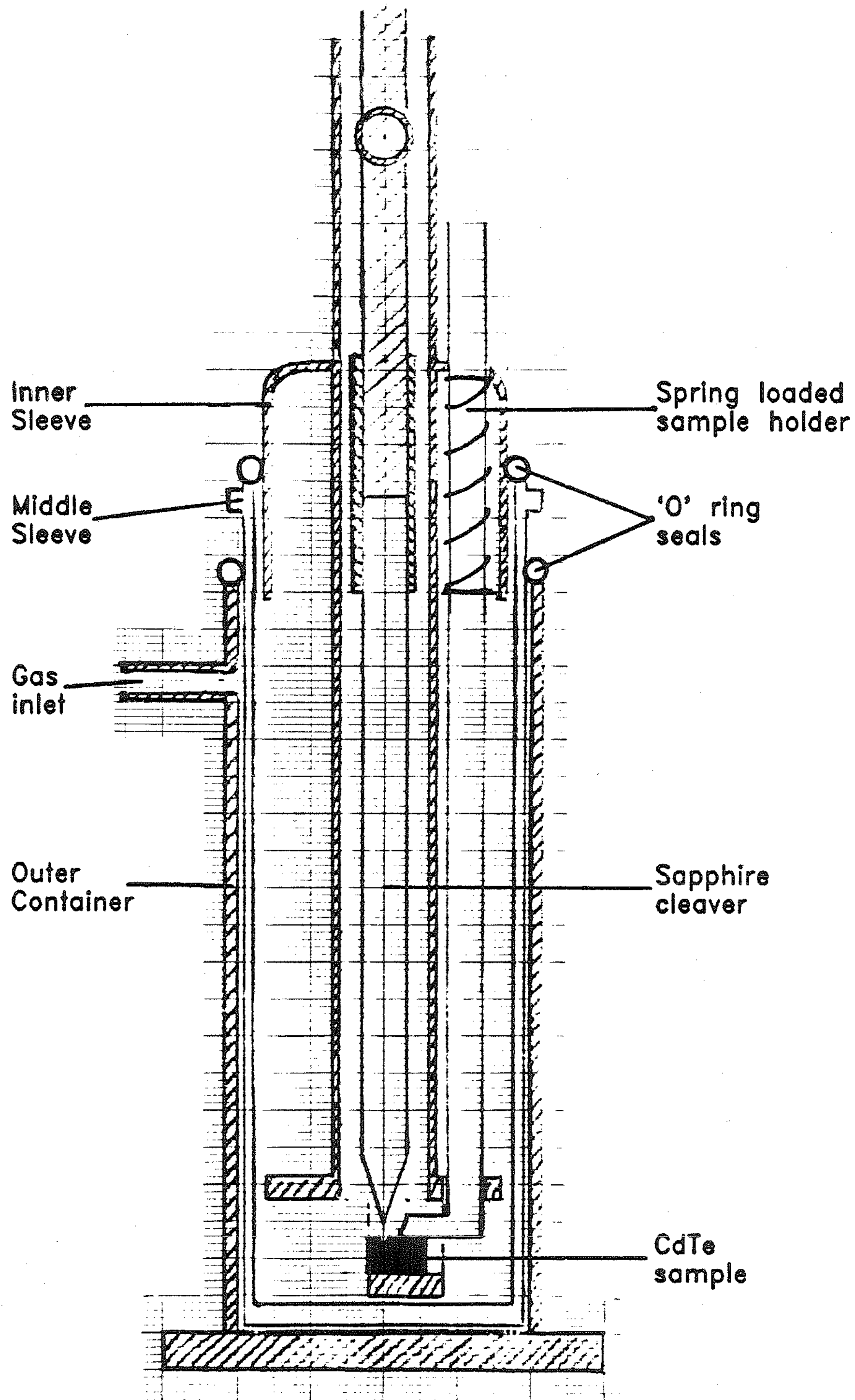

Figure C.1: This shows the engineering drawing of the *in situ* cleaving apparatus. The apparatus as shown is actual size.

placed next to the outer container adjacent to the Hg melt. The temperature of the Hg-melt is probably quite uniform because of convection mixing within the melt. A forming gas of 14% H_2 in He flows over the melt at all times to prevent atmospheric contamination. Furthermore, because Hg is involved, the whole experiment is performed in a glove box purged with N_2 gas and the glove box is in a fumehood. Many different growths could be performed with the same Hg melt because the freshly cleaved samples could be retrieved from the melt by removing the middle sleeve.

The Hg in the melt is high-purity triple-distilled Hg, and the Te to make the melt Te-rich is 99.999% pure. By extrapolation of the data in Ref. 6, the solubility of Te in Hg at 200 °C is 650 ppm and it decreases to 20 ppm at 100 °C. It is this decrease in the solubility that drives the crystal growth process.

Two growth procedures were used. The first involved heating the Te-saturated Hg-melt to a temperature of approximately 230 °C. After sufficient time for the melt to reach equilibrium, the temperature was reduced by 30 °C. Then the CdTe was cleaved and the melt allowed to cool down further at a rate of about 5 °C/min. When the melt temperature was 100 °C the freshly cleaved samples were taken out of the melt. The second growth procedure involved cleaving the crystal at the saturation temperature and then allowing the melt to cool at a rate of 2 °C/min for 20 °C, at which time the samples were taken out.

C.3 Results

Using the first procedure, growth was achieved for cleaving temperatures in the range 125 to 200 °C, with the best growth at the higher temperatures. The HgTe epitaxial layer was always striated. These features were caused by adjoined crystals approximately 1 μm wide by 1 μm thick and often 100 μm long, aligned along

the $[\bar{1}10]$ direction. The growth tended to nucleate at steps in the cleavage plane. The grown layers have been chemically analyzed using energy-dispersive x-ray spectrometry (EDS) and were found to be HgTe within the limits of this technique. The crystallinity has been investigated using double-crystal x-ray diffraction. Rocking curves show the appearance of a satellite peak that would correspond to the epitaxial HgTe layer, which has a .3% lattice mismatch with the substrate. However, results from Read camera x-ray diffraction studies indicated that the grown films are partly polycrystalline. Furthermore, ion channeling showed a 50% dechanneling rate, indicating that the HgTe layer was far from perfect.

The second growth procedure produced nonstriated growth. X-ray rocking curve measurements indicated a thin strain-relieved HgTe layer. EDS did not show the presence of HgTe; however, this absence could be because of the lack of surface sensitivity of this technique. This growth procedure was not investigated further.

Electrical measurements were taken from Schottky diodes made with the striated samples. These measurements consisted mainly of current-voltage *(I-V)* characteristics, which were not found to be completely thermionic in character. At elevated temperatures such as 350 K, the *I-V* measurements indicated a barrier of 0.73 eV with a quality factor of 1.25. These results are thermionic in character and are within the range measured by Kuech and McCaldin in Ref. 3 for MOCVD samples. However, at lower temperatures the measured barrier height became smaller and the quality factor increased, suggesting that other transport mechanisms dominate thermionic emission at the lower temperatures. It is possible that trapping defects at the heterojunction interface are responsible for the low-temperature *I-V* characteristics. Further electrical measurements were not pursued with these samples.

C.4 Summary and Conclusions

The novel *in situ* cleaving LPE technique did give low-temperature growth of HgTe on CdTe. However, the growth process was difficult to control and the resultant layers were partially polycrystalline. Furthermore, *I-V* measurements taken from Schottky diodes on these samples were not thermionic in character and indicated the presence of traps at the interface. Thus, the samples grown by this technique could not be used to measure the band offset at this heterostructures.

Since the time of this work, there have been various new measurements of the band offset for MBE-grown HgTe-CdTe heterostructures. For example, Chow *et al.* in Ref. 7 measured the band offset by looking at the thermionic current across single barrier HgTe-CdTe-HgTe structures. These measurements give a temperature-dependent valence-band offset, which at 300 K is 390 ± 75 meV.[7]

References

1. J.N. Schulman and T.C. McGill, Appl. Phys. Lett. **34**, 663 (1979).

2. G.Y. Wu, C. Mailhiot and T.C. McGill, Appl. Phys. Lett. **46**, 72 (1985).

3. T.F. Kuech and J.O. McCaldin, J. Appl. Phys. **53**, 3121 (1981).

4. J.P. Faurie, A. Million and J. Piaguet, Appl. Phys. Lett. **B 1 (41)**, 713 (1982).

5. Y. Guldner, G. Bastard, J.P. Vieren, M. Voos, J.P. Faurie and A. Million, Phys. Rev. Lett. **51**, 907 (1983).

6. A. Pajaczkowska, and E.Z. Dziuba, J. Crystal Growth **11**, 21 (1971).

7. D.H. Chow, J.O. McCaldin, A.R. Bonnefoi, T.C. McGill, I.K. Sou, and J.P. Faurie, Appl. Phys. Lett. **(51)**, 2230 (1987).

Appendix D

Equipment

D.1 Introduction

This appendix lists details, such as manufacturer's name and part number (PN), of the elements used to construct the apparatus described in this thesis. The apparatus described includes: (1) the CPM laser with optics and dye/absorber pumps; (2) the various diagnostic tools, especially the autocorrelator; and (3) the PECS apparatus. The appendix is in three sections, one for each of the pieces of equipment listed above. For each piece of equipment a figure is shown followed by a table listing the details of the equipment. The purchase order (PO) number, when listed refers to an indexed set of PO copies for elements purchased specifically for this project; these POs contain further details.

D.2 CPM Laser

See Chapter 2 for details of what each element is, and a description of how the laser works. The detailed drawing of the laser is reproduced in Fig. D.1. The CPM laser is constructed on a $2' \times 4'$ breadboard on top of a full-sized optical

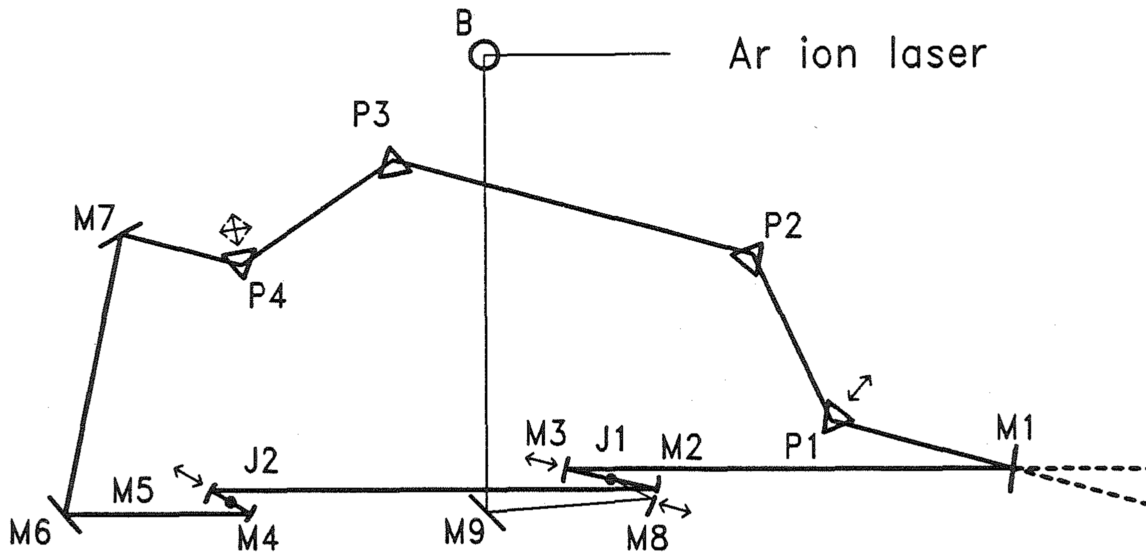

Figure D.1: Detailed configuration of compensated CPM laser. See Table D.1 for description of elements.

table. This allows holes to be drilled at positions J1 and J2 for these jets to drain easily. It is very important that all the optical elements be very securely mounted, because small vibrations of these elements can cause noise in the CPM output power. Table D.1 lists the elements of the laser, their manufacturers and part numbers and a brief description. Figure D.2 shows the block diagram of the dye/absorber pump systems. It is important to design the system so that the solutions can be easily changed. The collection of the solution below the jet is critical to the laser's stability; frothing must be minimized. Table D.2 lists the elements, their manufacturer and part number and a brief description.

D.3 Diagnostic Tools

Figure D.3 is a schematic diagram showing the various tools used to diagnose the CPM laser. Table D.3 lists the equipment used. Figure D.4 shows the colinear

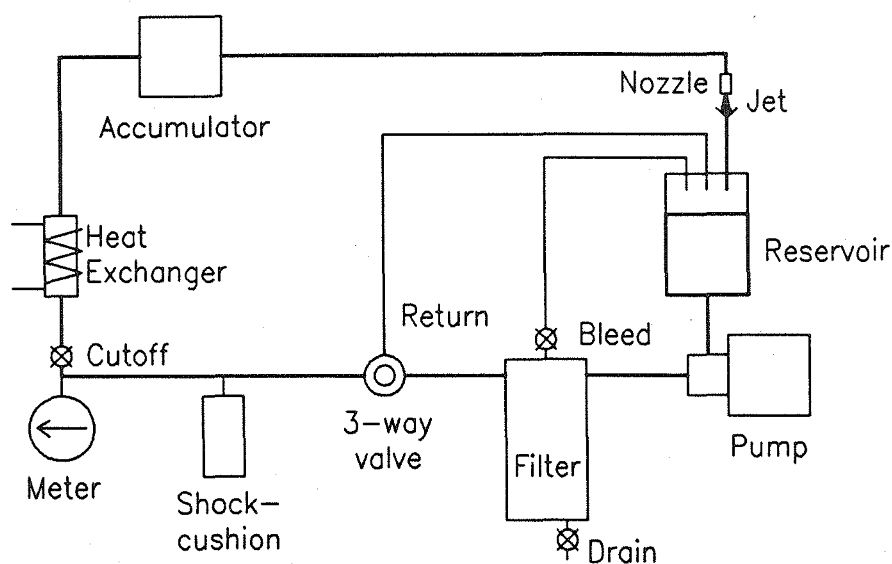

Figure D.2: Pump System. Schematic diagram of the absorber/dye pump systems. See Table D.2 for description of elements.

autocorrelator used for real-time determination of pulse shape, and Table D.4 lists the elements of the autocorrelator.

D.4 PECS Apparatus

Figure D.5 shows the schematic of the PECS apparatus and Table D.5 lists the elements used to construct this apparatus.

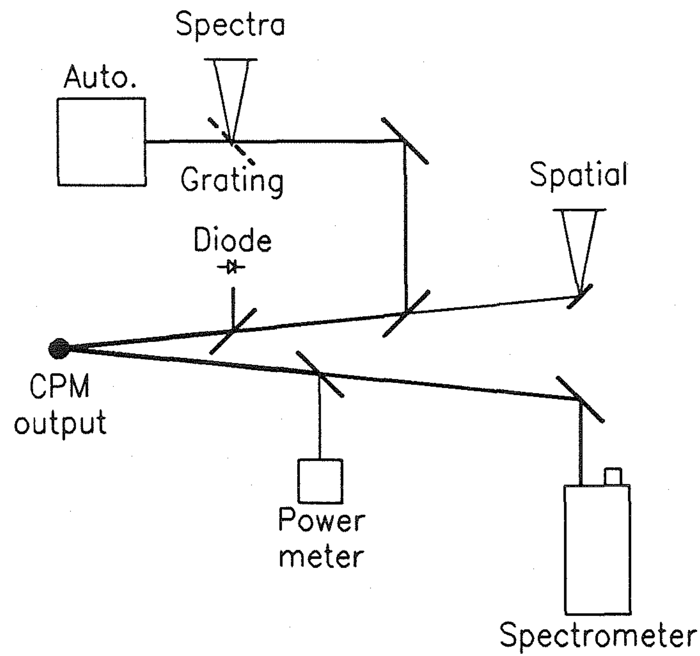

Figure D.3: Block diagram showing the tools used to diagnose the CPM laser.

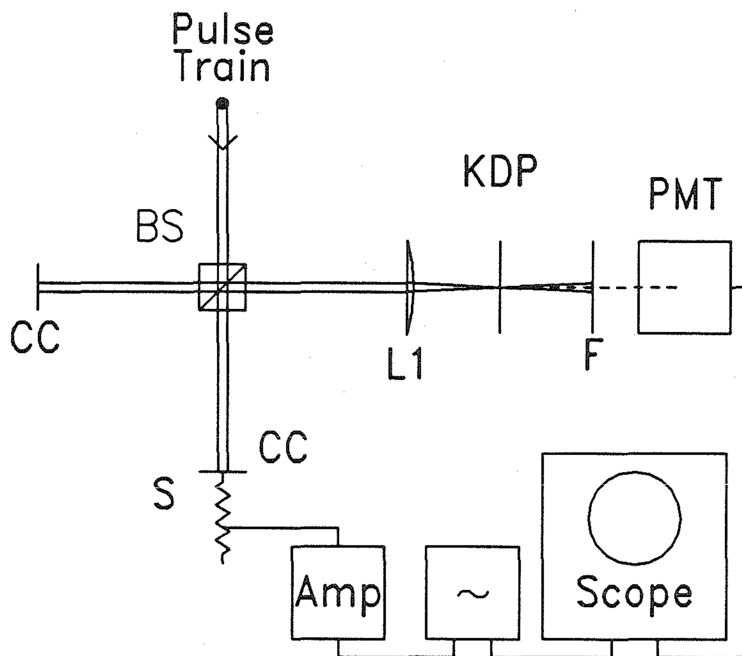

Figure D.4: Schematic diagram of the collinear autocorrelator used to make real-time autocorrelation measurements.

Table D.1: Details of Compensated CPM Laser.

Element	Supplier and Part Number	Description	P.O.
Ar laser	Coherent I-20UV		0-1
B	NRC 675 Beam Steerer	with 13E20BD.1 mirrors	II-1
Mi	Mounts: Klinger SL-50-BD	for all except M8	II-2
	Mounts: NRC MFM-075	for M8	G-29
	Trans: Klinger MR-80-25	where indicated	II-2
M1	CVI 2 or 3% Output coupler	1"×3/8", flat	G-23
M2-3	CVI 10 cm He-Ne H.R.	1/2"×3/8"	G-23
M4-5	CVI 5 cm He-Ne H.R.	1/2"×3/8"	G-23
M6-7	CVI flat He-Ne H.R. at 45°	1/2"×3/8"	G-23
M8	CVI 10 cm for 514.5 nm Ar	1/2"×3/8"	G-23
Ji	Mounts: Klinger MR50	xyz stage	II-2
J1	Coherent 0406-224-02	stock s.s. nozzle	I-9
J2	Coherent 0406-224-02	thinned s.s. nozzle	I-9
Pi	Mounts: Klinger P046	prism mounts	G-24
	Trans: Klinger MR50.16	trans. stages	G-24
P1-4	Spectra-P. G0044-000	Brewster angle prisms	G-26

Table D.2: Details of Dye/Absorber Pump Systems.

Element	Supplier and Part Number	Description	P.O.
Reservoir		s.s. beaker	0-1
Pump	Tuthill 9012	gear pump	I-1
Pump	Bodine 276/901	motor/controller	I-2
Filter	Acro-flow 12550	.8 μm filters	I-3
Valves	Whitey SS-1GS4	s.s. toggle valves	I-13
3-way valve	Cashco 1171-22-61	s.s. reg. valve	I-5
Shock-Cushion	Grees-Alaer 812-954	pulsation dampener	I-4
Meter	Marsh Gauge J8848	brass 0-100 psi	I-6
Heat-	Homebuilt	s.s. ball bearings	
exchanger	Neslab RTE-9B	recirculator	I-8
Accumulator	Spectra-P. 372B	for streamlined flow	I-11

Table D.3: Details of CPM Diagnostic Tools.

Element	Supplier and Part Number	Description	P.O.
P. meter	Spectra-P. 404	broadband	I-11
Diode	EG&G FND-100	high-speed diode	
Spatial	concave mirror		
Grating	Ealing E-O 36-4323	1200 l/mm vis. blaze	G-28

Table D.4: Details of Autocorrelator.

Element	Supplier and Part Number	Description	P.O.
B.S.	Opt. for Res. SCL-15	beam-splitter cube	II-7
Shaker	Ling Elec. 203B	shaker unit	II-3
	Trans-Tek 0240-0000	trans. transducer	G-14
Lens	Opt. for Res. L-25-51	visible lens f=51 mm	II-7
KDP	Cleveland Crystal	Q1XA10-KDP-I-57.7-620-C	II-5
Lens	Opt. for Res. LU-25-51	uv-lens f=51 mm	II-7
Filter	Schott Opt. UG-11	uv-pass filter	II-6
PMT	Hammamatsu 1P28	uv sensitive	G-9
	Pac. Int. 3150RF	PMT housing	G-9
	Kepco APh 2000M	PMT power supply	G-9
Osc.	Tektronix FG 501A	function generator	III-3
Amp	Radio-Shack 322024	PA amplifier	G-10

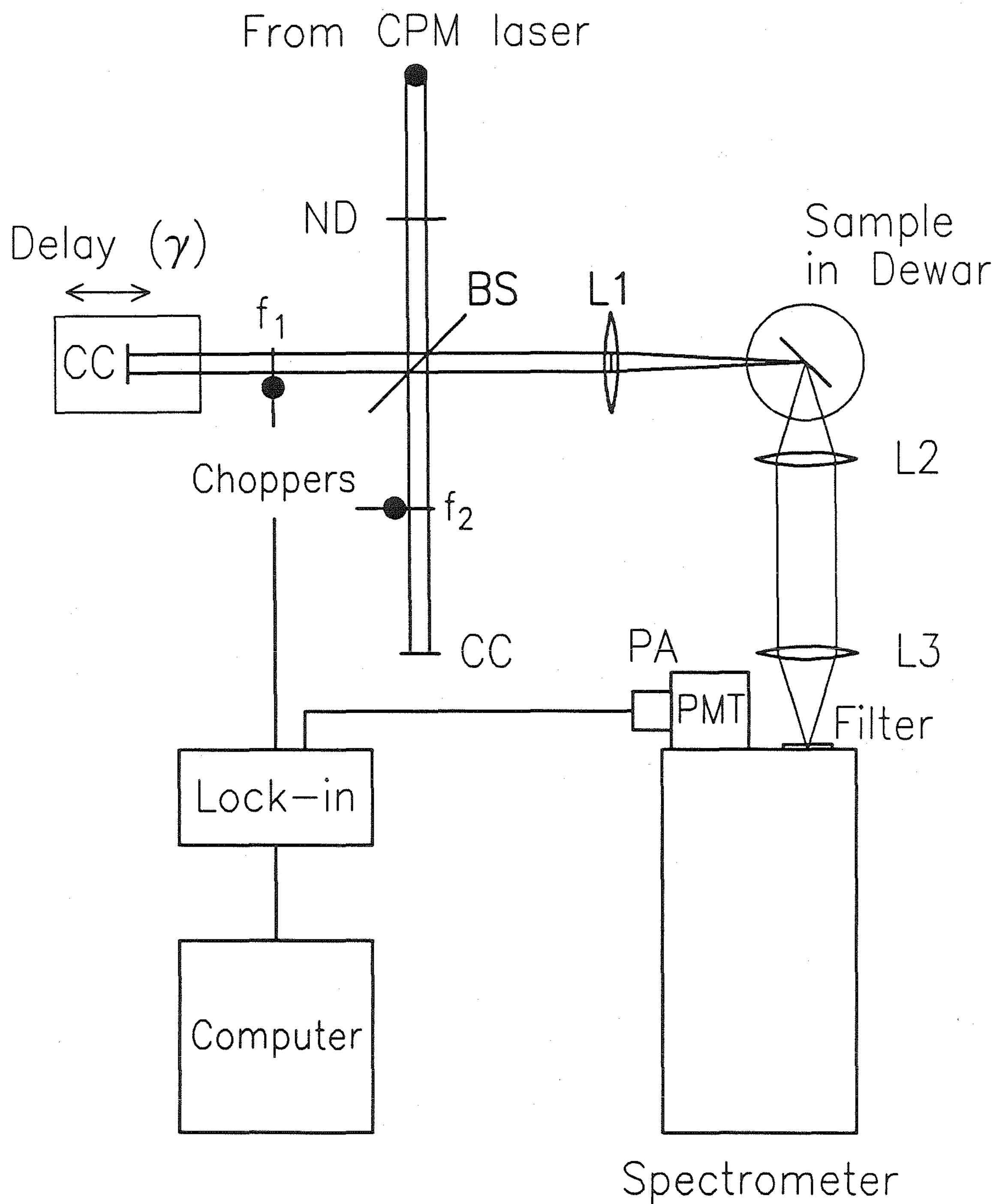

Figure D.5: Schematic of the photoluminescence excitation correlation spectroscopy apparatus. See associated table for description of elements.

Table D.5: Details of PECS Apparatus.

Element	Supplier and Part Number	Description	P.O.
ND	NRC 50G00-AV.2	attenuator disk	G-11
BS	Opt. for Res. MS-25P-615.0	beam-splitter plates	G-12
Choppers	PAR Model 125A	48 slot blade	II-4
CC	Opt. for Res. AC-38	corner cube	II-7
Delay	Klinger MT-160	stepper-motor stage	II-2
	Klinger CC-1.1	programmable controller	II-2
L1		f=150 mm lens	
Dewar 1	JANIS DT-8	stationary dewar	
Dewar 2	TI cold finger	moveable dewar	
	NRC 850-2"	translation actuators	
	NRC 855C	programmable controller	
L2,L3	f=120, 300 mm	collection lenses	
Filter	Melles-Griot 709		
Spect.	SPEX	double pass	
PMT	RCA GaAs	at -20 °C	
PA	Ithaco 1211	current preamp	
Lock-in	EG&G 5301	digital lock-in	
Comp.	HP 9836C	with IEEE interfaces	0-2

Appendix E

Variations of Photoluminescence and Lifetime with Laser Dose

E.1 Introduction

The band-to-band PL intensity and the carrier lifetimes measured using PECS for In-alloyed GaAs are found to vary with incident-pulsed laser-exposure time. Moreover, this variation depends on the incident-power density, the sample temperature, and the substrate surface preparation. Similar variations have been observed by other researchers.[1] The variations observed in this work are not found to be simple, and the details of why they occur are not completely understood. The intent of this appendix is to outline the extent of these variations, give some possible explanations for them, and describe the measures taken to reduce their effects.

The appendix is organized into four sections: The experimental section describes the apparatus, samples, and experimental procedures; the results section describes the experimental results for a series of five experiments; the discussion section discusses the results; and finally, the summary section summarizes the ap-

pendix and explains how the effects investigated in these experiments affect the work of Chapter 4.

E.2 Experimental

The experimental apparatus used in this appendix is identical to that described in Chapter 4. In particular, the translatable cold-finger dewar was operated so that the sample was in a vacuum with a pressure estimated to be less than 20 μTorr.

The In-alloyed GaAs samples used were annealed after growth at about 800 $^{\circ}$C for 30 min.. During the anneal the wafers were encapsulated in SiO_2. Annealed samples rather than as-grown samples were used because the annealed samples have a much more uniform band-to-band PL response over their surface. This uniformity reduces the importance of exact positioning of the analyzing laser spot.

The samples were analyzed with and without a surface passivation layer. The surface without the passivation layer was lightly etched to remove any surface oxide before analysis. The surface passivation was the same sodium sulfide passivation layer used in Chapter 4.[2] This was spun on the sample after a light etch of the surface to remove any oxide. In experiment III, 500 Å of the top surface was removed using an etch in $H_2O : H_3PO_4 : H_2O_2$ in the ratio 50 : 3 : 1 for 36 s.

All of the optical analysis was done with the CPM laser described in Chapter 2. In these experiments the characteristics of this laser were the same as when the laser was used in Chapter 4. The variation of PL intensity with laser exposure time was measured by moving the laser spot used in the PECS experiment to an unexposed surface, and monitoring the variations of the intensity of the peak of the band-to-band PL spectra with time. The variation of carrier lifetime with laser exposure time is measured by continually making PECS delay-time scans on the peak of the band-to-band PL spectra, while the laser remains incident on the

sample. The lifetime from one side of such a scan is then the lifetime averaged over the time taken for one-half of a full delay-time scan. A full scan took 40 s, so that the lifetime measured is an average of the lifetime over 20 s. The position of the analyzing spot on the sample could be reproduced even after repreparing the surface. This was achieved by repositioning the sample using a scribe mark on surface of the sample. This positioning technique was also used in Chapter 4.

E.3 Results

The results from five different experiments are listed below under separate headings.

I PL Intensity versus Exposure Time.

Figure E.1 shows the band-to-band PL intensity versus incident-laser exposure time. This figure shows that the size and direction of the band-to-band PL intensity variation depend on sample temperature and surface preparation. For the unpassivated surface: at 300 K the PL signal increases, while at 80 K the PL signal decreases. For the passivated surface: at 300 K the PL signal decreases, while at 80 K the PL signal increases. These curves are for a laser-pulse energy of 12 pJ. For an unpassivated surface at lower pulse energies, the direction of PL intensity variation is the same. However, the rate of variation is reduced as the pulse energy is reduced, until, for a pulse energy of 0.4 pJ, no variation is observed.

II Irreversibility of PL Variation.

The changes in the PL intensity for the unpassivated surface at 300 K were found to be irreversible. If the exposure was interrupted for periods of several minutes, no change in the PL intensity took place during the interruption. Even after several days the PL signal enhanced from an exposure

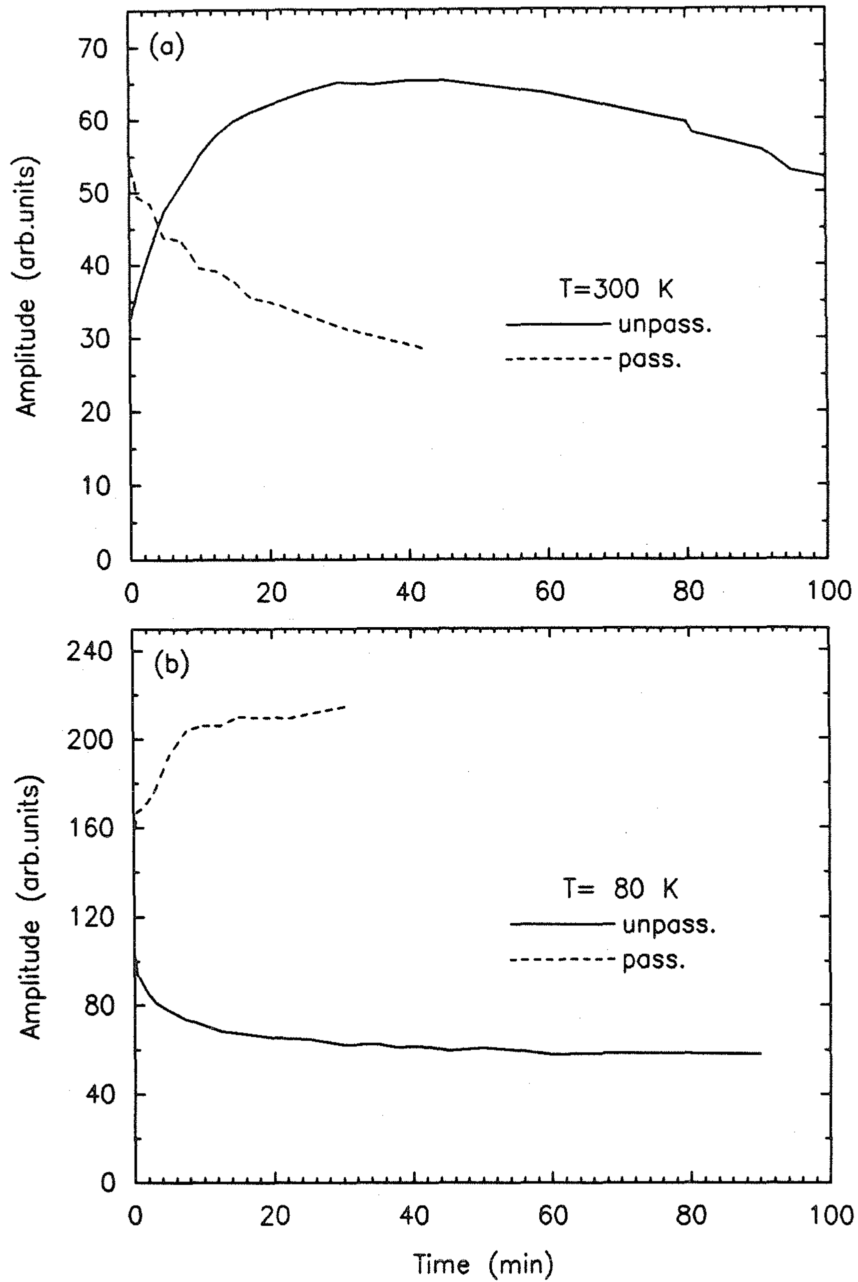

Figure E.1: PL intensity versus exposure time. These two graphs show the band-to-band PL intensity versus the laser exposure time. Plot (a) shows curves for sample temperature, T=300 K, and plot (b) shows curves for sample temperature, T=80 K. The solid curves are for an unpassivated surface, and the dashed curves are for a passivated surface. The incident-pulse energy was 12 pJ per pulse.

of one hour remained unchanged.

III Etching Top Layer of Exposed Surface.

After exposing an unpassivated sample to the incident laser at 300 K for one hour, the PL intensity increased by a factor of two at the position of analysis. However, after the top 500 Å were etched off the surface of the sample, the previously exposed spot was found to have a PL signal that was not enhanced. Thus, the PL intensity enhancement disappeared when the top surface was etched.

IV Lifetime Variation with Exposure Time.

Figure E.2 shows the carrier lifetime versus exposure time for the unpassivated surface at 80 K, and at 300 K. For comparison, along with this, there are plots of PL intensity versus exposure time. The scale of the corresponding PL intensity plot was chosen so that the curve overlapped the lifetime measurements. The plots show that at 80 and 300 K the lifetime and PL intensity are remarkably similar in their behavior with exposure time.

V Initial Lifetimes.

Figure E.3 shows the lifetime measured at two different positions shortly after the initial beam exposure for both an unpassivated and a passivated surface at 80 K and 300 K. The figure shows that the measured lifetime at 80 K is not affected by the passivation surface, while the lifetime at 300 K for the passivated surface is the same as the lifetime at 80 K and the lifetime at 300 K for the unpassivated surface is reduced by nearly a factor of two for positions (a) and (b).

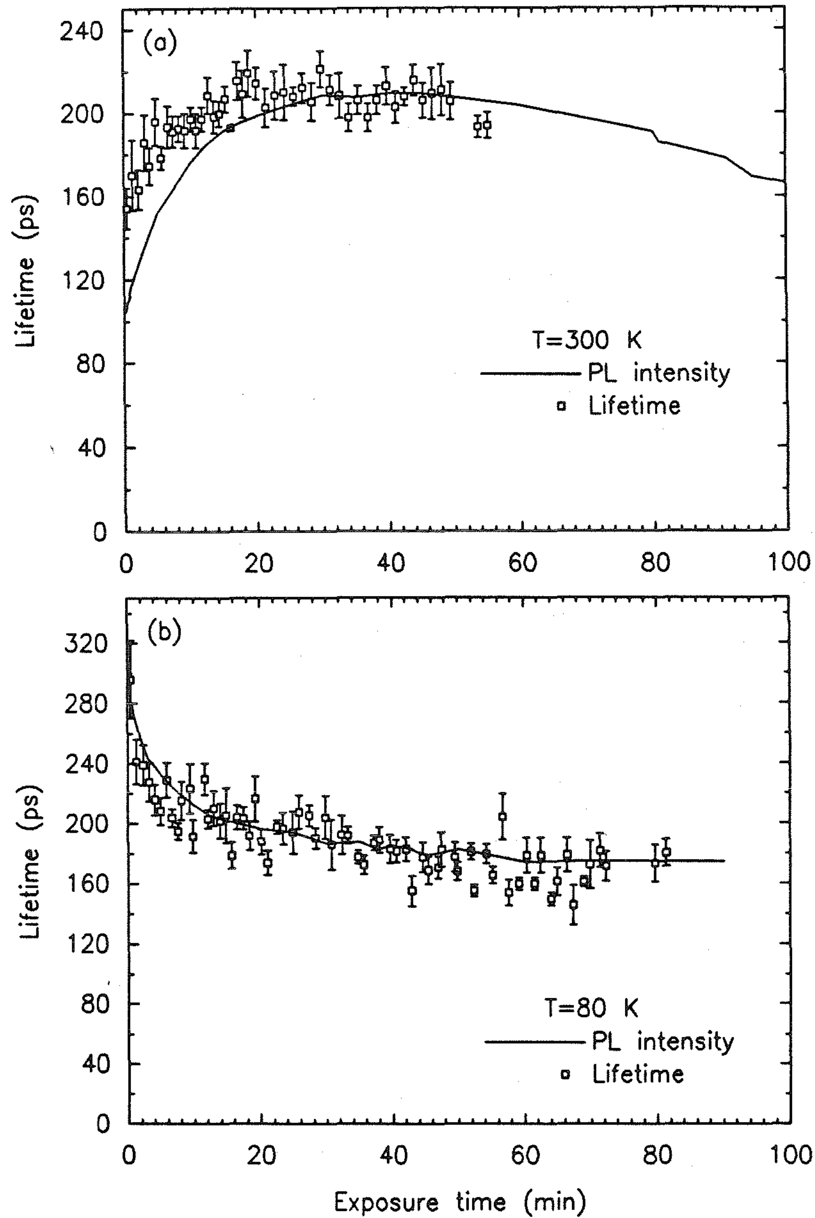

Figure E.2: Lifetime versus exposure time. These two graphs show the carrier lifetime versus the laser exposure time. Plot (a) shows lifetimes for a sample temperature of T=300 K, and plot (b) shows lifetimes for a sample temperature of T=80 K. The lifetimes are shown with unfilled squares, along with error bars. Also shown are the PL intensity versus exposure-time curves for the corresponding temperatures and surfaces. These are scaled to overlap the lifetime data.

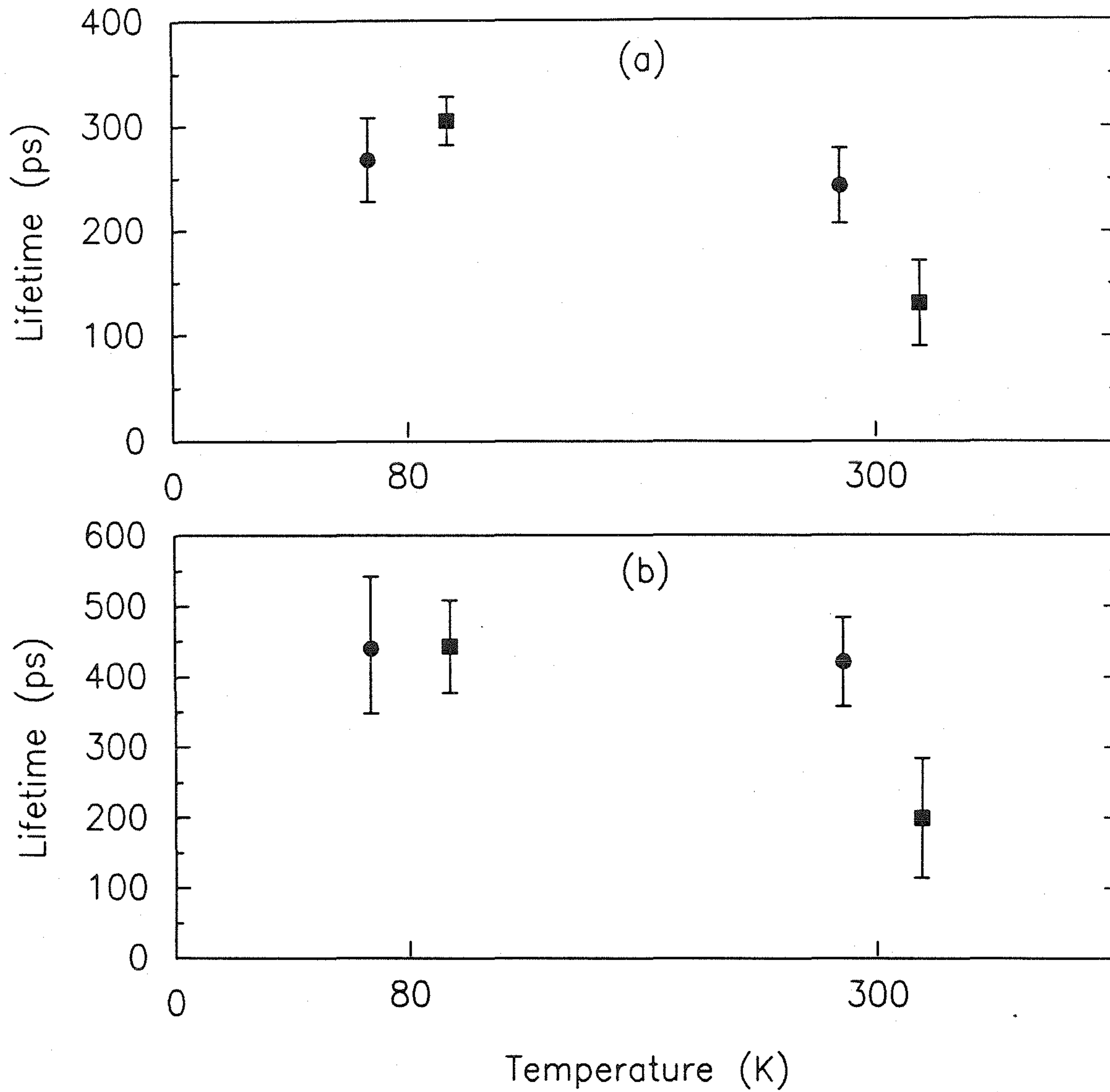

Figure E.3: Lifetimes at 80 and 300 K for passivated and unpassivated surfaces. These two graphs show carrier lifetimes at two different positions. The position in plot (a) corresponds to a smaller PL intensity than that in position (b). The squares mark the points for the unpassivated surface, while the circles mark the points for the passivated surface. The separation of the points along the temperature axis is for clarity of display only; the actual sample temperatures were 80 K and 300 K. The laser-pulse energy was about 4 pJ per pulse.

E.4 Discussion

The implications of the five experiments described above are discussed in this section.

The similarity of the plots of lifetime and PL intensity versus exposure time, shown in Fig. E.2, indicate that the variation of PL intensity results from the variation in the carrier lifetime as measured by PECS. The PL intensity variation follows the lifetime variation because the samples have carrier lifetimes that are dominated by non-band-to-band radiative recombination, such as trapping and surface recombination. For such samples, the band-to-band radiative recombination intensity is proportional to the carrier lifetime measured by PECS, as shown in Eqn. 3.11 of Chapter 3. Thus, the variation in PL intensity is due to the variation in the electronic properties that govern the carrier lifetime of the sample.

The lifetime measured by PECS is affected both by bulk traps and by surface recombination. Using τ_b and S_0 as the bulk lifetime and surface recombination velocity, respectively, then

$$\tau_b = \frac{1}{N_t \sigma_t v_{th}} \quad \text{and} \quad S_0 = N_s \sigma_s v_{th},$$

where N_t and σ_t, and N_s and σ_s are the density and capture cross section of the bulk and surface traps, respectively, and v_{th} is the thermal velocity of the carriers. Moreover, band-bending at the surface acts to reduce the number of electrons and holes that reach the surface.* This reduces the surface recombination velocity through

$$S = S_0 e^{-|\phi|/kT},$$

where ϕ is the amount of band-bending at the surface and S is the effective surface

*Although the samples are semi-insulating the laser pulse creates electron-hole plasma with density of about 10^{17} cm^{-2}, which results in band-bending within the absorption depth $\alpha = 0.25$ μm.

recombination velocity.[3] If the lifetime is dominated by bulk properties, then $\tau_{PL} = \tau_b$, where τ_{PL} is the lifetime measured by the PL signal. If the lifetime is dominated by surface properties, then τ_{PL} increases for a decrease in S and decreases for an increase in S. See Ref. 4 for the details of the dependence of τ_{PL} on S. The relative effect of bulk and surface recombination depends on the absorption depth of the incident radiation and the ambipolar diffusion length of the carriers. For these samples, the diffusion length, L, for lifetimes of 200 ps, are in the order of 1 μm, and the radiation absorption depth, α, is about 0.25 μm. Because L is greater than α, the contribution of surface recombination may be large.

Experiment III for an unpassivated surface shows that etching off the top 500 Å returns an exposed surface to its previously unexposed state, thus directly showing that the increase in PL intensity and lifetime at 300 K is a surface effect rather than a bulk effect. It is reasonable that the same is true at 80 K for an unpassivated surface and at 80 and 300 K for a passivated surface. It is unlikely that these variations are a result of the ambient atmosphere interacting with the surface, such as laser-assisted adsorption of molecular species on the surface, because the experiments were done in vacuum, and similar variations are observed with a 1 μm thick passivation layer. The increase in lifetime seen at 300 K for the unpassivated surface indicates either that defects at the initial surface are annealed out, or that the bands bend as the result of the creation of other surface defects. The latter explanation is more convincing. The results of experiment II shows that these changes in the surface properties are stable. The different behavior of the PL intensity at 80 and 300 K for the unpassivated surface indicates either that different defects are being created, or that traps are behaving differently at 80 and 300 K. The differences between the PL intensity behavior for the passivated and unpassivated surfaces indicate that the surfaces behave differently with the passivation layer present. This behavior may be due to the passivation layer's

reducing the density of surface states or repinning bands at the surface.

Figure E.3 indicates the importance of surface recombination at 80 and 300 K for the unpassivated and passivated surfaces. Because these lifetimes were measured shortly after laser exposure started with pulse energies of 4 pJ, these lifetimes are for a surface that has not yet been affected by the laser exposure.* Fig. E.3 shows that at 80 K the surface passivation has no effect on the lifetime measured, so that surface recombination is initially not important at 80 K. However, Fig. E.3 shows that at 300 K the surface passivation has a large effect on the lifetime measured. The strong dependence of the surface recombination on temperature may be due to various factors: First, since $v_{th} \propto (kT)^{\frac{1}{2}}$, S_0 is smaller at 80 K than at 300 K; second, band-bending reduces the surface recombination velocity by $\exp(-|\phi|/kT)$, which is a larger reduction at 80 K than at 300 K; finally, σ_s and N_s may also change with temperature, although the nature of this effect is probably small.

E.5 Summary

In summary, the variation of PL intensity with incident exposure results from the variation of surface recombination velocity, which affects the carrier lifetime. The variation of the surface recombination velocity probably takes place through the creation, by laser damage, of trapping defects at the surface, and through the bending of the electronic bands resulting from these traps. Such a mechanism explains both the increase and decrease in the PL intensity and carrier lifetimes with laser-exposure time, which are experimentally observed. For lifetimes measured after small exposure times, it is found that at 80 K the lifetimes are dominated by bulk capture with and without the surface passivation layer, while at 300 K the

*These are the same conditions for which the lifetime data of Chapter 4 were taken.

lifetimes for passivated surfaces are dominated by bulk capture, and the lifetimes for unpassivated surfaces have a large contribution from surface capture.

These conclusions imply that for the work of Chapter 4, where bulk rather than surface properties are of interest, it is important, especially at 300 K, to use the surface passivation. Moreover, lifetime measurements should be made at previously unexposed areas of the samples. These procedures were used in Chapter 4.

References

1. M.Y.A. Raja, S.R.J. Brueck, M. Osinki, and J. McInerney, Appl. Phys. Lett. **52**, 625 (1988).

   R.S. Besser, and C.R. Helms, Appl. Phys. Lett. **52**, 1707 (1988).

   H.J. Hovel, and D. Guidotti, IEEE Trans. Electron Devices **ED-32**, 2331 (1985).

   D. Guidotti, E. Hasan, H.J. Hovel, and M. Albert, Appl. Phys. Lett. **50**, 912 (1987).

2. E. Yablonovitch, R. Bhat, J.P. Harbison, and R.A. Logan, Appl. Phys. Lett. **50**, 1179 (1987).

3. C.J. Sandroff, R.N. Nottenburg, J.-C. Bischoff, and R. Bhat, Appl. Phys. Lett. **51**, 33 (1987).

4. M.S. Tyagi, J.F. Nijs, and R.J. Van Overstaeten, Solid-State Electron. **25**, 411 (1982).

   D.E. Ioannou, and R.J. Gledhill, J. Appl. Phys. **56**, 1797 (1984).